

# UC Santa Barbara

## UC Santa Barbara Electronic Theses and Dissertations

### Title

Crystal Growth Modeling and Morphology Prediction of Complex Organic Molecules

### Permalink

<https://escholarship.org/uc/item/7km212ck>

### Author

Padwal, Neha Amol

### Publication Date

2024

Peer reviewed|Thesis/dissertation

University of California  
Santa Barbara

# Crystal Growth Modeling and Morphology Prediction of Complex Organic Molecules

A dissertation submitted in partial satisfaction  
of the requirements for the degree

Doctor of Philosophy  
in  
Chemical Engineering

by

Neha A. Padwal

Committee in charge:

Professor Michael F. Doherty, Chair  
Professor M. Scott Shell  
Professor Sho Takatori  
Professor Anton Van der Ven

December 2024

The Dissertation of Neha A. Padwal is approved.

---

Professor M. Scott Shell

---

Professor Sho Takatori

---

Professor Anton Van der Ven

---

Professor Michael F. Doherty, Committee Chair

September 2024

Crystal Growth Modeling and Morphology Prediction of Complex Organic Molecules

Copyright © 2024

by

Neha A. Padwal

“If I have seen further, it is  
by standing on the shoulders  
of Giants”

---

— Isaac Newton (1642-1727)

You are not a chemist and you are not a business major, but you need to be able to take what a chemist produces and turn it into a viable business. You cannot do this with engineering alone; you have to be able to make things happen that are a surprise to both sides. If not, then you won't be needed as engineers because the company can do it without you.

- Prof. Michael F. Doherty to his students in the Chemical  
Engineering Process Design Course

*To my parents, Asmita Padwal and Amol Padwal*

## Acknowledgements

This journey of last five years has been a deeply enriching one full of learning, inspiration and, growth. I'm grateful to the numerous people who have been a part of this journey in their unique wondrous ways, although only a few could be mentioned in this finite space.

I want to extend my sincerest gratitude to my advisor, Mike. I hit the advisor jackpot and could not have asked for a better advisor or research group. In many ways, he is an ideal advisor, for he would give me the freedom to explore my own ideas but also venture with me down to the weeds of the problem when needed. It has been a privilege to learn from his invaluable insights on topics ranging from science, engineering to philosophy and life. His constant support and zest during the uncertainties of research, has been a source of tremendous encouragement and inspiration. I want to thank him for his counsel, advice, wisdom, all of which I'll continue to cherish and look forward to more.

I'd like to heartily thank my parents, dearest Mom and Dad, for always having my back. This would not have been possible without their unwavering support, encouragement and warmth. Their staunch belief in me continues to be a source of tremendous strength for me. I'm also grateful for my brother, Neeraj, for his enduring support. I want to thank him for always being a call away, and his dependable presence.

I'd also like to thank all the Doherty group members. I appreciate all the discussions, debates, feedback on my work and thank them for sharing their expertise with me. I'd like to especially mention Dr. Yongsheng Zhao, whom I had the pleasure of collaborating with, his continued guidance and for always taking the time out whenever his expertise was required. I'd like to thank Dr. Tobias Mazal, for our insightful research discussions and synergistic research collaborations; Robert Gee for his continued support with software development; Dr. Vikram Khanna, Sumeet Chaudhary, Dr. Yuanyuan Sun, Steven



Landis for their unique expertise and support on myriad research topics. I've learned tremendously from each one of them. I'd also like to acknowledge our funding sources, Enabling Technologies Consortium (ETC), Eli Lilly, and International Fine Particle Research Institute (IFPRI), for their financial support and encouragement, which made this work possible.

I'd also like to thank my committee members, Prof. Scott Shell, Prof. Sho Takatori, Prof. Anton Van der Ven, for their feedback, research discussions and ensuring I was on the right track. My committee meetings would always be insightful and an intellectual exercise giving me a perspective, owing to them. I'd also like to thank Prof. Jim Rawlings, Prof. Linda Petzold and Dr. Yuriy Abramov for their expertise, research insights and discussions.

I'm grateful to my alma mater, ICT, for welcoming me to a fostering network. I'd like to thank my professors for their mentorship and providing me with a strong foundation and instilling in me a penchant for research and scientific development. I'd like to thank my friends from ICT, with special mention to Atharva, Shreya, Supriya, Ninad, for their insights, advice and steadfast support. I sincerely appreciate them for being my champions, critics, guides - on both personal and professional fronts alike. It would not have been possible without all of them.

I'd also like to extend my gratitude to both my grandmothers, my *Aajis*, for always encouraging me to shoot for the stars and being the wind in my sails. I'd also like to thank my extended family, Shilpa *Mavshi*, Vedant, *Kaka*, for their encouragement and continued support. I'm eternally grateful to my late grandfather, my *Ajoba*, for being the greatest teacher and my biggest support. His belief in me continues to embolden me to strive harder towards my goals.

I'm also grateful for all the friendships I have garnered in Santa Barbara over the years, it has been a pleasure getting to know and befriend these wonderful people. I'd like

to especially thank Ramya, Ankit, Tinish, Tanmay, Aishwarya, Varshika and Benu, for making this place home and being my companions in this ride. Our countless adventures from camping & boating to the cookouts & long road-trips, will always be cherished. I thank them sincerely for making this journey even more fun, joyful, beautiful and colorful.

And last but not the least, I'm immensely thankful for my several amazing friends, family and mentors, who have helped me in this journey in their own unique ways. I cannot imagine having made it this far without them all.

# Curriculum Vitæ

Neha A. Padwal

## Education

- 2024 Ph.D. in Chemical Engineering (Expected), University of California, Santa Barbara.
- 2019 Bachelors in Chemical Engineering, Institute of Chemical Technology, Mumbai.

## Publications

Padwal, N. A.; Doherty, M. F. Nonequilibrium Crystal Growth Model for Organic Molecules of Real API Complexity. *Crystal Growth & Design* **2024**. (*Manuscript under review*)

Padwal, N. A.<sup>‡</sup>; Mazal, T.<sup>‡</sup>; Doherty, M. F., Modern Modeling and Simulation Approaches for Morphology Predictions of Molecular Crystals. *Industrial & Engineering Chemistry Research* **2024**. (*Manuscript in press*)

Padwal, N.A.; Doherty, M.F. Step Velocity Growth Models for Molecular Crystals: Two Molecules in the Unit Cell. *Crystal Growth & Design* **2024**, 24(11), 4368-4379.

Padwal, N.A.; Doherty, M.F., Simple Accurate Nonequilibrium Step Velocity Model for Crystal Growth of Symmetric Organic Molecules. *Crystal Growth & Design* **2022**, 22(6), 3656-3661.

## Conference Presentations

Padwal, N.A.; Doherty, M.F., 'Crystal Growth Modeling and Morphology Predictions Of Complex Organic Molecules', *International Fine Particle Research Institute*, Annual Meeting, Toronto, June **2024**.

Padwal, N.A.; Doherty, M.F., 'Growth Modeling for Morphology Predictions of Organic Molecular AB Crystals', *American Institute of Chemical Engineers*, Annual Meeting, Orlando, November **2023**.

Zhao, Y.; Padwal, N.A.; Doherty, M.F., 'Morphology Predictions of Crystals Grown From Mixture Solvents', *American Institute of Chemical Engineers*, Annual Meeting, Orlando, November **2023**.

Padwal, N.A.; Doherty, M.F., 'Crystal Growth Modeling and Morphology Predictions of Complex Organic Molecules', *16th Annual Clorox-Amgen Graduate Student Symposium*, Department of Chemical Engineering, University of California Santa Barbara, September **2023**.

Padwal, N.A.; Doherty, M.F., 'NonEquilibrium Kink Density Model for Organic Molecular Crystals with Two Growth Units', *American Institute of Chemical Engineers*, Annual Meeting, Phoenix, November **2022**.

Padwal, N.A.; Doherty, M.F., 'A Simple Accurate Non-Equilibrium Kink Density Model for Centro-Symmetric Molecules', *American Institute of Chemical Engineers*, Annual Meeting, Boston, November **2021**.

#### **Awards and Honors**

Doctoral Student Travel Grant, the Academic Senate, University of California Santa Barbara, **2022**.

International Doctoral Fellowship, **2020**.

Dr. B. M. Khadilkar Endowment Award, ICT - Mumbai, **2016**.

Innovation in Science Pursuit for Inspired Research Scholarship, Government of India, **2015**.

## Abstract

Crystal Growth Modeling and Morphology Prediction of Complex Organic Molecules

by

Neha A. Padwal

Crystalline materials are ubiquitous in our daily lives - from the silicon wafer chips in our electronic devices to food we thrive on and medicines prolonging our lifetime. Controlling crystal growth properties becomes crucial to engineering material functionality. A growth model is necessary for design, control and optimization of crystallization processes. Moreover, it allows efficient exploration of growth conditions to form crystals with desirable properties. Previous work on growth models has mainly focused on symmetric organic molecules, salts and inorganic crystals. However, in the majority of cases the molecules of interest are highly asymmetric and lack an inversion center. The current models are plagued with flawed assumptions, making them unfit for real asymmetric molecules. To that end, we have developed a novel growth theory that enables prediction of fundamental growth parameters within a broader class of mechanistic multiscale crystal growth models. The theory - ‘Simplified Steady-State Framework’ is based on identifying a small subset of most-probable surface events which dominate the surface kinetics. In this work, we demonstrate the framework and its application to a Kossel crystal, and AB-type crystal ( $Z = 2$ ). We developed a Symbolic-Numerical digital tool which allows generalization of the theory to crystals with various molecules in the unit cell and demonstrate its applicability to crystals with four growth units in the unit cell ( $Z = 4$ ). The overarching goal of the project is development of a in-silico tool based on reliable multiscale growth models to allow high throughput screening of design conditions for crystal engineering of the general class of asymmetric organic molecular crystals.

# Contents

|  |            |
|--|------------|
| <b>Acknowledgements</b>                                    | <b>vii</b> |
| <b>Curriculum Vitae</b>                                    | <b>x</b>   |
| <b>Abstract</b>  | <b>xii</b> |
| <b>List of Figures</b>                                     | <b>xvi</b> |
| <b>List of Tables</b>                                      | <b>xxv</b> |
| <b>1 Introduction</b>                                      | <b>1</b>   |
| 1.1 Nonmechanistic Modeling Approaches . . . . .           | 4          |
| 1.2 Mechanistic Modeling Approach . . . . .                | 10         |
| 1.3 Solvent Effects . . . . .                              | 24         |
| 1.4 Kossel and non Kossel Crystals . . . . .               | 27         |
| 1.5 Morphology Predictions and ADDICT . . . . .            | 29         |
| 1.6 Permissions and Attributions . . . . .                 | 32         |
| <b>Bibliography</b>  | <b>34</b>  |
| <b>2 Simplified Steady-State Framework: Kossel Crystal</b> | <b>45</b>  |
| 2.1 Introduction . . . . .                                 | 45         |
| 2.2 Background . . . . .                                   | 47         |
| 2.3 Rate Model . . . . .                                   | 48         |
| 2.4 Methods . . . . .                                      | 51         |
| 2.5 Results and Discussion . . . . .                       | 56         |
| 2.6 Morphology Predictions . . . . .                       | 59         |
| 2.7 Conclusion . . . . .                                   | 63         |
| <b>Bibliography</b>  | <b>64</b>  |

|          |   |            |
|----------|---|------------|
| <b>3</b> | <b>Simplified Steady-State Framework: Molecular AB Crystals</b> | <b>69</b>  |
| 3.1      | Introduction . . . . .  | 69         |
| 3.2      | AB Organic Crystal System . . . . .                             | 71         |
| 3.3      | Methods and Approach . . . . .                                  | 73         |
| 3.4      | Row Instability . . . . .                                       | 88         |
| 3.5      | Results and Discussion . . . . .                                | 92         |
| 3.6      | Morphology Predictions . . . . .                                | 96         |
| 3.7      | Conclusions . . . . .   | 98         |
|          | <b>Bibliography</b>   | <b>100</b> |
| <b>4</b> | <b>SSSF Model and Simulations: A Comparative Study</b>          | <b>106</b> |
| 4.1      | Introduction . . . . .  | 106        |
| 4.2      | Background . . . . .  | 107        |
| 4.3      | Methods . . . . .   | 109        |
| 4.4      | Results and Discussion . . . . .                                | 112        |
| 4.5      | Conclusion . . . . .  | 116        |
|          | <b>Bibliography</b>   | <b>118</b> |
| <b>5</b> | <b>Graph Network Theoretic Tool for Model Development</b>       | <b>121</b> |
| 5.1      | Introduction . . . . .  | 121        |
| 5.2      | Graph Network Theory . . . . .                                  | 124        |
| 5.3      | Surface Kinetics Perspective . . . . .                          | 125        |
| 5.4      | Methods . . . . .   | 127        |
| 5.5      | Numeric Engine . . . . .  | 140        |
| 5.6      | Morphology Predictions and ADDICT . . . . .                     | 143        |
| 5.7      | Discussion . . . . .  | 148        |
| 5.8      | Conclusion . . . . .  | 149        |
|          | <b>Bibliography</b>   | <b>152</b> |
| <b>6</b> | <b>Summary, Conclusion and Future Directions</b>                | <b>157</b> |
| 6.1      | Summary . . . . .   | 157        |
| 6.2      | Future Directions . . . . .                                     | 163        |
|          | <b>Bibliography</b>   | <b>168</b> |
|          | <b>Appendices</b>   | <b>169</b> |
| <b>A</b> | <b>Junctions, Sites and Identification of Major sites</b>       | <b>170</b> |
|          | <b>Bibliography</b>   | <b>186</b> |

|   |            |
|---|------------|
| <b>B Analysis of AB Crystal - Configurations 2 and 3</b>                                      | <b>188</b> |
| <b>Bibliography</b>   | <b>219</b> |
| <b>C Surface Partition Functions and Configuration Constraints</b>                            | <b>221</b> |
| <b>Bibliography</b>   | <b>226</b> |
| <b>D Identification &amp; Assignment of Step Configuration for <math>Z = 4</math> Crystal</b> | <b>227</b> |
| <b>Bibliography</b>   | <b>232</b> |
| <b>E SSSF &amp; Kink Cycle Frameworks: Similarities and Differences</b>                       | <b>233</b> |
| <b>Bibliography</b>   | <b>237</b> |



# List of Figures

|     |   |    |
|-----|---|----|
| 1.1 | Pictorial depiction of the Frank-Chernov Condition[8, 14] for predicting steady-state crystal morphology, considering cross-section of a crystal. $G_i$ is the relative perpendicular growth rate of face $i$ . $H_i$ is the perpendicular distance of face $i$ from the origin $O$ . . . . .   | 6  |
| 1.2 | Schematic depiction of various types of face structures based on the number of PBCs parallel to the face slice, as put forth by Hartman and Perdok.[23, 29, 30] Three types of faces depicted are $F$ , $S$ and $K$ face types, parallel to two, one and zero PBCs, respectively. Figure reproduced with permission from Lovette et al.[13]. Copyright 2008 American Chemical Society. . . . .  | 10 |
| 1.3 | Sequential events followed by a growth unit in the process of surface integration from solution (either solution-terrace-edge-kink or the solution-terrace-kink mechanisms): terrace adsorption is followed by diffusion of the growth unit to a nearby step. The growth unit further diffuses along the step to a nearby kink. The terrace $\phi_T$ , edge $\phi_E$ and kink energies $\phi_K$ are half the broken-bond interactions along terrace, edge and kink axes, respectively. Figure adapted with permission from Tilbury et al[32]. Copyright 2016 American Chemical Society. . . . . | 11 |
| 1.4 | Growth trajectory map of a flat $F$ face as a function of supersaturation. Figure reproduced with permission from Lovette et al.[13]. Copyright 2008, American Chemical Society. . . . .  | 14 |
| 1.5 | AFM deflection images of experimental observations of crystal growth mechanisms: a) spiral growth hillocks on L-cystine crystals. Figure reproduced with permission from Shtukenberg et al.[55]. Copyright 2013 National Academy of Sciences, b) 2D nuclei on crystal surface of metal-organic framework MOF-5 and c) MOF-5 crystal surface approaching rough growth. Figures reproduced with permission from Cubillas et al.[56]. Copyright 2012 WILEY-VCH Verlag GmbH & Co. KGaA, Weinheim. . . . .   | 16 |
| 1.6 | An anti-clockwise growth spiral on a crystal face. The spiral sides act as crystal steps growing via kink incorporation. . . . .  | 17 |

|      |   |    |
|------|---|----|
| 1.7  | Growth mechanism of a spiral starting from a screw dislocation, a) Top view of the face depicting movement of steps, b) perspective view of the crystal depicting spiral growth. The steps on the spiral follow the condition: (i) For a step $i$ , $v = 0$ for $l < l_c$ and $v = v_{\text{inf}}$ for $l > l_c$ . Figure reproduced with permission from Lovette et al.[13]. Copyright 2008 American Chemical Society. . . . .   | 18 |
| 1.8  | Growth of 2D nucleus over a crystal surface. . . . .  | 20 |
| 1.9  | Step diagram and depiction of surface energies along various components of a step surface. $\gamma^K$ , $\gamma^E$ , and $\gamma^T$ are the surface energies of kink, edge and terrace surfaces, respectively. $a_P$ is the growth unit width in the direction of step growth, $a_E$ is the growth unit width along the step and $h$ is the growth unit height. Figure adapted with permission from Tilbury et al.[32]. Copyright 2016 American Chemical Society . . . . .  | 26 |
| 1.10 | Interaction network across a slice of a) naphthalene (centrosymmetric growth unit), b) Tazofelone (Noncentrosymmetric growth unit). The interaction network is generated using the software ADDICT.[90] . . . . .   | 28 |
| 1.11 | ADDICT's crystal morphology prediction methodology implemented for naphthalene, a) crystal structure allows crystallographic and unit cell information, b) solid-state calculation of interaction energies provides the network of interactions and PBCs, c) mechanistic model calculations provide spiral-shape estimates, d) steady-state morphology from the relative growth rates. Figure reproduced with permission from Li et al.[90]. Copyright 2016 Elsevier Ltd. . . . .   | 30 |
| 2.1  | Schematic depiction of a crystal surface with a step growing laterally across the face through attachment of growth units at various sites especially <i>kinks</i> . 46   |    |
| 2.2  | Gibbs free energy landscape of attachment and detachment processes along the reaction co-ordinate, $q$ . State S denotes solvated growth unit and solvated kink site, state ‡ denotes the transition state with partially solvated growth unit and desolvated kink site, while state X denotes solvated kink site post surface integration of growth unit. $\Delta G^\ddagger$ is the free energy barrier to surface integration of the growth unit; $\Delta G = G_S - G_X$ is the free energy difference between the states S and X and depends on supersaturation. Figure reproduced with permission from Li et al.[17] Copyright 2016 American Chemical Society. . . . . | 49 |

|      |  |    |
|------|--|----|
| 2.3  | Energy of interactions of a crystal growth unit in different directions. The interactions are categorised as intraedge (kink), interedge (edge), interslice (terrace) axes. The kink ( $\phi_K$ ), edge ( $\phi_E$ ) and terrace ( $\phi_T$ ) energies correspond to broken interactions along respective axes facing the solution. The reverse kink ( $\phi_{RK}$ ), reverse edge ( $\phi_{RE}$ ) and reverse terrace ( $\phi_{RT}$ ) energies correspond to satisfied interactions along respective axes that hold the growth unit to the crystal. Figure adapted with permission from Tilbury et al.[20]. Copyright 2017 American Chemical Society. . . . . | 50 |
| 2.4  | Surface kinetics diagram of a step along a Kossel crystal, depicting the most-probable event space $M$ within the sample space of all events $U$ . . .   | 52 |
| 2.5  | Most-likely surface events that result in formation or destruction of single kinks. Growth units colored yellow mark changes in configuration during the event. . . . .  | 54 |
| 2.6  | Most-likely surface events that result in formation or destruction of double-kinks. Growth units colored yellow mark changes in configuration during the event. . . . .  | 54 |
| 2.7  | Plot of non-equilibrium kink density for a Kossel crystal vs $S$ at bond energy $\beta\phi = 2.5$ . kMC simulation data points for the same Kossel system are obtained from Cuppen et al.[16] . . . . .  | 56 |
| 2.8  | Plot of normalized step velocity for a Kossel crystal vs $S - 1$ at bond energies: (a) $\beta\phi = 2.5$ , (b) $\beta\phi = 3$ . The kMC simulation data points for the same Kossel system at $\beta\phi = 2.5$ and 3 are obtained from Cuppen et al.[16] and Joswiak et al.[14], respectively. . . . .  | 58 |
| 2.9  | Crystal habit predicted by non-equilibrium model vs experimental data for the case of naphthalene growth from ethanol. Low and moderate $\sigma$ experimental morphologies are adapted with permission from Grimbergen et al.[35]. Copyright 1998 American Chemical Society . . . . .  | 61 |
| 2.10 | Crystal habits of the orthorhombic polymorph of Rubrene: a) predicted by non-equilibrium model, b) experimentally grown crystals by physical vapor transport. Figure reproduced with permission from De Boer et al.[36] Copyright 2004 WILEY-VCH Verlag GmbH & Co. KGaA, Weinheim.   | 62 |
| 3.1  | Different step configurations observed for an AB type organic crystal. The PBCs illustrate examples of real network of interactions along corresponding step configurations. The PBCs are generated by the software AD-DICT.[19] . . . . .   | 72 |

|     |   |    |
|-----|---|----|
| 3.2 | <p>(a) Predominant kink and edge junctions along step configuration 1 with alternating rows of growth units A and B (b) Crystalline lattice directions defined around a growth unit, namely, kink, edge, terrace and reverse kink, reverse edge and reverse terrace axes. <math>\phi_K, \phi_E, \phi_T</math> represent half of the bond energy formed by the growth unit along the <i>kink</i>, <i>edge</i> and <i>terrace</i> directions, respectively. These are the broken bond interactions exposed to the solvent. Similarly, <math>\phi_{RK}, \phi_{RE}, \phi_{RT}</math> represent half of the bond energy formed by the growth unit along the <i>reverse kink</i>, <i>reverse edge</i> and <i>reverse terrace</i> directions, respectively. The reverse bonds characterize interactions formed by the growth unit with the crystalline lattice. The lattice directions are aggregate descriptors and need not be orthogonal for real crystals. The step dimensions are characterized by propagation length (<math>a_P</math>), step height (<math>h</math>) and growth unit width (<math>a_E</math>). Figure reproduced with permission from Tilbury et al.[18]. Copyright 2017 American Chemical Society. . . . .</p> | 75 |
| 3.3 | <p>Schematic description of surface sites prevalent on step configuration 1 and surface events given by arrow descriptors. The surface sites can be segregated into two sets: 1) Subset <math>M</math> consists of <i>major sites</i> and <i>most-likely events</i> transform major sites into each other, 2) All other sites are assumed to sparsely populate the step surface and belong to subset <math>L</math>. A few <math>L</math> sites are depicted here, there are many more. The events which transform sites within subset <math>L</math> or across subsets occur at low probabilities and are categorised as the <i>less-likely events</i>. The <i>most-likely events</i> and <i>less-likely events</i> are depicted by solid and dashed arrows, respectively. The sample space of all surface sites along the step is the union of the two sets <math>U = M \cup L</math>. . . . .</p>  | 77 |
| 3.4 | <p>Step surface of configuration 1: Interaction spheres around growth units at various site types and the corresponding detachment rates are as follows: 1) B adatom (<math>j_{B,0}^-</math>), 2) east-facing A kink (<math>j_{A,1}^-</math>), 3) A edge (<math>j_{A,2}^-</math>), 4) west-facing A kink (<math>j_{A,1}^-</math>), 5) east-facing AB kink (<math>j_{A,1}^-</math>). The reverse interactions mark bonds formed by growth units with the crystal. The terrace and reverse terrace bonds are perpendicular to the page and not depicted for simplicity. . . . .</p>   | 79 |
| 3.5 | <p>Partition function of a site composed of adjoining junctions: A edge and A kink. Given the position of A edge, <math>\alpha</math> sums over all junctions that can be contiguous to it. Given the position of A kink, <math>\beta</math> sums over all permissible junctions that can be contiguous to it. East and west-facing kinks of the same type are identical for configuration 1 and therefore have equal kink densities (<math>\rho_A^e = \rho_A^w = \frac{\rho_A}{2}</math>, <math>\rho_B^e = \rho_B^w = \frac{\rho_B}{2}</math>). For <math>\alpha</math> summation, only east-facing A kink is structurally permissible to adjoin A edge. Similarly, only west-facing B kink is structurally permissible. As a result, <math>\rho_A</math> and <math>\rho_B</math> are halved in the summation. . . . .</p>   | 81 |

|      |   |     |
|------|---|-----|
| 3.6  | Most-likely events causing formation and destruction of A kinks. . . . .  | 83  |
| 3.7  | NEQ kink density predictions for step configuration 1 vs kink anisotropy $\Delta_k$ along the kink axis at $S = 1$ . Here $\phi_B^K = \phi_A^K + \Delta_k$ , $\phi_A^K = 2.5k_B T$ , $\phi_A^E = \phi_B^E = \phi_A^T = \phi_A^{RT} = \phi_B^T = \phi_B^{RT} = 2.5k_B T$ . As dictated by step configuration 1, $\phi_A^K = \phi_A^{RK}$ , $\phi_B^K = \phi_B^{RK}$ , $\phi_A^E = \phi_B^{RE}$ , $\phi_B^E = \phi_A^{RE}$ . . . . .  | 92  |
| 3.8  | (a) Normalized step velocity $\frac{v}{k^+ a_P x_{sat}}$ vs kink anisotropy $\Delta_k$ along kink axis at $S = 1.1$ for this model and kMC simulations from the literature[18] for step configuration 1. ( $\phi_A^K = 4k_B T$ , $\phi_A^E = \phi_B^E = 4k_B T$ , $\phi_A^T = \phi_B^T = 4k_B T$ ), (b) Normalized step velocity $\frac{v}{k^+ a_P x_{sat}}$ vs edge anisotropy $\Delta_e$ along edge axis at $S = 1.1$ for this model and kMC simulations from the literature[18] for step configuration 1 ( $\phi_A^E = 2k_B T$ , $\phi_A^K = \phi_B^K = 2k_B T$ , $\phi_A^T = \phi_B^T = 2k_B T$ ). Step velocity is normalized with respect to the propagation length $a_P$ , attachment rate constant $k^+$ and solubility $x_{sat}$ to allow comparison with the kMC data. . . . .  | 94  |
| 3.9  | Normalized step velocity $\frac{v}{k^+ a_P}$ vs supersaturation plots on a) a log scale and b) linear scale, for step [011] on non-Kossel (011) face of a naphthalene crystal graph following the notation of Cuppen et al.[9]. Such a step corresponds to step configuration 1. The kMC simulations were performed by Cuppen et al.[9] for the same crystal graph with interaction network characterized by $\phi_a = 2k_B T$ , $\delta = \frac{\phi_q}{\phi_p}$ , such that $2\phi_a = \phi_p + \phi_q$ for different values of $\delta$ . . . . .  | 95  |
| 3.10 | (a) Experimental shape observations of OWIVEY form I in ethanol/water 9:1 solution. Figure reproduced with permission from Larpent et al.[44]. Copyright 2021 American Chemical Society. (b) Model-based in-silico morphology predictions. . . . .  | 98  |
| 4.1  | Flow diagram outlining the kMC simulation methodology. Figure and caption adapted with permission from Mazal et al.[19] Copyright 2024 American Chemical Society. . . . .   | 111 |
| 4.2  | SSSF model predictions (lines) for densities of distinct kink types, namely, A kink density (red solid line), B kink density (green solid line), AB kink density (yellow solid line) and BA kink density (blue solid line) on Configuration 1 with kMC simulation results (dots) of respective kink densities at varied dimensionless kink anisotropy, $\beta\Delta_K$ , at $S = 1.0$ , where $\beta = \frac{1}{k_B T}$ . The dashed lines of corresponding colors, provides the equilibrium model[1] predictions under the same interaction anisotropic conditions. The interaction spheres of A and B growth units are: $\phi_B^K = \phi_A^K + \Delta_K$ , $\phi_A^K = 2.5k_B T$ , and $\phi_A^E = \phi_B^E = \phi_A^T = \phi_A^{RT} = \phi_B^T = \phi_B^{RT} = 2.5k_B T$ . For Configuration 1, $\phi_A^{RK} = \phi_A^K$ and $\phi_B^{RK} = \phi_B^K$ . As we move to the right along the abscissa, we increase the B kink energy, while keeping the A kink energy constant. . . | 112 |

- 4.3 SSSF model predictions (lines) for distinct kink types on Configuration 1 with kMC simulation results (dots) at varied dimensionless edge anisotropy,  $\beta\Delta_E$ , at  $S = 1.1$ . Here  $\phi_B^E = \phi_A^E + \Delta_E$ ,  $\phi_A^E = 2k_B T$ , and  $\phi_A^K = \phi_B^K = \phi_A^T = \phi_B^T = 2k_B T$ . For the interactions in reverse kink and reverse terrace directions are  $2k_B T$ . For Configuration 1,  $\phi_A^{RE} = \phi_B^E$  and  $\phi_B^{RE} = \phi_A^E$ . kMC simulations were conducted at  $S = 1.1, T = 298$  K in a box of size  $2500 \times 240$  growth units for up to 300 million MC steps. . . . . 114
- 4.4 (a) Kink density and (b) normalized step velocity  $\frac{v}{a_P x_{sat}}$  model predictions and kMC simulation results for Configuration 1 as a function of dimensionless edge anisotropy,  $\beta\Delta_E$ , at  $S = 1.5$ . The interaction spheres of A and B growth units are:  $\phi_B^E = \phi_A^E + \Delta_E$ ,  $\phi_A^E = 3k_B T$ ,  $\phi_A^K = \phi_B^K = \phi_A^T = \phi_B^T = \phi_A^{RT} = \phi_B^{RT} = 3k_B T$ . As per step topology,  $\phi_A^{RE} = \phi_B^E$  and  $\phi_B^{RE} = \phi_A^E$ . Simulation data are averaged over 5 simulations conducted at  $S = 1.5, T = 298$  K in a box of size  $750 \times 250$  growth units for 5 million MC steps. . . . . 115
- 4.5 (a) Kink density and (b) normalized step velocity  $\frac{v}{a_P x_{sat}}$  model predictions and kMC simulation results for Configuration 1 as a function of dimensionless kink anisotropy,  $\beta\Delta_K$ , at  $S = 1.5$ . The interaction spheres of A and B growth units are:  $\phi_B^K = \phi_A^K + \Delta_K$ ,  $\phi_A^K = 3k_B T$ ,  $\phi_A^E = \phi_B^E = \phi_A^{RE} = \phi_B^{RE} = \phi_A^T = \phi_B^T = \phi_A^{RT} = \phi_B^{RT} = 3k_B T$ . As per step topology  $\phi_A^{RK} = \phi_B^K$  and  $\phi_B^{RK} = \phi_A^K$ . Simulation data are averaged over 5 simulations conducted at  $S = 1.5, T = 298$  K in a box of size  $750 \times 250$  growth units for 5 million MC steps. . . . . 116
- 5.1 Schematic depiction of a crystal surface with a step growing laterally across the face through attachment of growth units at various sites especially *kinks*. 122
- 5.2 A general multi-directed graph network. The nodes are denoted by red dots and characterized by  $n_i$ . The arcs are directional and connect two nodes within the graph, characterized by  $\hat{e}_{i,j}$  where  $i$  and  $j$  are the start node and end node, respectively. The nodes and arc attributes are embedded with customized properties. The global attribute  $G$  characterizes the graph and embedded with graph properties. . . . . 125
- 5.3 A Kossel step comprises of single type of growth unit or multiple growth units which have identical surrounding interaction networks. The PBC network (dots are growth units, lines are interactions) illustrate two examples: single growth unit vs multiple growth units which are energetically equivalent. PBC networks are generated using the software ADDICT.[32] 130

|      |   |     |
|------|---|-----|
| 5.4  | a) Surface kinetics diagram of a step along a Kossel crystal, depicting the most-probable event space $M$ within the sample space of all events $U$ . b) The corresponding graph network diagram for the most-probable events along the Kossel step. The nodes denote the <i>major sites</i> and the arcs denote the most-probable events capturing the interactions between the nodes. The attachment and detachment events are denoted by the solid and dashed lines, respectively. $j^+$ and $j_k^-$ are the attachment and detachment elementary rates, respectively, where $k$ is the number of kink detachment bonds. . . . .   | 131 |
| 5.5  | Step configurations occurring along an AB crystal ( $Z = 2$ ) and corresponding illustrations of PBC networks. (dots are molecules, lines are interactions) PBC networks are generated using the software ADDICT.[32]   | 134 |
| 5.6  | Crystal face with two molecules in the unit cell, AB crystals, constitute steps of three configurations depicted in Fig. 3.2, out of which associated diagrams for configuration 1 with alternate A and B rows are illustrated: a) Surface kinetics diagram depicting the most-probable event space $M$ within the sample space of all events $U$ . b) The corresponding graph network diagram for the most-probable events along the AB step. The nodes denote the <i>major sites</i> and the arcs denote the most-probable events capturing the interactions between the nodes. The attachment and detachment events are denoted by the solid and dashed lines, respectively. | 135 |
| 5.7  | Example step configurations for crystals with 4 molecules in the unit cell: 1) rows of single growth units, 2) rows comprising of a subset of all growth units, 3) a single row-type consisting of all growth units. Illustrations of periodic bond chains for corresponding step configurations in crystal networks. PBC networks are generated using the software ADDICT.[32] .   | 138 |
| 5.9  | Illustration of parametric continuation performed to arrive at the solution to the final crystal step with anisotropic bonds. The solid dots are the growth units and solid lines are the interactions. Different colored lines and dots, depict distinct interactions and growth units, respectively. The interaction networks are generated using ADDICT.[32] . . . . .   | 142 |
| 5.10 | (a) Experimental shape observations of Tazofelone (CSD ref code:WIMBAV13) in toluene. Figure reproduced with permission from Price et al.[38]. Copyright 2014 Elsevier B.V. (b) Model-based in-silico morphology prediction of Tazofelone in toluene. . . . .   | 144 |
| 5.11 | (a) Experimental shape observations of benzoic acid (CSD ref code:BENZAC02) in water. Figure reproduced with permission from Liang et al.[39]. Copyright 2017 Elsevier Ltd. (b) Model-based in-silico morphology prediction of benzoic acid monomer in water, (c) Model-based in-silico morphology prediction of benzoic acid dimer in water. . . . .   | 146 |

|      |  |     |
|------|--|-----|
| 5.12 | (a) Experimental shape observations of lovastatin (CSD ref code: CEK-BEZ) in isopropanol. Reproduced with permission from Kuvadia and Doherty[4]. Copyright 2011 American Chemical Society. (b) Model-based in-silico morphology prediction of lovastatin in isopropanol. . . . .  | 147 |
| 5.8  | Graph network diagram for the step configuration with alternate rows of four growth units A, B, C and D. The nodes denote the <i>major sites</i> and the arcs denote the most-probable events capturing the interactions between the nodes. The attachment and detachment events are denoted by the solid and dashed lines, respectively. . . . .  | 151 |
| 6.1  | Periodic bond chain network for faces of centrosymmetric and non-centrosymmetric growth units: a)Face (110) of naphthalene (centrosymmetric growth unit) (b) Face (011) of paracetamol (non-centrosymmetric growth unit). Different line colors denote different bond energies, and the bond strength is proportional to the line thickness.[1] The PBCs are generated using the software ADDICT.[3] . . . . .   | 164 |
| A.1  | Edge, kink and double-kink junctions and corresponding densities. . . . .  | 171 |
| A.2  | Surface kinetics diagram of a step along a Kossel crystal, depicting the most-probable event space $M$ within the sample space of all events $U$ . . .   | 173 |
| A.3  | Energy of interactions of a crystal growth unit in different directions. The interactions are categorised in intraedge (kink), interedge (edge), interslice (terrace) axes. The kink ( $\phi_K$ ), edge ( $\phi_E$ ) and terrace ( $\phi_T$ ) energies correspond to broken interactions along respective axes facing the solution. The reverse kink ( $\phi_{RK}$ ), reverse edge ( $\phi_{RE}$ ) and reverse terrace ( $\phi_{RT}$ ) energies correspond to satisfied interactions along respective axes that hold the growth unit to the crystal. Figure adapted from Tilbury et al.[2] . . . | 174 |
| A.4  | Most-likely surface processes affecting single and double-kink density through creation and annihilation events. . . . .   | 176 |
| A.5  | Plot of normalised step velocity $v/(a_P k^+ x_{sat})$ vs $S - 1$ for Kossel crystals at bond energies: (a) $\beta\phi = 2$ , (b) $\beta\phi = 2.5$ and (c) $\beta\phi = 3$ . kMC simulation data points at $\beta\phi = 2, 3$ are obtained from Joswiak et al.[7] and at $\beta\phi = 2.5$ are obtained from Cuppen et al.[8] . . . . .   | 178 |
| A.6  | Plot of total kink density, $\rho_T$ vs driving force $\sigma = S - 1$ at $\beta\phi = 3$ calculated using the non-equilibrium model in Eqs. (9), (10) and (15) in the paper and its quadratic approximation. . . . .  | 181 |
| B.1  | Step configurations encountered on an organic crystal with two growth units A and B. PBCs are generated using the software ADDICT.[1] . . .  | 189 |
| B.2  | Predominant junctions along step configuration 2: edge, single and double kinks. The superscripts $e$ and $w$ denote east and west facing kinks, respectively. . . . .   | 190 |



|     |  |     |
|-----|--|-----|
| B.3 | Predominant junctions along step configuration 3: edge, single and double kinks. The superscript $e$ and $w$ denote east and west facing kinks, respectively. . . . .  | 197 |
| B.4 | Normalized step velocity vs supersaturation $S$ for (a) [100] step on non-Kossel (001) face (step configuration 2), (b) [011] step on non-Kossel (100) face (step configuration 3) of a naphthalene crystal graph. The step velocity is normalized by $a\frac{k_B T}{h} \equiv a_P k^+$ , where $a$ is the step propagation length and $h$ is the Planck's constant. The solid lines are generated by our model, dots depict kMC data taken from literature[4]. The two colors correspond to the two different values of $\delta$ . (Refer Cuppen et al.[4]) . . . . . | 204 |
| B.5 | Periodic bond chain networks across the following <i>flat F</i> faces of OWIVEY (A) (0 $\bar{1}$ 1), (B) (0 $\bar{1}$ 0), and (C) ( $\bar{1}$ 11). PBCs are generated using the software ADDICT.[1] . . . . .  | 206 |
| B.6 | Spiral shapes for the following <i>F</i> faces of OWIVEY (A) (0 $\bar{1}$ 1), (B) (0 $\bar{1}$ 0), and (C) ( $\bar{1}$ 11). Spiral shapes are generated using the software ADDICT.[1] . . . . .  | 207 |
| B.7 | a)SSSF model-based morphology prediction of Celecoxib grown in toluene at 333 K and $S = 1.02$ b) SEM photographs of celecoxib recrystallized from toluene at 60°C. Figure reproduced with permission from Modi et al.[11]. Copyright 2013 American Chemical Society. . . . .  | 207 |
| B.8 | a) SSSF model-based morphology prediction of $\beta$ -glycine grown in ethanol at 298K and $S = 1.01$ , b) Snapshot of $\beta$ -glycine grown in (v/v) water-ethanol solvent mixture. Figure reproduced with permission from Ferrari et al.[12]. Copyright 2003 American Chemical Society. . . . .   | 208 |
| B.9 | a)SSSF model-based morphology prediction of Piracetam grown in isopropanol at 293 K and $S = 1.1$ , b) Micrograph of Piracetam polymorph II crystals grown in isopropanol. Figure reproduced with permission from Lynch et al.[13]. Copyright 2021 American Chemical Society. . . . .  | 209 |
| C.1 | Collections of kink types constrained by growth units along step configuration with checkered pattern of A and B growth units, resulting in partition functions $Q_1$ and $Q_2$ , respectively. . . . .  | 223 |
| C.2 | Some configuration types of steps on crystals with four growth units in the unit cell namely A, B, C and D. . . . .  | 224 |
| C.3 | Collections of kink types constrained by A growth unit along step configuration 1 with rows of growth units, resulting in the partition function $Q_1$ . PBCs are generated using the software ADDICT.[1] . . . . .  | 225 |
| D.1 | All permissible step configuration types for a crystal with four growth units A, B, C, D in the unit cell. PBC networks are generated using the software ADDICT.[1] . . . . .  | 229 |
| D.2 | Examples of crystallographically impermissible configurations in a crystal with 4 and 2 growth units in the unit cell, respectively. . . . .   | 231 |

# List of Tables

A.1 Configuration table of major sites for a Kossel step and their influence on single-height kinks. The *Attachment* column denotes the change in the number of single-height kinks upon incorporation of relevant growth unit at the site of interest. The *Detachment* column denotes the change in the number of single-height kinks upon detachment of growth unit from the site of interest. Events marked ‘—’ convert the site into another out of the most-likely space and hence are not considered. The *attachment* and *detachment rate* columns provide the rate of respective elementary reactions along the step surface. The attachment rate is isotropic for all sites while detachment rate depends upon the growth unit detached and the number of neighboring kink bonds broken. The *site density* depends on the density of adjoining junctions and the appropriate partition function to account for the surface correlations. The sites are representative of their corresponding mirror images, since the east and west facing kinks have equivalent interaction networks. Similar tables can be constructed for all the predominant edge and kink types. . . . . 182

|     |   |     |
|-----|---|-----|
| A.2 | Configuration table of major sites for a Kossel step and their influence on double-height kinks. The <i>Attachment</i> column denotes the change in the number of double-height kinks upon incorporation of relevant growth unit at the site of interest. The <i>Detachment</i> column denotes the change in the number of single-height kinks upon detachment of growth unit from the site of interest. Events marked ‘-’ convert the site into another out of the most-likely space and hence are not considered. The <i>attachment</i> and <i>detachment rate</i> columns provide the rate of respective elementary reactions along the step surface. The attachment rate is isotropic for all sites while detachment rate depends upon the growth unit detached and the number of neighboring kink bonds broken. The <i>site density</i> depends on the density of adjoining junctions and the appropriate partition function to account for the surface correlations. The sites are representative of their corresponding mirror images, since the east and west facing kinks have equivalent interaction networks. Similar tables can be constructed for all the predominant edge and kink types. . . . . | 184 |
| B.1 | OWIVEY - ethanol system calculation results for intermediate variables including: $\phi_{PBC}$ - average strength of periodic bond chain in kcal/mol, $a_P$ - average propagation length in $\text{\AA}$ , $a_E$ - average growth unit width along the step in $\text{\AA}$ , $l_c$ - critical length of the step in $\text{\AA}$ , $v$ - step velocity in $\text{\AA}/s$ , conf - step configuration type from Fig. 3.1, $d_{hkl}$ - interplanar spacing of the face in $\text{\AA}$ , $G$ - growth rate of the face and $R$ - relative growth rate of the face. . . . .   | 205 |
| B.2 | Configuration table of major sites for step configuration 1 and their influence on A kinks. The <i>Attachment</i> column denotes the change in the number of A kinks upon incorporation of relevant growth unit at the site of interest. The <i>Detachment</i> column denotes the change in the number of A kinks upon detachment of growth unit from the site of interest. Events marked ‘-’ convert the site into another out of the most-likely space and hence are not considered. The <i>attachment</i> and <i>detachment rate</i> columns provide the rate of respective elementary reactions along the step surface. The attachment rate is isotropic for all sites while detachment rate depends upon the growth unit detached and the number of neighboring kink bonds broken. The <i>site density</i> depends on the density of adjoining junctions and the appropriate partition function to account for the surface correlations. The sites are representative of their corresponding mirror images, since the east and west facing kinks have equivalent interaction networks. Similar tables can be constructed for all the predominant edge and kink types. . . . .                              | 210 |

- B.3 Configuration table of major sites for step configuration 2 and their influence on east-facing A kinks. The *Attachment* column denotes the change in the number of east A kinks upon incorporation of relevant growth unit at the site of interest. The *Detachment* column denotes the change in the number of east A kinks upon detachment of growth unit from the site of interest. Events marked ‘–’ convert the site into another out of the most-likely space and hence are not considered. The *attachment* and *detachment rate* columns provide the rate of respective elementary reactions along the step surface. The attachment rate is isotropic for all sites while detachment rate depends upon the growth unit detached and the number of neighboring bonds broken. The *site density* depends on the density of adjoining junctions and the partition function to account for the surface correlations. Sites 3-6 and 11-16 will have corresponding west-facing counterparts, which are left out of the table because of their lack of impact on east-facing A kinks. Construction of master equations for west-facing kinks will require the consideration of corresponding west-facing sites. Similar tables can be constructed for all the predominant edge and kink types. . 213
- B.4 Configuration table of major sites for step configuration 3 and their influence on east-facing A kinks. The *Attachment* column denotes the change in the number of A kinks upon incorporation of relevant growth unit at the site of interest. The *Detachment* column denotes the change in the number of A kinks upon detachment of growth unit from the site of interest. Events marked ‘–’ convert the site into another out of the most-likely space and hence are not considered. The *attachment* and *detachment rate* columns provide the rate of respective elementary reactions along the step surface. The attachment rate is isotropic for all sites while detachment rate depends upon the growth unit detached and the number of neighboring bonds broken. The *site density* depends on the density of adjoining junctions and the appropriate partition function to account for the surface correlations. Sites 3-6 and 11-16 will have corresponding west-facing counterparts, which are left out of the table because of their lack of impact on east-facing A kinks. Construction of master equations for west-facing kinks will require the consideration of corresponding west-facing sites. Similar tables can be constructed for all the predominant edge and kink types. . 216

# Chapter 1

## Introduction

“No one can pretend that the overall position on mathematical models in current use for design is satisfactory. Progress is required in both directions, towards simpler models which give an adequate representation for the early stages of design and towards more accurate models which reflect the true influence of design variables for use in the later stages of design. On the latter question, the problem is not so much one of numerical techniques but one of basic understanding of the physical mechanisms involved. ... Real progress can only come from painstaking and detailed experimental and theoretical work over the whole field of chemical engineering.”[1] (Prof. Roger Sargent (1926-2018), Father of Process Systems Engineering)

With technological advances, process modeling and simulation software have revolutionized the field of chemical engineering and process manufacturing in the last few decades. Aspen Hysys, Aspen plus, CHEMCAD, gPROMS are the industry standard for process modeling, simulation and design of various mainstream chemical operations and have enabled streamlining the design of safe, efficient and sustainable processes. This has also saved the chemical and hydrocarbon industry significant investment in time,

and revenues and energy by allowing multi-variable design, control and optimization of capital and operational costs. This was made possible due to the years of fundamental research that enabled development of fundamental and process models, design principles and subsequently simulation techniques that allow rapid prediction of system behaviours for a range of input design variables.

On the other hand, the global pharmaceutical industry, valued at over a trillion USD (in 2017)[2] has long been plagued with significant investment cost and long drug development timelines right from the discovery stage to the bedside stage. On an average, for a single drug to reach the patients requires investment of over 2 billion dollars, with merely 6-10 years remaining of patent-protected production of the drug.[3, 4] Over 90% of small molecule active pharmaceutical ingredients (APIs) are delivered in crystalline form.[4] A significant cause of the high costs is the R&D investments. The financial burden is compounded by the lack of predictive models and simulation software for crystal engineering and in-silico crystal design. This entails heavy investment in experiments and empirical methodologies towards design and optimization of crystallization processes. Hence, comprehensive in-depth fundamental research is pivotal in key areas of crystal structure prediction, solubility prediction, nucleation, crystal dissolution and growth studies, crystal morphology selection. Multi-pronged and coordinated research efforts at the intersection of experiments, theory and computations will expand and advance our understanding of crystal growth and enable development of *crystals with a purpose*. [5] In this work, we propose and deep dive into a new crystal growth theory for modeling growth parameters and combine it with computations and experimental observations from the literature in an effort to predict and thereby control crystal growth behaviour.

Apart from pharmaceutical industry, crystalline materials are ubiquitous in a range of industries including materials and semiconductors, food and beverage, fuel cells, nanotechnology, chemicals, and polymers. Controlling and maintaining the properties of

these crystalline materials is key to capturing the desired functionality of the product. The substrates grown under different conditions give rise to crystals with a diverse range of crystal properties. In order to explore the continuum of crystal properties, we require the predictive ability of a growth function given the nature of growth conditions. This predictive nature traces back to the need for a growth model that captures the physics and chemistry of crystal growth. A growth model enables prediction of various crystal properties such as the crystal shape or morphology, crystal size and polymorph or the crystal structure. The final product functionality dictates desired properties of the crystals. Any slight change in these properties could drastically affect key formulation properties like toxicity, bioavailability, catalytic activity, dispersability, mechanical properties, etc.[4, 6] For instance, within the pharmaceutical space, a uniform distribution of equidimensional crystals is desirable since they offer better dissolution, as well as ease of processing. Bioavailability, a critical pharmacokinetic parameter, is the percentage of ingested drug reaching systemic circulation. For low-solubility drugs, the bioavailability depends on the dissolution behaviour of crystal facets and needs to be optimized to ensure adequate amounts of the API reaches its target in human bodies. In catalysis, specific facets of the crystalline surfaces offer higher catalytic properties and hence plate-like morphology is preferred which exposes facets with the highest catalytic activity. On the other hand, in LEDs rod-like crystals are desired since the anisotropy of properties provides directional sensitivity to external stimuli.

Apart from the tunability of crystal-specific properties, a model is also necessary for design and control of crystallization processes. The process systems engineering architecture is built upon mathematical models describing the system's behaviour change in response to design variables. Hence a growth model enables design of crystallization process systems, installment of control systems and optimization of design variables with respect to cost, energy requirement whilst growing crystals with desired properties and

functionality.

Experiments have popularly been employed for exploring the space of growth parameters to trace the corresponding crystal property domain. Such an approach is time and energy intensive and also ineffective in exploration of nuances in the crystal property continuum to arrive at the global optimum that can potentially be achieved for a wide range of growth conditions such as temperature, supersaturation and solvent conditions. Growth models can better guide design of experiments in screening of parametric space for optimal conditions of production.

Mathematical modeling of crystal growth phenomenon plays a key role in crystal habit predictions. Crystal habit is the shape of the crystal and crystal morphology relates to the specific faces bounding the crystal surface. The growth models can be used for shape and morphology prediction based on relative growth rate estimates.[7, 8] The population balance theory[9], widely used for modeling distribution of properties of a particulate systems, also needs to be supplied with growth models to obtain the size distribution of crystals and the associated dynamics. Growth models can also inform control of polymorph in an MSMPR (Mixed Suspension Mixed Product Removal) crystallizer, as derived through a linear stability analysis.[10] In case of batch crystallizers, polymorph selection hinges on induction time of the most stable form. Hence, growth models are indispensable to devise rational design principles for crystallization processes as well as crystal form attributes.

## 1.1 Nonmechanistic Modeling Approaches

Given the diverse advantages, several growth models have been proposed in literature. The growth models can be broadly categorised into the nonmechanistic and mechanic approaches. The nonmechanistic modeling approaches are based on associating the growth



rate to a substrate physical quantity based on approximate empirical observations. The mechanistic approach is based on encapsulating the growth mechanism at various scales through solid-state physics, surface chemistry and thermodynamics. Major nonmechanistic models are mentioned below,

### 1.1.1 Gibbs' thermodynamic model

One of the first models for informing crystal habit was put forth by Gibbs around 1879.[11] Gibbs proved that at equilibrium, the total surface free energy of the crystal will be minimized. The total surface energy contributes to the free energy penalty upon crystal formation and is proportional to the surface area  $A_i$  of each face  $i$  with a surface energy of  $\gamma_i$ . The free energy reward is incurred due to phase change into a more thermodynamically stable crystal phase.

$$\Delta G = -\frac{V\Delta\mu}{V_M} + \sum_i \gamma_i A_i \quad (1.1)$$

where  $\Delta\mu$  is the difference in chemical potentials of the substrate crystal and solution phases,  $V$  and  $V_M$  are the crystal volume and molecular volume, respectively. The equilibrium crystal shape is attained when the free energy is minimized and we get,

$$\sum_i \gamma_i dA_i = 0 \quad (1.2)$$

The crystal shape which satisfies the above constraint is given by the Wulff construction.[12]

$$\frac{\gamma_1}{H_1} = \frac{\gamma_2}{H_2} = \dots = \frac{\gamma_i}{H_i} = 1 \quad (1.3)$$

where  $H_i$  is the perpendicular distance of face  $i$  from a common origin. Note that the orientation of the facets is characterized by Miller indices and fixed by the crystallography.

However, the equilibrium shape is usually not attainable for crystals owing to the high reorganization barriers, except for smaller crystals such as nanocrystals, wherein thermodynamics plays a greater role. Hence, kinetics of crystal growth will determine the crystal habit and determine the shape of the crystal instead of the thermodynamics, as also noted by Gibbs in a footnote of his article. Crystal habit is dominated by the kinetically slowest-growing facets and  $\sum_i \gamma_i A_i$  will not usually be minimized.[11, 13] Analogous

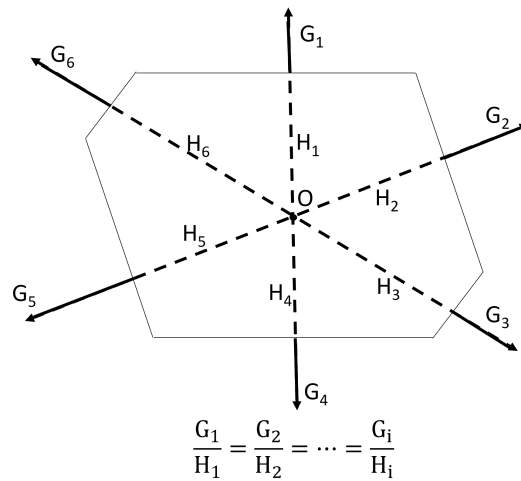


Figure 1.1: Pictorial depiction of the Frank-Chernov Condition[8, 14] for predicting steady-state crystal morphology, considering cross-section of a crystal.  $G_i$  is the relative perpendicular growth rate of face  $i$ .  $H_i$  is the perpendicular distance of face  $i$  from the origin  $O$ .

to the thermodynamically-controlled Wulff construct, the kinetically-controlled shape of the crystal will reach a fixed time-independent steady-state shape and is given by the Frank-Chernov Condition.[8, 14]

$$\frac{G_1}{H_1} = \frac{G_2}{H_2} = \dots = \frac{G_i}{H_i} \quad (1.4)$$

where  $G$  is the perpendicular growth rate of face  $i$ . The condition states that the distance of a face  $i$  from a fixed origin will be proportional to its growth rate as depicted in Fig. 1.1. Zhang et.al.[15, 16] and Snyder et.al.[17] constructed a set of linear differential

equations governing dynamic evolution of shape in conditions of growth and dissolution. Steady-state analysis of differential equations revealed that the crystal evolves into a unique shape at steady-state during constant growth conditions regardless of the initial seed habit, which is given by the Frank-Chernov condition in Eq. 1.4. This steady-state shape is a function of relative growth rates, which allows shape prediction without estimation of rate constants. However, the unique steady-state shape during dissolution is unstable and hence the system will continuously evolve away from the steady-state. The Frank-Chernov condition forms the basis of shape construction from relative growth rate calculations using the growth models in the rest of this dissertation.

### 1.1.2 BFDH model

One of the first nonequilibrium models for crystal habit was put forth by Bravais, Friedel, Donnay and Harker (BFDH).[18–20] The BFDH model posits that the growth rate ( $G_{hkl}$ ) of a crystal face with Miller indices ( $hkl$ ) is inversely proportional to the interplanar spacing ( $d_{hkl}$ ) between successive layers of the face. This is based on the general experimental observation that the faces dominating crystal shapes have high interplanar spacing. Interplanar spacing is a crystallographic quantity and is a function of the Miller indices and lattice parameters and constant for a given face. Hence, the model can be easily implemented since it only requires the crystal unit cell parameters and yields single shape prediction for a given crystal.

$$G_{hkl} \propto \frac{1}{d_{hkl}} \quad (1.5)$$

Although the model has shown to provide good estimates for some vapor-grown crystals, it is usually not accurate for solution grown crystals.[21, 22]

### 1.1.3 The Attachment Energy Model

Hartman and Perdok[23] initially introduced the concept of *attachment energy*. It is defined as the energy per growth unit released when slice of the face ( $hkl$ ) is attached to the crystal. On the contrary, *slice energy* is the energy per growth unit released upon the slice formation. A growth unit is the species integrating along the crystal surface. (e.g., molecule, ion) The *lattice energy* is the sum total of all solid-state interactions between growth units in the crystal. Hence, the lattice energy is the combination of attachment energy and slice energy.

$$E^{lat} = E^{att} + E^{slice} \quad (1.6)$$

Attachment energy is the aggregate of out-of-slice interaction energies, while slice energy is the aggregate of in-slice interactions. Hartman and Bennema[24], later put forth the attachment energy model which posits that the growth rate of a crystal face is proportional to its attachment energy.

$$G_{hkl} \propto E_{hkl}^{att} \quad (1.7)$$

The model is based on the tenet that the stronger the bonds attaching the in-slice growth units to the crystal, the faster will be the growth of the slice. The attachment energy model has been observed to be an improvement over the BFDH model, since it goes beyond the crystallographic inputs and accounts for the interaction energies between growth units.[21] However, the model provides a single prediction for a given crystal and does not account for the growth environment and hence it cannot explain the dynamic shape changes observed for crystals in changing environments. To that end, the modified attachment energy (MAE) aims to account for the solvent conditions by interfacing the solid-state attachment energies with the solution environment of interest. MAE models commonly utilize molecular dynamics (MD) simulations or force field-based molecular

modeling to calculate the binding energies of solvent-crystal interactions to account for additives, temperature, and solvent-mixtures.[25–28] Apart from the computational expense, the method is still based on an arbitrary linear functional form of dependence of the growth rates with respect to attachment energies. Lack of kinetics-based and mechanistic inputs to the model restricts its ability to provide predictions for a range of crystal-environment systems.

### 1.1.4 Periodic Bond Chain Model

In a series of pivotal papers, Hartmann and Perdok[23, 29, 30] introduced the concept of periodic bond chains to draw a connection between solid-state energetic and crystal surface morphology. Periodic Bond Chains (PBCs) are chains of repeating strong inter-growth unit interactions. A PBC vector provides the crystallographic directions which are aligned with strong supramolecular bonds. Hartman and Perdok laid down guidelines for PBC selection and highlighted their implications on crystal morphology. The theory is based on the hypothesis that the high bond energy chains inform morphology developments in crystal growth such that prominent faces comprise of at least two strong PBCs.

According to the theory, there are three types of faces, depending on the number of PBCs running parallel through the face slice: flat faces ( $F$  faces) with at least two parallel PBCs, stepped faces ( $S$  faces) with a single PBC and kinked faces ( $K$  faces) with no PBC parallel to the face slice. The  $F$  faces are the slowest growing stable faces, growing layer-by-layer and hence usually have a *flat* surface topography. In the mechanistic modeling section 1.2, we study the role of PBCs in the growth of  $F$  faces. The  $S$  and  $K$  faces are the faster growing faces, owing to low detachment barriers from lack of strong in-slice interactions. The crystal surface is usually dominated by the slowest-growing  $F$  faces,

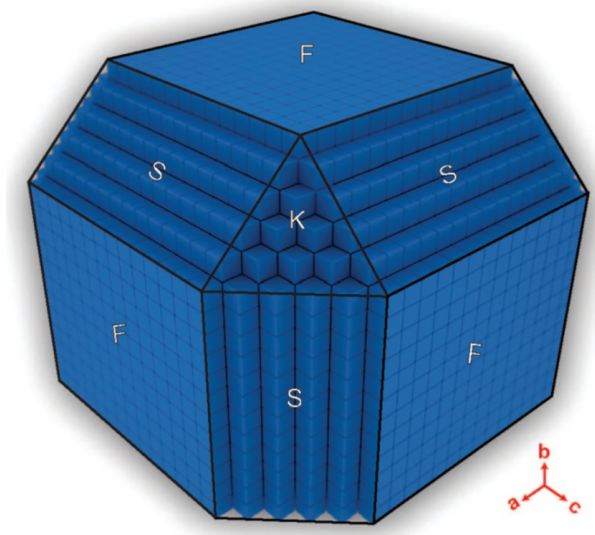


Figure 1.2: Schematic depiction of various types of face structures based on the number of PBCs parallel to the face slice, as put forth by Hartman and Perdok.[23, 29, 30] Three types of faces depicted are  $F$ ,  $S$  and  $K$  face types, parallel to two, one and zero PBCs, respectively. Figure reproduced with permission from Lovette et al.[13]. Copyright 2008 American Chemical Society.

since the  $S$  and  $K$  faces grow much faster causing them to grow-out of the crystal shape.

## 1.2 Mechanistic Modeling Approach

Crystal growth is a multiscale process occurring across various time and length scales - from surface integration of molecules to propagation of 2D nuclei across the crystal surface. A mechanistic approach to modeling is a hierarchical framework with constituent atomistic, mesoscale to continuum-scale models, transmitting information down or up the hierarchy. Such a hierarchy can be broadly segregated into two levels: *atomistic* and *continuum* scale models.[31] *Atomistic models* govern the elementary rates of attachment and detachment and the solid-state physics and surface chemistry. *Continuum models* govern the kinematics of growth depending on the growth mechanisms. Such an ab initio framework accounts for the crystallography, solid-state physics, surface chemistry at the interfacial level as well as the growth kinematics. This is contingent on fundamental

understanding of crystal growth at various scales to effectively model the impact of growth conditions as a function of temperature, supersaturation and solvent and their interplay.

### 1.2.1 Atomistic Modeling: Step kinetics

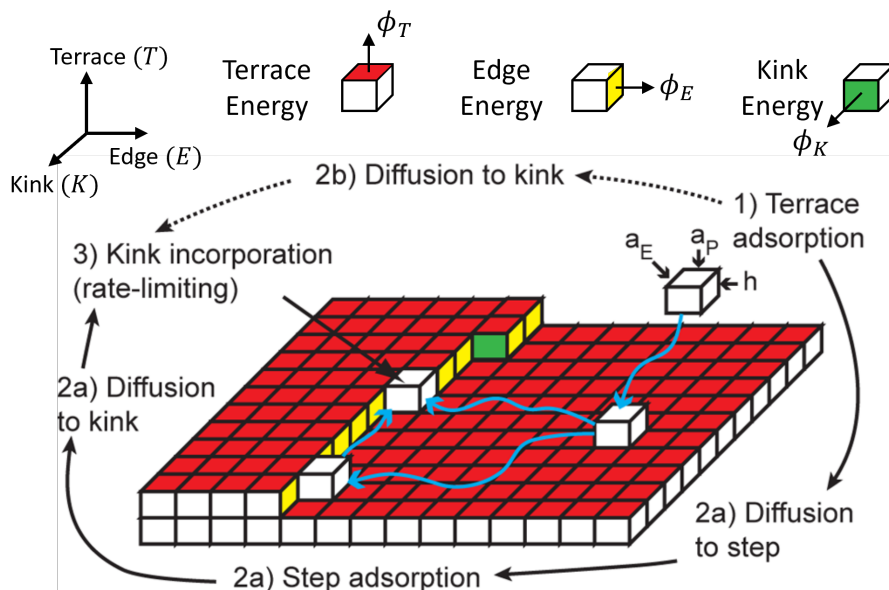


Figure 1.3: Sequential events followed by a growth unit in the process of surface integration from solution (either solution-terrace-edge-kink or the solution-terrace-kink mechanisms): terrace adsorption is followed by diffusion of the growth unit to a nearby step. The growth unit further diffuses along the step to a nearby kink. The terrace  $\phi_T$ , edge  $\phi_E$  and kink energies  $\phi_K$  are half the broken-bond interactions along terrace, edge and kink axes, respectively. Figure adapted with permission from Tilbury et al[32]. Copyright 2016 American Chemical Society.

Crystal growth at the most fundamental scale occurs via incorporation of growth units at various sites along the surface. A growth unit (GU) is the chemical species that integrates itself into a crystal surface when a driving force is applied (e.g., molecule, ion, dimer). These growth units could be identical in the solution but incorporated into the lattice in different orientations (e.g., organic crystals) or distinguishable in solution (e.g., ionic or mixed crystals). The surface sites which are most favorable for attachment

are *kinks*, because of their low energy penalty and ability to regenerate itself.[33–40] *Kinks* are regenerated after incorporation of growth units, thereby acting as catalytic sites resulting in further growth. A generalised pathway for growth unit attachment is depicted in Fig. 1.3. The growth unit diffuses from the bulk solution to a terrace site followed by partial desolvation. It then diffuses to an edge followed by diffusion along the edge to a kink site leading to kink incorporation. Gradual GU incorporation at kinks propels the step in the normal direction at a constant rate termed as the *step velocity*. Studies of step dynamics for step velocity modeling are broadly divided into two categories: 1) diffusion of growth units[41, 42], and 2) direct integration at kinks[37, 38, 43–45]. In this work, we assume surface diffusion is fast enough and rate is limited by kink integration of growth units.[32] The assumption is most appropriate for solvent-grown and melt-grown crystals, wherein the free energy barrier is dominated by desolvation of growth units.[39] This allows treating surface integration as a reaction process and the elementary attachment and detachment rates are modelled as microkinetic expressions. The step propagation is often considered to grow entirely from attachment at kinks, hence step velocity  $v$  of a step  $i$  critically depends on the density of kinks.[41, 46–48]

$$v = a_P u_k \rho_k \tag{1.8}$$

where  $a_P$  is the step propagation length,  $\rho_k$  is the kink density and  $u_k$  is the kink rate. The kink rate is the net rate of attachment events at the kinks and modelled via suitable elementary rate models.[36, 46, 49, 50] The kink densities are frequently modelled at equilibrium using Frenkel’s equilibrium kink density  $\rho_{eq}$  formulation[51] based on the Boltzmann distribution.

$$\rho_{eq} = \frac{2 \exp(-\beta \phi_k)}{1 + 2 \exp(-\beta \phi_k)} \tag{1.9}$$



where  $\beta = \frac{1}{k_B T}$  is the thermodynamic beta,  $k_B$  is Boltzmann constant,  $T$  is temperature, and  $\phi_k$  is the kink energy. The new theory introduced later in Chapter 2 will overcome the equilibrium assumption in Eq. 1.9 to provide a nonequilibrium kink density model. The kink rate depends on the elementary attachment and detachment rates modelled by the random rain model[46] and is given by,

$$\begin{aligned} u_k &= j^+ - j_k^- \\ j^+ &= k^+ x_{sat} S \\ j_k^- &= k_{k,i}^- \end{aligned} \tag{1.10}$$

where  $x_{sat}$  is the solubility or saturation mole fraction,  $S$  is supersaturation,  $k^+$  is the attachment rate constant,  $k_{k,i}^- = k^+ e^{\Delta W_k \beta}$  is the detachment rate constant, and  $\Delta W_k$  is the work of detachment at kinks and is the summation of interactions broken along kink, edge and terrace axes.

$$\Delta W_k = 2\phi^{RK} + 2\phi^{RE} + 2\phi^{RT} \tag{1.11}$$

where  $\phi^{RK}, \phi^{RE}$  and  $\phi^{RT}$  are the interaction energies along reverse kink, reverse edge and reverse terrace directions, respectively. Expressions for  $k^+$  can be modelled through reaction rate theory. For crystals with a single growth unit in the lattice such as Kossel crystals (see section 1.4), where all kinks are equivalent, the net rate of attachment  $u_k$  will be constant across all kinks as derived in supplementary information of Sun et al.[52],

$$\begin{aligned} u_k &= j^+ - j_k^- \\ &= k^+ x_{sat} (S - 1) \end{aligned} \tag{1.12}$$

Hence, *step velocity* and *kink density* are the important parameters obtained from atomistic models. These parameters are supplied to the continuum-scale models and ul-

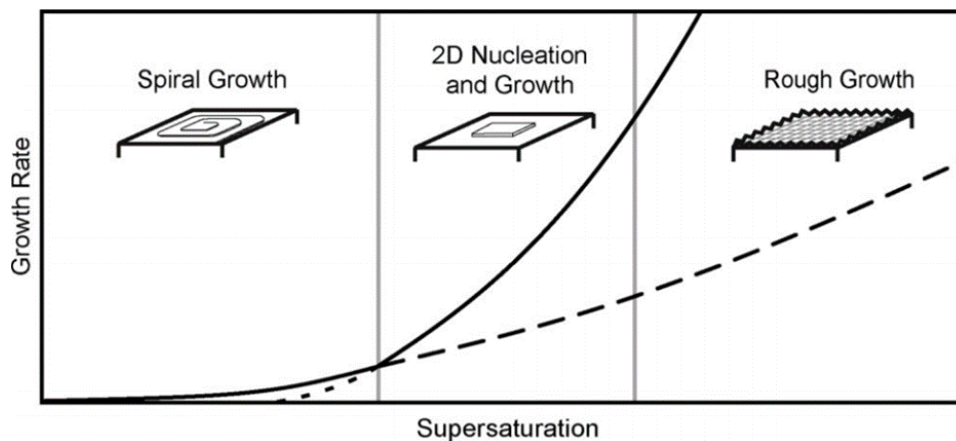


Figure 1.4: Growth trajectory map of a flat  $F$  face as a function of supersaturation. Figure reproduced with permission from Lovette et al.[13]. Copyright 2008, American Chemical Society.

mately determine the growth rates. In chapter 2, we delve further into several other kink density and step velocity models and propose a novel theory for estimation of nonequilibrium kink density and step velocities for asymmetric molecular crystals.

### 1.2.2 Continuum Modeling: Mechanisms of Crystal Growth

A crystal face grows in different regimes depending on the supersaturation. The evolution of regimes with increase in supersaturation was observed experimentally by Land and De Yoreo.[53] At a given supersaturation, a crystal face will grow in the regime that yields fastest rate. Hence, it is possible for a crystal to have different faces growing in different regimes. Fig. 1.4 depicts a typical growth map for a crystal face. At low supersaturation, crystal growth is dominated by the classical Burton Cabrera Frank (BCF) spiral growth mechanism,[41] in which screw dislocations provide the surface for attachment of GUs. At moderate supersaturation, growth occurs by the 2D nucleation regime, which has two sub-regimes. In the birth and spread sub-regime, formation of a 2D nucleus of critical size is the rate determining step, after which it grows continuously across the crystal surface. In the poly-nuclear sub-regime, nucleation rate is high and growth

of multiple nuclei collectively contributes to growth of that layer. At very high supersaturation, surface integration of GUs is no longer the rate determining step and transport effects must be accounted for. However, industrial crystallizers generally operate in the layered growth regimes (spiral growth and 2D nucleation), since rough growth conditions result in excessive secondary nucleation. Note, that such a transition is peculiar to the F faces. The stepped and kink faces are always within the rough regime, because of a zero roughening transition temperature.[54] Fig. 1.5 provides Atomic Force Microscopy (AFM) deflection images of crystal surfaces growing in spiral growth, 2D nucleation and transition to rough growth regimes.

During layered growth, the mechanistic route to modeling growth rate  $G$  estimates the slice height  $h$  grown and time required to grow the slice ( $\tau$ ) of a face ( $hkl$ ), which depends on the growth mechanism or regime.

$$G_{hkl} = \left( \frac{h}{\tau} \right)_{hkl} \quad (1.13)$$

where  $\tau$  is the spiral rotation time for spiral regime and face coverage time for the 2D nucleation regime.

## Spiral Growth

In a landmark paper in 1951, Burton-Cabrera-Frank[41] proposed the spiral growth mechanism which posits that the imperfections in crystals, particularly screw dislocations provide a renewable surface area for incorporation of growth units and hence growth of the crystal giving rise to growth hillocks depicted in Fig. 1.6. The theory granted explanation for high crystal growth rates observed at low supersaturation, which could not be explained by the 2D nucleation owing to high free energy barriers. Since then many spirals have been observed on crystal surfaces by AFM.[57–59] The dynamics of

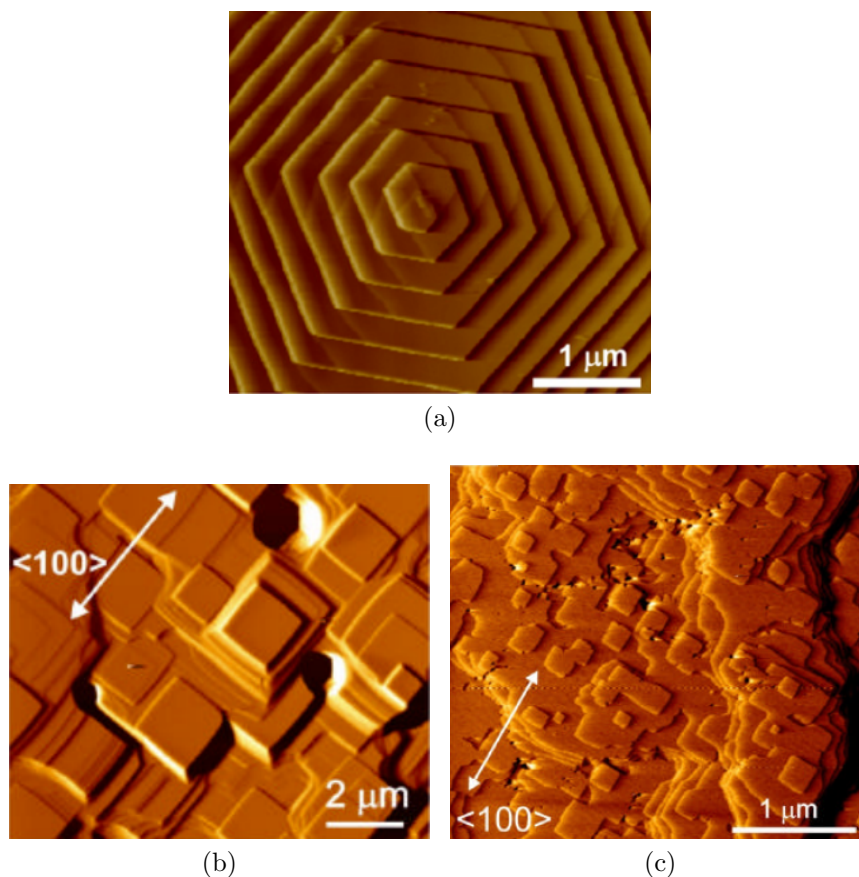


Figure 1.5: AFM deflection images of experimental observations of crystal growth mechanisms: a) spiral growth hillocks on L-cystine crystals. Figure reproduced with permission from Shtukenberg et al.[55]. Copyright 2013 National Academy of Sciences, b) 2D nuclei on crystal surface of metal-organic framework MOF-5 and c) MOF-5 crystal surface approaching rough growth. Figures reproduced with permission from Cubillas et al.[56]. Copyright 2012 WILEY-VCH Verlag GmbH & Co. KGaA, Weinheim.

initial formation of a spiral from a screw dislocation are depicted in Fig. 1.7, wherein the dislocation exposes a step providing surface for GU attachment causing it to grow outward. As the step grows it exposes another step, which in turn starts growing upon reaching a certain length termed as the *critical length*  $l_c$ . Depending on the direction of the dislocation, the process continues to generate clockwise or anticlockwise spirals. The spiral edges grow via step propagation as discussed in section 1.2.1 and the rate of their growth is given by the step velocity. Henceforth, the concepts of *edge* and *step* will be used synonymously in this chapter. The growth rate of the face depends on the duration

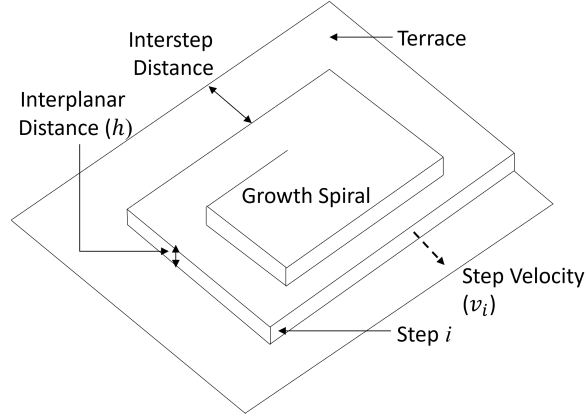


Figure 1.6: An anti-clockwise growth spiral on a crystal face. The spiral sides act as crystal steps growing via kink incorporation.

required for the spiral to complete a single turn, which is the spiral rotation time  $\tau_s$ . Since each edge of the spiral only starts progressing in the normal direction once it has reached its critical length, the rotation time is the duration required for all the steps to reach their respective critical lengths.

$$G = \frac{h}{\tau_s} \quad (1.14)$$

$$\tau_s = \sum_i \frac{l_{c,i+1} \sin(\alpha_{i,i+1})}{v_i}$$

where  $i$  characterises a particular step and its properties,  $l_{c,i}$  is the critical length of step  $i$ ,  $\alpha_{i,i+1}$  is the angle between the orientations of steps  $i$  and  $i+1$  and  $v_i$  is the step velocity of step  $i$ . The critical length of a step  $i$  is evaluated by the contributions to the Gibbs free energy change during step dynamics. Upon addition of a layer of atoms along step  $i$ , the free energy change  $\Delta G$  increases due to increase in surface area, while it reduces due to crystallization into a more thermodynamically stable state.[60, 61]

$$\frac{\Delta G(n_i)}{k_B T} = 2 \frac{\phi_{k,i}}{k_B T} (1 - \delta_{n_i}) - n_i \ln(1 + \sigma) \quad (1.15)$$

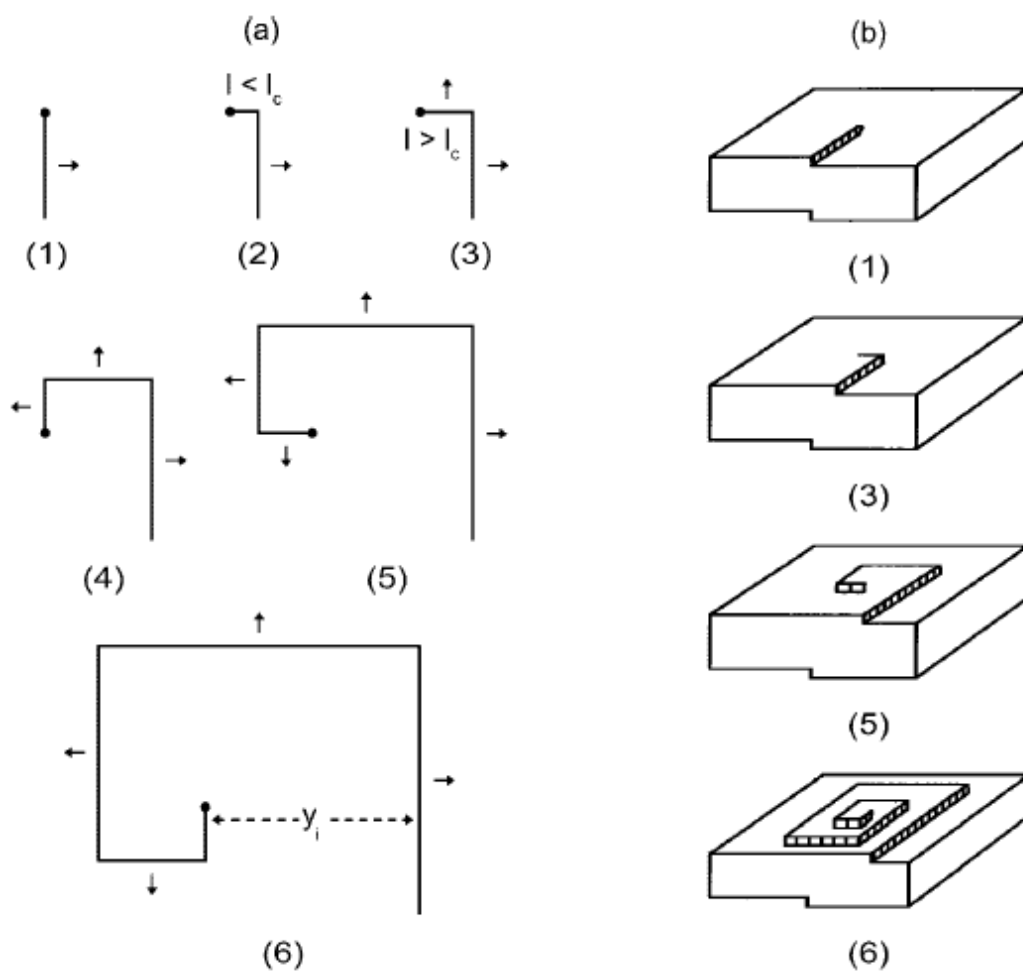


Figure 1.7: Growth mechanism of a spiral starting from a screw dislocation, a) Top view of the face depicting movement of steps, b) perspective view of the crystal depicting spiral growth. The steps on the spiral follow the condition: (i) For a step  $i$ ,  $v = 0$  for  $l < l_c$  and  $v = v_{\text{inf}}$  for  $l > l_c$ . Figure reproduced with permission from Lovette et al.[13]. Copyright 2008 American Chemical Society.

where  $\sigma = \frac{x}{x_{sat}} - 1$  is the crystallization driving force,  $x$  is the solute mole fraction,  $x_{sat}$  is the saturation mole fraction,  $\phi_k$  is the kink energy, the Kronecker delta  $\delta_{n_i}$  ensures that the surface penalty vanishes when there are no growth units along the step ( $n_i = 0$ ). The number of growth units ( $n_i$ ) along step  $i$  is expressed as a function of its length  $l_i$  as

$$n_i = \frac{l_i}{a_{E,i}} \quad (1.16)$$

where  $a_{E,i}$  is the intermolecular distance along step  $i$ . At the critical length  $l_{c,i}$ , the Free energy change in Eq. 1.15 becomes zero and we get,

$$l_{c,i} = \frac{2a_{e,i}\phi_{k,i}}{k_B T \ln(1 + \sigma)} \quad (1.17)$$

Step velocity  $v_i$  is the rate at which the step progresses in the normal direction. Voronkov's condition[62] is used for instructing step dynamics which takes the form of a heaviside function.

$$v_i = \begin{cases} 0 & l \leq l_{c,i} \\ v_i^{\text{inf}} & \text{else} \end{cases} \quad (1.18)$$

The condition states that the step begins to advance at a constant velocity, only after the length of the edge reaches its critical length. The step velocity  $v_i^{\text{inf}}$ , henceforth referred to as  $v_i$ , is modelled through atomistic modeling such as Eq. 1.8. Constant step velocity would ensue constant distances between respective sides of spirals which is in agreement with experimental observations.[63, 64] Substituting Eqs. 1.12,1.14, 1.17 in the growth model provides,

$$G = (k^+ x_{sat}) \left( \frac{h}{\tau^*} \right) (\sigma \ln(1 + \sigma)) \quad (1.19)$$

Here, the first factor is solvent dependent, the second factor is face dependent and the third factor depends on supersaturation.  $\tau^*$  denotes the rotation time expression with

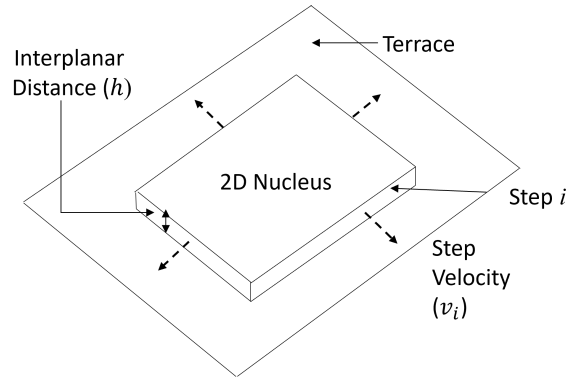


Figure 1.8: Growth of 2D nucleus over a crystal surface.

supersaturation dependence extracted out. Most industrial crystals are grown within the spiral growth regime since it offers a controlled growth environment.

## 2D Birth and Spread

As supersaturation is increased, the barrier to formation of a 2D nucleus on crystal facets reduces and 2D nucleation becomes the predominant growth regime. The regime manifests itself in two subregimes: 2D birth and spread[65] (low nucleation rates) and polynuclear[66] (high nucleation rates). In 2D birth and spread mechanism, the rate determining factor is the formation of a critical sized 2D nucleus, which subsequently grows across the crystal face. In this subregime, the growth rate depends on the 2D face coverage time. The full derivations of face coverage time in birth & spread and polynuclear regimes for polygonal nuclei across solvent-grown crystals are covered by Lovette et al.[48] and Tilbury et al.[61], respectively.

The face coverage time is derived by solving for full coverage by the growing 2D nucleus for a constant nucleation rate.[48, 65] The face coverage of 2D birth and spread  $\tau_{2D,B+S}$  is a function of nucleation rate  $J$  and step velocities  $v_i$  of the nucleus edges.

$$\tau_{2D,B+S} = (Jf)^{-1/3} \quad (1.20)$$



where  $f$  is a function of step velocity ( $v_i$ ) and tangential velocity ( $v_i^t$ ) of the nucleus edges  $i$ .

$$f = \frac{1}{6} \sum_{i=1}^N v_i v_i^t \quad (1.21)$$

Similar to the spiral edges, the edges of a 2D nuclei grow via step propagation and modelled via kink incorporation as given in Eq. 1.8. This reinforces the importance of step velocity models in growth rates of layered growth mechanisms, since the rotation time of a spiral as well as the face coverage time depend on the rate of progression of steps. The tangential step velocity ( $v_i^t$ ) of step  $i$  is a function of its step velocity and that of its adjacent steps  $i - 1$  and  $i + 1$ . If a step is growing fast enough, it can have a negative tangential velocity and hence disappear eventually from the growing nucleus.[47] The activated process of 2D nucleation occurs through formation of a critical-sized 2D nucleus such that its formation occurs at an energetic expense, while growth is energetically favorable. Hence, the nucleation rate  $J$  takes the form[48],

$$J = \kappa_{2D} e^{-\beta \Delta G_c} \quad (1.22)$$

where  $\kappa_{2D}$  is the prefactor and  $\Delta G_c$  is the free energy barrier for formation of a 2D critical nucleus. The free energy barrier  $\Delta G_c$  is obtained by aggregating surface energy penalty and volume reward of crystallization.  $\Delta G$  is differentiated to solve for the size of the critical nucleus and upon resubstitution we get[61],

$$\frac{\Delta G_c}{k_B T} = \frac{1}{4} \left( \frac{s_F \phi_E}{k_B T} \right)^2 \left( \frac{1}{\ln(1 + \sigma)} \right)^2 \quad (1.23)$$

The most stable steps along a crystallographic plane align with chains of strong repeating interactions[47] and hence provided by the periodic bond chains studied in Section 1.1.4. Hence the shape of the critical nucleus and shape factor depend on the PBC directions

and strength of their interactions.[61] The prefactor ( $\kappa_{2D}$ ) in Eq. 1.22 can be obtained by applying stationary nucleation rate theory for circular nuclei to critical polygonal nuclei, whose edges align with PBCs[67, 68] and rewriting  $J$  as,

$$J = zw_C^+ C_0^{2D} \quad (1.24)$$

where  $z$  is the Zeldovich factor[67],  $w_C^+$  is the total rate of attachment to critical nucleus[68],  $C_0^{2D}$  is the concentration of critical nuclei on the face. The expression for Zeldovich factor[67, 69] upon resubstitution and simplification is given by[61],

$$z = \left( \frac{-\frac{d^2 \Delta G}{dn^2} |_{n=n_c}}{2\pi k_B T} \right)^{1/2} = \left( \frac{s_F \phi_E}{8\pi k_B T n_c^{3/2}} \right)^{1/2} \quad (1.25)$$

where  $s_F$  is the shape factor and  $n_c$  is the number of molecules within the critical-sized nucleus, which can be calculated as a function of lattice and solid-state parameters. For estimation of  $w_C^+$ , all the attachment event rates ( $j^+$ ) at all the kinks on all the edges  $i$  of the nucleus are considered.[61]

$$w_C^+ = \sum_{i=1}^N n_{C,i} \rho_{k,i} j^+ \quad (1.26)$$

where  $n_{C,i}$  is the number of molecules in the critical nucleus along step  $i$ . The attachment rate can be estimated through the rate model expressed in Eq. 1.10 and constant across all steps, since solubility is a crystal-solvent property. The concentration of adsorption sites ( $C_0^{2D}$ ) on the face will depend upon the squared mean of characteristic length of molecules along the edge.

$$C_0^{2D} = \frac{1}{\left( \frac{1}{N} \sum_{i=1}^N a_{E,i} \right)^2} \quad (1.27)$$

where  $a_E$  is the intermolecular width along step  $i$ . Hence, all fundamental and interme-

diated parameters in the growth model expression can be evaluated with the exception of the rate constant  $k^+$ . Substitution of the expressions in Eq. 1.20, provides us with the growth rate of face in 2D birth and spread regime to a multiplicative constant  $k^+$ . This is analogous to the spiral growth model in Eq. 1.19.

## 2D Polynuclear

As we further increase the supersaturation, the nucleation rate increases such that multiple 2D nuclei collectively contribute to the face coverage. In this regime, growth is dominated by the nucleated areas instead of the lateral growth of nuclei via step propagation. Hence, the face coverage time depends on the area of a critical nucleus  $A_c$  in polynuclear regime and given by,

$$\tau = \frac{1}{JA_c} \quad (1.28)$$

where the area can be evaluated from directions and strength of PBC interactions.[61]

The above mechanistic framework for spiral growth and 2D nucleation provides a mathematical description of the phenomenon. All the parameters can be evaluated from the equations above, except for the rate constant ( $k^+$ ) in the rate model. Providentially, the growth models in layered regimes are all linear with respect to the rate constant. Hence the assumption of isotropic  $k^+$  allows estimation of relative growth rates and consequently crystal shape, by means of the Frank-Chernov Condition in Eq. 1.4 and Fig. 1.1.

## Rough growth

As supersaturation is increased further, the molecular incorporation into crystal surface sites ceases to be the rate determining step. The growth of crystal surfaces is now

restricted by how fast the substrate can diffuse across the surface boundary layer and is available for its incorporation into kink sites. This describes the onset for rough growth regime and mass transfer starts to dominate the growth rates. Lovette et al.[13] conducted scaling analysis on the mass, heat and momentum balance equations for a crystallization process system and based on the orders of magnitudes of the dimensionless numbers demonstrated that in the layered growth regimes surface integration is rate-limiting. As the driving force increases, the surface integration is fast enough to not be the bottleneck for crystal growth. The rough growth is characterized by coarse surfaces with significant number of kinks, owing to the high attachment rates. The growth is no longer layer-by-layer, instead rapid attachment is observed across all types of sites across the crystal facet. It must be noted that there can be different faces growing in different mechanisms or regimes depending on the face properties. Generally, the low index faces have more in-plane interactions and tend to grow by layered mechanisms, referred to as  $F$  faces. On the contrary, the high index faces have low in-slice interactions and high broken-bond interactions at the surface. This results in a significant number of kinks along the faces. The rough growing faces typically grow 10-100 times faster than that of crystals in layered growth regimes.[13] As a result, the  $S$  and  $K$  faces usually grow out of the morphology, or if present, cause anisotropic needle or plate-like behaviour.

### 1.3 Solvent Effects

The choice of solvent has the potential to dramatically affect the morphology.[32] Proper consideration of solvent effects remains crucial to reliable prediction of crystal properties. The presence of a solvent incurs differential effects on surface energy of various crystal faces, altering rates of molecular attachment and detachment. The change of surface energies will influence all the interactions ( $\phi_s$ ) within the rate model. Within

the mechanistic framework, the solvent-modified interactions are captured within the elementary rates of attachment  $j^+$  and detachment  $j^-$  in the form of the works  $\Delta W$  such as Eq. 1.11. The work of detachment at kinks  $\Delta W_k$  is the summation of bond energies broken during detachment along the edge, kink or terrace axes and is given by

$$\Delta W_k = 2(\phi^{RK} + \phi^{RE} + \phi^{RT}) \quad (1.29)$$

where  $\phi^{RK}$ ,  $\phi^{RE}$ ,  $\phi^{RT}$  denote broken bond energies in reverse kink, reverse edge and reverse terrace directions, respectively as depicted in Fig. 2.3. The prefactor of 2 accounts for the convention that  $\phi$  represents half the bond energy between growth units. Alternatively, the work is expressed with respect to the surface energies as,

$$\Delta W_k = 2(\gamma^K a_P h + \gamma^E a_E h + \gamma^T a_E a_P) \quad (1.30)$$

where  $\gamma^K$ ,  $\gamma^E$ , and  $\gamma^T$  are the surface energies of kink, edge and terrace surfaces, respectively.  $a_P$ ,  $a_E$  and  $h$  are geometrical dimensions of the growth unit as depicted in Fig. 1.9.

Presence of a solvent affects the interfacial energy at the crystal surface. Specifically the kink, edge and terrace broken bond energies at the surface will be altered based on the interaction between crystal-solvent. Molecular dynamics (MD) simulations have been widely performed towards quantification of solvent effects.[70, 71] In order to allow rapid calculations, we use the bulk-interface approximation (Dupré equation[72]) to evaluate solvent-modified bond energies, notwithstanding high fidelity of MD predictions. Based on this approximation, the crystal-solvent interface energy depends on the individual crystal  $\gamma_S$  and solvent cohesive energies  $\gamma_S$  and their work of adhesion  $\Delta W_{ad,XS}$ . [47, 73,

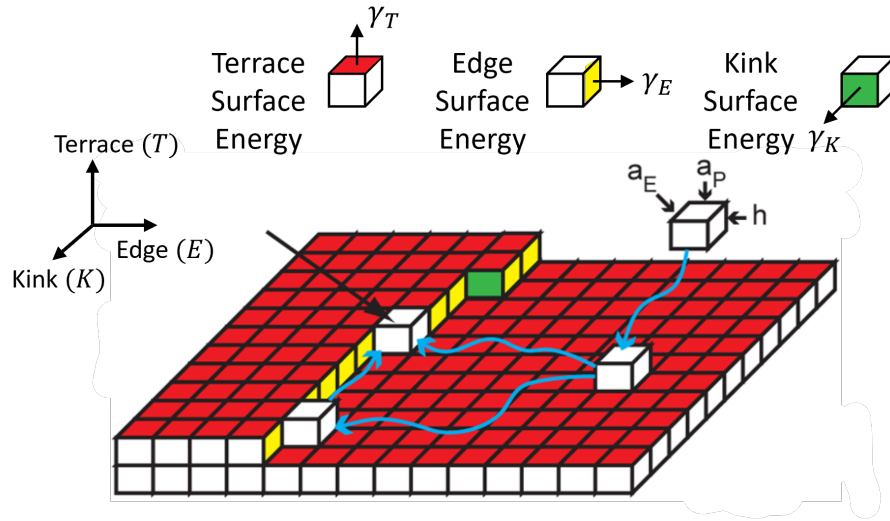


Figure 1.9: Step diagram and depiction of surface energies along various components of a step surface.  $\gamma^K$ ,  $\gamma^E$ , and  $\gamma^T$  are the surface energies of kink, edge and terrace surfaces, respectively.  $a_P$  is the growth unit width in the direction of step growth,  $a_E$  is the growth unit width along the step and  $h$  is the growth unit height. Figure adapted with permission from Tilbury et al.[32]. Copyright 2016 American Chemical Society

74]

$$\gamma_{XS} = \gamma_X + \gamma_S - \Delta W_{ad,XS} \quad (1.31)$$

where  $S$  and  $X$  denote solvent and crystal properties, respectively. The  $\gamma_{XS}$  may be  $\gamma^K$ ,  $\gamma^E$ , or  $\gamma^T$ . Several empirical relations have been proposed for expressing the work of adhesion  $W_{ad,XS}$  such as the Berthelot relation[75], Girifalo and Good's parametric correction[76], Owen and Wendt's modification[77], Fowkes' method[78], etc. In this work, we utilize van Oss, Chaudhury and Good[79, 80] solvent model, which provides a practical approach to obtaining surface energies in the presence of solvent. The model has been successfully applied for morphology predictions of various crystal-solvent systems and allows fast estimation of solvent effects.[73, 81–83]

Assuming surface energies are a combination of acid-base and dispersive components,

$$\gamma_{XS} = (\gamma_X^d + \gamma_X^{AB}) + (\gamma_S^d + \gamma_S^{AB}) - (W_{ad,XS}^d + W_{ad,XS}^{AB}) \quad (1.32)$$

where  $d$  and  $AB$  refer to dispersive and acid-base components, respectively. The cohesive interactions generally have two components: coulombic character based on partial charges obtained from electron density calculations and dispersive character. According to van Oss, Chaudhury and Good[79, 80], the work of adhesion is estimated by taking a geometric mean of the decoupled dispersive and acid-base components of the cohesive energies independently. The acid-base character is further separated into donating (+) and accepting (-) components. Hence, the acid-based component of work of adhesion consists of separate terms matching donating and accepting characteristics of crystal-solvent.

$$\begin{aligned} W_{ad,XS}^d &= 2\sqrt{\gamma_X^d \gamma_S^d} \\ W_{ad,XS}^{AB} &= 2\sqrt{\gamma_X^+ \gamma_S^-} + 2\sqrt{\gamma_X^- \gamma_S^+} \end{aligned} \quad (1.33)$$

The dispersive and acid-base components of individual solvent  $\gamma_S$  and crystal  $\gamma_X$  interactions are evaluated by appropriate atom-atom forcefields for the system of interest. For instance, the AMBER forcefield[84, 85] was initially developed for proteins and nucleic acid and subsequently generalized into GAFF[86] (Generalized Amber force field) for organic molecules. The Lifson forcefield is developed specifically for amides and carboxylic acid.[87] The Coloumb-London-Pauli (CLP)[88] forcefield has been parameterized specifically for crystals and will be used in our analysis for organic molecular crystals. The solvent-modified interfacial interaction energies are then estimated using Eqs. (1.32) and (1.33) and subsequently to calculate the solvent-modified work of detachment in Eq. 1.30.

## 1.4 Kossel and non Kossel Crystals

A Kossel Crystal is a cubic lattice of growth units forming equal interactions with each of its six nearest neighbors.[33] Such a crystal forms a network of isotropic interactions with a single type of growth unit. Examples of Kossel crystals in nature are limited, such

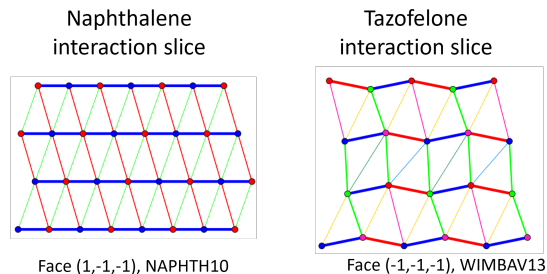


Figure 1.10: Interaction network across a slice of a) naphthalene (centrosymmetric growth unit), b) Tazofelone (Noncentrosymmetric growth unit). The interaction network is generated using the software ADDICT.[90]

as a polymorph of Polonium.[89] Owing to their simplicity, Kossel crystals act as testing subjects for crystal growth models. The vast majority of growth units are non-Kossel and are broadly classified into two categories: Centrosymmetric and Noncentrosymmetric. Centrosymmetric molecules have an inversion center that coincides with its center of mass. These molecules have symmetric interaction spheres. The same bonds are exposed to the solution at all the kink sites irrespective of step and face. Owing to isotropic interactions, the centrosymmetric molecules behave in a Kossel-like fashion and the Kossel models can be readily applied to Centrosymmetric molecules. Examples of this molecule class are succinic acid and naphthalene. The noncentrosymmetric molecules do not have an inversion centre and form asymmetric network of interactions. This results in various types of kinks along different steps and faces. Moreover, steps with multiple growth units consist of various configurations of steps as discussed later in Section 3.2. Asymmetry of the molecule is distinct from asymmetry of the crystalline lattice.[81] A centrosymmetric molecule has an inversion center aligned with its center of mass. Centrosymmetric space groups have an inversion center as one of their symmetry elements. Examples of such space groups are  $P2_1/c$  and  $P2/c$ .

The models discussed in the subsequent chapters in this dissertation pertain to growth units with varying levels of complexity, irrespective of the space group, the molecule is



crystallizing in. The new theory, namely Simplified Steady-State Framework, introduced in Chapter 2 is first demonstrated for Kossel crystals and applied to naphthalene and rubrene to demonstrate its utility for real molecules. Chapter 3 demonstrates extension of the theory to crystals of noncentrosymmetric molecules with two growth units in the unit cell and further generalized in Chapter 5 to various growth units in the unit cell.

## 1.5 Morphology Predictions and ADDICT

In previous sections, we summarized the multi-scale mechanistic modeling framework, solid-state periodic bond chains, solvent effects and crystallographic faces types. These distinct calculations form the basis of the software ADDICT[90–92], developed by the Doherty research group at the University of California Santa Barbara. ADDICT stands for “Advanced Design and Development of Industrial Crystallization Technology” and is a crystal morphology prediction tool which allows calculation, visualization, and analysis of the crystal habit formed as a function of the growth environment such as temperature, supersaturation and solvent. Inputs to the software are crystallographic information, Gaussian electron density calculations (partial charges on atoms), and growth environment descriptors (design variables). Sequential explanation of ADDICT’s workflow to obtain morphology predictions is outlined below,

1. The inputs to ADDICT are .cif and .mol2 files. The cif file provides the crystallographic input in the form of crystal structure data, symmetry operations, space group and unit cell data. The X-ray extinction conditions of the space group dictate stable low-index  $F$  faces with maximum in-plane interactions. Gaussian[93] and antechamber[94] can be utilized for electron density calculations to obtain mol2 files with restrained electrostatic potential (RESP) charges. The mol2 file provides the partial charges on atoms which are acted upon by appropriate atom-atom force-

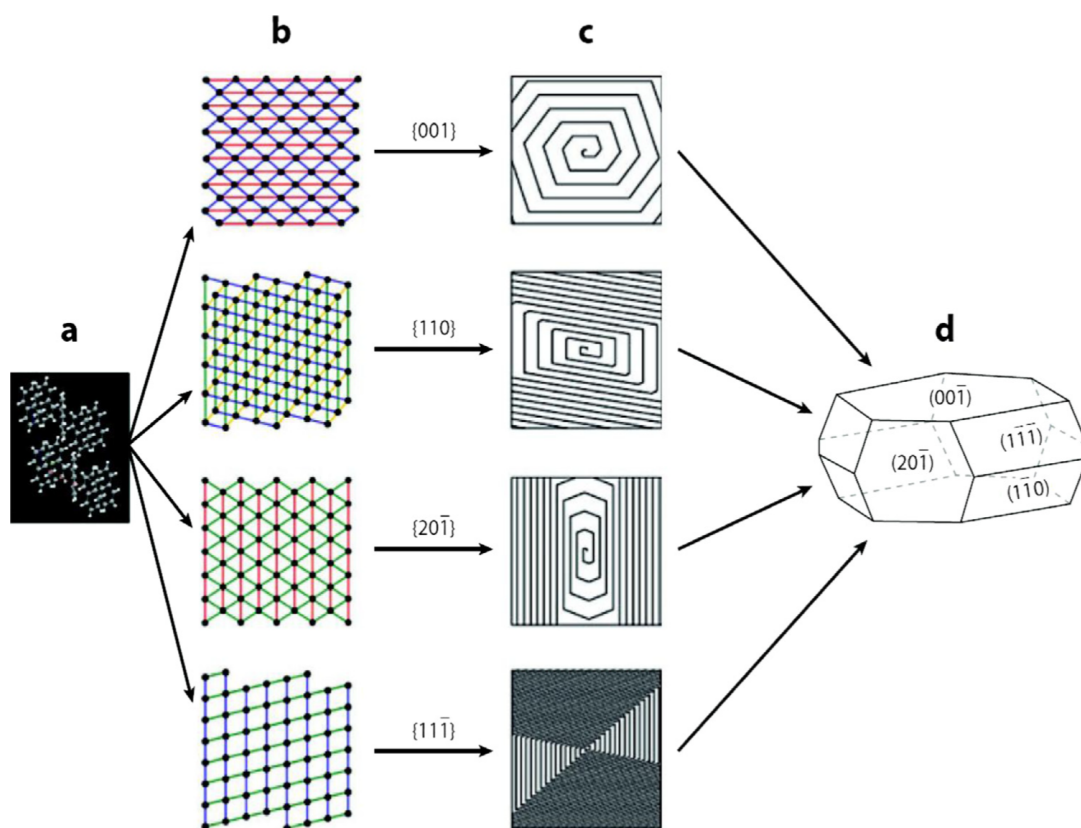


Figure 1.11: ADDICT's crystal morphology prediction methodology implemented for naphthalene, a) crystal structure allows crystallographic and unit cell information, b) solid-state calculation of interaction energies provides the network of interactions and PBCs, c) mechanistic model calculations provide spiral-shape estimates, d) steady-state morphology from the relative growth rates. Figure reproduced with permission from Li et al.[90]. Copyright 2016 Elsevier Ltd.

fields. GAFF[86], CLP[88], and Lifson[87] are some of the forcefields built into ADDICT. The intermolecular interaction energy calculations provide the network of interactions running parallel to  $F$  face planes. The dispersive and coulombic contributions to interactions are stored, for later modification of surface energies in the presence of a solvent.

2. Chains of strong interaction chains, the PBCs, as discussed in Section 1.1.4, are then identified based on a PBC algorithm elaborated by Li et al.[90] The aim is to evaluate the directions of the most-stable steps emerging as edges of spirals and 2D nuclei. These steps are assumed to align with PBC vectors.[47, 48, 81] Such an assumption is acceptable so long as the roughening transition has not been reached.[95] Once the steps are identified, energetic calculations are performed to estimate the solvent-modified kink, edge and terrace bond energies using the vOCG[79, 80] solvent model for each step.
3. With the interaction network and PBC directions in place, the atomistic growth models (Section 1.2.1) within the mechanistic growth modeling framework are applied to estimate parameters such as the kink densities and step velocity for each of the steps.
4. The continuum models (Section 1.2.2) are then applied to estimate relative growth rates of the faces from kink densities and step velocities. The growth models allow estimation of growth rates up to a multiplicative constant, specifically the rate constant  $k^+$ . Estimation of the rate constant requires knowledge of the free energy landscape and hence contingent upon rare event molecular simulations, vastly extending the timescale of calculations. Nonetheless, growth models of all the layered regimes are linear in the rate constant, allowing relative growth rate estimation, without  $k^+$  estimates. After all the  $F$  faces are modeled in their appropriate

regimes, the Frank-Chernov condition[14, 96] is used to obtain the steady-state crystal shape by calculating the perpendicular distances from the origin given their relative growth rates.

$$\frac{R_1}{x_1} = \frac{R_2}{x_2} = \dots = \frac{R_n}{x_n} = 1 \quad (1.34)$$

where  $R_f$  is the relative growth rate of face  $f$ ,  $x_f$  is the perpendicular distance of face  $f$  from the origin. Estimation of  $x_f$  for all the faces allows prediction of crystal morphology as the convex hull of all the faces.

Such a methodology allows fast mechanistic model-based calculations for crystal morphology predictions, since it does not require some of the expensive simulation techniques. The enumerated calculations are modularized and hence performed in silos, which allows the flexibility to incorporate new features and algorithms by integration at the appropriate stage and utilizing the rest of the workflow. Chapter 2 introduces a novel framework for obtaining step velocities. The new model will be integrated at stage 3) to obtain renewed morphology prediction, retaining rest of ADDICT’s workflow. This serves as a validation step for the new model by comparing how the crystal habit fares against experimental observations and other models for a given set of growth conditions.

## 1.6 Permissions and Attributions

The content of this thesis is organized in the form of chapters, parts of which are published as journal articles and enumerated below.

1. The content of Chapter 2 is reproduced in part with permission from:  
Padwal, N.A.; Doherty, M.F., Simple Accurate Nonequilibrium Step Velocity Model for Crystal Growth of Symmetric Organic Molecules. *Crystal Growth & Design* **2022**, 22(6), 3656-3661.

DOI:10.1021/acs.cgd.1c01366. Copyright 2022 American Chemical Society.

2. The content of Chapter 3 is reproduced in part with permission from:

Padwal, N.A.; Doherty, M.F. Step Velocity Growth Models for Molecular Crystals: Two Molecules in the Unit Cell. *Crystal Growth & Design* **2024**, 24(11), 4368-4379.

DOI:10.1021/acs.cgd.3c01508. Copyright 2024 American Chemical Society.

3. The contents of Chapter 4 is the result of a joint collaboration with Dr. Tobias Mazal and reproduced in part with permission from:

Padwal, N. A.<sup>‡</sup>; Mazal, T.<sup>‡</sup>; Doherty, M. F., Modern Modeling and Simulation Approaches for Morphology Predictions of Molecular Crystals. *Industrial & Engineering Chemistry Research* **2024**. (*In press*)

Unpublished work copyright 2024 American Chemical Society.

4. The contents of Chapter 5 is reproduced in part with permission from:

Padwal, N. A.; Doherty, M. F., Nonequilibrium Crystal Growth Model for Organic Molecules of Real API Complexity. *Crystal Growth & Design*. (*Manuscript under review*)

---

<sup>‡</sup> These authors contributed equally to this work

# Bibliography

- (1) Sargent, R. Integrated design and optimization of processes. *Chemical Engineering Progress* **1967**, *63*, 71–+.
- (2) Mikulic, M. Revenue of the worldwide pharmaceutical market from 2001 to 2019, 2020.
- (3) Burcham, C. L.; Doherty, M. F.; Peters, B. G.; Price, S. L.; Salvalaglio, M.; Reutzel-Edens, S. M.; Price, L. S.; Addula, R. K. R.; Francia, N.; Khanna, V., et al. Pharmaceutical Digital Design: From Chemical Structure through Crystal Polymorph to Conceptual Crystallization Process. *Crystal Growth & Design* **2024**, *24*, 5417–5438.
- (4) Variankaval, N.; Cote, A. S.; Doherty, M. F. From form to function: Crystallization of active pharmaceutical ingredients. *AIChE Journal* **2008**, *54*, 1682–1688.
- (5) Braga, D. Crystal engineering, Where from? Where to? *Chemical communications (Cambridge, England)* **2003**, *9*, 2751–4.
- (6) Yang, H. G.; Sun, C. H.; Qiao, S. Z.; Zou, J.; Liu, G.; Smith, S. C.; Cheng, H. M.; Lu, G. Q. Anatase TiO<sub>2</sub> single crystals with a large percentage of reactive facets. *Nature* **2008**, *453*, 638–641.
- (7) Frank, F. C. On the Kinematic Theory of Crystal Growth and Dissolution Processes, II. *Zeitschrift für Physikalische Chemie* **1972**, *77*, 84–92.

## BIBLIOGRAPHY

---

- (8) Chernov, A. A. The kinetics of the growth forms of crystals. *Soviet Physics Crystallography* **1963**, *7*, 728–730.
- (9) Ramkrishna, D., *Population balances: Theory and applications to particulate systems in engineering*; Elsevier: 2000.
- (10) Farmer, T. C.; Carpenter, C. L.; Doherty, M. F. Polymorph selection by continuous crystallization. *AIChE Journal* **2016**, *62*, 3505–3514.
- (11) Gibbs, J. W., *The scientific papers of J. Willard Gibbs*; Longmans, Green and Company: 1906; Vol. 1.
- (12) Wulff, G. Xxv. zur frage der geschwindigkeit des wachstums und der auflösung der krystallflächen. *Zeitschrift für Kristallographie-Crystalline Materials* **1901**, *34*, 449–530.
- (13) Lovette, M. A.; Browning, A. R.; Griffin, D. W.; Sizemore, J. P.; Snyder, R. C.; Doherty, M. F. Crystal Shape Engineering. *Industrial & Engineering Chemistry Research* **2008**, *47*, 9812–9833.
- (14) Frank, F. C. On the kinematic theory of crystal growth and dissolution processes. *Growth and Perfection of Crystal* **1958**, *411*.
- (15) Zhang, Y.; Doherty, M. F. Simultaneous prediction of crystal shape and size for solution crystallization. *AIChE journal* **2004**, *50*, 2101–2112.
- (16) Zhang, Y.; Sizemore, J. P.; Doherty, M. F. Shape evolution of 3-dimensional faceted crystals. *AIChE journal* **2006**, *52*, 1906–1915.
- (17) Snyder, R. C.; Doherty, M. F. Faceted crystal shape evolution during dissolution or growth. *AIChE journal* **2007**, *53*, Publisher: Wiley Online Library, 1337–1348.
- (18) Bravais, A., *Études cristallographiques par M. Auguste Bravais*; Gauthier-Villars: 1866.

## BIBLIOGRAPHY

---

- (19) Friedel, G. Etudes sur la loi de Bravais. *Bulletin de Minéralogie* **1907**, *30*, 326–455.
- (20) Donnay, J. D. H.; Harker, D. A new law of crystal morphology extending the law of Bravais. *American Mineralogist: Journal of Earth and Planetary Materials* **1937**, *22*, 446–467.
- (21) Brunsteiner, M.; Price, S. L. Morphologies of organic crystals: sensitivity of attachment energy predictions to the model intermolecular potential. *Crystal Growth & Design* **2001**, *1*, 447–453.
- (22) Lin, C.; Gabas, N.; Canselier, J.; Pepe, G. Prediction of the growth morphology of aminoacid crystals in solution: I.  $\alpha$ -Glycine. *Journal of Crystal Growth* **1998**, *191*, 791–802.
- (23) Hartman, P.; Perdok, W. G. On the relations between structure and morphology of crystals. I. *Acta Crystallographica* **1955**, *8*, Publisher: International Union of Crystallography, 49–52.
- (24) Hartman, P.; Bennema, P. The attachment energy as a habit controlling factor: I. Theoretical considerations. *Journal of Crystal Growth* **1980**, *49*, 145–156.
- (25) Walker, E. M.; Roberts, K. J.; Maginn, S. J. A molecular dynamics study of solvent and impurity interaction on the crystal habit surfaces of  $\epsilon$ -caprolactam. *Langmuir* **1998**, *14*, 5620–5630.
- (26) Lu, J.; Ulrich, J. An improved prediction model of morphological modifications of organic crystals induced by additives. *Crystal Research and Technology: Journal of Experimental and Industrial Crystallography* **2003**, *38*, 63–73.
- (27) Clydesdale, G.; Roberts, K.; Docherty, R. Modelling the morphology of molecular crystals in the presence of disruptive tailor-made additives. *Journal of Crystal Growth* **1994**, *135*, 331–340.



## BIBLIOGRAPHY

---

- (28) Yang, L.; Dong, Y. Crystal morphology study of N, N'-diacetylchitobiose by molecular dynamics simulation. *Carbohydrate research* **2011**, *346*, 2457–2462.
- (29) Hartman, P.; Perdok, W. G. On the relations between structure and morphology of crystals. II. *Acta Crystallographica* **1955**, *8*, Publisher: International Union of Crystallography, 521–524.
- (30) Hartman, P.; Perdok, W. G. On the relations between structure and morphology of crystals. III. *Acta Crystallographica* **1955**, *8*, Publisher: International Union of Crystallography, 525–529.
- (31) Cuppen, H. M., *Theory and simulations of crystal growth. Fundamental steps in morphology prediction*; [Sl: sn]: 2005.
- (32) Tilbury, C. J.; Green, D. A.; Marshall, W. J.; Doherty, M. F. Predicting the Effect of Solvent on the Crystal Habit of Small Organic Molecules. *Crystal Growth & Design* **2016**, *16*, 2590–2604.
- (33) Kossel, W. Zur theorie des kristallwachstums. *Nachrichten von der Gesellschaft der Wissenschaften zu Göttingen, Mathematisch-Physikalische Klasse* **1927**, *1927*, 135–143.
- (34) Stranski, I. N. Zur theorie des kristallwachstums. *Zeitschrift für physikalische Chemie* **1928**, *136*, 259–278.
- (35) Kim, S. H.; Dandekar, P.; Lovette, M. A.; Doherty, M. F. Kink rate model for the general case of organic molecular crystals. *Crystal Growth & Design* **2014**, *14*, 2460–2467.
- (36) Li, J.; Tilbury, C. J.; Joswiak, M. N.; Peters, B.; Doherty, M. F. Rate Expressions for Kink Attachment and Detachment During Crystal Growth. *Crystal Growth & Design* **2016**, *16*, 3313–3322.

## BIBLIOGRAPHY

---

- (37) Chernov, A. A.; Rashkovich, L. N.; DeYoreo, J. J. In *AIP Conference Proceedings*, 2007; Vol. 916, pp 34–47.
- (38) Zhang, J.; Nancollas, G. H. Kink density and rate of step movement during growth and dissolution of an AB Crystal in a nonstoichiometric solution. *Journal of Colloid and Interface Science* **1998**, *200*, 131–145.
- (39) Cuppen, H. M.; Meekes, H.; van Veenendaal, E.; van Enkevort, W. J. P.; Bennema, P.; Reedijk, M. F.; Arsic, J.; Vlieg, E. Kink density and propagation velocity of the [010] step on the Kossel (100) surface. *Surface Science* **2002**, *506*, 183–195.
- (40) Cuppen, H. M.; Meekes, H.; van Enkevort, W. J. P.; Vlieg, E. Kink incorporation and step propagation in a non-Kossel model. *Surface Science* **2004**, *571*, 41–62.
- (41) Burton, W. K.; Cabrera, N.; Frank, F. C. The growth of crystals and the equilibrium structure of their surfaces. *Philosophical Transactions of the Royal Society of London. Series A, Mathematical and Physical Sciences* **1951**, *243*, 299–358.
- (42) Chernov, A. A. The spiral growth of crystals. *Soviet Physics Uspekhi* **1961**, *4*, 116.
- (43) Voronkov, V. V. Non-equilibrium structure of an elementary step. *Soviet Physics Crystallography* **1968**, *13*, 13–28.
- (44) Vekilov, P. G. What determines the rate of growth of crystals from solution? *Crystal Growth and Design* **2007**, *7*, 2796–2810.
- (45) Lovette, M. A.; Doherty, M. F. Multisite models to determine the distribution of kink sites adjacent to low-energy edges. *Physical Review E—Statistical, Nonlinear, and Soft Matter Physics* **2012**, *85*, 021604.
- (46) Van der Eerden, J. P. In *Handbook of Crystal Growth, Vol. 1*, Hurle, D. T. J., Ed.; Elsevier: Amsterdam, 1993; Chapter 5, p 307.

## BIBLIOGRAPHY

---

- (47) Snyder, R. C.; Doherty, M. F. Predicting crystal growth by spiral motion. *Proceedings of the Royal Society A: Mathematical, Physical and Engineering Sciences* **2009**, *465*, 1145–1171.
- (48) Lovette, M. A.; Doherty, M. F. Predictive modeling of supersaturation-dependent crystal shapes. *Crystal Growth & Design* **2012**, *12*, 656–669.
- (49) Binsbergen, F. A reconsideration of polymer crystallization theory. *Kolloid-Zeitschrift und Zeitschrift für Polymere* **1970**, *238*, 389–395.
- (50) Metropolis, N.; Rosenbluth, A. W.; Rosenbluth, M. N.; Teller, A. H.; Teller, E. Equation of state calculations by fast computing machines. *The journal of chemical physics* **1953**, *21*, 1087–1092.
- (51) Frenkel, J. On the Surface Motion of Particles on Crystals and Natural Roughness of Crystal Faces. *Journal of Physics USSR* **1945**, *9*, 392.
- (52) Sun, Y.; Tilbury, C. J.; Reutzel-Edens, S. M.; Bhardwaj, R. M.; Li, J.; Doherty, M. F. Modeling Olanzapine Solution Growth Morphologies. *Crystal Growth & Design* **2018**, *18*, 905–911.
- (53) Land, T. A.; De Yoreo, J. J. The evolution of growth modes and activity of growth sources on canavalin investigated by in situ atomic force microscopy. *Journal of Crystal Growth* **2000**, *208*, 623–637.
- (54) Deij, M.; Cuppen, H.; Meeke, H.; Vlieg, E. Steps on surfaces in modeling crystal growth. *Crystal Growth & Design* **2007**, *7*, 1936–1942.
- (55) Shtukenberg, A. G.; Zhu, Z.; An, Z.; Bhandari, M.; Song, P.; Kahr, B.; Ward, M. D. Illusory spirals and loops in crystal growth. *Proceedings of the National Academy of Sciences* **2013**, *110*, 17195–17198.

## BIBLIOGRAPHY

---

- (56) Cubillas, P.; Anderson, M. W.; Attfield, M. P. Crystal Growth Mechanisms and Morphological Control of the Prototypical Metal–Organic Framework MOF-5 Revealed by Atomic Force Microscopy. *Chemistry–A European Journal* **2012**, *18*, 15406–15415.
- (57) Yip, C. M.; Ward, M. D. Atomic force microscopy of insulin single crystals: direct visualization of molecules and crystal growth. *Biophysical journal* **1996**, *71*, 1071–1078.
- (58) Paloczi, G. T.; Smith, B. L.; Hansma, P. K.; Walters, D. A.; Wendman, M. A. Rapid imaging of calcite crystal growth using atomic force microscopy with small cantilevers. *Applied physics letters* **1998**, *73*, 1658–1660.
- (59) Vekilov, P. G.; Alexander, J. I. D. Dynamics of layer growth in protein crystallization. *Chemical reviews* **2000**, *100*, 2061–2090.
- (60) Lovette, M. A.; Doherty, M. F. Reinterpreting edge energies calculated from crystal growth experiments. *Journal of Crystal Growth* **2011**, *327*, Publisher: Elsevier, 117–126.
- (61) Tilbury, C. J.; Doherty, M. F. Modeling layered crystal growth at increasing supersaturation by connecting growth regimes. *AIChE Journal* **2017**, *63*, Publisher: Wiley Online Library, 1338–1352.
- (62) Voronkov, V. V. Dislocation mechanism of growth with a low kink density. *Soviet Physics Crystallography* **1973**, *18*, 19–223.
- (63) Teng, H. H.; Dove, P. M.; De Yoreo, J. J. Kinetics of calcite growth: surface processes and relationships to macroscopic rate laws. *Geochimica et Cosmochimica Acta* **2000**, *64*, 2255–2266.

## BIBLIOGRAPHY

---

- (64) Rimer, J. D.; An, Z.; Zhu, Z.; Lee, M. H.; Goldfarb, D. S.; Wesson, J. A.; Ward, M. D. Crystal growth inhibitors for the prevention of L-cystine kidney stones through molecular design. *Science* **2010**, *330*, 337–341.
- (65) Cuppen, H. M.; Meekes, H.; van Enckevort, W. J. P.; Vlieg, E. Birth-and-spread growth on the Kossel and a non-Kossel surface. *Journal of Crystal Growth* **2006**, *286*, 188–196.
- (66) Ohara, M. Modeling crystal growth rates from solution. *Englewood Cliffs* **1973**.
- (67) Zeldovich, Y. B. On the theory of new phase formation: cavitation. *Acta Physicochem., USSR* **1943**, *18*, 1.
- (68) Kashchiev, D., *Nucleation*; Elsevier: 2000.
- (69) Onsager, L. Crystal statistics. I. A two-dimensional model with an order-disorder transition. *Physical Review* **1944**, *65*, 117.
- (70) Shi, W.; Xia, M.; Lei, W.; Wang, F. Solvent effect on the crystal morphology of 2, 6-diamino-3, 5-dinitropyridine-1-oxide: A molecular dynamics simulation study. *Journal of Molecular Graphics and Modelling* **2014**, *50*, 71–77.
- (71) Shim, H.-M.; Kim, J.-W.; Koo, K.-K. Molecular interaction of solvent with crystal surfaces in the crystallization of ammonium sulfate. *Journal of Crystal Growth* **2013**, *373*, 64–68.
- (72) Dupré, A.; Dupré, P., *Théorie mécanique de la chaleur*; Gauthier-Villars: 1869.
- (73) Lovette, M. A.; Doherty, M. F. Needle-shaped crystals: causality and solvent selection guidance based on periodic bond chains. *Crystal Growth & Design* **2013**, *13*, 3341–3352.
- (74) Winn, D.; Doherty, M. F. Modeling crystal shapes of organic materials grown from solution. *AIChE journal* **2000**, *46*, 1348–1367.

## BIBLIOGRAPHY

---

- (75) Berthelot, D. Sur le mélange des gaz. *Compt. Rendus* **1898**, *126*, 15.
- (76) Girifalco, L.; Good, R. J. A theory for the estimation of surface and interfacial energies. I. Derivation and application to interfacial tension. *The Journal of Physical Chemistry* **1957**, *61*, 904–909.
- (77) Owens, D. K.; Wendt, R. Estimation of the surface free energy of polymers. *Journal of applied polymer science* **1969**, *13*, 1741–1747.
- (78) Fowkes, F. M. Attractive forces at interfaces. *Industrial & Engineering Chemistry* **1964**, *56*, 40–52.
- (79) Van Oss, C. J.; Chaudhury, M.; Good, R. J. Monopolar surfaces. *Advances in Colloid and Interface Science* **1987**, *28*, 35–64.
- (80) Van Oss, C.; Good, R.; Chaudhury, M. Additive and nonadditive surface tension components and the interpretation of contact angles. *Langmuir* **1988**, *4*, 884–891.
- (81) Kuvadia, Z. B.; Doherty, M. F. Spiral Growth Model for Faceted Crystals of Non-Centrosymmetric Organic Molecules Grown from Solution. *Crystal Growth & Design* **2011**, *11*, 2780–2802.
- (82) Tilbury, C. J.; Joswiak, M. N.; Peters, B.; Doherty, M. F. Modeling Step Velocities and Edge Surface Structures during Growth of Non-Centrosymmetric Crystals. *Crystal Growth & Design* **2017**, *17*, 2066–2080.
- (83) Mazal, T.; Doherty, M. F. Modeling Morphologies of Organic Crystals via Kinetic Monte Carlo Simulations: Noncentrosymmetric Growth Units. *Crystal Growth & Design* **2024**, *24*, 3756–3770.
- (84) Weiner, S. J.; Kollman, P. A.; Case, D. A.; Singh, U. C.; Ghio, C.; Alagona, G.; Profeta, S.; Weiner, P. A new force field for molecular mechanical simulation of

## BIBLIOGRAPHY

---

- nucleic acids and proteins. *Journal of the American Chemical Society* **1984**, *106*, 765–784.
- (85) Weiner, S. J.; Kollman, P. A.; Nguyen, D. T.; Case, D. A. An all atom force field for simulations of proteins and nucleic acids. *Journal of Computational Chemistry* **1986**, *7*, 230–252.
- (86) Wang, J.; Wolf, R. M.; Caldwell, J. W.; Kollman, P. A.; Case, D. A. Development and testing of a general amber force field. *Journal of Computational Chemistry* **2004**, *25*, 1157–1174.
- (87) Lifson, S.; Hagler, A.; Dauber, P. Consistent force field studies of intermolecular forces in hydrogen-bonded crystals. 1. Carboxylic acids, amides, and the C: O. cntdot.. cntdot.. cntdot. H-hydrogen bonds. *Journal of the American Chemical Society* **1979**, *101*, 5111–5121.
- (88) Gavezzotti, A. Efficient computer modeling of organic materials. The atom–atom, Coulomb–London–Pauli (AA-CLP) model for intermolecular electrostatic-polarization, dispersion and repulsion energies. *New Journal of Chemistry* **2011**, *35*, 1360–1368.
- (89) Markov, I. fundamentals of nucleation, crystal growth, and epitaxy. *Crystal growth for beginners* **1995**, *1*.
- (90) Li, J.; Tilbury, C. J.; Kim, S. H.; Doherty, M. F. A design aid for crystal growth engineering. *Progress in Materials Science* **2016**, *82*, 1–38.
- (91) Landis, S.; Zhao, Y.; Doherty, M. F. Digital design of crystalline solids. *Computers & Chemical Engineering* **2020**, *133*, 106637.
- (92) Zhao, Y.; Tilbury, C. J.; Landis, S.; Sun, Y.; Li, J.; Zhu, P.; Doherty, M. F. A New Software Framework for Implementing Crystal Growth Models to Materials of Any Crystallographic Complexity. *Crystal Growth & Design* **2020**, *20*, 2885–2892.

## BIBLIOGRAPHY

---

- (93) Frish, M.; Trucks, G.; Schlegel, H.; Scuseria, G.; Robb, M.; Cheeseman, J.; Scalmani, G.; Barone, V.; Mennucci, B.; Paterson, G. Gaussian 09, revision A. 02. *Gaussian Inc, Wallingford CT* **2009**.
- (94) Wang, J.; Wang, W.; Kollman, P. A.; Case, D. A. Antechamber: an accessory software package for molecular mechanical calculations. *J. Am. Chem. Soc* **2001**, *222*.
- (95) Cuppen, H.; Meekes, H.; Van Enkevort, W.; Vlieg, E.; Knops, H. Nonequilibrium free energy and kinetic roughening of steps on the Kossel (001) surface. *Physical Review B* **2004**, *69*, 245404.
- (96) Chernov, A. A. The kinetics of the growth forms of crystals. *Soviet Physics Crystallography* **1963**, *7*, 728–730.



# Chapter 2

## Simplified Steady-State Framework: Kossel Crystal

Reproduced in part with permission from:

Padwal, N.A.; Doherty, M.F., Simple Accurate Nonequilibrium Step Velocity Model for Crystal Growth of Symmetric Organic Molecules. *Crystal Growth & Design* **2022**, 22(6), 3656-3661.

DOI:10.1021/acs.cgd.1c01366. Copyright 2022 American Chemical Society.

### 2.1 Introduction

Well-formed faceted crystals normally grow via layered growth mechanisms wherein steps flow across crystal surfaces propelling the face to grow normally in a layered fashion. Under a wide range of conditions, the slowest event is the incorporation of growth units (molecules, ions, etc.) into the crystal surface. Bulk diffusion and surface diffusion are fast relative to growth unit incorporation.[1] Growth models play a key role in crystal morphology prediction and control. Mechanistic models are capable of providing fast and

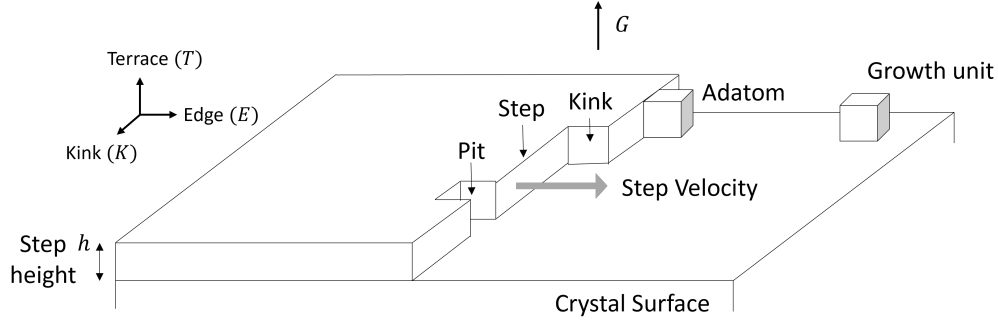


Figure 2.1: Schematic depiction of a crystal surface with a step growing laterally across the face through attachment of growth units at various sites especially *kinks*.

accurate predictions of morphology by accounting for surface kinetics, and fundamental sub-processes that result in growth of the crystal.[2, 3] Layered crystal growth regimes studied in Chapter 1, such as the spiral and 2D nucleation, are preferred for controlled crystallization conditions. Growth rate of the crystal face growing in such regimes is a strong function of the step velocity - the constant rate at which steps progress across the crystal surface. The step velocity depends on the density of favorable sites of attachment, namely *kinks*, along the step. Kink sites are particular of interest because attachment at these sites occurs with no change in exposed surface area, thus no increase in crystal surface energy. Moreover, the kinks regenerate themselves upon incorporation of growth units, and act as catalytic species paving the way for further growth of the steps. In growth models, kink density is often approximated by its equilibrium value.[4–7] Hence, Frenkel's equilibrium density[8] given by Eq. (2.1) or multi-height equilibrium density[9] given by Eq. (2.2) are normally used for kink density modeling.

$$\rho_{eq}^1 = \frac{2e^{-\beta\phi_k}}{1 + 2e^{-\beta\phi_k}} = \frac{2}{2 + e^{\beta\phi_k}} \quad (2.1)$$

$$\rho_{eq}^\infty = \frac{2 \sum_{n=1}^{\infty} e^{-n\beta\phi_k}}{1 + 2 \sum_{n=1}^{\infty} e^{-n\beta\phi_k}} = \frac{2}{1 + e^{\beta\phi_k}} \quad (2.2)$$

where  $\phi_k$  is the strength of interactions along the kink axis between growth units,  $\beta = \frac{1}{k_B T}$ ,  $k_B$  is the Boltzmann constant and  $T$  is the absolute temperature. Increasing  $\beta$  corresponds to reducing the system temperature and vice versa. Increasing  $\phi$  corresponds to increasing the strength of interactions between growth units, thereby increasing the energy required to detach a growth unit from a crystal surface.

This chapter discusses previous models for Kossel crystal discussed in Section 1.4 and proposes a new theory for modeling nonequilibrium kink density. Since centrosymmetric molecules behave in a Kossel-like fashion[10], we apply the new theory to habit predictions of naphthalene and rubrene to demonstrate its utility for real molecules.

## 2.2 Background

The development of several non-equilibrium kink density models rests on a steady-state principle first suggested by Voronkov[11] in 1970, and implemented for single kinks. Such an idea was also independently suggested by Frank[12] in 1974. The steady-state principle states that kink density is determined by the rate of nucleation and annihilation of kinks by collision. Subsequently, several models have been devised, following this steady-state principle. Zhang and Nancollas[13] built a kinetic steady-state framework for low kink densities on an infinitely long step. Joswiak et al.[14] devised a one-dimensional nucleation framework employing the Becker-Doring model. Van der Eerden[15] formulated a non-equilibrium steady-state kink density expression by modeling surface events assuming statistical independence of adjoining sites and excludes multi-height kinks. This framework was further extended by Cuppen et al.[16] in a landmark paper that models non-equilibrium multi-height kink density in a rigorous framework, which considers all possible step configurations, accounting for kinks of all heights. In addition to kinks, these configurations include many low-probability events such as multi-height nuclei,

multi-height pits, etc. This model exhibits excellent agreement with simulations and reduces to Eq. (2.2) at equilibrium. However, none of these models readily extend to more realistic molecules of interest, such as active pharmaceutical ingredient molecules. This necessitates the development of a non-equilibrium kink density model precise enough to capture dominant supersaturation effects yet simple enough to be applied to a wide range of molecules.

In this chapter, we employ Voronkov[11] and Frank's[12] steady-state principle and simplify the framework of Cuppen et al.[16] for Kossel crystals with a focus on only the high density surface structures. The resulting Simplified Steady-State Framework (SSSF) is based on identification of the most-concentrated surface sites and the high-probability surface processes which capture majority of the supersaturation effects. The surface events then are employed for steady-state analysis via balancing the rates of kink-forming and kink-destroying events. Such a methodology provides a nonequilibrium kink density model as a function of supersaturation for a Kossel crystal and by extension crystals of centrosymmetric molecules. Only single and double height kinks are considered, while multi-height kinks are neglected due to their low probability. The total kink density is then utilised for step velocity predictions, which are then compared with kinetic Monte Carlo (kMC) simulations taken from the literature.[14] In the subsequent chapters, we will demonstrate generalizations of the framework to more complex non-Kossel molecular crystals.

## 2.3 Rate Model

A schematic Gibbs free energy plot of attachment and detachment surface processes is depicted in Fig. 2.2. Treating the surface integration step like a reaction allows for modeling the attachment and detachment rates, as given by Eq. (2.3).[5, 17–19] For the

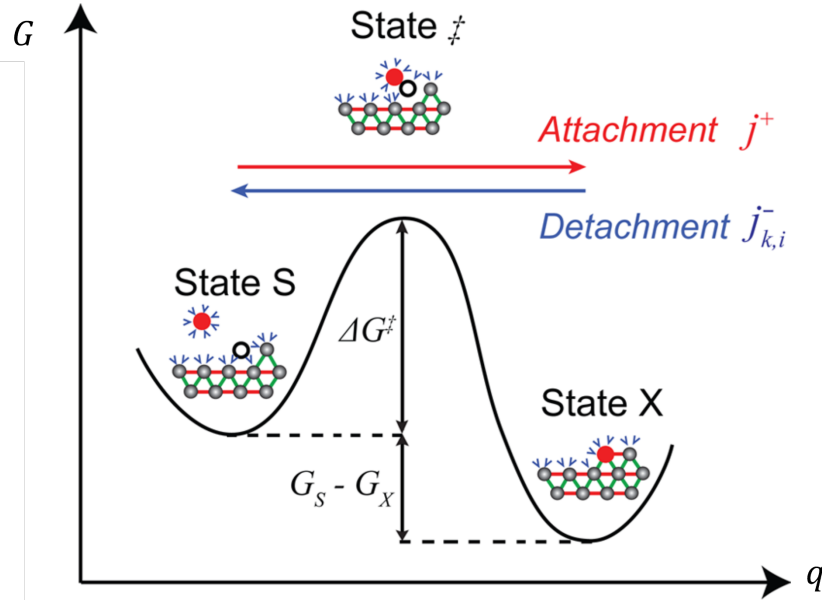


Figure 2.2: Gibbs free energy landscape of attachment and detachment processes along the reaction co-ordinate,  $q$ . State S denotes solvated growth unit and solvated kink site, state  $\ddagger$  denotes the transition state with partially solvated growth unit and desolvated kink site, while state X denotes solvated kink site post surface integration of growth unit.  $\Delta G^\ddagger$  is the free energy barrier to surface integration of the growth unit;  $\Delta G = G_S - G_X$  is the free energy difference between the states S and X and depends on supersaturation. Figure reproduced with permission from Li et al.[17] Copyright 2016 American Chemical Society.

attachment process,  $\Delta G$  is assumed to be dominated by desolvation of molecule in the solution phase and independent of the site of attachment. The detachment rate depends on the work of detachment and thereby site-dependent. Such a rate model is referred to as the random rain model[15]. Li et al.[17] proposed a modification of the model to account for the solvent effects. The work is attributed to summation of energies of bonds broken and depends on the energetic environment within the step. In the presence of solvent, the interaction energies  $\phi$ s must account for the solvent-induced surface energy changes as discussed in Section 1.3

$$\begin{aligned}
 j^+ &= k^+ x_{sat} S \\
 j_i^- &= k_i^- = k^+ e^{-\beta \Delta W_i}
 \end{aligned}
 \tag{2.3}$$

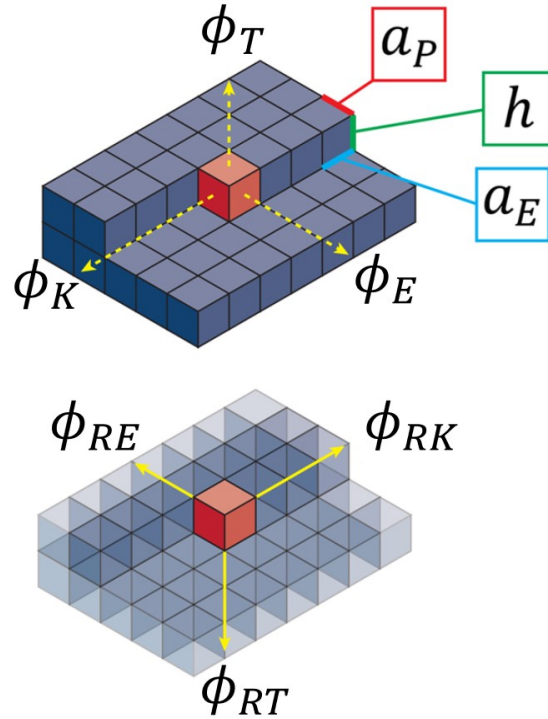


Figure 2.3: Energy of interactions of a crystal growth unit in different directions. The interactions are categorised as intraedge (kink), interedge (edge), interslice (terrace) axes. The kink ( $\phi_K$ ), edge ( $\phi_E$ ) and terrace ( $\phi_T$ ) energies correspond to broken interactions along respective axes facing the solution. The reverse kink ( $\phi_{RK}$ ), reverse edge ( $\phi_{RE}$ ) and reverse terrace ( $\phi_{RT}$ ) energies correspond to satisfied interactions along respective axes that hold the growth unit to the crystal. Figure adapted with permission from Tilbury et al.[20]. Copyright 2017 American Chemical Society.

where  $j^+$  is the attachment rate,  $k^+$  is the attachment rate constant,  $k_i^-$  is the detachment rate constant,  $x_{sat}$  is the solute saturation mole fraction,  $S = \frac{x}{x_{sat}}$  is the supersaturation,  $j_i^-$  is the detachment rate from a site with  $i$  nearest-neighbors along the edge (kink axis), and  $\Delta W_i$  is the work of detachment from site  $i$ . Hence  $i = 0, 1, 2$  denote edge, kink and pit sites, respectively. For a detachment from a kink, the work is given by,

$$\Delta W_1 = 2\phi_{RK} + 2\phi_{RE} + 2\phi_{RT} \quad (2.4)$$

where  $\phi_{RK}$ ,  $\phi_{RE}$  and  $\phi_{RT}$  are the interactions energies along reverse kink, reverse edge and reverse terrace axes, respectively, as depicted in Fig. 2.3. The factor of two accounts for the fact that  $\phi$ s are half the bond strengths. Microscopic reversibility of the rate model[17] gives the following expression for saturation mole fraction,

$$x_{sat} = e^{-\beta\Delta W_1} \quad (2.5)$$

The attachment rate constant  $k^+$  is modeled using appropriate rate theory such as the transition state theory[21] or Kramers-type barrier crossing[22].

$$k^+ = \nu e^{-\beta\Delta G^\ddagger} \quad (2.6)$$

where  $\nu$  is the frequency factor and  $\Delta G^\ddagger$  is the activation free energy barrier.

## 2.4 Methods

SSSF is based on the hypothesis that only a small set of densely-populated sites and their interactions between each other, control majority of the surface kinetics. We start from identifying the predominant kinks which are prevalent in highest concentrations. As the kink height increases, the exposed broken bond interactions increase and the kink density drastically reduces. Hence, the most-concentrated structures along a step are the single and double-height kinks apart from the edge junction, which characterize flat-regions on the step. Multi-height kinks beyond double-height are neglected due to their low probability of occurrence along the step. The predominant junctions such as the kinks and edge give rise to several types of sites along the step. The *major sites* are the ones which densely occupy the configuration space and constitute of the predominant kinks and edge. The major sites identified for such a step are depicted within the most-

likely space (green oval) in Fig. 5.4a. Refer Appendix A for elaborate discussions on predominant junctions (kink and edge), sites, identification and tables of major-sites and most-likely events.

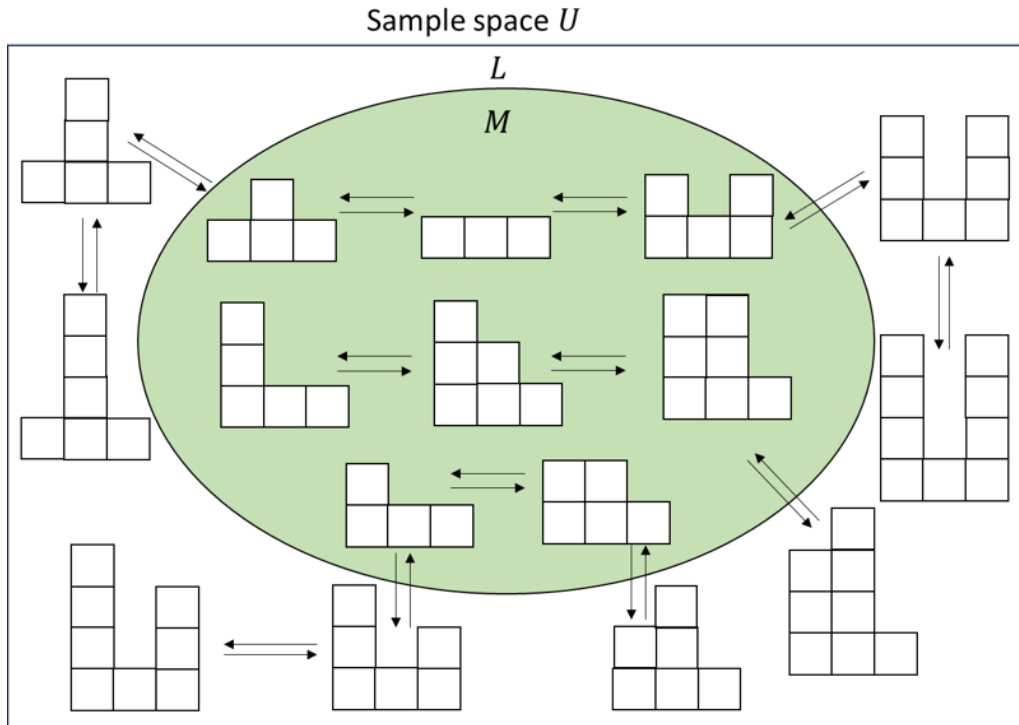


Figure 2.4: Surface kinetics diagram of a step along a Kossel crystal, depicting the most-probable event space  $M$  within the sample space of all events  $U$ .

A crystal step is populated by various types of sites such as pits, kink sites and edge sites. At any given supersaturation, the sites are constantly subjected to attachment and detachment events, which result in frequent inter-conversion of sites into one another. With regard to kinks, these processes can be categorised into three types:

1. Kink forming: Processes such as 1-D nucleation result in formation of kinks.
2. Kink destroying: Processes such as kink collision destroy kinks
3. Kink unaltering: Processes such as attachment at kinks leave the number of kinks along the edge unchanged.



It is important to note that the above categorization of processes is kink type-specific (single-height, multi-height, etc). It is possible that an event that forms a single-height kink also destroys a double-height kink in the process. Hence, different processes can be grouped into the above three classes for each type of kink.

The various surface sites are constantly undergoing transformations through attachment and detachment events. SSSF is based on identifying the crucial high probability events which dominate the surface kinetics and subsequently the supersaturation events. Within SSSF, we define the *most-likely events* as the events which convert the major sites with each other. The most-likely events are then utilized in the steady-state analysis. Fig. 2.4 schematically depicts the major sites within the space  $M$  (green oval) and the most-likely events (directed arrows) which characterize the interactions between the major sites.

Steady-state analysis is performed for the single and double-height kinks based on balancing the rates of kink forming and kink destroying events to capture supersaturation effects on kink density. Only the high concentration major sites are considered to maintain simplicity of the framework for later application to more complex molecules.

### 2.4.1 Single-height Kinks

We parse through the most-likely events in search of relevant processes forming or destroying single-height kinks. Fig. 2.5 schematically depicts processes affecting single kinks. Attachment and detachment from site configurations (1) and (2), respectively, form kinks. Similarly, attachment and detachment from site configurations (3) and (4), respectively, destroys kinks. Hence, nucleation and pit-formation are single kink forming events, while kink collision and de-nucleation are single kink destroying events. This allows us to construct a steady-state master equation for single kinks given by Eq. (2.7).

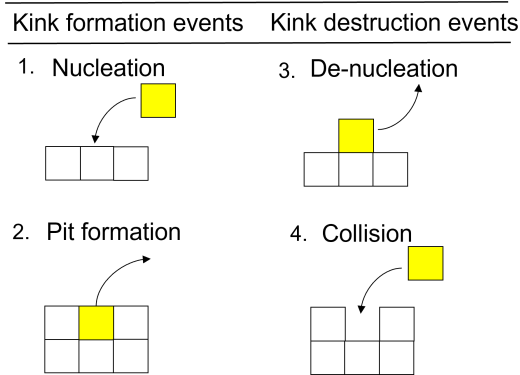


Figure 2.5: Most-likely surface events that result in formation or destruction of single kinks. Growth units colored yellow mark changes in configuration during the event.

Refer to Appendix A for detailed derivation and table of major sites and the most-likely surface processes.

$$\rho_0^2(j^+ + j_2^-) = \frac{\rho_1^2}{4}(j^+ + j_0^-) \quad (2.7)$$

where  $\rho_0$  is the density of edge,  $\rho_1$  is the single kink density,  $j_0^-$  is the detachment rate from edge sites and  $j_2^-$  is the detachment rate from pit sites.

### 2.4.2 Double-height Kinks

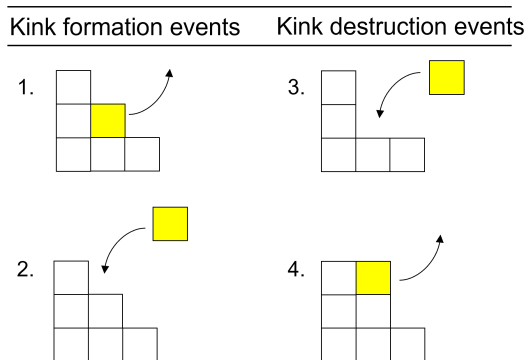


Figure 2.6: Most-likely surface events that result in formation or destruction of double-kinks. Growth units colored yellow mark changes in configuration during the event.

Similarly, we parse through the most-likely events in search of events affecting the density of double-height kinks. Fig. 2.6 depicts dominant processes affecting the density of double-

kinks. In the figure, detachment and attachment at site configurations (1) and (2), respectively, form a double-kink. Similarly, attachment and detachment at site configurations (3) and (4), respectively, destroys double-kinks. The master equation for double-kinks given by Eq. (2.8) is a mathematical representation of the balance.

$$\frac{\rho_1^2}{2}(j^+ + j_1^-) = \rho_2 \rho_0 (j^+ + j_1^-) \quad (2.8)$$

where  $\rho_2$  is the density of double-kinks and  $j_1^-$  is the detachment rate from kink sites. It is noteworthy that a similar steady-state equation can be constructed for the edge densities, however the equation is linearly dependent on the steady-state equations of the single and double kinks. Since we only consider three types of sites, edge, kink, and double-kink, their densities must sum to unity.

$$\rho_0 + \rho_1 + \rho_2 = 1 \quad (2.9)$$

The model thus consists of Eqs. (2.7), (2.8) and (2.9) which can be solved to yield our simplified non-equilibrium (NEQ) kink density expressions for single and double-kinks.

$$\rho_1 = 2 \left( \frac{-2\tilde{e}\tilde{p} + (\tilde{e} + 2\tilde{p})\sqrt{\tilde{e}\tilde{p}}}{\tilde{e}^2 + 4\tilde{p}^2} \right) \quad (2.10)$$

$$\rho_2 = 2\tilde{p} \left( \frac{\tilde{e} + 2\tilde{p} - 2\sqrt{\tilde{e}\tilde{p}}}{\tilde{e}^2 + 4\tilde{p}^2} \right) \quad (2.11)$$

where

$$\tilde{e} = j^+ + j_0^- = k^+ x_{sat} S + k_0^- = k^+ (x_{sat} S + e^{-\beta \Delta W_0}) \quad (2.12)$$

and

$$\tilde{p} = j^+ + j_2^- = k^+ x_{sat} S + k_2^- = k^+ (x_{sat} S + e^{-\beta \Delta W_2}) \quad (2.13)$$

Note that these kink density expressions do not analytically reduce to the multi-height equilibrium density expression at  $S = 1$ . This is because we are only accounting for the predominant processes. Analytical equivalency at equilibrium is acquired only when all possible site configurations are accounted.[16] However, the NEQ model-predicted kink density at equilibrium accounts for about 99.4% of total kinks at  $\beta\phi = 2.5$ , and is numerically indistinguishable from the multi-height equilibrium kink density. The percentage only increases with  $\beta\phi$  as contributions from multi-height kinks reduce drastically with increasing  $\beta\phi$ .

## 2.5 Results and Discussion

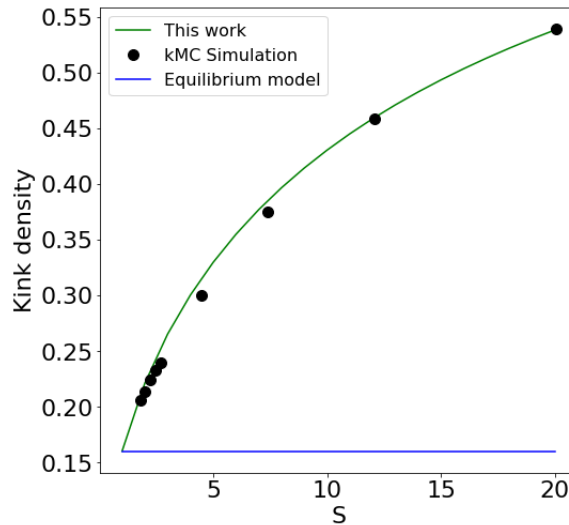


Figure 2.7: Plot of non-equilibrium kink density for a Kossel crystal vs  $S$  at bond energy  $\beta\phi = 2.5$ . kMC simulation data points for the same Kossel system are obtained from Cuppen et al.[16]

The step velocity,  $v$ , expression when kink sites are the primary sites of attachment

is given by (Refer to Appendix A),

$$v = a_P k^+ \rho_T x_{sat} (S - 1) \quad (2.14)$$

where  $a_P$  is the step propagation length,  $\rho_T$  is the total kink density and estimated as the sum of kinks of all heights in Eq. (2.16). Step velocity is normalised so as to focus on the effect of kink density and distill out the effect of other parameters on step velocity.

$$\frac{v}{a_P x_{sat} k^+} = \rho_T (S - 1) \quad (2.15)$$

$$\rho_T = \rho_1 + \rho_2 \quad (2.16)$$

An alternative approach to modeling step velocity is the aggregate of all the rates of most-likely attachment and detach events such that,

$$v = a_P \left\{ \left( \frac{\rho_1^2}{4} j^+ + \rho_0 \rho_1 j^+ + \rho_0^2 j^+ + \rho_2 \rho_0 j^+ + \frac{\rho_1^2}{2} j^+ \right) - \left( \frac{\rho_1^2}{4} j_0^- + \rho_0 \rho_1 j_1^- + \rho_0^2 j_2^- + \rho_2 \rho_0 j_1^- + \frac{\rho_1^2}{2} j_1^- \right) \right\} \quad (2.17)$$

where the first term is the collection of all attachment events and the second term is the collection of all detachment events. In the rest of the chapter, we'll be using Eq. 2.15 for analysis because of its simplicity. However Eq. 2.17 provides a general approach to modeling step velocity consistent with SSSF and allows generalization to complex crystals to be studied in subsequent chapters.

The total kink density estimated for a Kossel crystal using Eqs. (2.16), (2.10) and (2.11) is plotted as a function of supersaturation at  $\beta\phi = 2.5$  in Fig. 2.7. This model is compared with the multi-height equilibrium kink density model given by Eq. (2.2) along with kMC simulation data for the same Kossel system taken from the literature.[16] The equilibrium kink density depends only on the bond strength  $\beta\phi$  and predicts a

single value, hence depicted by the horizontal line. The equilibrium model deviates strongly from the observed behavior and is a poor estimate as supersaturation increases. The non-equilibrium kink density is a strong function of supersaturation and increases monotonically with increase in driving force. This is due to the increase in attachment rates with supersaturation, while detachment rates remain the same. The model lines up with the kMC simulation data despite only accounting for the single and double kinks, validating the basis of the approach.

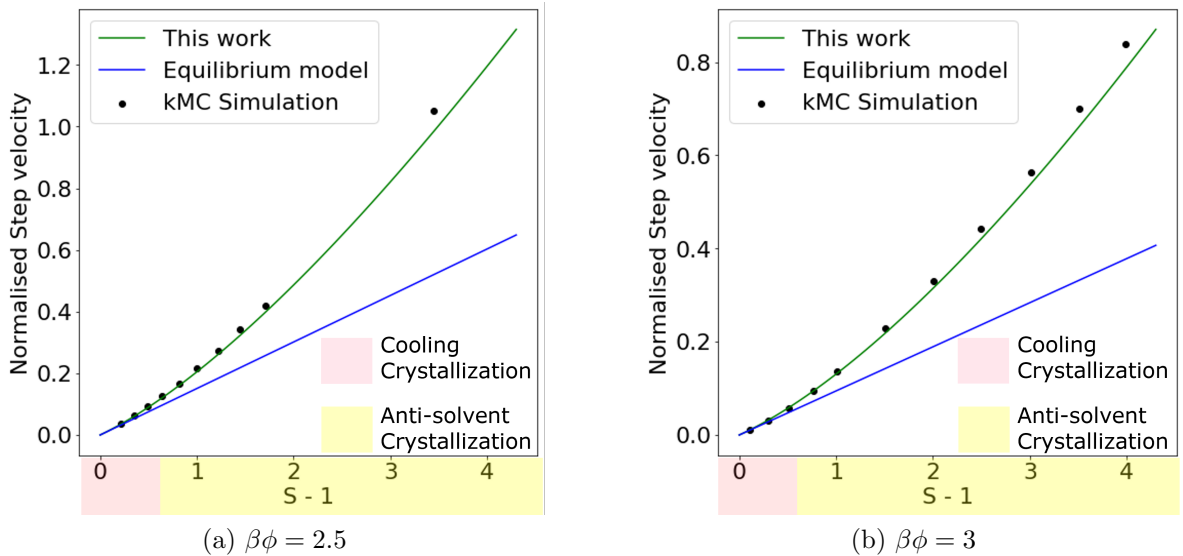


Figure 2.8: Plot of normalized step velocity for a Kossel crystal vs  $S - 1$  at bond energies: (a)  $\beta\phi = 2.5$ , (b)  $\beta\phi = 3$ . The kMC simulation data points for the same Kossel system at  $\beta\phi = 2.5$  and 3 are obtained from Cuppen et al.[16] and Joswiak et al.[14], respectively.

In Fig. 2.8, normalized step velocity predictions obtained from the NEQ (Eqs. (2.10), (2.11)) and equilibrium kink density models (Eq. (2.2)) are compared with kMC simulation data from the literature.[14, 16] Increase in supersaturation increases the rate of attachment ( $j+$ ) and kink density and hence step velocity monotonically increases. The model is in excellent agreement with kMC simulations despite accounting for only single and double height kinks. Step velocity predictions from the equilibrium kink density model deviate strongly from the kMC simulations as supersaturation increases. Hence,

the equilibrium model can be applied only for small deviations from  $S = 1$  (e.g.,  $\sigma \approx 0.5$ ), as is normally the case in cooling crystallization. However, anti-solvent crystallization normally occurs at higher values of supersaturation where the non-equilibrium kink density model is required.

It is well known that at low values of driving force  $\sigma = S - 1$ , the step velocity,  $v$ , is approximately linear in  $\sigma$  and the face growth rate,  $G$  is approximately quadratic in  $\sigma$  as previously shown by Sours et al.[23] and Vekilov[5]. Over a wider range of  $\sigma$ , e.g.,  $1 < \sigma < 5$  we show in Appendix A that

$$\rho_T \sim \rho_{eq} + a\sigma + b\sigma^2 \quad (2.18)$$

$$v \sim (\rho_{eq} + a\sigma + b\sigma^2) \sigma \quad (2.19)$$

$$G \sim (\rho_{eq} + a\sigma + b\sigma^2) \sigma \ln(\sigma + 1) \quad (2.20)$$

The order of the polynomial fit for kink density is at least quadratic and depends on the value of  $\beta\phi$  in the underlying mechanistic model.

## 2.6 Morphology Predictions

In order to validate the model with shape predictions, we deployed the morphology prediction software, ADDICT. ADDICT's infrastructure combines mechanistic crystal growth engine[7, 24], solid-state energy, solvent effects and crystallography calculations. The inputs to the program are crystal lattice parameters, solvent information, and solid-state energetics. The Generalized Amber Force Field (GAFF) force field[25] is used for solid-state interaction calculations. Periodic bond chains provide the structural information and interaction environment of the most-stable within the crystal. As discussed in Section 1.5, integrating the non-equilibrium model (Eqs. (2.10), (2.11), (2.16)) for step

velocity estimates into the growth engine[2, 3, 26], enables relative growth rate predictions for the slow-growing faces. The Frank-Chernov condition[27, 28] in Eq. (2.21) is used to obtain the steady-state crystal shape by calculating the distance of faces from an origin given their relative growth rates.

$$\frac{R_1}{x_1} = \frac{R_2}{x_2} = \dots = \frac{R_n}{x_n} \quad (2.21)$$

where  $R_i$  is the relative growth rate of face  $i$ ,  $x_i$  is the relative perpendicular distance of face  $i$  from the origin.

Christofides and coworkers[29–32] have shown that kMC simulations are an effective tool for predicting the face growth rates of lysozyme protein crystals. Their kMC growth rate results are in good agreement with experiment. The predictions are captured by fitting the simulated growth rate vs supersaturation curve to a third order polynomial expression that is then used in a population balance model to predict crystal shape distributions under various open loop and closed loop scenarios. The model developed in this chapter can be used in a similar population balance setting, in which there is only one adjustable parameter, namely  $k^+$ . This parameter also needs to be estimated in the Christofides approach. However, one advantage of our model is that no other growth rate parameters need to be estimated. Moreover, it is worth mentioning that there is a known method for predicting  $k^+$  from molecular simulation, as reported by Joswiak et al.[33, 34] for sodium chloride crystal growth from aqueous solution.

### 2.6.1 Naphthalene

Model-predicted habits of naphthalene are compared with experimental habits at three different ranges of supersaturation in Fig. 2.9. The proposed non-equilibrium framework accurately predicts the crystal shapes at high and low levels of supersatura-



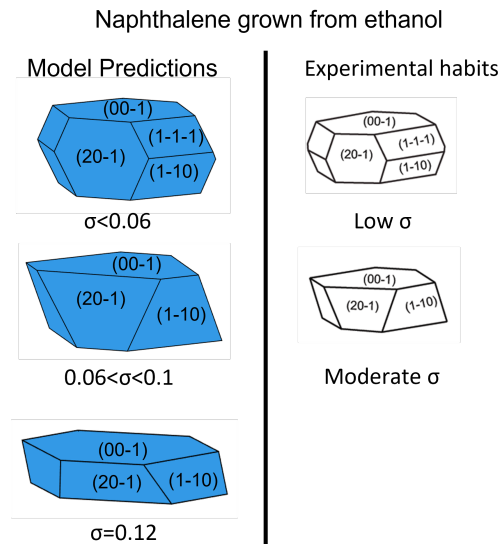


Figure 2.9: Crystal habit predicted by non-equilibrium model vs experimental data for the case of naphthalene growth from ethanol. Low and moderate  $\sigma$  experimental morphologies are adapted with permission from Grimbergen et al.[35]. Copyright 1998 American Chemical Society

tion. In this case, shape change with increase in driving force is observed due to change in growth regime from spiral to 2D birth & spread for the (1-1-1) faces that propels them off the steady-state crystal shape. The non-equilibrium kink density model was also used for estimating morphology at much higher supersaturations (such as  $\sigma = 1.5$ ,  $S = 2.5$ ) where the equilibrium kink density model fails completely. The growth mechanism remains unchanged on each face up to this value of supersaturation and the crystal morphology remains similar to the predicted morphology shown in Fig. (2.9) at  $\sigma = 0.12$ .

## 2.6.2 Rubrene

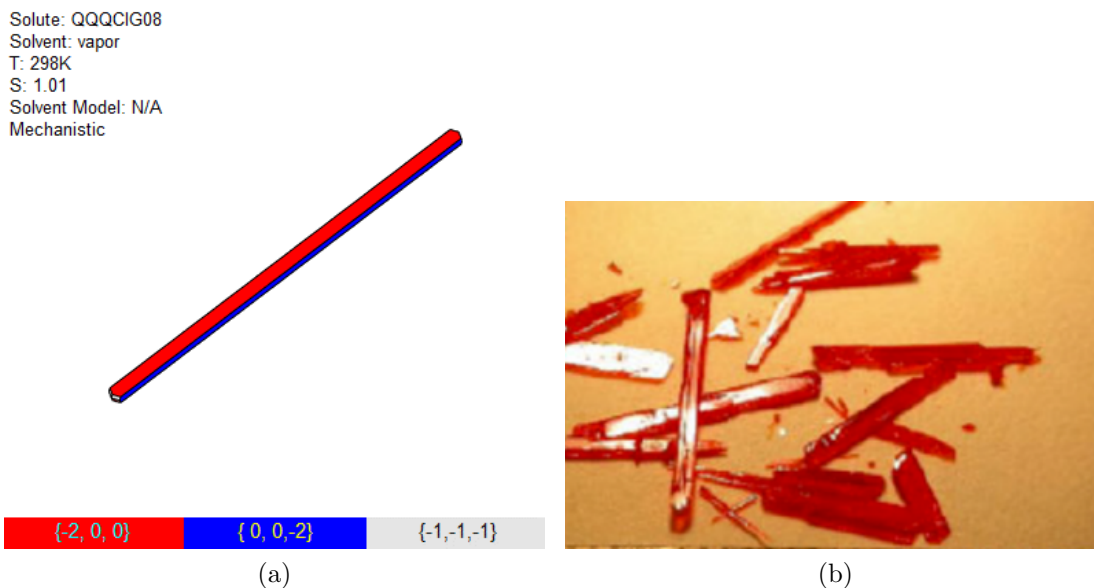


Figure 2.10: Crystal habits of the orthorhombic polymorph of Rubrene: a) predicted by non-equilibrium model, b) experimentally grown crystals by physical vapor transport. Figure reproduced with permission from De Boer et al.[36] Copyright 2004 WILEY-VCH Verlag GmbH & Co. KGaA, Weinheim.

Rubrene is a polycyclic aromatic hydrocarbon, commonly used in light emitting diodes and field-effect transistors. The crystal structure of orthorhombic Rubrene with CSD ref code QQQCIG08 is used for calculations. It crystallizes in the space group  $Cmca$ . The unit cell has 4 molecules in the unit cell and the asymmetric unit is a quarter of the molecule, hence  $Z = 4$  and  $Z' = 0.25$ . The unit cell parameters are  $a = 26.838\text{\AA}$ ,  $b = 7.1810\text{\AA}$ ,  $c = 14.332\text{\AA}$ ,  $\alpha = 90^\circ$ ,  $\beta = 90^\circ$ ,  $\gamma = 90^\circ$ . Model-based predictions of the orthorhombic polymorph of Rubrene are depicted in Fig. 2.10a for a growth environment with  $T = 298\text{K}$  and  $S = 1.01$ . In experimental studies, the crystals are grown through vapor deposition and characterized by an elongated needle or thin plate-like habit.[36] The model predicts a long rod-like morphology and aligns with the experimental observations. Hence, the model is successful in providing reliable habit predictions for crystals with centrosymmetric organic molecules.

## 2.7 Conclusion

The simplified steady-state framework provides the platform for constructing master equations by considering only the concentrated site configurations and event rates. The master equations are then solved to obtain a non-equilibrium kink density model for Kossel crystals and centrosymmetric molecules. The model is validated with respect to kMC simulations. Integration of SSSF model into ADDICT allowed morphology predictions, which demonstrated excellent agreement with experimental observations. The lowest order polynomial approximation of the non-linear function for  $\rho_T$  as a function of driving force  $\sigma = S - 1$  is quadratic. This results in step velocity being at least cubic in  $\sigma$ . However, most of the molecules of practical significance are complex and lack an inversion center. Such a steady-state methodology will be generalised to non-Kossel crystals in the subsequent chapters.

# Bibliography

- (1) Lovette, M. A.; Browning, A. R.; Griffin, D. W.; Sizemore, J. P.; Snyder, R. C.; Doherty, M. F. Crystal Shape Engineering. *Industrial & Engineering Chemistry Research* **2008**, *47*, 9812–9833.
- (2) Landis, S.; Zhao, Y.; Doherty, M. F. Digital design of crystalline solids. *Computers & Chemical Engineering* **2020**, *133*, 106637.
- (3) Li, J.; Tilbury, C. J.; Kim, S. H.; Doherty, M. F. A design aid for crystal growth engineering. *Progress in Materials Science* **2016**, *82*, 1–38.
- (4) Snyder, R. C.; Doherty, M. F. Predicting crystal growth by spiral motion. *Proceedings of the Royal Society A: Mathematical, Physical and Engineering Sciences* **2009**, *465*, 1145–1171.
- (5) Vekilov, P. G. What determines the rate of growth of crystals from solution? *Crystal Growth and Design* **2007**, *7*, 2796–2810.
- (6) Winn, D.; Doherty, M. F. A new technique for predicting the shape of solution-grown organic crystals. *AIChE journal* **1998**, *44*, 2501–2514.
- (7) Tilbury, C. J.; Green, D. A.; Marshall, W. J.; Doherty, M. F. Predicting the Effect of Solvent on the Crystal Habit of Small Organic Molecules. *Crystal Growth & Design* **2016**, *16*, 2590–2604.

## BIBLIOGRAPHY

---

- (8) Frenkel, J. On the Surface Motion of Particles on Crystals and Natural Roughness of Crystal Faces. *Journal of Physics USSR* **1945**, *9*, 392.
- (9) Leamy, H. J.; Gilmer, G. H.; Jackson, K. A. In *Surface Physics of Materials, Vol. 1*, M., B. J., Ed.; Academic Press: Amsterdam, 1975; Chapter 3, p 121.
- (10) Kuvadia, Z. B.; Doherty, M. F. Spiral Growth Model for Faceted Crystals of Non-Centrosymmetric Organic Molecules Grown from Solution. *Crystal Growth & Design* **2011**, *11*, 2780–2802.
- (11) Voronkov, V. V. Movement of an elementary step by means of formation of one-dimensional nuclei. *Soviet Physics Crystallography* **1970**, *15*, 8.
- (12) Frank, F. C. Nucleation-controlled growth on a one-dimensional growth of finite length. *Journal of Crystal Growth* **1974**, *22*, 233–236.
- (13) Zhang, J.; Nancollas, G. H. Kink densities along a crystal surface step at low temperatures and under nonequilibrium conditions. *Journal of Crystal Growth* **1990**, *106*, 181–190.
- (14) Joswiak, M. N.; Peters, B.; Doherty, M. F. Nonequilibrium Kink Density from One-Dimensional Nucleation for Step Velocity Predictions. *Crystal Growth & Design* **2018**, *18*, 723–727.
- (15) Van der Eerden, J. P. In *Handbook of Crystal Growth, Vol. 1*, Hurle, D. T. J., Ed.; Elsevier: Amsterdam, 1993; Chapter 5, p 307.
- (16) Cuppen, H. M.; Meeke, H.; van Veenendaal, E.; van Enckevort, W. J. P.; Bennema, P.; Reedijk, M. F.; Arsic, J.; Vlieg, E. Kink density and propagation velocity of the [010] step on the Kossel (100) surface. *Surface Science* **2002**, *506*, 183–195.

## BIBLIOGRAPHY

---

- (17) Li, J.; Tilbury, C. J.; Joswiak, M. N.; Peters, B.; Doherty, M. F. Rate Expressions for Kink Attachment and Detachment During Crystal Growth. *Crystal Growth & Design* **2016**, *16*, 3313–3322.
- (18) Chernov, A. A.; Rashkovich, L. N.; DeYoreo, J. J. In *AIP Conference Proceedings*, 2007; Vol. 916, pp 34–47.
- (19) Petsev, D. N.; Chen, K.; Gliko, O.; Vekilov, P. G. Diffusion-limited kinetics of the solution–solid phase transition of molecular substances. *Proceedings of the National Academy of Sciences* **2003**, *100*, 792–796.
- (20) Tilbury, C. J.; Joswiak, M. N.; Peters, B.; Doherty, M. F. Modeling Step Velocities and Edge Surface Structures during Growth of Non-Centrosymmetric Crystals. *Crystal Growth & Design* **2017**, *17*, 2066–2080.
- (21) Eyring, H. The activated complex in chemical reactions. *The Journal of Chemical Physics* **1935**, *3*, 107–115.
- (22) Kramers, H. A. Brownian motion in a field of force and the diffusion model of chemical reactions. *Physica* **1940**, *7*, 284–304.
- (23) Sours, R. E.; Zellelow, A. Z.; Swift, J. A. An in situ atomic force microscopy study of uric acid crystal growth. *The Journal of Physical Chemistry B* **2005**, *109*, 9989–9995.
- (24) Lovette, M. A.; Doherty, M. F. Predictive modeling of supersaturation-dependent crystal shapes. *Crystal Growth & Design* **2012**, *12*, 656–669.
- (25) Wang, J.; Wolf, R. M.; Caldwell, J. W.; Kollman, P. A.; Case, D. A. Development and testing of a general amber force field. *Journal of Computational Chemistry* **2004**, *25*, 1157–1174.

## BIBLIOGRAPHY

---

- (26) Zhao, Y.; Tilbury, C. J.; Landis, S.; Sun, Y.; Li, J.; Zhu, P.; Doherty, M. F. A New Software Framework for Implementing Crystal Growth Models to Materials of Any Crystallographic Complexity. *Crystal Growth & Design* **2020**, *20*, 2885–2892.
- (27) Frank, F. C. On the kinematic theory of crystal growth and dissolution processes. *Growth and Perfection of Crystal* **1958**, *411*.
- (28) Chernov, A. A. The kinetics of the growth forms of crystals. *Soviet Physics Crystallography* **1963**, *7*, 728–730.
- (29) Kwon, J. S.-I.; Nayhouse, M.; Christofides, P. D.; Orkoulas, G. Modeling and control of crystal shape in continuous protein crystallization. *Chemical Engineering Science* **2014**, *107*, 47–57.
- (30) Kwon, J. S.-I.; Nayhouse, M.; Christofides, P. D.; Orkoulas, G. Modeling and control of shape distribution of protein crystal aggregates. *Chemical Engineering Science* **2013**, *104*, 484–497.
- (31) Kwon, J. S.-I.; Nayhouse, M.; Christofides, P. D.; Orkoulas, G. Modeling and control of protein crystal shape and size in batch crystallization. *AIChE Journal* **2013**, *59*, 2317–2327.
- (32) Nayhouse, M.; Kwon, J. S.-I.; Christofides, P. D.; Orkoulas, G. Crystal shape modeling and control in protein crystal growth. *Chemical engineering science* **2013**, *87*, 216–223.
- (33) Joswiak, M. N.; Peters, B.; Doherty, M. F. In Silico Crystal Growth Rate Prediction for NaCl from Aqueous Solution. *Crystal Growth & Design* **2018**, *18*, 6302–6306.
- (34) Joswiak, M. N.; Doherty, M. F.; Peters, B. Ion dissolution mechanism and kinetics at kink sites on NaCl surfaces. *Proceedings of the National Academy of Sciences* **2018**, *115*, 656–661.

## BIBLIOGRAPHY

---

- (35) Grimbergen, R. F. P.; Reedijk, M. F.; Meekes, H.; Bennema, P. Growth behavior of crystal faces containing symmetry-related connected nets: a case study of naphthalene and anthracene. *The Journal of Physical Chemistry B* **1998**, *102*, 2646–2653.
- (36) De Boer, R.; Gershenson, M.; Morpurgo, A.; Podzorov, V. Organic single-crystal field-effect transistors. *physica status solidi (a)* **2004**, *201*, 1302–1331.



# Chapter 3

## Simplified Steady-State Framework: Molecular AB Crystals

Reproduced in part with permission from:

Padwal, N.A.; Doherty, M.F. Step Velocity Growth Models for Molecular Crystals: Two Molecules in the Unit Cell. *Crystal Growth & Design* **2024**, 24(11), 4368-4379.

DOI:10.1021/acs.cgd.3c01508. Copyright 2024 American Chemical Society.

### 3.1 Introduction

Industrial crystals are normally grown at temperatures and supersaturations conducive to layered growth mechanisms such as spiral growth or 2D nucleation. Such regimes ensure gradual addition of growth layers with low impurity uptake. Within the layered regimes, the rate determining step is the integration of growth units along the crystal surface.[1] Hence, surface diffusion and bulk diffusion are neglected. On the atomic scale, growth of crystal layers occurs via attachment of growth units mainly at kink sites along steps.[2–9] Gradual incorporation of growth units at various sites on a step in such

a manner propels it in the normal direction at a rate called the *step velocity*. The velocities of steps along faces eventually determine the face growth rate and subsequently the morphology, since crystal shape is dominated by the slowest-growing faces.[10] Hence, appropriate step velocity models are crucial in mechanistic crystal growth models for accurate prediction of crystal properties.

For a Kossel crystal, step kinetics and the influence of supersaturation and temperature on kink density and step velocity are well-studied. Several nonequilibrium kink density and step velocity models have been proposed for the Kossel case. The nonequilibrium kink density models are based on Frank and Voronkov's[11, 12] steady-state principle and include Zhang and Nancollas[13], van der Eerden,[14], Cuppen et al.[8], Joswiak et al.[15] However, these models are not readily extended to realistic molecular crystals. Chapter 2 introduced the novel theory of Simplified Steady-State Framework (SSSF) accounting for only the most-likely surface events influencing formation and destruction of the predominant kink types. The theory provides the road map for formulation of steady-state equations of the predominant kink types such as the single-height kink, double-height kink and the edge junction. In this chapter, we generalise and extend SSSF to asymmetric molecular crystals with two growth units in the unit cell. Note that Kossel models can be applied to centrosymmetric growth units (e.g., symmetric organic molecules), owing to the presence of an inversion centre in these molecules as discussed in Section 1.4.

One of the deepest unsolved problems in crystal growth is the development of a model to capture step velocity at high supersaturation for real asymmetric molecules which have asymmetric bonding interactions with their neighbors i.e. the non-Kossel crystals. The key quantity needed for such models is accurate knowledge of the density of surface docking sites along the moving crystal steps as a function of supersaturation i.e. the kink density. The first model was developed in 1945 for Kossel Crystals by Frenkel[16] based on statistically independent kinks and equilibrium considerations. Not surprisingly, he

found that the equilibrium kink densities were Boltzmann distributed. This model, and extensions of it for non-Kossel crystals, has been used universally to this day[7, 9, 17, 18]. However, the application of Boltzmann statistics to non-Kossel crystals is both conceptually and quantitatively incorrect, owing to spatial correlations between surface sites[9], even under equilibrium conditions. But we continue to use them because there is no known alternative.

Crystal growth is inherently a non-equilibrium phenomenon and only occurs when the solution is supersaturated. Many practical crystallization processes occur far from equilibrium. Moreover, when the solute molecules being crystallized are asymmetric they arrange themselves in very specific patterns, as they must, so that they create a three dimensional solid with long-range crystallographic order. The surface sites are not spatially independent.[9] In this work, we abandon both the equilibrium thinking, and the spatial independence thinking. Instead, we develop a fully non-equilibrium approach in which we identify the subset of most-concentrated surface sites that incorporate the correct crystallographic relationships between the molecules. We limit the number of kink types to include only those that are the most likely to occur - single and double kinks and edges. That is the key simplification that makes the approach tractable. We then formulate a set of steady-state master equations for the *birth rate* and *death rate* of kinks which can be solved to determine the kink density. The resulting model is relatively simple. It applies both near to and far from equilibrium, and correctly accounts for configurational constraints via the use of conditional probabilities.

## 3.2 AB Organic Crystal System

In this chapter, we study the AB organic crystal with two growth units A and B in the unit cell. The growth units are molecules in this study but in general can be ions, atoms,

dimers, etc. The growth units are the same component and identical in solution but integrate into the crystal lattice in different orientations. The molecules are allowed to be non-centrosymmetric and do not necessarily have an inversion center. Hence, the AB system can be characterized with  $Z = 2$  and  $Z' = 1, 2$ , where  $Z$  is the number of molecules in the unit cell and  $Z'$  is the number of molecules in the asymmetric unit. Asymmetry of the molecule is distinct from asymmetry of the crystalline lattice.[17] A centrosymmetric molecule has an inversion center aligned with its center of mass. Centrosymmetric space groups have an inversion center as one of their symmetry elements. Examples of such space groups are  $P2_1/c$  and  $P2/c$ . Models developed in this chapter are applicable to asymmetric molecules crystallizing in any space group. Such a crystal will comprise

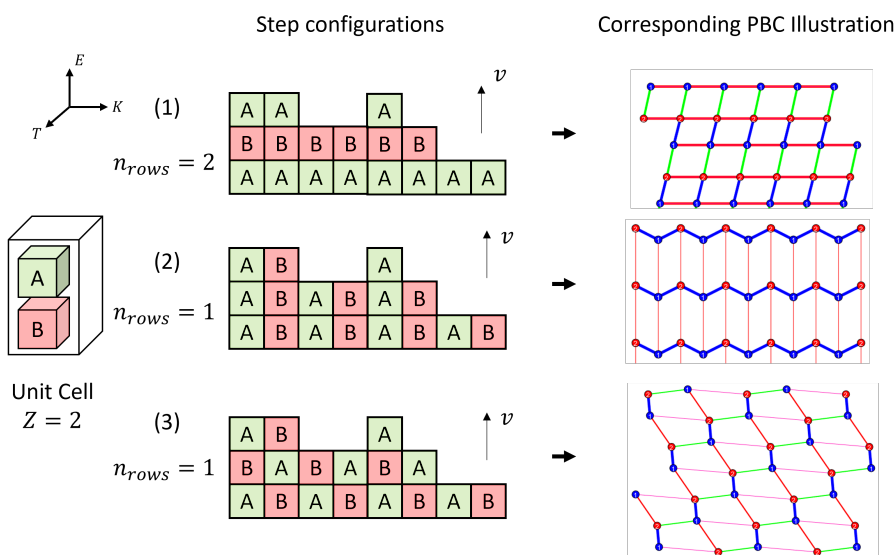


Figure 3.1: Different step configurations observed for an AB type organic crystal. The PBCs illustrate examples of real network of interactions along corresponding step configurations. The PBCs are generated by the software ADDICT.[19]

of steps with various local step structures of  $A$  and  $B$  growth units. This gives rise to various step configurations as demonstrated in Fig. 3.1: alternating rows of  $A$  and  $B$  (configuration 1), alternating columns of  $A$  and  $B$  (configuration 2) and checkered pattern (configuration 3). Steps in different configurations constitute different kink types and undergo different surface processes resulting in distinct step kinetics and must be

analysed in silos.

Surface processes along a step consist of attachment and detachment of growth units at various sites such as a pit, edge, and especially kink sites. A surface (step) process can result in formation or destruction of different types of kinks. At steady-state, the densities of all kink types settle to constant values. Therefore, the net rate of formation must equal the net rate of destruction for each of the kink types owing to multiple surface processes under steady-state conditions[11, 12]. This is captured by the steady-state master equations. Cuppen et al.[8], in their analysis of nonequilibrium kink density for Kossel crystals, rigorously accounted for all possible surface events and constructed steady-state equations for all heights of kinks summing to  $\infty$ . In chapter 2, we introduced the Simplified Steady-State Framework (SSSF) based on the hypothesis that only a few of the surface events with greatest probability capture major supersaturation effects and hence the overall surface kinetics. Therefore, the steady-state equations or *master equations* only involve the most-likely events in this work. This allows drastic simplification of the model equations, which are then solved simultaneously in a numerical nonlinear calculation to obtain supersaturation dependence of the kink densities. The model-based predictions of kink density and step velocity are then compared to kMC simulations from literature and serve as a validation for the model. The model-predictions of step velocities are then integrated within the framework of the software ADDICT (Advanced Design and Development of Industrial Crystallization Technology)[19] to obtain model-based morphology predictions.

### 3.3 Methods and Approach

In this chapter, we extend and generalise the SSSF to the case of AB type crystals. We perform steady-state analysis for the predominant junctions (e.g., single and double

kinks and edges) accounting for only the most-probable events forming and destroying the kinks. The majority of surface events have low probability and are neglected to maintain simplicity of the framework. Although less-likely surface events are excluded from the framework, the steady-state equations derived must satisfy certain constraints owing to step topology and multiplicity of growth units. This is unlike the Kossel steps with a singular type of growth unit. The constraints are as follows,

1. Stoichiometric constraints: the net rate of attachment of the two growth units A and B should be equal in order to maintain overall stoichiometry of the unit cell. The stoichiometric constraint provides a consistency check for the master equations to satisfy.
2. Surface configuration constraints: In contrast to the Kossel case, the surface occurrence of kinks along the step are no longer structurally independent, but correlated to their neighboring kinks to maintain the local step structure. Hence, conditional probabilities are employed to accurately capture the probability of site occurrence along steps, as discussed in Section 3.3.1.

Section 3.3.1 provides details on identification of densely-populated sites along the step, and derives master equations accounting for high-probability surface events. The steady-state equations thereby derived are then solved numerically to obtain nonequilibrium kink densities as a function of supersaturation and other growth parameters such as temperature, and solvent-modified surface interaction energies. The kink densities estimated are then used for step velocity predictions through net attachment rate calculations of each growth unit in the unit cell. Section 3.3.2 provides a detailed explanation of step velocity modeling as a function of nonequilibrium kink densities.

### 3.3.1 Modeling Nonequilibrium Kink Density

In this section, we discuss in detail the steady-state analysis and derive equations governing step kinetics for step configuration 1 with alternating rows of A and B. Refer to Appendix B for steady-state analysis of step configurations 2 and 3. A sequential approach is outlined below, starting from identification of predominant junctions/kinks, major surface sites and most-probable surface events:

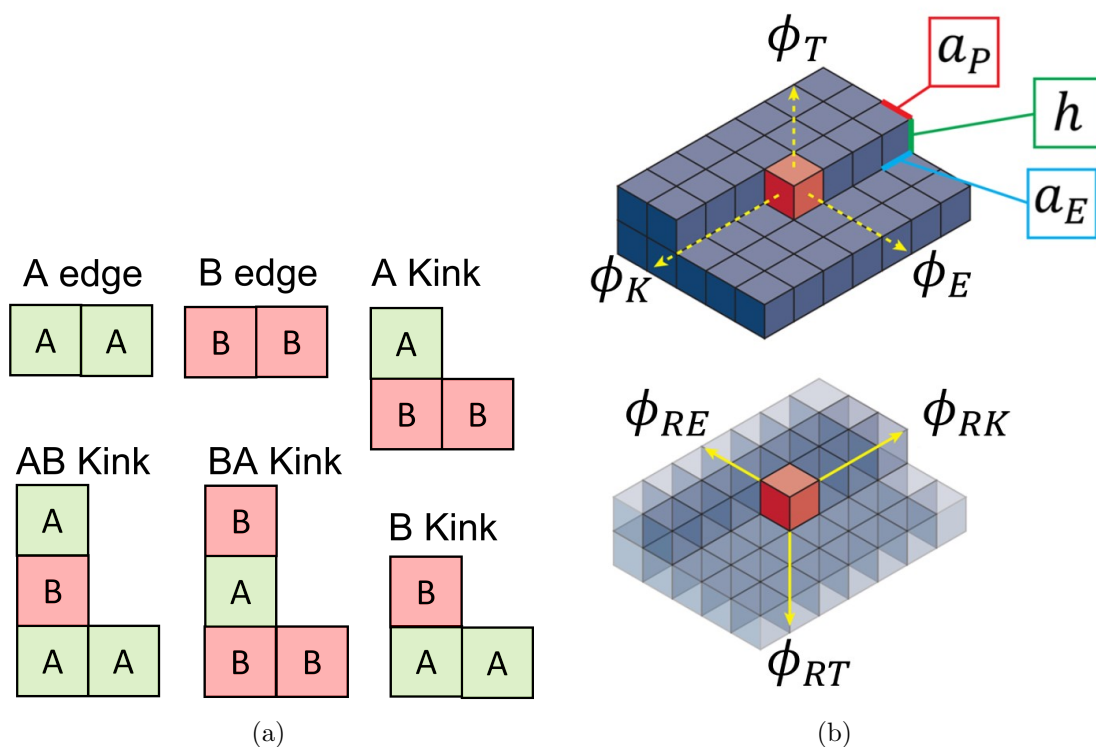


Figure 3.2: (a) Predominant kink and edge junctions along step configuration 1 with alternating rows of growth units A and B (b) Crystalline lattice directions defined around a growth unit, namely, kink, edge, terrace and reverse kink, reverse edge and reverse terrace axes.  $\phi_K$ ,  $\phi_E$ ,  $\phi_T$  represent half of the bond energy formed by the growth unit along the *kink*, *edge* and *terrace* directions, respectively. These are the broken bond interactions exposed to the solvent. Similarly,  $\phi_{RK}$ ,  $\phi_{RE}$ ,  $\phi_{RT}$  represent half of the bond energy formed by the growth unit along the *reverse kink*, *reverse edge* and *reverse terrace* directions, respectively. The reverse bonds characterize interactions formed by the growth unit with the crystalline lattice. The lattice directions are aggregate descriptors and need not be orthogonal for real crystals. The step dimensions are characterized by propagation length ( $a_P$ ), step height ( $h$ ) and growth unit width ( $a_E$ ). Figure reproduced with permission from Tilbury et al.[18]. Copyright 2017 American Chemical Society.

1. Identification of predominant junctions: Predominant junctions are the ones with minimum broken bond interactions at the interface and are expected to densely populate the step surface and hence the configuration space. This includes the lowest energy junction types - edges, followed by single kinks and then double kinks. (Refer to Appendix A for detailed discussion on junctions and sites) Henceforth, kink junctions are referred to as simply *kinks*. We truncate the junction space at double kinks since the concentration of kinks reduces exponentially with increase in kink height. In an AB non-Kossel crystal, kinks consist of multiple types: A and B single kinks, AB and BA double kinks, ABA and BAB triple kinks, etc. To maintain simplicity, only the most populated junctions are included in the steady-state analysis i.e., the edge, single and double-height kinks, with all kink heights  $\geq 3$  excluded. For step configuration 1, the predominant junctions are namely: A edge, B edge, A kink, B kink, AB kink and BA kink and depicted in Fig. 3.2. For step configuration 1, the east and west-facing kinks are equivalent since they have alike energetic environments. On the contrary, for step configurations 2 and 3, the east and west-facing kinks have dissimilar energetic environments and are treated as distinct in Appendix B.
2. Identification of major sites and most-likely events: Sites comprise of adjoining junctions or kinks, thus site densities are proportional to the product of individual kink densities that form the site. An order-of-magnitude analysis is conducted to shortlist major sites prevalent on the steps. For instance, the edge junctions, single and double kinks are observed on the steps in decreasing orders of magnitude. This allows us to identify the *major sites* which will densely-populate the step surface similar to the procedure undertaken for Kossel crystal in Section A. For step configuration 1, major sites are the sites which populate subset  $M$  in Fig. 3.3



and provided in Table B.2. The surface events occurring with higher probability along the step are the ones which act on major sites, transforming them into other major sites. These are the so-called *most-likely events* and they are identified by subjecting the major sites to attachment and detachment of a growth unit. All the other type of surface events are less-likely and not accounted for in the framework i.e., events transforming sites across subsets  $M$  and  $L$  and events transforming sites within subset  $L$ . Refer to Appendix B for the table of major sites, most-likely events, associated rates and density of sites for step configurations 1, 2 and 3.

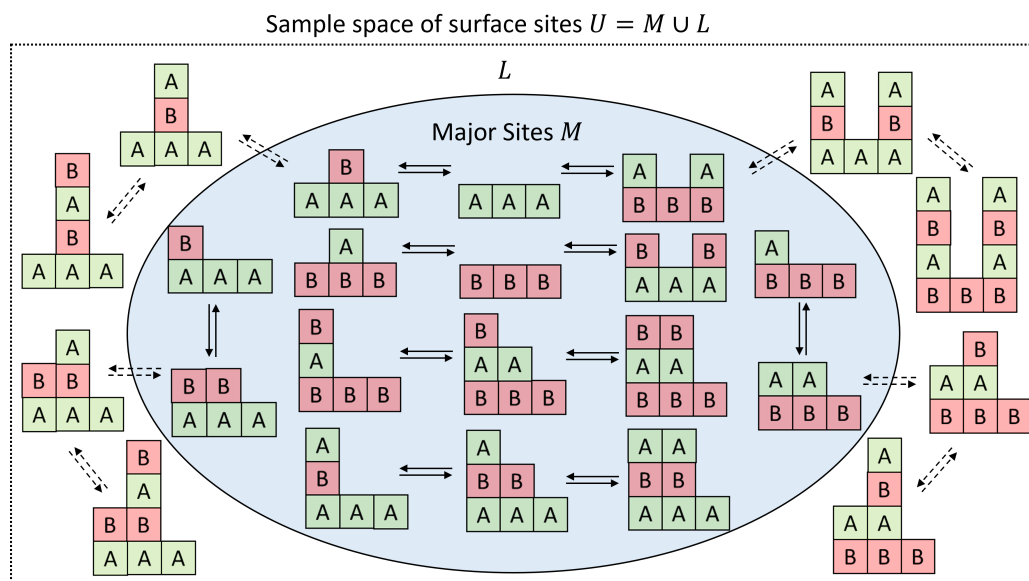


Figure 3.3: Schematic description of surface sites prevalent on step configuration 1 and surface events given by arrow descriptors. The surface sites can be segregated into two sets: 1) Subset  $M$  consists of *major sites* and *most-likely events* transform major sites into each other, 2) All other sites are assumed to sparsely populate the step surface and belong to subset  $L$ . A few  $L$  sites are depicted here, there are many more. The events which transform sites within subset  $L$  or across subsets occur at low probabilities and are categorised as the *less-likely events*. The *most-likely events* and *less-likely events* are depicted by solid and dashed arrows, respectively. The sample space of all surface sites along the step is the union of the two sets  $U = M \cup L$ .

3. Rate modeling: A stochastic approach is undertaken in modeling single-particle elementary surface attachment and detachment rates. Surface diffusion is neglected, which is justifiable for solvent-grown crystals owing to high free energy desolvation

barriers for surface integration of growth units.add ref The rate model utilized is based on a modification of the random rain model[14] by Li et al.[5] which accounts for the thermodynamics of crystallization, detailed balance and solvent effects. The attachment rate  $j^+$  is modeled as a first order physical reaction in solute composition; and detachment rate  $j_i^-$  as zeroth order. The attachment rate is assumed to be isotropic and independent of the site of attachment[4, 17, 19–21] and growth unit, resulting in  $j_A^+ = j_B^+ = j^+$ . The detachment rate  $j_{A,i}^-$  or  $j_{B,i}^-$  depends on the work of detachment  $\Delta W_i$  and hence is a function of the growth unit detached (A or B) and the number of lateral neighbors  $i$  at the site of detachment.

$$j^+ = k^+ x_{sat} S = k^+ e^{-\beta \overline{\Delta W}_{sat}} S \quad (3.1)$$

$$j_{A,i}^- = k_{A,i}^- = k^+ e^{-\beta \Delta W_{A,i}} \quad (3.2)$$

$$j_{B,i}^- = k_{B,i}^- = k^+ e^{-\beta \Delta W_{B,i}} \quad (3.3)$$

where  $S$ : supersaturation,  $k^+$ : attachment rate constant,  $\Delta W_{A,i}$ : work of detachment of A from site type  $i$ ,  $\Delta W_{B,i}$ : work of detachment of B from site type  $i$ , and  $x_{sat} = e^{-\beta \overline{\Delta W}_{sat}}$  is the saturation mole fraction. Here,  $i$  is the site type and characterises the sites where  $i$  is the number of intra-row (along the kink axis) bonds broken. The work of detachment  $\Delta W_i$  is the summation of all the bonds broken during detachment and depends on the reverse kink, reverse edge and reverse terrace bond energies of the growth unit dissociated at the site of detachment.

$$\Delta W_{A,i} = 2i\phi_A^{RK} + 2\phi_A^{RE} + 2\phi_A^{RT} \quad (3.4)$$

$$\Delta W_{B,i} = 2i\phi_B^{RK} + 2\phi_B^{RE} + 2\phi_B^{RT} \quad (3.5)$$

where  $i$  is the number of bonds broken along the row and characterizes the type of

sites. The factor of two accounts for the convention that  $\phi$ s are half the total bond strength. Fig. 3.4 depicts interaction spheres of growth units at various site types of step configuration 1. The reverse interactions determine the detachment rates at the corresponding sites. For instance, detachment of an adatom from a step results in  $i = 0$ , since no bonds along the row are broken. During detachment from kinks a single bond is broken along the kink axis and hence  $i = 1$ . Detachment from every type of site requires the breaking of one reverse edge bond and one reverse terrace bond, hence prefactors for  $\phi^{RE}$  and  $\phi^{RT}$  are dropped. For step configuration 1, the east and west-facing kinks are equivalent since they have identical energetic environments. Mathematically, this translates to the relation  $\phi_A^K = \phi_A^{RK}$ ,  $\phi_B^K = \phi_B^{RK}$ , which are satisfied for steps belonging to configuration 1. Refer to Appendix B for analysis of step configurations 2 and 3, wherein east and west-facing kinks have distinct energetic environments and warrant separate treatments. The saturation

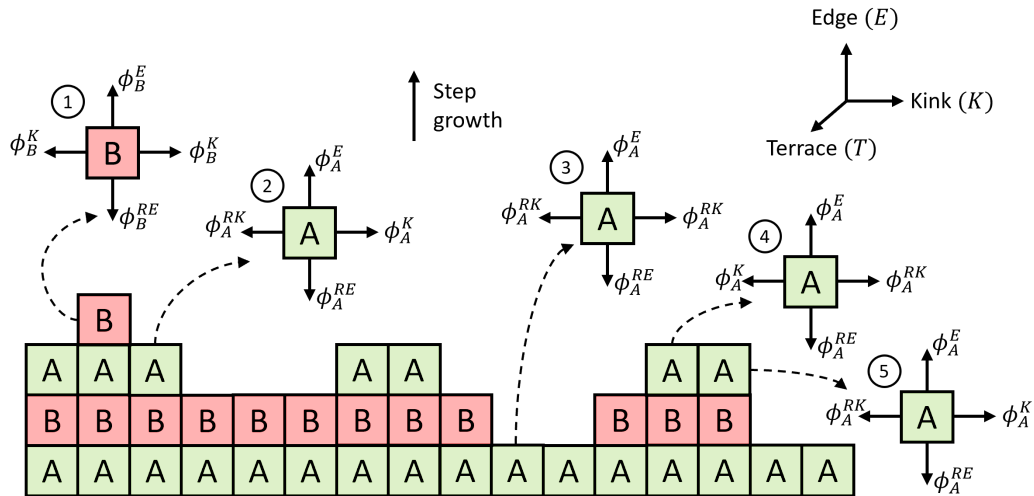


Figure 3.4: Step surface of configuration 1: Interaction spheres around growth units at various site types and the corresponding detachment rates are as follows: 1) B adatom ( $j_{B,0}^-$ ), 2) east-facing A kink ( $j_{A,1}^-$ ), 3) A edge ( $j_{A,2}^-$ ), 4) west-facing A kink ( $j_{A,1}^-$ ), 5) east-facing AB kink ( $j_{A,1}^-$ ). The reverse interactions mark bonds formed by growth units with the crystal. The terrace and reverse terrace bonds are perpendicular to the page and not depicted for simplicity.

work of detachment,  $\overline{\Delta W}_{sat}$ , is the average of works of detachment of the growth units A and B across all site types. Such a definition of  $x_{sat}$  ensures all unique intermolecular bond energies in the interaction spheres of all the growth units in the unit cell are accounted for and interfaced with the appropriate growth environment.

$$\overline{\Delta W}_{sat} = \frac{\overline{\Delta W}_A + \overline{\Delta W}_B}{2} \quad (3.6)$$

$$= \phi_A^{RK} + \phi_A^{RE} + \phi_A^{RT} + \phi_B^{RK} + \phi_B^{RE} + \phi_B^{RT} \quad (3.7)$$

Depending on the growth environment, the interactions are solvent-modified using appropriate solvent models[22–25] as discussed in Section 1.3. The rate constants  $k_A^+$  and  $k_B^+$  are a function of the desolvation barriers and since the growth units are identical in solution the rate constants are assumed to be approximately equal.[9, 17, 18]

4. Event Rate Modeling: Following the earlier methodologies[8, 14] of modeling surface processes, the rate of incorporation into a surface site is the product of elementary rate of attachment/detachment and number density of the pertaining site, thereby effectively making the attachment rates second order. A site of attachment or detachment is defined by the adjoining junctions  $J1$  and  $J2$ . From step 1 above, a junction is a type of kink or edge. The site density depends on the densities of adjoining junctions that constitute the site.[26] For Kossel crystals, the junctions can be treated as statistically independent[27] and the probability of the site occurring is the product of densities of constituting junctions. Thus,

$$\rho_s(J1, J2) = \rho_{J1} \times \rho_{J2} \quad (3.8)$$

where  $\rho_s$  is the site density,  $\rho_{J1}$  and  $\rho_{J2}$  are the densities of adjoining junctions,

respectively.

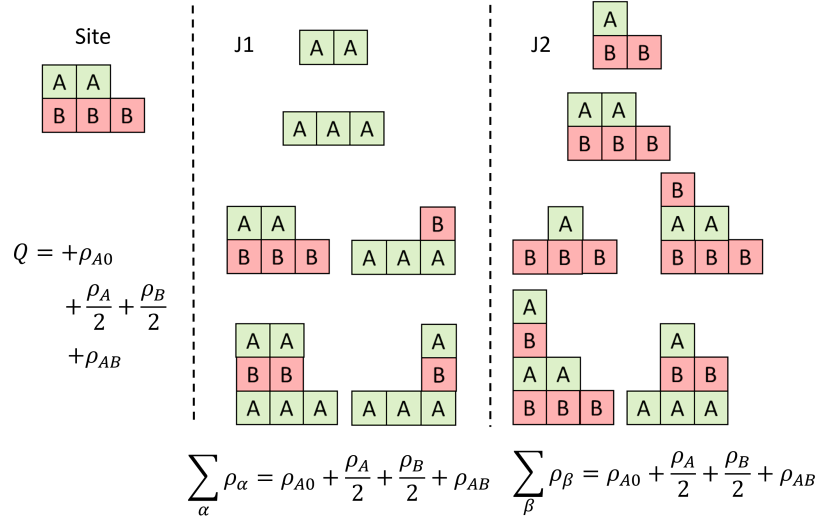


Figure 3.5: Partition function of a site composed of adjoining junctions: A edge and A kink. Given the position of A edge,  $\alpha$  sums over all junctions that can be contiguous to it. Given the position of A kink,  $\beta$  sums over all permissible junctions that can be contiguous to it. East and west-facing kinks of the same type are identical for configuration 1 and therefore have equal kink densities ( $\rho_A^e = \rho_A^w = \frac{\rho_A}{2}$ ,  $\rho_B^e = \rho_B^w = \frac{\rho_B}{2}$ ). For  $\alpha$  summation, only east-facing A kink is structurally permissible to adjoin A edge. Similarly, only west-facing B kink is structurally permissible. As a result,  $\rho_A$  and  $\rho_B$  are halved in the summation.

For non-Kossel crystals, incoming molecules from the solution can only be docked in specific orientations depending on the spatial location. This restricts permissible neighboring kinks. In order to maintain the topology of step configuration, the positions of kinks are correlated and are no longer structurally independent. The presence of a junction  $J1$  at a location constrains the neighboring junctions in the same manner only A growth unit is integrated along A rows in configuration 1. We use conditional probabilities[28] to account for the spatial correlation between

kinks by modeling site probabilities as follows,

$$\rho_s(J1, J2) = P(J1 \cap J2) = P(J1|J2)P(J2) \quad (3.9)$$

$$= \frac{\rho_{J1}}{\sum_{\beta} \rho_{\beta}} \rho_{J2} \quad (3.10)$$

$$\rho_s(J1, J2) = P(J2 \cap J1) = P(J2|J1)P(J1) \quad (3.11)$$

$$= \frac{\rho_{J2}}{\sum_{\alpha} \rho_{\alpha}} \rho_{J1} \quad (3.12)$$

where the denominators are summations  $\sum_{\alpha} \rho_{\alpha}$  and  $\sum_{\beta} \rho_{\beta}$  over all possible junctions that can adjoin  $J1$  and  $J2$ , respectively. By the commutative nature of intersection probabilities, the intersection of sets must be equal such that  $P(J1 \cap J2) = P(J2 \cap J1)$ . This results in the two summations to be equal and gives rise to a partition function  $Q$ .

$$Q = \sum_{\alpha} \rho_{\alpha} = \sum_{\beta} \rho_{\beta} \quad (3.13)$$

A partition function in the context of a given step configuration is a collection of kink densities arising out of constraints to maintain surface topology. For step configuration 1, functions  $\sum_{\alpha} \rho_{\alpha}$  and  $\sum_{\beta} \rho_{\beta}$  are equal for each pair of neighboring junctions. Figure 3.5 provides structural representations of  $\sum_{\alpha} \rho_{\alpha}$  and  $\sum_{\beta} \rho_{\beta}$  for a specific site. Analysis of structurally permissible kink density sets for each of the growth units along configuration 1, renders two partition functions,  $Q_1$  and  $Q_2$

which are given by,

$$Q_1 = \rho_{A0} + \frac{\rho_A}{2} + \frac{\rho_B}{2} + \rho_{AB} \quad (3.14)$$

$$Q_2 = \rho_{B0} + \frac{\rho_A}{2} + \frac{\rho_B}{2} + \rho_{BA} \quad (3.15)$$

where  $\rho_A$ ,  $\rho_B$ ,  $\rho_{AB}$ ,  $\rho_{BA}$ ,  $\rho_{A0}$ ,  $\rho_{B0}$  are the densities of A kink, B kink, AB kink, BA kink, A edge and B edge, respectively.  $Q_1$  and  $Q_2$  are utilized in steady-state equation models in the following subsection. In the subsequent master equation analysis, the spatial kink correlations are accounted for in the form of conditional probabilities utilizing partition functions. In the case of configurations where  $\sum_{\alpha} \rho_{\alpha}$  and  $\sum_{\beta} \rho_{\beta}$  are distinct collections of kink densities, the commutative property dictates equivalence of  $\sum_{\alpha} \rho_{\alpha}$  and  $\sum_{\beta} \rho_{\beta}$  functions. This results in additional equations in the form of configurational constraints on kink densities, which are appended to the steady-state master equations. Refer to Appendix C for a generalized approach to evaluating partition functions and configurational constraints for a given step configuration with variable number of growth units.

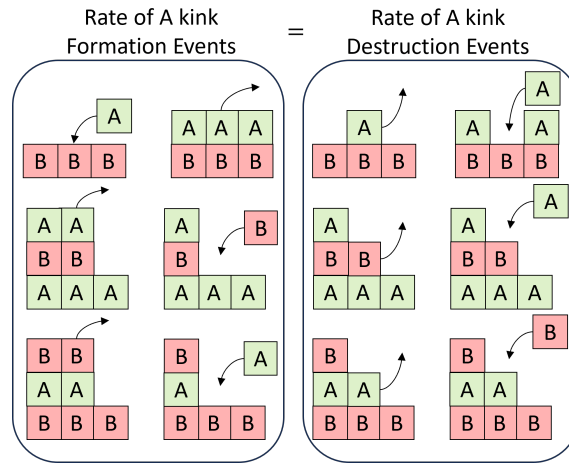


Figure 3.6: Most-likely events causing formation and destruction of A kinks.

5. Construction of Master Equations: Once the most-likely events have been identi-

fied and their rates modeled, building master equations requires identifying how each of the most-likely events affect the predominant junctions. According to the steady-state principle[11, 12], the rate of formation of kinks must equal the rate of destruction. In SSSF, the rate of formation is the summation of rates of all the most-likely surface processes forming the specific junction/kink, similarly the rate of destruction is the summation of rates of surface processes destroying the junction/kink of interest. This permits construction of master equations for the predominant junctions. For instance, events in the most-likely subset  $M$  in Fig. 3.3 which affect the density of A kinks are depicted in Fig. 3.6. Refer to Table B.2 for the detailed list of most-likely events, corresponding rates and their influence on A kinks. The resulting master equation for A kink is,

$$\begin{aligned}
& 2j^+ \frac{\rho_{B0}^2}{Q_2} + 2j_{A,2}^- \frac{\rho_{A0}^2}{Q_1} - 2j^+ \frac{\rho_A^2}{4Q_2} - 2j_{A,0}^- \frac{\rho_A^2}{4Q_1} \\
& + [(j^+ + j_{A,1}^-) \frac{\rho_{AB}\rho_{A0}}{Q_1} - (j^+ + j_{B,1}^-) \frac{\rho_A\rho_B}{2Q_2} \\
& + (j^+ + j_{B,1}^-) \frac{\rho_{BA}\rho_{B0}}{Q_2} - (j^+ + j_{A,1}^-) \frac{\rho_A\rho_B}{2Q_1}] = 0
\end{aligned} \tag{3.16}$$

where  $j^+$ : attachment rate,  $j_{A,i}^-$ : detachment rate of A from site type  $i$ ,  $j_{B,i}^-$ : detachment rate of B from a site type  $i$ . It can be shown that the terms in square brackets get cancelled through the method of substitution. Similarly, master equations are constructed for B kinks,

$$\begin{aligned}
& 2j^+ \frac{\rho_{A0}^2}{Q_1} + 2j_{B,2}^- \frac{\rho_{B0}^2}{Q_2} - 2j^+ \frac{\rho_B^2}{4Q_1} - 2j_{B,0}^- \frac{\rho_B^2}{4Q_2} \\
& + [(j^+ + j_{A,1}^-) \frac{\rho_{AB}\rho_{A0}}{Q_1} - (j^+ + j_{B,1}^-) \frac{\rho_A\rho_B}{2Q_2} \\
& + (j^+ + j_{B,1}^-) \frac{\rho_{BA}\rho_{B0}}{Q_2} - (j^+ + j_{A,1}^-) \frac{\rho_A\rho_B}{2Q_1}] = 0
\end{aligned} \tag{3.17}$$



AB kinks,

$$(j^+ + j_{B,1}^-) \frac{\rho_A \rho_B}{2Q_2} - (j^+ + j_{A,1}^-) \frac{\rho_{AB} \rho_{A0}}{Q_1} = 0 \quad (3.18)$$

BA kinks,

$$(j^+ + j_{A,1}^-) \frac{\rho_A \rho_B}{2Q_1} - (j^+ + j_{B,1}^-) \frac{\rho_{BA} \rho_{B0}}{Q_2} = 0 \quad (3.19)$$

B edge junction,

$$\begin{aligned} & 2j^+ \frac{\rho_B^2}{4Q_1} + 2j_{A,0}^- \frac{\rho_A^2}{4Q_1} + j^+ \frac{\rho_{A0} \rho_B}{Q_1} + j_{A,1}^- \frac{\rho_{A0} \rho_A}{Q_1} - 2(j^+ + j_{B,2}^-) \frac{\rho_{B0}^2}{Q_2} \\ & \quad - j^+ \frac{\rho_A \rho_{B0}}{Q_2} - j_{B,1}^- \frac{\rho_{B0} \rho_B}{Q_2} \\ & \quad + [(j^+ + j_{A,1}^-) \frac{\rho_A \rho_B}{2Q_1} - (j^+ + j_{B,1}^-) \frac{\rho_{BA} \rho_{B0}}{Q_2}] = 0 \end{aligned} \quad (3.20)$$

and A edge junction,

$$\begin{aligned} & 2j^+ \frac{\rho_A^2}{4Q_2} + 2j_{B,0}^- \frac{\rho_B^2}{4Q_2} + j^+ \frac{\rho_A \rho_{B0}}{Q_2} + j_{B,1}^- \frac{\rho_{B0} \rho_B}{Q_2} - 2(j^+ + j_{A,2}^-) \frac{\rho_{A0}^2}{Q_1} \\ & \quad - j^+ \frac{\rho_{A0} \rho_B}{Q_1} - j_{A,1}^- \frac{\rho_{A0} \rho_A}{Q_1} \\ & \quad + [(j^+ + j_{B,1}^-) \frac{\rho_A \rho_B}{2Q_2} - (j^+ + j_{A,1}^-) \frac{\rho_{AB} \rho_{A0}}{Q_1}] = 0 \end{aligned} \quad (3.21)$$

The steady-state analysis provides six master equations with six unknown variables. Each surface event results in formation of a junction in the process of destroying another junction (or regeneration). This results in the set of master equations to be linearly dependent since they are homogeneous and constructed from the same set of most-likely surface events. As a result, the equations must be coupled with the normalization condition. The normalization condition ensures the probability densities sum to unity.

$$\rho_{A0} + \rho_{B0} + \rho_A + \rho_B + \rho_{AB} + \rho_{BA} = 1 \quad (3.22)$$

The set of equations given by Eqs. (3.16-3.20, 3.22) provide six independent equations with six unknown variables ( $\rho$ 's) along with design parameters ( $T$  and  $S$ ) and system parameters ( $\phi$ 's) which can be solved for the nonequilibrium kink densities. An additional equation can be constructed to establish the stoichiometric constraint such that the net attachment rates of the two growth units are equal to enforce the stoichiometry of the unit cell. However, the stoichiometric constraint equation turns out to be linearly dependent on the above set of equations, hence the model equations automatically satisfy the stoichiometric constraint.

6. Solving Master equations: The set of equations generated from the steady-state analysis satisfy surface configurational and stoichiometric constraints. The equations are a function of all the kink densities and elementary rates of attachment/detachment. The rates in turn depend on design parameters such as supersaturation, temperature and system-specific parameters such as solid-state interactions and solvent-modified bond energies. The site-specific works of detachment and solvent-modified bond energies are obtained using an appropriate force field (e.g., GAFF[29], CLP[30], etc.) and solvent model (e.g., COSMO[25]) as detailed in section 1.3. Note that the supersaturation dependence arises from the attachment rate.

Solving the equations simultaneously allows estimation of nonequilibrium (NEQ) kink density as a function of temperature, solid-state energetics and supersaturation. In this work, we solve the equations numerically using a nonlinear root solver in the optimize subpackage in SciPy library of Python. The numerical solutions are compared with kMC simulations for varying levels of anisotropy. Anisotropy is a quantitative measure of nonhomogeneity in the crystalline interaction spheres between the two growth units A and B. Refer to section 3.5 for the results and

detailed analysis.

### 3.3.2 Step Velocity

Above, the most-likely events are identified and used for generation of master equations to determine kink densities. We use the same approach for step velocity modeling, hypothesizing that the same most-likely surface processes encapsulate major contributions to the motion of a step. The net rate of attachment of A growth units  $J_A$  is the summation of all the events resulting in its attachment or detachment from sites.

$$J_A = \sum_i^M \dot{A}_i^+ - \dot{A}_i^- \quad (3.23)$$

$$J_B = \sum_i^M \dot{B}_i^+ - \dot{B}_i^- \quad (3.24)$$

$\dot{A}_i^+$  is the event rate  $i$  associated with attachment of A growth units.  $\dot{A}_i^-$  is the event rate  $i$  associated with detachment of A growth units. Similarly  $\dot{B}_i^+$  and  $\dot{B}_i^-$  are the attachment and detachment rates of B growth units at site  $i$ , respectively. The events in the subset  $M$  (previously used in master equation formulation) are employed for estimation of  $J_A$  and  $J_B$ . The quantities  $\dot{A}_i^\pm$ ,  $\dot{B}_i^\pm$  depend on the NEQ kink densities which couples the previous master equation formulation and the step velocity model. The net attachment rates are,

$$\begin{aligned} J_A = & j^+ \left( \frac{\rho_{B0}^2}{Q_2} + \frac{\rho_A \rho_{B0}}{Q_2} + \frac{\rho_A^2}{4Q_2} + \frac{\rho_A \rho_B}{2Q_2} + \frac{\rho_{BA} \rho_{B0}}{Q_2} \right) \\ & - \left( j_{A,2}^- \frac{\rho_{A0}^2}{Q_1} + j_{A,1}^- \frac{\rho_A \rho_{A0}}{Q_1} + j_{A,0}^- \frac{\rho_A^2}{4Q_1} + j_{A,1}^- \frac{\rho_B \rho_A}{2Q_1} + j_{A,1}^- \frac{\rho_{A0} \rho_{AB}}{Q_1} \right) \end{aligned} \quad (3.25)$$

$$\begin{aligned}
J_B = & j^+ \left( \frac{\rho_{A0}^2}{Q_1} + \frac{\rho_B \rho_{A0}}{Q_1} + \frac{\rho_B^2}{4Q_1} + \frac{\rho_{AB} \rho_{A0}}{Q_1} + \frac{\rho_B \rho_A}{2Q_1} \right) \\
& - \left( j_{B,2}^- \frac{\rho_{B0}^2}{Q_2} + j_{B,1}^- \frac{\rho_B \rho_{B0}}{Q_2} + j_{B,0}^- \frac{\rho_B^2}{4Q_2} + j_{B,1}^- \frac{\rho_A \rho_B}{2Q_2} + j_{B,1}^- \frac{\rho_{BA} \rho_{B0}}{Q_2} \right)
\end{aligned} \tag{3.26}$$

By stoichiometry, the net rates of A and B are equal. Let the equivalent net rate be  $J = J_A = J_B$ . Thus the step velocity  $v$  is proportional to the aggregate of net attachment rates of all the growth units, with propagation length as the proportionality constant. The equality  $J_A = J_B$  also serves as an additional consistency check that the NEQ kink densities must satisfy.

$$v = a_P J_A + a_P J_B = 2a_P J \tag{3.27}$$

where  $a_P$  is the average step propagation length. Such a formulation of step velocity as an aggregate of surface processes is identical to developments in an AFM experiment or a kMC simulation i.e., steps progress owing to the net attachment of all growth units at various sites along a step. [8, 9, 31, 32]

### 3.4 Row Instability

In Fig. 3.1, step configuration 1 has two row types: an A row and a B row. The two rows have different energy attributes and expose different broken-bond interactions to the solution. Such an anisotropy in row structures is captured by the concept of row instability, introduced by Kuvadia and Doherty[17]. Accordingly, a row is defined to be stable if the magnitude of interactions attaching it to the crystal is greater than the broken bond interactions exposed to the solution. Reverse edge and terrace bonds fasten the row to the crystal, and edge and terrace bonds are the broken-bonds at the surface exposed to the solution. If for the row under consideration  $\phi^{RE} + \phi^{RT} > \phi^E + \phi^T$ , it is

stable and if  $\phi^{RE} + \phi^{RT} < \phi^E + \phi^T$ , it is an unstable row. Such a definition of unstable rows assigns a logical value of either stable or unstable to a row without commenting on relative instabilities between different row types.

Tilbury et al.[18] introduced thermodynamic and kinetic row instabilities, allowing for quantitative comparative analyses between different types of rows. Thermodynamic row instability compares the averaged summation of edge and terrace energies across all kinks spanning the row. Different row types  $r$  along an edge (e.g., A and B rows) are characterized by different values of the arithmetic averages,  $\overline{\phi_{k,r}^E + \phi_{k,r}^T}$ . The summation averages out the broken interactions along the exposed surface of a row. The larger the summation, the less stable is the row relative to other rows.

Kuvadia and Doherty[17] derived a net kink rate expression assuming a cyclic progression of kinks along the step. Later Tilbury et al.[18] formally introduced the concept of *kink cycle*, along with *maximal* and *submaximal kink cycles*. A kink cycle is a periodic cycle of incorporation of growth units at various kinks spanning single or multi-height kinks. Maximal kink cycles are the ones which incorporate all the growth units in the unit cell. Kink cycles which incorporate only a fraction of growth units in the unit cell are termed as submaximal kink cycles. Multiple kink cycles can coexist along an edge resulting in a highly interdependent nature of kink kinetics. Kinetic instability compares the averaged work of detachment of kinks in a maximal kink cycle ( $\overline{\Delta W}_{sat}$ ) to that of the averaged work of detachment of kinks in kink cycle along row  $r$  of interest  $\overline{\Delta W}_r$ .

The average work of detachment must be equal for maximal cycles on all edges of all faces and this averaged work defines the saturation mole fraction  $x_{sat} = e^{-\beta \overline{\Delta W}_{sat}}$ . When  $\overline{\Delta W}_r > \overline{\Delta W}_{sat}$ , the row is stable owing to lower detachment rate. When  $\overline{\Delta W}_r < \overline{\Delta W}_{sat}$  the row is unstable owing to higher detachment rates and postulated to demonstrate dissolution-like behavior even under supersaturated conditions. Kinetic stability defined in such a manner provides a comprehensive definition for row stability since it accounts

for the intra-row interactions i.e., kink energy. This is unlike the previous definitions for row stability which only account for the inter-row (edge energy) and inter-face (terrace) interactions.

Kinetic instability is more relevant for a growing crystal under supersaturated conditions and denotes a higher rate of detachment of growth units along the row. Tilbury et al.[18] compared row instability between A and B rows by quantitatively assessing the average work of detachments of A and B kinks along the respective rows. In this work, we compare row stabilities by comparing average works of detachment across all site types for the respective rows  $r$ . The higher the detachment work  $\overline{\Delta W}_r$  along a row, the lower is the rate of detachment and hence higher the net attachment events for the row. Higher values of  $\overline{\Delta W}_r$  correspond to higher kinetic stability. We use the following criteria to determine the stability of rows: an A row is kinetically stable for,

$$\overline{\Delta W}_A > \overline{\Delta W}_B \quad (3.28)$$

and a B row is kinetically stable for

$$\overline{\Delta W}_B > \overline{\Delta W}_A. \quad (3.29)$$

Alternatively, Joswiak et al.[33] account for the supersaturation effects while defining stability for A and B rows by considering the free energy change during attachment at kink sites along the row relative to the other rows. Since kink sites are regenerated during attachment, a net negative free energy change during kink attachment events corresponds to a stable row progression. The anisotropy of interactions between A and B rows can be characterized by deviation of respective works of detachment at kink sites from the

average work of detachment, such that

$$\begin{aligned}\delta_A &= \overline{\Delta W}_{sat} - \Delta W_A \\ \delta_B &= \overline{\Delta W}_{sat} - \Delta W_B\end{aligned}\tag{3.30}$$

From Eq. 3.6,  $\overline{\Delta W}_{sat}$  is the average detachment work from a kink site, which results in  $\delta_A = -\delta_B$ . The change in free energy  $\Delta G$  when a growth unit is attached along an A row is  $-\ln S + \delta_A$ , and along a B row is  $-\ln S + \delta_B$ . The  $-\ln S$  term relates to the free energy reward associated to phase change to a stable phase under supersaturated conditions, while the  $\delta$  term accounts for the surface penalty. The  $\delta$  value determines whether a kink attachment and subsequently growth of a 1-D nucleus along the row, will result in decrease or increase of free energy. According to such a definition for row instability, the growth unit with a negative surface penalty or  $\delta$  value will always be stable owing to a negative value for  $\Delta G$ . However the growth unit with a positive  $\delta$  value, will be stable only at higher supersaturations  $S > e^\delta$ .

It must be noted that such definitions of row stability only refer to step configuration 1 owing to the presence of distinct row types. The concept of row stability does not exist for step configurations 2 and 3, since each comprise of a single row type. The definitions can be extended to multi-growth unit step configurations consisting of multiple types of rows, such as the row configuration of four growth units depicted in Fig. 30 of Kuvadia and Doherty[17].

The kink cycle framework, introduced by Kuvadia and Doherty[17] and formally defined by Tilbury et al.[18], is based on ordering the attachment and detachment surface processes in a sequential progression. The simplified steady-state framework models the attachment and detachment processes as functions of kink densities and rate kinetics. Unlike the kink cycle framework, SSSF does not assign a sequence to the events. Alter-

natively, SSSF discretizes the cyclic kink progression and models individual attachment and detachment events to organize them in the form of steady-state equations. Moreover, the kink cycle framework assumes 1D nucleation to be rapid enough to not play a rate-determining role during step progression. Hence the kink cycle framework attributes step progression entirely to kink attachment events and does not account for 1D nucleation in step velocity modeling. SSSF accounts for the kink formation events in the form of 1D nucleation, kink destructions via collisions, along with attachment at kink sites. Hence, the two frameworks are consistent with each other, but differ in their treatment of sequential vs non-sequential surface events and consideration of 1D nucleation. Refer to Appendix E for a thorough examination of the kink cycle framework, its resemblance to SSSF, and the areas where the two frameworks differ.

### 3.5 Results and Discussion

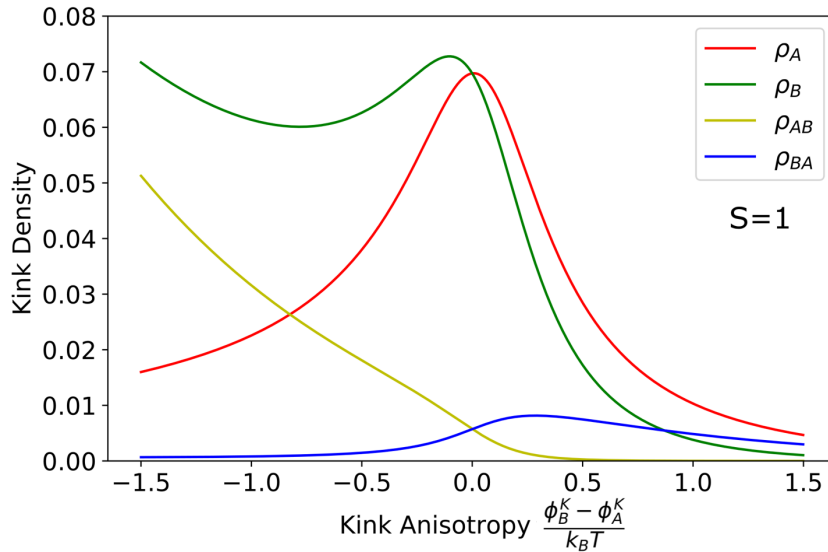


Figure 3.7: NEQ kink density predictions for step configuration 1 vs kink anisotropy  $\Delta_k$  along the kink axis at  $S = 1$ . Here  $\phi_B^K = \phi_A^K + \Delta_k$ ,  $\phi_A^K = 2.5k_B T$ ,  $\phi_A^E = \phi_B^E = \phi_A^T = \phi_B^T = \phi_A^{RT} = \phi_B^{RT} = 2.5k_B T$ . As dictated by step configuration 1,  $\phi_A^K = \phi_A^{RK}$ ,  $\phi_B^K = \phi_B^{RK}$ ,  $\phi_A^E = \phi_B^{RE}$ ,  $\phi_B^E = \phi_A^{RE}$ .



We begin by applying the kink density model to the case of equilibrium conditions ( $S = 1$ ). NEQ kink densities are obtained from numerical solution of equations (Eq. 3.16-3.20, 3.22) for varied levels of anisotropy at  $S = 1$ . The abscissa in Fig. 3.7 represent anisotropy along kink axis  $\Delta_k$ , while keeping the edge and terrace interactions constant and equal to  $2.5k_B T$ . In this figure increasing anisotropy refers to increasing the kink energy of B growth units from  $1k_B T$  to  $4k_B T$  while keeping the A kink energy constant at  $2.5k_B T$ . This allows decoupling the effect of various directional growth unit interactions on kink density. Along the abscissa axis, the zero point is the Kossel crystal where the growth units acquire identical interaction spheres and all  $\phi$ 's are equal. The A and B kink densities intersect to give Kossel single-height kink density, AB and BA curves intersect to give Kossel double-height kink density.

For negative anisotropies,  $\overline{\Delta W}_A > \overline{\Delta W}_B$  which results in a stable A row according to Eq. 3.28. For positive anisotropies,  $\overline{\Delta W}_B > \overline{\Delta W}_A$  which results in a stable B row according to Eq. 3.29. The single kink densities are larger than the double kink densities for most values of abscissa except at high values of anisotropy. This is because increasing anisotropy increases the inter-molecular bond strength between B growth units and hence stabilizes the B row. An AB kink allows exposure of A rows on both sides and hence become favorable for negative anisotropies when A is the more stable row. This also explains why B kinks are densely populated at negative anisotropies and A kinks for positive anisotropy. Further increase in anisotropy increases the energy of creation of kinks and reduces the kink densities. In Chapter 4, Fig. 4.2 superimposes Fig. 3.7 with kMC simulation data points.

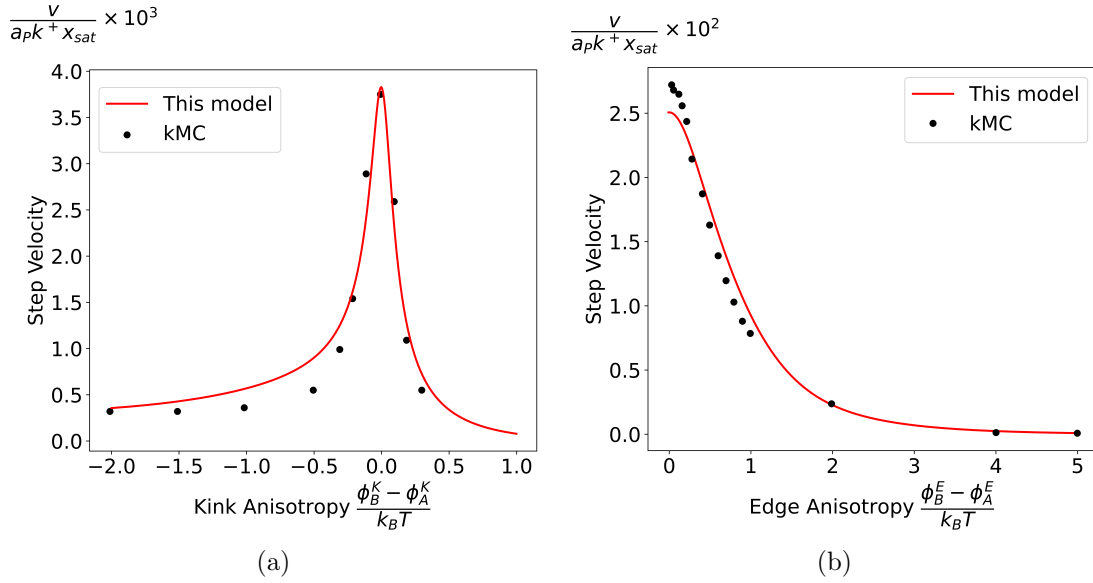


Figure 3.8: (a) Normalized step velocity  $\frac{v}{k^+ a_P x_{sat}}$  vs kink anisotropy  $\Delta_k$  along kink axis at  $S = 1.1$  for this model and kMC simulations from the literature[18] for step configuration 1. ( $\phi_A^K = 4k_B T$ ,  $\phi_B^E = \phi_B^E = 4k_B T$ ,  $\phi_A^T = \phi_B^T = 4k_B T$ ), (b) Normalized step velocity  $\frac{v}{k^+ a_P x_{sat}}$  vs edge anisotropy  $\Delta_e$  along edge axis at  $S = 1.1$  for this model and kMC simulations from the literature[18] for step configuration 1 ( $\phi_A^E = 2k_B T$ ,  $\phi_A^K = \phi_B^K = 2k_B T$ ,  $\phi_A^T = \phi_B^T = 2k_B T$ ). Step velocity is normalized with respect to the propagation length  $a_P$ , attachment rate constant  $k^+$  and solubility  $x_{sat}$  to allow comparison with the kMC data.

In Fig. 3.8a, normalized step velocity is graphed as a function of kink anisotropy, at a constant supersaturation of  $S = 1.1$ . The normalization allows mapping the effect of kink densities on step velocity while eliminating the effect of other system parameters such as rate constant and propagation length. The normalized step velocity has a peak at the Kossel point. This is because the growth units and consequently the A & B rows become identical at the Kossel point, thus the kinks progress independently of each other. As anisotropy is introduced on either side of the Kossel point, one of the rows is stabilized and becomes favorable as the step progresses, which results in kink cycles[17]. Kink cycle formation results in a highly inter-dependent motion of kinks and results in reduced step velocity with increase in the magnitude of anisotropy.

In Fig. 3.8b, normalized step velocity is reported as a function of anisotropy along the edge  $\Delta_e$  at a constant value of  $S = 1.1$ . The two growth units differ in their interactions along edge axes and form equivalent interactions along kink and terrace axes. Hence the zero-point along the abscissa marks the Kossel point where step velocity peaks. Increase in anisotropy favors step A over B and velocity plunges owing to kink cycle formation. As observed from Figs. 3.8a and 3.8b, normalized step velocity demonstrates strong dependence on the solid-state interactions, with an exponential drop with increasing anisotropy along kink, edge or terrace axes.

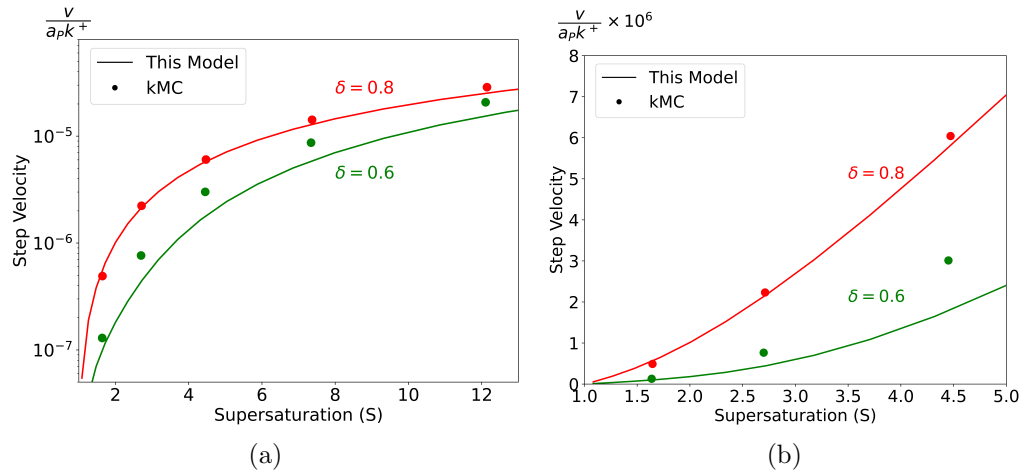


Figure 3.9: Normalized step velocity  $\frac{v}{k+a_P}$  vs supersaturation plots on a) a log scale and b) linear scale, for step  $[01\bar{1}]$  on non-Kossel (011) face of a naphthalene crystal graph following the notation of Cuppen et al.[9]. Such a step corresponds to step configuration 1. The kMC simulations were performed by Cuppen et al.[9] for the same crystal graph with interaction network characterized by  $\phi_a = 2k_B T$ ,  $\delta = \frac{\phi_q}{\phi_p}$ , such that  $2\phi_a = \phi_p + \phi_q$  for different values of  $\delta$ .

In Fig. 3.9, normalized step velocity is plotted as a function of supersaturation for step  $[01\bar{1}]$  on non-Kossel (011) face of a model crystal graph[34, 35] derived from the naphthalene crystal system and compared with kMC simulations from the literature.[9] Such a step corresponds to step configuration 1. Fig. 3.9b provides insights into the nature of dependence of step velocity on the driving force, while Fig. 3.9a presents long

range behaviour of model and simulation predictions. In this crystal system, anisotropy is quantified by the ratio  $\delta$ . Step velocity exhibits a nonlinear monotonic increase with supersaturation. This can be attributed to increase in the number of kinks along the edge, which increases the prevailing sites of attachment along with an increase in the frequency of attachment events. The nonlinear nature of the increase can be attributed to the nonlinear nature of dependence of kink density on supersaturation.[26] The velocity decreases with decrease in  $\delta$  for the same supersaturation. Similar to the previous plots in Fig. 3.8a and Fig. 3.8b, this is an attribute of kink cycle formation that results in interdependence amongst kink progressions.

In the case of crystals with distinct components A and B, the free energy barriers to surface integration of growth units will be different. Hence, the rate constant  $k^+$  in the rate model will be distinct for the two growth units. As a result, the step velocity can no longer be normalized with respect to  $k^+$  as done in Fig. 3.8 and Fig. 3.9. The rate constants for each of the components will then have to be estimated and supplied to the models for step velocity predictions. The models can be re-derived to account for the multiplicity of rate constants and solved numerically in a similar manner as outlined above. Several studies have explored AB systems with distinct components including inorganic crystals[21, 36], ionic crystals[37, 38], semiconductor crystals[39], among others.

## 3.6 Morphology Predictions

We applied the above modeling approach to a real API for which experimental morphology studies have been reported in the literature. We utilized the software ADDICT's framework[19, 40, 41] based on mechanistic models for crystal morphology predictions, solid-state and interfacial and crystallographic calculations. Prerequisites and inputs to ADDICT are system-specific and design parameters such as the crystallographic .cif file,

gaussian[42] and antechamber[43] electron density calculations to determine atomic partial charges (.mol2 files), and growth conditions such as temperature, supersaturation and solvent information as well as selection of an appropriate forcefield and solvent model. In Chapter 1, Section 1.5 elaborates ADDICT’s methodology in detail and explains the role of atomistic models, such as SSSF, within the broader workflow.

Integration of SSSF within ADDICT’s framework, in place of the in-built atomistic model, allowed estimation of kink densities and step velocities for all the steps on different facets of the crystal. The step velocities are then processed by the continuum model within ADDICT by selection of appropriate growth regimes for various facets, to yield relative growth rates and subsequently the morphology and shape prediction. Following such a routine, we applied the steady-state framework to doravirine precursor form I (CSD refcode: OWIVEY) and compared it to experimental shape studies.

### 3.6.1 Case Study: Doravirine precursor

Doravirine is a pharmaceutical organic reverse transcriptase inhibitor launched by Merck and Co., and used for treating HIV/AIDS.[44] A starting material to doravirine is an ethyl ester compound as reported in the literature. [45, 46] The doravirine precursor (CSD refcode: OWIVEY) is recrystallized in an important step during production to purge the impurities out. The experimental shape studies were conducted in an ethanol/water 9:1 solvent mixture and the crystals were aged at around 0°C. OWIVEY form I crystallizes in the spacegroup  $P-1$  and has two growth units in the unit cell with  $Z = 2$  and one asymmetric unit  $Z' = 1$ . The important face families are  $\{0\bar{1}0\}$ ,  $\{0\bar{1}1\}$  and  $\{\bar{1}\bar{1}1\}$  as depicted in the habit predicted by SSSF in Fig. 3.10b. The CLP forcefield[30] was used to calculate solid-state interactions. The van-Oss-Chaudhary-Good solvent model[22, 23] based on estimations of dispersive and acid-base components of the

adhesive energy is employed for obtaining solvent-modified bond energies. Morphology predictions were performed in ethanol to simplify solvent calculations. SSSF-based morphology predictions provide a parallelepiped shape under described growth conditions, which is similar to experimental observations[44] in Fig.3.10a. Refer Appendix B for intermediate calculations and results.

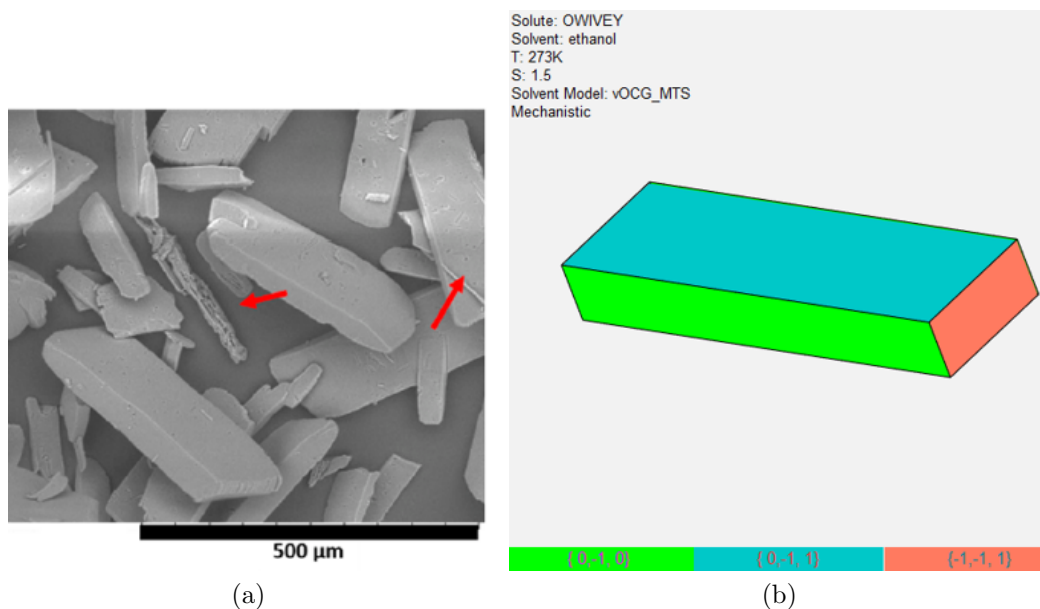


Figure 3.10: (a) Experimental shape observations of OWIVEY form I in ethanol/water 9:1 solution. Figure reproduced with permission from Larpent et al.[44]. Copyright 2021 American Chemical Society. (b) Model-based in-silico morphology predictions.

## 3.7 Conclusions

The SSSF provides an engineering recipe to obtain fundamental quantities of kink density and step velocity within the mechanistic crystal growth models. The framework is based on a steady-state analysis of predominant kinks to balance the rates of formation and destruction. The equations obtained through the analysis are conditioned to satisfy configurational and stoichiometric constraints before numerical solution. This establishes a simplified pathway for obtaining equilibrium kink densities as well as NEQ

kink densities for non-Kossel crystals. This is substantial step towards accurate growth models because the current Boltzmann distribution approaches for equilibrium kink density modeling only provide a rough approximation, owing to lack of surface correlation accountability. Furthermore, the framework provides a step velocity description based on aggregation of all attachment and detachment most-probable surface events. This allows rapid predictions of NEQ kink densities and step velocities as a function of design and system-specific parameters such as supersaturation, temperature and solid-state energetics for organic AB-type crystals of general complexity such as API's, OLED's, etc. The step velocities can then be used for growth rate predictions through the multi-scale mechanistic growth engine[20, 36, 47, 48] as detailed in Section 1.2. Prediction of growth rates allows mapping growth conditions to properties such as morphology, size distribution and polymorph. Chapter 4 further analyses the model predictions for varying conditions of supersaturation, interactions and compares it with corresponding kMC simulations.

The methodology can be extended for organic crystals with  $Z > 2$  in a similar fashion: identification of step configurations, construction of steady-state equations for the predominant kink and edge junctions, followed by numerical solution to obtain NEQ kink densities and subsequently step velocities. However, with increase in the number of growth units, the major sites and most-likely events to monitor will also rise in proportion. This necessitates a strategy to automate the process of model building and model solution. Chapter 5 will introduce a novel symbolic-numeric tool which allows generalization of SSSF approach to variable number of growth units in the unit cell through network theory and allows computation model development and execution. The new model will enable rapid high-fidelity morphology predictions for crystals grown at all supersaturation, including at high supersaturation such as via antisolvent crystallization.

# Bibliography

- (1) Lovette, M. A.; Browning, A. R.; Griffin, D. W.; Sizemore, J. P.; Snyder, R. C.; Doherty, M. F. Crystal Shape Engineering. *Industrial & Engineering Chemistry Research* **2008**, *47*, 9812–9833.
- (2) Kossel, W. Zur theorie des kristallwachstums. *Nachrichten von der Gesellschaft der Wissenschaften zu Göttingen, Mathematisch-Physikalische Klasse* **1927**, *1927*, 135–143.
- (3) Stranski, I. N. Zur theorie des kristallwachstums. *Zeitschrift für physikalische Chemie* **1928**, *136*, 259–278.
- (4) Kim, S. H.; Dandekar, P.; Lovette, M. A.; Doherty, M. F. Kink rate model for the general case of organic molecular crystals. *Crystal Growth & Design* **2014**, *14*, 2460–2467.
- (5) Li, J.; Tilbury, C. J.; Joswiak, M. N.; Peters, B.; Doherty, M. F. Rate Expressions for Kink Attachment and Detachment During Crystal Growth. *Crystal Growth & Design* **2016**, *16*, 3313–3322.
- (6) Chernov, A. A.; Rashkovich, L. N.; DeYoreo, J. J. In *AIP Conference Proceedings*, 2007; Vol. 916, pp 34–47.



## BIBLIOGRAPHY

---

- (7) Zhang, J.; Nancollas, G. H. Kink density and rate of step movement during growth and dissolution of an AB Crystal in a nonstoichiometric solution. *Journal of Colloid and Interface Science* **1998**, *200*, 131–145.
- (8) Cuppen, H. M.; Meekes, H.; van Veenendaal, E.; van Enkevort, W. J. P.; Bennema, P.; Reedijk, M. F.; Arsic, J.; Vlieg, E. Kink density and propagation velocity of the [010] step on the Kossel (100) surface. *Surface Science* **2002**, *506*, 183–195.
- (9) Cuppen, H. M.; Meekes, H.; van Enkevort, W. J. P.; Vlieg, E. Kink incorporation and step propagation in a non-Kossel model. *Surface Science* **2004**, *571*, 41–62.
- (10) Zhang, Y.; Sizemore, J. P.; Doherty, M. F. Shape evolution of 3-dimensional faceted crystals. *AIChE journal* **2006**, *52*, 1906–1915.
- (11) Frank, F. C. Nucleation-controlled growth on a one-dimensional growth of finite length. *Journal of Crystal Growth* **1974**, *22*, 233–236.
- (12) Voronkov, V. V. Movement of an elementary step by means of formation of one-dimensional nuclei. *Soviet Physics Crystallography* **1970**, *15*, 8.
- (13) Zhang, J.; Nancollas, G. H. Kink densities along a crystal surface step at low temperatures and under nonequilibrium conditions. *Journal of Crystal Growth* **1990**, *106*, 181–190.
- (14) Van der Eerden, J. P. In *Handbook of Crystal Growth, Vol. 1*, Hurle, D. T. J., Ed.; Elsevier: Amsterdam, 1993; Chapter 5, p 307.
- (15) Joswiak, M. N.; Peters, B.; Doherty, M. F. Nonequilibrium Kink Density from One-Dimensional Nucleation for Step Velocity Predictions. *Crystal Growth & Design* **2018**, *18*, 723–727.
- (16) Frenkel, J. On the Surface Motion of Particles on Crystals and Natural Roughness of Crystal Faces. *Journal of Physics USSR* **1945**, *9*, 392.

## BIBLIOGRAPHY

---

- (17) Kuvadia, Z. B.; Doherty, M. F. Spiral Growth Model for Faceted Crystals of Non-Centrosymmetric Organic Molecules Grown from Solution. *Crystal Growth & Design* **2011**, *11*, 2780–2802.
- (18) Tilbury, C. J.; Joswiak, M. N.; Peters, B.; Doherty, M. F. Modeling Step Velocities and Edge Surface Structures during Growth of Non-Centrosymmetric Crystals. *Crystal Growth & Design* **2017**, *17*, 2066–2080.
- (19) Li, J.; Tilbury, C. J.; Kim, S. H.; Doherty, M. F. A design aid for crystal growth engineering. *Progress in Materials Science* **2016**, *82*, 1–38.
- (20) Lovette, M. A.; Doherty, M. F. Predictive modeling of supersaturation-dependent crystal shapes. *Crystal Growth & Design* **2012**, *12*, 656–669.
- (21) Dandekar, P.; Doherty, M. F. A mechanistic growth model for inorganic crystals: Solid-state interactions. *AIChE Journal* **2014**, *60*, 3707–3719.
- (22) Van Oss, C. J.; Chaudhury, M.; Good, R. J. Monopolar surfaces. *Advances in Colloid and Interface Science* **1987**, *28*, 35–64.
- (23) Van Oss, C.; Good, R.; Chaudhury, M. Additive and nonadditive surface tension components and the interpretation of contact angles. *Langmuir* **1988**, *4*, 884–891.
- (24) Kaelble, D. H., *Physical chemistry of adhesion*; New Jersey: Wiley-Interscience: 1971.
- (25) Klamt, A.; Schüürmann, G. COSMO: a new approach to dielectric screening in solvents with explicit expressions for the screening energy and its gradient. *Journal of the Chemical Society, Perkin Transactions 2* **1993**, 799–805.
- (26) Padwal, N. A.; Doherty, M. F. Simple Accurate Nonequilibrium Step Velocity Model for Crystal Growth of Symmetric Organic Molecules. *Crystal Growth & Design* **2022**, *22*, 3656–3661.

- (27) Cuppen, H. M.; Meekes, H.; van Enckevort, W. J. P.; Bennema, P.; Vlieg, E. The effects of kink correlation and the Monte Carlo probability scheme on the step structure and velocity. *Surface science* **2003**, *525*, 1–12.
- (28) Dekking, F. M.; Kraaikamp, C.; Lopuhaä, H. P.; Meester, L. E., *A Modern Introduction to Probability and Statistics: Understanding why and how*; Springer: 2005; Vol. 488.
- (29) Wang, J.; Wolf, R. M.; Caldwell, J. W.; Kollman, P. A.; Case, D. A. Development and testing of a general amber force field. *Journal of Computational Chemistry* **2004**, *25*, 1157–1174.
- (30) Gavezzotti, A. Efficient computer modeling of organic materials. The atom–atom, Coulomb–London–Pauli (AA-CLP) model for intermolecular electrostatic-polarization, dispersion and repulsion energies. *New Journal of Chemistry* **2011**, *35*, 1360–1368.
- (31) Sours, R. E.; Zellelow, A. Z.; Swift, J. A. An in situ atomic force microscopy study of uric acid crystal growth. *The Journal of Physical Chemistry B* **2005**, *109*, 9989–9995.
- (32) Rimer, J. D.; An, Z.; Zhu, Z.; Lee, M. H.; Goldfarb, D. S.; Wesson, J. A.; Ward, M. D. Crystal growth inhibitors for the prevention of L-cystine kidney stones through molecular design. *Science* **2010**, *330*, 337–341.
- (33) Joswiak, M. N.; Peters, B.; Doherty, M. F. Crystal step edges with alternating rows of growth units: 1D nucleation and step velocity. *Journal of Crystal Growth* **2023**, *604*, 127042.
- (34) Grimbergen, R.; Meekes, H.; Bennema, P.; Strom, C.; Vogels, L. On the prediction of crystal morphology. I. The Hartman–Perdok theory revisited. *Acta Crystallographica Section A: Foundations of Crystallography* **1998**, *54*, 491–500.

## BIBLIOGRAPHY

---

- (35) Bennema, P. In *Handbook of Crystal Growth, Vol. 1A*, Hurle, D. T. J., Ed.; Elsevier: Amsterdam, 1993; Chapter 7, p 477.
- (36) Dandekar, P.; Kuvadia, Z. B.; Doherty, M. F. Engineering Crystal Morphology. *Annual Review of Materials Research* **2013**, *43*, 359–386.
- (37) Joswiak, M. N.; Doherty, M. F.; Peters, B. Ion dissolution mechanism and kinetics at kink sites on NaCl surfaces. *Proceedings of the National Academy of Sciences* **2018**, *115*, 656–661.
- (38) Joswiak, M. N.; Peters, B.; Doherty, M. F. In Silico Crystal Growth Rate Prediction for NaCl from Aqueous Solution. *Crystal Growth & Design* **2018**, *18*, 6302–6306.
- (39) Akutsu, N.; Sugioka, Y.; Murata, N. Surface roughness changes induced by stoichiometric deviation in ambient phase for two-component semiconductor crystals. *Crystals* **2020**, *10*, 151.
- (40) Landis, S.; Zhao, Y.; Doherty, M. F. Digital design of crystalline solids. *Computers & Chemical Engineering* **2020**, *133*, 106637.
- (41) Zhao, Y.; Tilbury, C. J.; Landis, S.; Sun, Y.; Li, J.; Zhu, P.; Doherty, M. F. A New Software Framework for Implementing Crystal Growth Models to Materials of Any Crystallographic Complexity. *Crystal Growth & Design* **2020**, *20*, 2885–2892.
- (42) Frish, M.; Trucks, G.; Schlegel, H.; Scuseria, G.; Robb, M.; Cheeseman, J.; Scalmani, G.; Barone, V.; Mennucci, B.; Paterson, G. Gaussian 09, revision A. 02. *Gaussian Inc, Wallingford CT* **2009**.
- (43) Wang, J.; Wang, W.; Kollman, P. A.; Case, D. A. Antechamber: an accessory software package for molecular mechanical calculations. *J. Am. Chem. Soc* **2001**, *222*.

- (44) Larpent, P.; Iuzzolino, L.; Schoell, J.; Codan, L.; Tan, M.; Newman, J. A.; Lee, A. Y. Bullet-Proofing Doravirine (MK-1439) Starting Material Supply: Rapid Identification and Response to a New Polymorph of Ethyl Ester. *Crystal Growth & Design* **2021**, *21*, 4207–4219.
- (45) Gauthier Jr, D. R.; Sherry, B. D.; Cao, Y.; Journet, M.; Humphrey, G.; Itoh, T.; Mangion, I.; Tschaen, D. M. Highly efficient synthesis of HIV NNRTI doravirine. *Organic letters* **2015**, *17*, 1353–1356.
- (46) Campeau, L.-C.; Chen, Q.; Gauvreau, D.; Girardin, M.; Belyk, K.; Maligres, P.; Zhou, G.; Gu, C.; Zhang, W.; Tan, L., et al. A robust kilo-scale synthesis of doravirine. *Organic Process Research & Development* **2016**, *20*, 1476–1481.
- (47) Snyder, R. C.; Doherty, M. F. Predicting crystal growth by spiral motion. *Proceedings of the Royal Society A: Mathematical, Physical and Engineering Sciences* **2009**, *465*, 1145–1171.
- (48) Tilbury, C. J.; Green, D. A.; Marshall, W. J.; Doherty, M. F. Predicting the Effect of Solvent on the Crystal Habit of Small Organic Molecules. *Crystal Growth & Design* **2016**, *16*, 2590–2604.

# Chapter 4

## SSSF Model and Simulations: A Comparative Study

Reproduced in part with permission from:

Padwal, N. A.<sup>‡</sup>; Mazal, T.<sup>‡</sup>; Doherty, M. F., Modern Modeling and Simulation Approaches for Morphology Predictions of Molecular Crystals. *Industrial & Engineering Chemistry Research* **2024**. (*Manuscript in press*)

Unpublished work copyright 2024 American Chemical Society.

### 4.1 Introduction

Mechanistic modeling of crystal growth is a specialized class of models which accounts for solid-state physics, interfacial chemistry and continuum mechanics across multiple time and length scales. In case of layered growth mechanisms such as spiral growth and 2D birth & spread, flow of steps across the crystal surface in a layer-by-layer fashion results in normal growth of the facets. Hence, the study of step dynamics is an important element in the development of accurate growth models. The rate of progression of steps

is referred to as the step velocity; which critically depends on the density of sites of attachment along the step and frequency of attachment events by solute molecules at these sites. Prominent sites of attachment are *kinks*, since incorporation at kinks occurs with little surface energy expense and the kinks are regenerated upon incorporation of growth units. This results in the step velocity being a strong function of kink density. Chapter 2 introduced the theoretical basis of Simplified Steady-State Framework, its methodology and proof-of-concept application to crystals of centrosymmetric molecules such as naphthalene and rubrene. Chapter 3 generalizes the theory to AB crystals which comprise of several step configurations with distinct surface correlation conditions. Chapter 3 compares the model-based step velocity predictions with kMC from literature and applies it to API molecular crystals. In this chapter, we will further explore the SSSF-based NEQ kink density and step velocity predictions and perform a comparative study with kMC simulations for varying conditions of supersaturation and directional interaction asymmetry. The NEQ kink densities are also compared with an equilibrium kink density model from literature[1] (at supersaturation of unity) to demonstrate the importance of accounting for spatial correlations in case of noncentrosymmetric molecules.

## 4.2 Background

In noncentrosymmetric molecular crystals, molecule asymmetry translates to anisotropies in the network of bonding interactions around growth units. The number of molecules in the unit cell is characterized by  $Z$ , and the molecules are usually labelled as A, B, C, etc. The molecules are identical in the solution phase, but integrate into crystal in different orientations and are hence characterized as distinct growth units A, B, C, etc. Within the crystal, the different molecules have distinct spheres of interactions connecting them to neighboring molecules. This results in different types of kink sites with unequal rates

of detachment, which subsequently affect the step velocity in a distinct manner. As a result, kink density models must account for the anisotropy of interactions as well as the effect of supersaturation and temperature to provide accurate step velocity predictions.

For bimolecular crystals with growth units A and B, several studies towards modeling and simulation of step velocity have been reported. Chernov and coworkers [2–4] derived kink rate expression for binary and ternary crystal systems of dissociating substrates such as ionic compounds. Zhang and Nancollas[5] derived kink density and step velocity expressions for AB crystal steps growing under nonequilibrium conditions based on the kink Creation–Propagation–Collision (CPC) Model[6]. Cuppen et al.[7] proposed a step velocity model for an AB crystal system based on independent progression of A and B kinks, and compared the model along with other models from the literature[3, 5] and with kMC simulations. Cuppen et al. concluded that no single step velocity expression provided a complete description for all step types; rather, the step velocity expression depends on the local step structure. Kuvadia and Doherty[8] derived an overall kink rate formulation for ABCD crystals and compared model-based morphology predictions with experimental observations. Koo and coworkers compared several crystal growth models based on morphology predictions and studied the impact of local growth unit concentration[9, 10] on crystallization. Tilbury et al.[1] proposed a step velocity model based on relative timescales of reorganisation and kink annihilation and validated it with kMC simulations.

The earlier multi-molecular kink density models are based on the equilibrium Boltzmann distribution, which assumes statistical and spatial independence of surface kink sites. This remains a major limitation of existing kink density models since kink sites along step edges of asymmetric molecules are surface correlated owing to the step topology.[7] This renders the existing kink density models seriously deficient, even under equilibrium conditions. SSSF provides the unique ability to account for the spatial depen-



dence of kink sites through conditional probabilities during construction of steady-state equations to obtain the step velocity model.[11, 12] In subsequent sections, we will further analyse the SSSF model-based predictions with respect to the equilibrium models.

Kinetic Monte Carlo (kMC) simulations allow us to examine the temporal evolution of processes for which we know all possible events and their corresponding rates. Monte Carlo (MC) algorithms are often utilized to investigate physicochemical systems, including but not limited to that of crystal growth kinetics [13]. Other fields of study in which kMC is frequently used include heterogeneous catalysis, mineralogy, and reaction kinetics[14–17]. Such an approach offers a distinct route to calculate relevant crystal growth parameters such as step velocities and face growth rates; kMC simulations of crystal growth may be used to study crystal surface phenomena (i.e., behavior of spiral edges) to determine step velocities.

In this chapter, we apply our comparative analysis of model-based SSSF's and kMC simulations' predictions to step configuration 1 of AB molecular crystals with alternate rows of A and B.

## 4.3 Methods

### 4.3.1 Model Development

The SSSF[11, 12] is based on the hypothesis that step kinetics are predominantly influenced by the most-likely surface processes obtained via tracking densely populated sites along the step. Step dynamics comprise a large number of processes which simultaneously generate and destroy various types of kinks along the surface. Chapter 3 provides elaborate discussion on development of master equations ( Eq. 3.16-3.21) and their numerical solution to obtain NEQ kink densities. The step velocities are then estimated

through expressions of net rates (Eq. 3.25-3.26) from the estimated NEQ kink densities.

Anisotropy  $\Delta$  is the quantitative difference between interaction energies formed by growth units A and B in the unit cell. Anisotropy can be defined as specific to a crystallographic axis. Along kink axis, the kink anisotropy  $\Delta_K$  is the difference between A and B kink energies such that  $\Delta_K = \phi_B^K - \phi_A^K$ . Along edge axis, the edge anisotropy  $\Delta_E$  is the difference between A and B edge energies such that  $\Delta_E = \phi_B^E - \phi_A^E$ . For a Kossel crystal[18] with a single growth unit, all interactions are equal and the anisotropy is zero. In the results and discussion section, the model-based kink density and step velocity predictions are compared with simulations as a function of kink and edge anisotropy.

### 4.3.2 kMC Simulations

kMC simulations are utilized to investigate step behavior for the determination of kink density and step velocities. The solid-on-solid rejection-free lattice kMC simulations are performed. The general simulation workflow is depicted in Fig. 4.1. Steps are initialized as flat structures with a levelled step front. The step evolves in time owing to attachment and detachment of growth units across the step surface. The modified random-rain model given in Eq. 3.1 is utilized for modeling elementary rates of attachment and detachment events. The total rate,  $\Gamma_{tot}$ , is the sum of the rates for all events possible for a given system configuration. At each Monte Carlo move, an event is carried out which influences the step front. Randomly generated numbers determine the type of event as well as the duration between events,  $\Delta t$ . The process is repeated to evaluate the effect of multiple sequential events on the step front. This allows estimation of various step characteristics such as density of kinks along the step surface and the step velocity. Progression and regression of the step front relates to its growth and dissolution, respectively. The inputs to the simulation are growth conditions (i.e., supersaturation and temperature) as well as

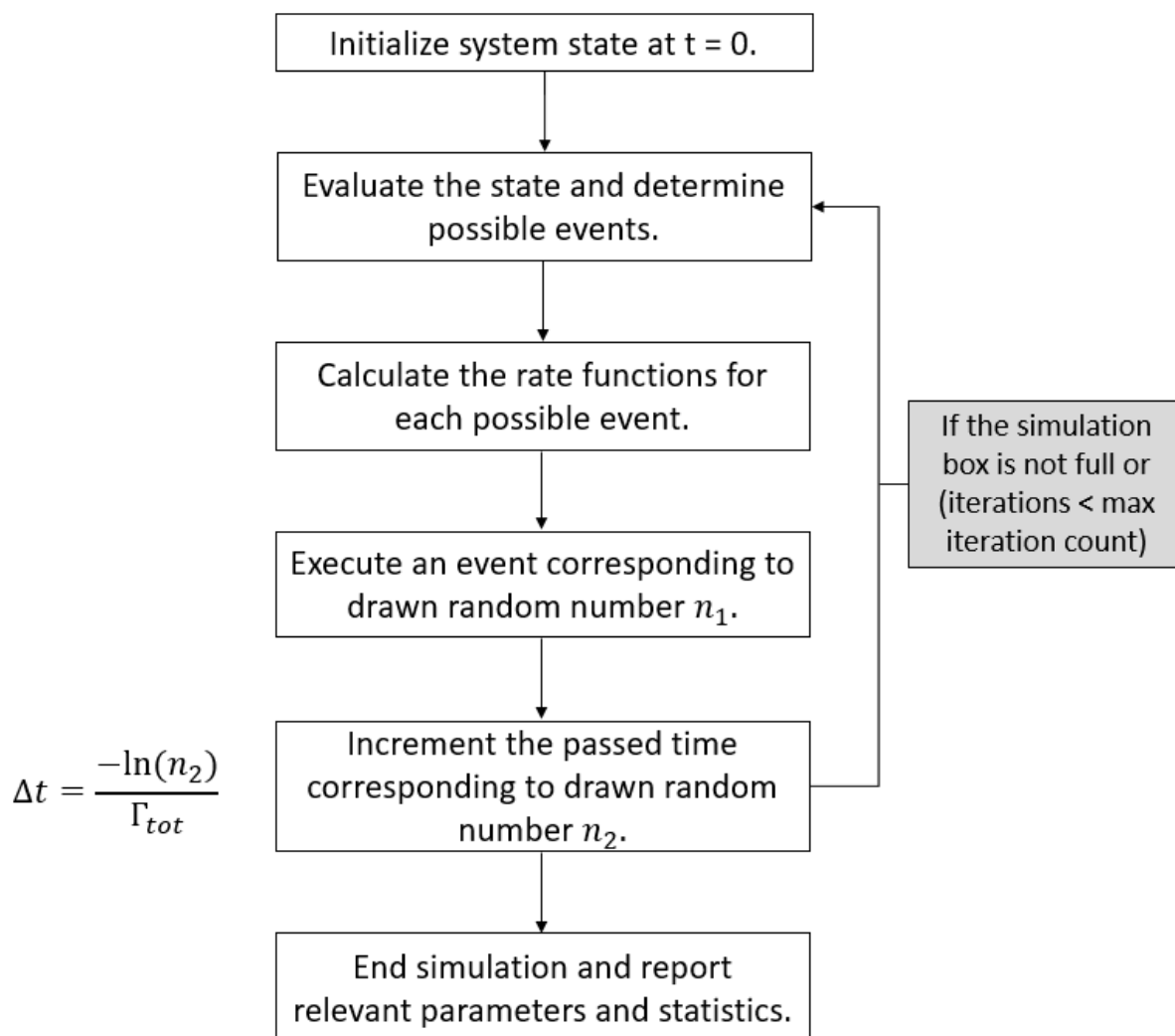


Figure 4.1: Flow diagram outlining the kMC simulation methodology. Figure and caption adapted with permission from Mazal et al.[19] Copyright 2024 American Chemical Society.

simulation parameters (i.e., box size and iteration count). A comprehensive description of the underlying methodology of employing kMC simulations for morphology predictions for a general growth unit as well as impurity-mediated crystal growth is provided by Mazal et al.[19–21]

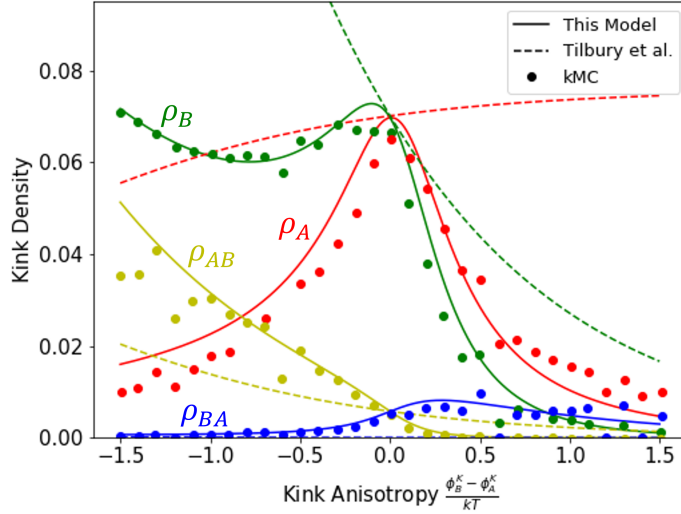


Figure 4.2: SSSF model predictions (lines) for densities of distinct kink types, namely, A kink density (red solid line), B kink density (green solid line), AB kink density (yellow solid line) and BA kink density (blue solid line) on Configuration 1 with kMC simulation results (dots) of respective kink densities at varied dimensionless kink anisotropy,  $\beta\Delta_K$ , at  $S = 1.0$ , where  $\beta = \frac{1}{kT}$ . The dashed lines of corresponding colors, provides the equilibrium model[1] predictions under the same interaction anisotropic conditions. The interaction spheres of A and B growth units are:  $\phi_B^K = \phi_A^K + \Delta_K$ ,  $\phi_A^K = 2.5k_B T$ , and  $\phi_A^E = \phi_B^E = \phi_A^T = \phi_A^{RT} = \phi_B^T = \phi_B^{RT} = 2.5k_B T$ . For Configuration 1,  $\phi_A^{RK} = \phi_A^K$  and  $\phi_B^{RK} = \phi_B^K$ . As we move to the right along the abscissa, we increase the B kink energy, while keeping the A kink energy constant.

## 4.4 Results and Discussion

We deploy SSSF to model molecular systems having two noncentrosymmetric growth units in the unit cell. Model predictions and kMC simulation results are compared below for Step Configuration 1, the case of alternating rows of growth units. Kink density and step velocity are individually examined as predicted by the two approaches as functions of the anisotropy in bond energies between distinct growth units.

### 4.4.1 Kink Density

Figure 4.2 compares kink densities predicted by the SSSF model (Eqns. 3.16-3.22), depicted by solid lines, with kMC simulations, depicted by dots, at equilibrium conditions

( $S = 1$ ), for varying levels of kink anisotropy. Anisotropy quantifies the differences in interaction strengths of the two growth units along kink, edge or terrace axes. Kink anisotropy introduces asymmetry in interactions between the growth units along kink direction. Hence zero kink anisotropy depicts the Kossel point since the two growth units have identical interaction networks around them. Also shown in the figure are equilibrium predictions using the Boltzmann kink density model depicted by dashed lines for corresponding kinks.[1]

The differences between the two mechanistic model predictions (solid lines versus dashed lines) are due to surface correlations. The equilibrium kink density model based on Boltzmann description assumes the various kinks along steps to be statistically independent. The topology of the step imposes constraints on permissible neighboring kinks which translates to spatially correlated kink distribution along the step surface. SSSF accounts for the interaction amongst kinks along the surface and hence the local surface correlation. This explains the ability of the SSSF to provide nonequilibrium kink densities which capture simulation trends away from the Kossel point.

Figure 4.3 compares model-predicted kink densities (SSSF) with kMC simulations for varied levels of edge anisotropy. The kink energies for A and B are the same which explains the equivalent A and B kink densities for varying levels of anisotropy. As anisotropy increases from 0 to 5 along the abscissa, A rows become relatively more stable compared to B rows. The double kink  $\rho_{AB}$  allows exposure of A rows on either sides of the kink, which results in the rise in  $\rho_{AB}$  with increasing stability of A rows. Similarly,  $\rho_{BA}$  exposes B rows on either side and hence its density decreases with anisotropy.

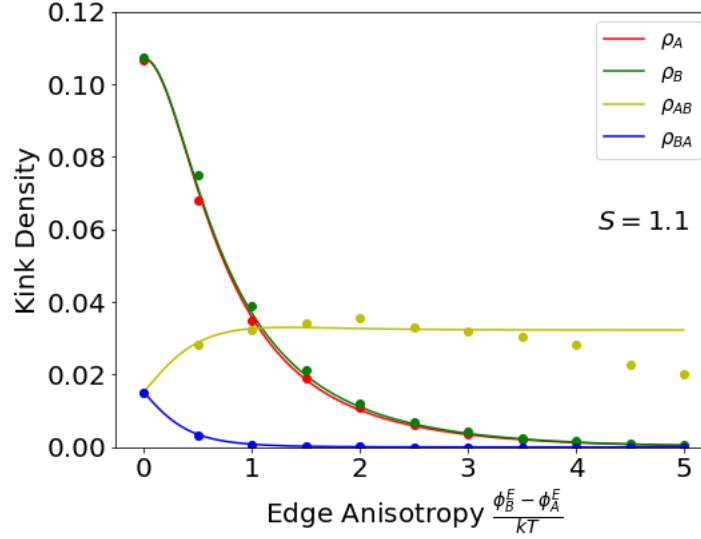


Figure 4.3: SSSF model predictions (lines) for distinct kink types on Configuration 1 with kMC simulation results (dots) at varied dimensionless edge anisotropy,  $\beta\Delta_E$ , at  $S = 1.1$ . Here  $\phi_B^E = \phi_A^E + \Delta_E$ ,  $\phi_A^E = 2k_B T$ , and  $\phi_A^K = \phi_B^K = \phi_A^T = \phi_A^{RT} = \phi_B^T = 2k_B T$ . For the interactions in reverse kink and reverse terrace directions are  $2k_B T$ . For Configuration 1,  $\phi_A^{RE} = \phi_B^E$  and  $\phi_B^{RE} = \phi_A^E$ . kMC simulations were conducted at  $S = 1.1$ ,  $T = 298$  K in a box of size  $2500 \times 240$  growth units for up to 300 million MC steps.

#### 4.4.2 Step Velocity

In Figure 4.4, kink densities and step velocity are plotted as a function of the dimensionless edge anisotropy. We define the edge anisotropy as the difference in edge energies between growth units A and B:  $\Delta_E = \phi_B^E - \phi_A^E$ . Practically, we can interpret edge anisotropy as the energetic difference between the two growth units along the edge axis, where the sign of  $\Delta_E$  describes which growth unit experiences stronger forward edge bonds. Hence, the 0 mark along the abscissa represents the Kossel crystal where the two growth units become identical and the respective plots of A and B kink densities intersect. We see that the SSSF kink density model predictions exhibit good qualitative agreement with the kMC simulation data. Deviations for A and B kink densities can be ascribed to second order supersaturation effects or long range surface correlations. Nevertheless, the model is able to capture average surface kinetics of step progression as

demonstrated by excellent agreement for the normalized step velocity predictions.

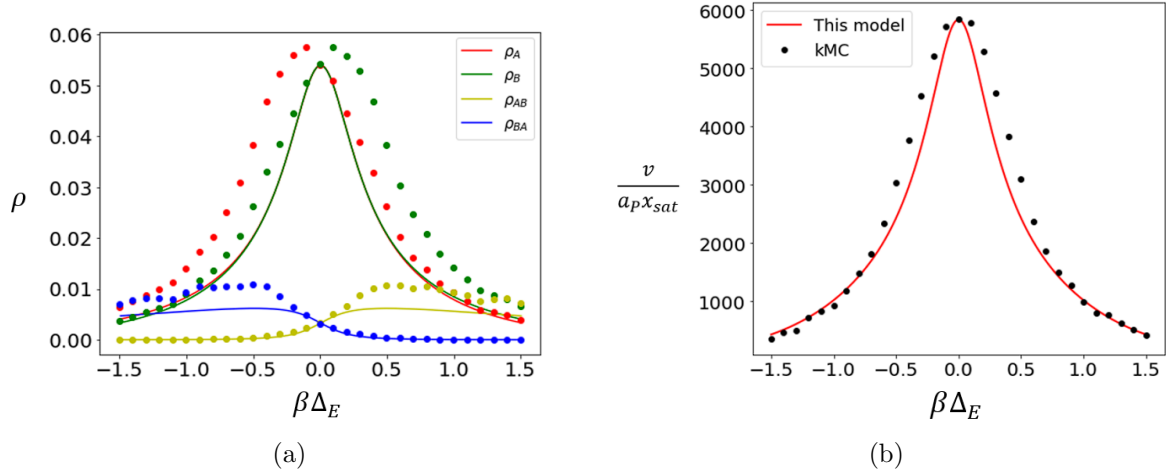


Figure 4.4: (a) Kink density and (b) normalized step velocity  $\frac{v}{a_p x_{sat}}$  model predictions and kMC simulation results for Configuration 1 as a function of dimensionless edge anisotropy,  $\beta\Delta_E$ , at  $S = 1.5$ . The interaction spheres of A and B growth units are:  $\phi_B^E = \phi_A^E + \Delta_E$ ,  $\phi_A^E = 3k_B T$ ,  $\phi_A^K = \phi_B^K = \phi_A^T = \phi_A^{RT} = \phi_B^T = 3k_B T$ . As per step topology,  $\phi_A^{RE} = \phi_B^E$  and  $\phi_B^{RE} = \phi_A^E$ . Simulation data are averaged over 5 simulations conducted at  $S = 1.5$ ,  $T = 298$  K in a box of size  $750 \times 250$  growth units for 5 million MC steps.

Figure 4.5 depicts kink density and step velocity plots as a function of kink anisotropy. We may define the kink anisotropy as the difference in kink energies between growth units A and B:  $\Delta_K = \phi_B^K - \phi_A^K$ . Since the 0 value along abscissa represents the Kossel crystal, A and B kink densities intersect at the point. The step velocity model demonstrates excellent agreement with the kMC notwithstanding deviations in kink density predictions.

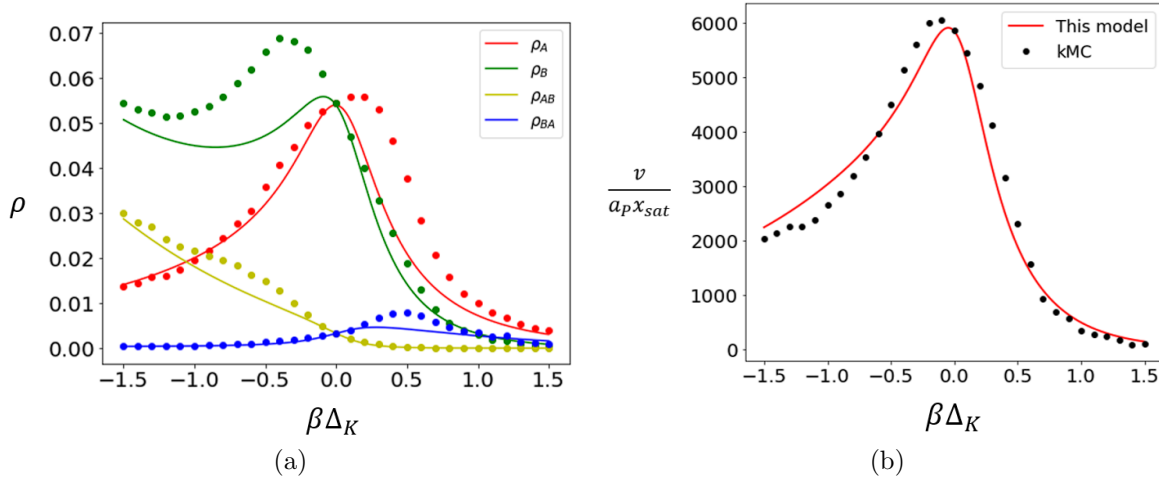


Figure 4.5: (a) Kink density and (b) normalized step velocity  $\frac{v}{a_p x_{sat}}$  model predictions and kMC simulation results for Configuration 1 as a function of dimensionless kink anisotropy,  $\beta\Delta_K$ , at  $S = 1.5$ . The interaction spheres of A and B growth units are:  $\phi_B^K = \phi_A^K + \Delta_K$ ,  $\phi_A^K = 3k_B T$ ,  $\phi_A^E = \phi_B^E = \phi_A^{RE} = \phi_B^{RE} = \phi_A^T = \phi_A^{RT} = \phi_B^T = \phi_B^{RT} = 3k_B T$ . As per step topology  $\phi_A^{RK} = \phi_A^K$  and  $\phi_B^{RK} = \phi_B^K$ . Simulation data are averaged over 5 simulations conducted at  $S = 1.5, T = 298$  K in a box of size  $750 \times 250$  growth units for 5 million MC steps.

## 4.5 Conclusion

We have compared two approaches for determining step velocities and face growth rates of molecular crystals: SSSF model and the kMC simulations. The SSSF model-based approach accounts for only the most-probable surface events to generate master equations followed by numerical solution of the nonlinear set of equations. The resulting NEQ kink density and step velocity predictions are then compared to kMC simulations for varying levels of interaction anisotropy and supersaturation. We see good agreement of SSSF model predictions with kMC simulation results. Each approach correctly accounts for both nonequilibrium effects (i.e.,  $S \geq 1$ ) and for the fact that sites are correlated by the surface configurations introduced by the crystallography of noncentrosymmetric molecules. On the contrary, the equilibrium kink density model deviates from SSSF and



kMC simulation predictions, owing to the lack of accountability of interdependence in surface structures. Overall, exhibition of good convergence between SSSF model and simulations further substantiates reliability of the model in providing rapid crystal property estimations. In Chapter 5, we will deep dive into a new programmatic framework for automation and generalisation of SSSF to crystals with variable number of growth units in the unit cell.

# Bibliography

- (1) Tilbury, C. J.; Joswiak, M. N.; Peters, B.; Doherty, M. F. Modeling Step Velocities and Edge Surface Structures during Growth of Non-Centrosymmetric Crystals. *Crystal Growth & Design* **2017**, *17*, 2066–2080.
- (2) Chernov, A. A.; Rashkovich, L. N.; DeYoreo, J. J. In *AIP Conference Proceedings*, 2007; Vol. 916, pp 34–47.
- (3) Chernov, A. A.; Rashkovich, L. N.; Vekilov, P. G. Steps in solution growth: dynamics of kinks, bunching and turbulence. *Journal of Crystal Growth* **2005**, *275*, 1–18.
- (4) Chernov, A.; Petrova, E.; Rashkovich, L. Dependence of the CaOx and MgOx growth rate on solution stoichiometry. Non-Kossel crystal growth. *Journal of Crystal Growth* **2006**, *289*, 245–254.
- (5) Zhang, J.; Nancollas, G. H. Kink density and rate of step movement during growth and dissolution of an AB Crystal in a nonstoichiometric solution. *Journal of Colloid and Interface Science* **1998**, *200*, 131–145.
- (6) Zhang, J.; Nancollas, G. H. Kink densities along a crystal surface step at low temperatures and under nonequilibrium conditions. *Journal of Crystal Growth* **1990**, *106*, 181–190.

## BIBLIOGRAPHY

---

- (7) Cuppen, H. M.; Meekes, H.; van Enkevort, W. J. P.; Vlieg, E. Kink incorporation and step propagation in a non-Kossel model. *Surface Science* **2004**, *571*, 41–62.
- (8) Kuvadia, Z. B.; Doherty, M. F. Spiral Growth Model for Faceted Crystals of Non-Centrosymmetric Organic Molecules Grown from Solution. *Crystal Growth & Design* **2011**, *11*, 2780–2802.
- (9) Shim, H.-M.; Koo, K.-K. Prediction of growth habit of  $\beta$ -cyclotetramethylene-tetranitramine crystals by the first-principles models. *Crystal Growth & Design* **2015**, *15*, 3983–3991.
- (10) Shim, H.-M.; Kim, J.-W.; Koo, K.-K. Molecular interaction of solvent with crystal surfaces in the crystallization of ammonium sulfate. *Journal of Crystal Growth* **2013**, *373*, 64–68.
- (11) Padwal, N. A.; Doherty, M. F. Simple Accurate Nonequilibrium Step Velocity Model for Crystal Growth of Symmetric Organic Molecules. *Crystal Growth & Design* **2022**, *22*, 3656–3661.
- (12) Padwal, N. A.; Doherty, M. F. Step Velocity Growth Models for Molecular Crystals: Two Molecules in the Unit Cell. *Crystal Growth & Design* **2024**, *24*, 4368–4379.
- (13) Andersen, M.; Panosetti, C.; Reuter, K. A Practical Guide to Surface Kinetic Monte Carlo Simulations. *Front. Chem.* **2019**, *7*, 202.
- (14) Pineda, M.; Stamatakis, M. Kinetic Monte Carlo simulations for heterogeneous catalysis: Fundamentals, current status, and challenges. *The Journal of Chemical Physics* **2022**, *156*, 120902.
- (15) Kurganskaya, I.; Trofimov, N.; Luttge, A. A Kinetic Monte Carlo Approach to Model Barite Dissolution: The Role of Reactive Site Geometry. *Minerals* **2022**, *12*, 639.

## BIBLIOGRAPHY

---

- (16) Katsoulakis, M. A.; Vlachos, D. G. Coarse-grained stochastic processes and kinetic Monte Carlo simulators for the diffusion of interacting particles. *The Journal of Chemical Physics* **2003**, *119*, 9412–9427.
- (17) Stamatakis, M.; Vlachos, D. G. A graph-theoretical kinetic Monte Carlo framework for on-lattice chemical kinetics. *The Journal of Chemical Physics* **2011**, *134*, 214115.
- (18) Kossel, W. Zur theorie des kristallwachstums. *Nachrichten von der Gesellschaft der Wissenschaften zu Göttingen, Mathematisch-Physikalische Klasse* **1927**, *1927*, 135–143.
- (19) Mazal, T.; Doherty, M. F. Modeling Morphologies of Organic Crystals via Kinetic Monte Carlo Simulations: Centrosymmetric Growth Units. *Crystal Growth & Design* **2024**, *24*, 179–192.
- (20) Mazal, T.; Doherty, M. F. Modeling Impurity-Mediated Crystal Growth and Morphologies of Centrosymmetric Molecules. *Crystal Growth & Design* **2022**, *23*, 369–379.
- (21) Mazal, T.; Doherty, M. F. Modeling Morphologies of Organic Crystals via Kinetic Monte Carlo Simulations: Noncentrosymmetric Growth Units. *Crystal Growth & Design* **2024**, *24*, 3756–3770.

# Chapter 5

## Graph Network Theoretic Tool for Model Development

Reproduced in part with permission from:

Padwal, N. A.; Doherty, M. F. Nonequilibrium Crystal Growth Model for Organic Molecules of Real API Complexity. *Crystal Growth & Design*. (Manuscript under review)

### 5.1 Introduction

The mechanistic approach to crystal modeling is based on a multi-scale framework.[1–3] The mechanistic models encapsulate models at various scales, from atomistic to continuum, to capture the effect of molecular events on macroscopic properties, as discussed in Chapter 1. At the mesoscopic scale, propagation of steps across crystal surfaces is crucial for the growth of facets, as depicted in Fig. 5.1. The step velocity, which is the rate of step propagation, is an important parameter required for determination of crystal growth properties.[4–6] Special sites namely *kinks* along the steps are key to providing renewable docking points for attachment of molecules or growth units.[7–10]

Hence, the *step velocity* depends on *kink density*. The majority of kink density models are Boltzmann distribution-based equilibrium models[6, 11, 12] that fail to account for the spatial correlation between surface sites or *kinks*. [6, 13] Chapters 2 and 3 elucidates SSSF, a theoretical modeling approach, for predicting the kink density under nonequilibrium conditions of crystal growth and its influence on step velocity for the simple Kossel step ( $Z' = 0.5$ )[14] and step types for an AB-type crystal ( $Z = 2$ ). [13] In this chapter we

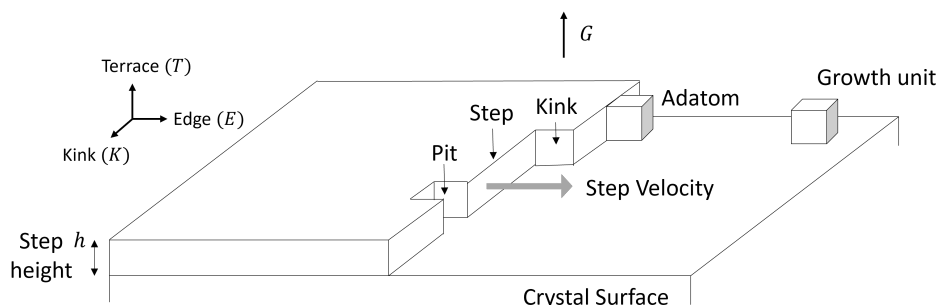


Figure 5.1: Schematic depiction of a crystal surface with a step growing laterally across the face through attachment of growth units at various sites especially *kinks*.

generalize the framework to the general case of  $n$  noncentrosymmetric molecules in the unit cell. The key to unlocking the generalization is the use of graph network theory to develop the steady-state state equations that define the NEQ kink density.

Graphs have been commonly used in modeling a wide range of applications including social network[15], image classification[16], cyber security[17], protein folding and interfaces[18, 19], epidemiology[20], natural language processing[21] owing to their broad expressive capabilities. The last decade has seen a significant effort in graph neural networks (GNN) as well as variation of GNNs such as graph convolution networks, graph attentions networks and graph recurrent networks and their application to a variety of deep learning tasks. On the other hand, graphical interpretation of nonstructured data types such as text and images have accelerated research in graph reasoning models. The application of graph theory extends beyond neural networks into the fields of crystal

engineering and crystal growth.

The concept of networks in crystal growth has long been prevalent for representing the supramolecular crystal interactions in the form of periodic bond chains (PBC), although not articulated as networks.[22–24] A PBC is a 1D chain of strong repeating interactions connecting molecules. Inspired from graph theory, the concept of crystal graph was introduced by treating the molecules as point objects and the strong inter-molecular interactions within the first coordination sphere as bonds connecting the point objects.[25] Such crystal graphs are 3D network representations of crystal structure and are infinite, and need to be truncated to finite sizes through periodicity of crystals. Strom[26, 27] developed a programmable method using graph-theoretic concepts and algorithms for identification of PBCs and their directions. The crystal graph-based systems were then extensively studied and modeled for several types of crystal structures to inform the growth behaviours of crystal faces[28–31]

In this chapter, we demonstrate the application of graph network theory to allow implementation and generalization of SSSF to crystal steps with many growth units in the unit cell (any  $Z$ ). The implementation of SSSF to a crystal entails pertinent sub-problems such as,

1. Identification of Step Configurations: Crystals with  $n$  number of growth units will give rise to steps of several configurations. All the possible configuration types need to be identified and appropriately assigned for real PBC networks and explained in Appendix D.
2. Generation of master equations and configurational constraint equations: Graph theory allows generation of master equations and will be detailed in Section 5.3. The relevant partition functions and configurational constraints (refer Appendix C) are separated generated and appended with the master equations, which provides

the set of model equations.

3. Numerical solution of model equations: The model equations are over-defined with more equations than the number of variables. Matrix operations allow transforming the overdefined set to a well-defined set and removal of the superfluous equations. The well-defined set is then solved numerically to obtain NEQ kink densities as outlined in Section 5.5.
4. Application to real crystals and morphology prediction: Section 5.6 outlines the workflow undertaken for applying graph theoretic implementation of SSSF to crystals of realistic complexity.

Unlike the neural networks, the models developed in this work are not data-driven. Nonetheless, graph network construct provides a suitable layout for streamlining the surface kinetic description of sites and their interactions. We represent components of a crystal surface as a graph of surface sites connected by surface events. Such a representation allows effective information storage and transfer for computational implementation of SSSF model. The computational tool enables crystal type-specific model development and allows the prediction of several graph attributes such as NEQ kink densities and step velocities for any given crystal step configurations.

## 5.2 Graph Network Theory

A graph is a data structure type expressing connections between objects. A general graph network consists of nodes and arcs and global attributes. Nodes are point objects within a network, and arcs demonstrate connections between nodes as depicted in Fig. 5.2. We use the terminology *arc* instead of the more common *edge*, since edge has alternate definition in Fig. 5.1 and also referred in previous chapters. The node and



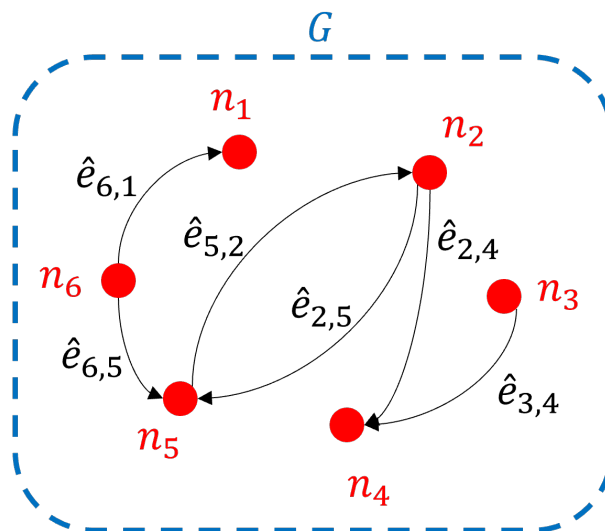


Figure 5.2: A general multi-directed graph network. The nodes are denoted by red dots and characterized by  $n_i$ . The arcs are directional and connect two nodes within the graph, characterized by  $\hat{e}_{i,j}$  where  $i$  and  $j$  are the start node and end node, respectively. The nodes and arc attributes are embedded with customized properties. The global attribute  $G$  characterizes the graph and embedded with graph properties.

arc attributes are embedded with several properties of their own. For instance, a node can be assigned a number identity, degree, number of neighbors, etc. Arcs are lines connecting two nodes in the graph. An arc can be directional or weighted. Hence, an arc is characterized by a number identity, weight and direction or other properties of interest. The global attributes characterize the graph as a whole such as number of nodes, average degree of connectivity, longest path, clustering coefficient, etc.

### 5.3 Surface Kinetics Perspective

The implementation of the Simplified Steady-State Framework is based on identification of the *major sites*, a set of surface sites with the highest probabilities given a step configuration of a crystal structure. From the surface kinetics perspective, *major sites* constitute the graph nodes. The *most-likely events* are the surface events which transform *major sites* into other *major sites*. When projected onto the graph, the most-

likely events become the graph arcs connecting nodes. The nodes are embedded with site attributes such as the kink types which constitute the site. The arcs are embedded with event attributes such as the rate of the event, the type of growth unit displaced by the event, etc. Such an abstraction allows the analysis of how the different kink types are formed or destroyed by parsing through all the most-likely events, thereby streamlining the development of steady-state equation balances based on the rate of formation and destruction of various kink types.

A digital implementation of SSSF allows a flexible scaffold for identification of *major sites* as well as *most-likely events*. The set of major sites can then be expanded to account for more sites or contracted to simplify the equations. If we were to increase the number of major sites within the definition, the model equations will naturally alter. Different metrics can be programmed for identification of the major sites and events. Moreover, the program allows rapid model development for different step configurations with any number of growth units. Such a steady-state analysis is specific to the local step structure and hence the step configuration of the crystal; just as SSSF has been previously implemented for the individual step configurations in silos in Chapter 3. In order to offer such a versatility over model-building and solving, we have developed the computational network-theoretic tool. The tool allows generalization of the framework to crystals with multiple growth units in the unit cell.

The computational tool broadly comprises of two engines, symbolic and numeric, respectively. The symbolic engine develops the model, while the numeric engine solves the model equations to provide the NEQ kink densities. The tool is fully programmed in python and will enable implementation of SSSF for versatile model-building for crystals with various  $Z$  values, i.e., Kossel, AB crystals, but also crystals with four or more growth units in the unit cell. Such a computational encoding of the algorithm offers flexibility within metrics employed for model generation. The symbolic engine is based on modeling

the surface kinetics as a network encapsulating the site interactions. The numeric engine is based on a nonlinear equation solver and parametric continuation which makes solving for highly asymmetric crystal interactions tractable.

In the subsequent section, we elaborate on the tool engine and methodology for a general crystal and later demonstrate its application to specific steps.

## 5.4 Methods

The computational model tool comprises of two separate engines: 1) Symbolic Engine and 2) Numerical Engine. Chapter 2 provided a systematic approach for the execution of the SSSF framework for a Kossel crystal step and Chapter 3 demonstrated its generalization to the three step configurations on a AB-type crystal. Such a systematic stage-by-stage approach is divided across the symbolic and numeric engines of the tool and outlined as follows,

### 5.4.1 Symbolic Engine

The symbolic engine performs the function of developing models in the symbolic space. The sympy and networkx packages are employed for building equations in python. Within the symbolic engine, we visualize surface kinetic transformations in terms of a network such that the surface sites become nodes and the surface events become arcs, which connect multiple surface sites. Surface events are the attachment and detachment processes occurring along steps which transform different surface sites into each other. The networkx package allows modeling the crystal surface kinetic process as a network. Within SSSF, the set of major sites pave the way for identification of most-probably surface events by studying the interplay of how these major sites interact with each other.

1. **Predominant kinks and major sites:** Initial stage is the identification of predominant kinks, i.e., single and double-height kinks along with the edge junctions. Refer Appendix A for detailed discussion on junctions and sites. The predominant kinks are the critical sites of attachment along the step and when placed at adjoining positions give rise to the major sites. Major sites are the high-density structures along steps, which capture the effect of kinks and have an influential impact on the surface kinetics. The major sites for a Kossel step are given in Fig 5.4a.

The major sites become the nodes within the network. (Refer to Fig. 5.4) The nodes are embedded with the site attributes such as the kinks which constitute the site, site density, its structure, and constituting kinks. In case of multiple growth units along the step, surface correlation gives rise to partition functions and configurational constraints, which are utilized in steady-state equations.[13]. Refer to Appendix C for obtaining surface configurational constraints and partition functions for a given step configuration.

2. **Most-likely events:** The next stage is identifying the interactions between the major sites. To that end, the major sites are then subjected to attachment and detachment operations, to output two new sites, respectively. If the newly formed site belongs to the list of major sites, then a connection is identified. Such a connection is a most-likely event, which is an attachment or a detachment event depending on the initial operation. Another possibility is that the newly formed site does not belong to the set of major sites, in which case the event is not a most-probable event and hence not an arc within the network. The process is repeated till all the arcs are identified, which constitute our final set of most-probable events.

The most-likely events depict connections between the sites and become directed arcs within the network (as shown in Fig. 5.4b). The arcs are embedded with event

- attributes such as the event rate, the growth unit mobilized, and a flag indicating whether it is an attachment or a detachment event.
3. Construction of master equations: The steady-state principle states that the net rates of formation and destruction will be equal for each type of kink. The steady-state master equations are constructed to balance event rates which form or destroy the predominant kink types. The most-likely events form the basis of building master equations. We parse through the most-likely events and explore the impact of each event on individual kinks. The rate of the event would contribute positively to the master equation of the kink it forms and negatively to the kink it destroys. Chapter 3 elaborates on modeling event rates, which considers the elementary attachment and detachment rates and the density of kinks which constitute the site. For instance, consider the nucleation event which forms kinks from edges. The rate of a nucleation event  $j^+ \rho_0^2$  contributes to the formation of single-kinks in Eq. 5.2 and contributes to the destruction of edge junctions in Eq. 5.4. The process is repeated for each event and the its rate expression is added to the relevant master equation.
  4. Additional surface constraints: Apart from the master equations, we need additional equations to fully define the system.[13] The normalization condition sums all kink densities to unity. The east-west equivalence states that the net east-kink densities must equal the net west-kink densities. The configurational constraints for multi-growth-unit crystal surfaces capture the spatial correlation between different kinks.
  5. Construction of step velocity model: SSSF states that the the each attachment and detachment event positively and negatively contributes to the step velocity, respectively. The velocity is the sum of the net rates of attachment of each growth

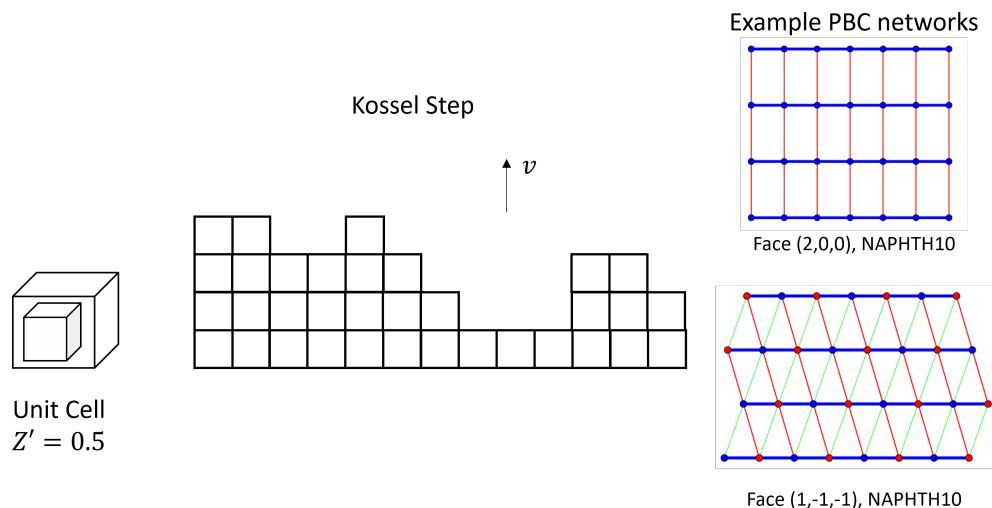


Figure 5.3: A Kossel step comprises of single type of growth unit or multiple growth units which have identical surrounding interaction networks. The PBC network (dots are growth units, lines are interactions) illustrate two examples: single growth unit vs multiple growth units which are energetically equivalent. PBC networks are generated using the software ADDICT.[32]

unit along the step.

The subsequent sections illustrate the networks of crystals and their application towards model building for steps prevalent on a range of crystal types. A Kossel crystal consists of growth units with identical interaction spheres from centrosymmetric molecules, which give rise to a single-type of step configuration depicted in Fig. 5.3.

### Application to Surface Kinetics: Kossel Crystal

In a Kossel crystal, growth units have an inversion center ( $Z' \leq 0.5$ ) which results in identical interaction spheres for all the growth units in the unit cell. Fig. 5.3 illustrates PBC network examples for a Kossel step: 1) A single type of growth unit (blue dot), 2) distinct growth units (blue and red dots) that are energetically equivalent. As a result, a single step configuration is observed on such crystals, which is the Kossel step. For a Kossel step, the predominant junctions are single and double-height kinks along with

the edge junction.[14] The major sites identified for such a step are depicted within the most-likely space (green oval) in Fig. 5.4a. Refer to Appendix A for major site selection from predominant junctions. The interaction between the major sites are then identified, which become the most-likely events and depicted by the directed black arrows. The surface site network in Fig. 5.4a is then converted to the graph network in Fig. 5.4b, by interpreting the sites and events as nodes and arcs, respectively. Parsing through

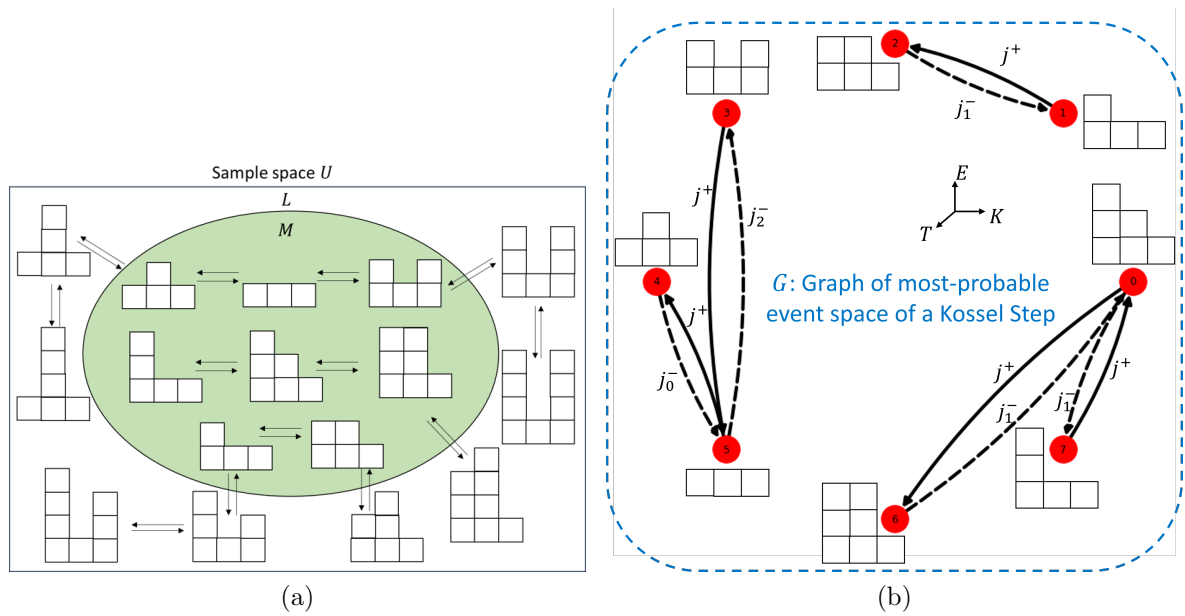


Figure 5.4: a) Surface kinetics diagram of a step along a Kossel crystal, depicting the most-probable event space  $M$  within the sample space of all events  $U$ . b) The corresponding graph network diagram for the most-probable events along the Kossel step. The nodes denote the *major sites* and the arcs denote the most-probable events capturing the interactions between the nodes. The attachment and detachment events are denoted by the solid and dashed lines, respectively.  $j^+$  and  $j_k^-$  are the attachment and detachment elementary rates, respectively, where  $k$  is the number of kink detachment bonds.

the most-likely events, allows us to generate the master equations for the predominant kink densities: edge density  $\rho_0$ , single-height kink density  $\rho_1$  and the double-height kink density  $\rho_2$ . Li et al. proposed a rate model for elementary surface rates, accounting for the thermodynamics and solvent effects of crystal surfaces as put forth in Section 2.3.

Based on the rate model, the attachment rate is isotropic and depends on the solute composition in solution ( $x$ ), while the detachment rate depends on the bonds broken during the process. The elementary attachment and detachment rates are given by,

$$\begin{aligned} j^+ &= k^+ x_{sat} S \\ j_i^- &= k^+ e^{-\beta \Delta W_i} \end{aligned} \quad (5.1)$$

where  $x_{sat}$  is the saturation mole fraction and  $k^+$  is the attachment rate constant,  $S = \frac{x}{x_{sat}}$  is the supersaturation. The attachment rate constant follows an Arrhenius equation, expressed as  $k^+ = \nu_0 \exp(-\beta \Delta G^\ddagger)$ , where  $\nu_0$  represents a frequency factor and  $\Delta G^\ddagger$  denotes the activation free energy barrier. The attachment rate is assumed to be isotropic across the crystal surface. The detachment rate of a growth unit  $j_i^-$  is site-dependent, and characterized by the number of bonds broken,  $i$ , along the kink axis.

The master equation for the single-height kink is,

$$2\rho_0^2(j^+ + j_2^-) + [2\rho_2\rho_0(j^+ + j_1^-)] = 2\frac{\rho_1^2}{4}(j^+ + j_0^-) + [2\frac{\rho_1^2}{2}(j^+ + j_1^-)] \quad (5.2)$$

It can be shown that the terms in square brackets cancel out, through substitution of Eq. 5.3 in Eq. 5.2. The double-height kink steady-state equation is,

$$\frac{\rho_1^2}{2}(j^+ + j_1^-) = \rho_2\rho_0(j^+ + j_1^-) \quad (5.3)$$

In contrast to kinks, the flat portions of a step are characterized by edge junctions with a density of  $\rho_0$ .

$$2\frac{\rho_1^2}{4}(j^+ + j_0^-) = 2\rho_0^2(j^+ + j_2^-) \quad (5.4)$$

The equations are linearly-dependent and combined with the normalization equation to



solve numerically.

$$\rho_0 + \rho_1 + \rho_2 = 1 \quad (5.5)$$

The equation set is then fed to the numerical engine to solve for the kink densities. Within the numerical engine, once the kink densities are solved for, they are then supplied to Eq. 5.6 to obtain the step velocities. The step velocity model is built by summing over all the attachment and detachment rates such that

$$v = a_P \left( \frac{\rho_1^2}{4} j^+ + \rho_0^2 j^+ + \rho_2 \rho_0 j^+ + \frac{\rho_1^2}{2} j^+ \right) - \left( \frac{\rho_1^2}{4} j_0^- + \rho_0^2 j_2^- + \rho_2 \rho_0 j_1^- + \frac{\rho_1^2}{2} j_1^- \right) \quad (5.6)$$

where the first term is the collection of all attachment events and the second term is the collection of all detachment events. The symbolic engine effectively generates Eqs. 5.2-5.6.

### Application to Surface Kinetics: AB Crystal

AB crystals, with two molecules in the unit cell, consist of steps belonging to the three types of configurations depicted in Fig. 5.5. The molecules are identical in solution but differently oriented in the unit cell. ( $Z = 2$ ) The SSSF implementation depends on the local step structure and hence the step configuration. In this section, we illustrate the network theory application to the step configuration with alternate rows of A and B. A general  $Z = 2$  crystal may display steps of all configurations and hence the model equations must be derived for each of the step configurations in silos. Appendix D elaborates on assignment of configuration to steps based on PBC networks.

We start from identification of the predominant kinks: A and B single kinks, AB and BA double kinks and A and B edges. Major sites composed of the predominant kinks are then identified in a manner similar to the Kossel step. The interactions between the major sites become the most-likely events. The surface site network is recast into a

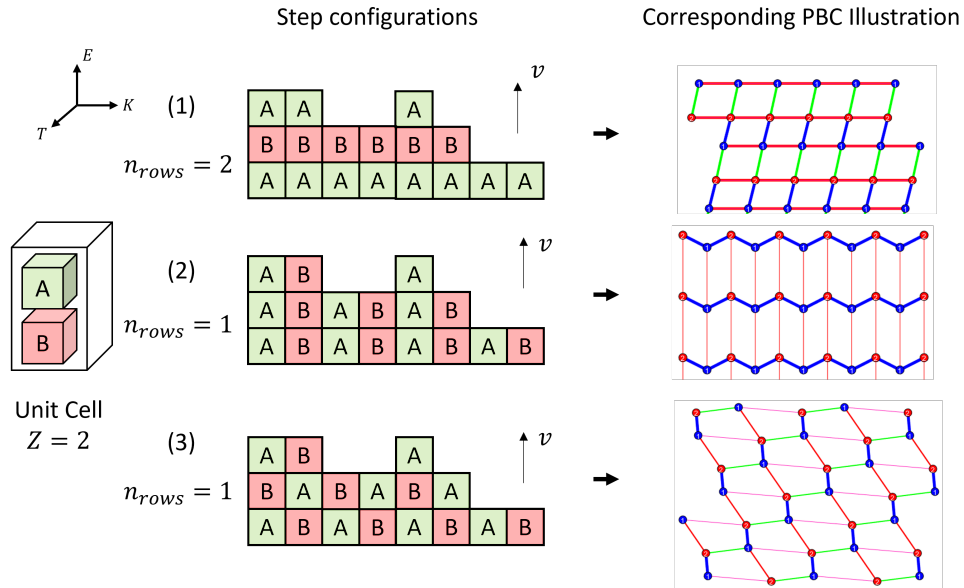


Figure 5.5: Step configurations occurring along an AB crystal ( $Z = 2$ ) and corresponding illustrations of PBC networks. (dots are molecules, lines are interactions) PBC networks are generated using the software ADDICT.[32]

graph network shown in Fig. 5.6 through an interpretation of major sites and most-likely events as nodes and arcs, respectively. The nodes and arcs are also embedded with the necessary attributes to provide the inputs to model development.

Li et al's[33] modified random-rain model is utilized for the elementary attachment rates similar to the previous Kossel crystal. The attachment rate  $j^+$  is isotropic, and the detachment rate  $j_{\{A,B\},i}^-$  characterized by the growth unit detached and  $i$  neighbors along the kink axis. The elementary rates are embedded in arc attributes of pertaining events. The surface partition functions  $Q_1$  and  $Q_2$ , which depend on the surface topology, are obtained via investigating surface correlations. (Refer to Appendix C) The partition functions are utilized for modeling density of major sites and become part of the node attributes. For alternate A and B rows in Configuration 1, the partition functions are

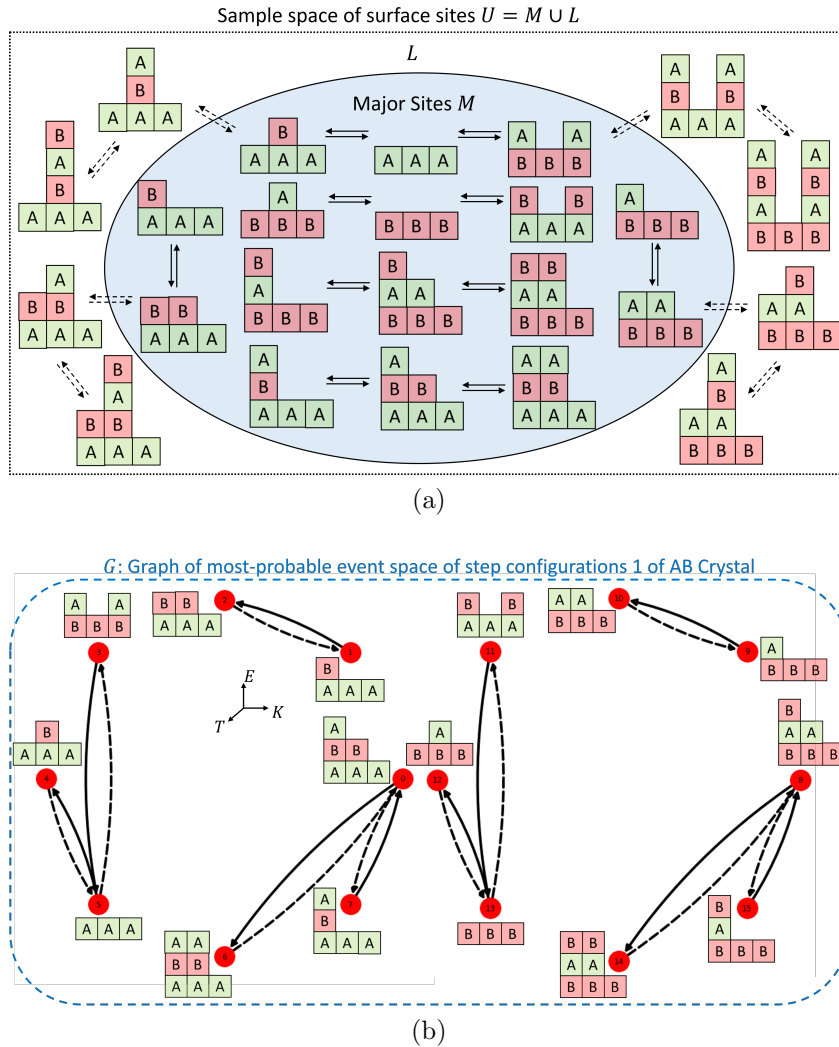


Figure 5.6: Crystal face with two molecules in the unit cell, AB crystals, constitute steps of three configurations depicted in Fig. 3.2, out of which associated diagrams for configuration 1 with alternate A and B rows are illustrated: a) Surface kinetics diagram depicting the most-probable event space  $M$  within the sample space of all events  $U$ . b) The corresponding graph network diagram for the most-probable events along the AB step. The nodes denote the *major sites* and the arcs denote the most-probable events capturing the interactions between the nodes. The attachment and detachment events are denoted by the solid and dashed lines, respectively.

given by

$$Q_1 = \rho_{A0} + \frac{\rho_A}{2} + \frac{\rho_B}{2} + \rho_{AB} \tag{5.7}$$

$$Q_2 = \rho_{B0} + \frac{\rho_A}{2} + \frac{\rho_B}{2} + \rho_{BA} \tag{5.8}$$

where  $\rho_A$ ,  $\rho_B$ ,  $\rho_{AB}$ ,  $\rho_{BA}$ ,  $\rho_{A0}$ ,  $\rho_{B0}$  are the densities of A kink, B kink, AB kink, BA kink, A edge junction and B edge junction, respectively. Parsing through the most-likely events, allows us to generate the master equations for the predominant kink densities as follows: The master equation for A kink is,

$$\begin{aligned}
& j^+ \frac{\rho_{B0}^2}{Q_2} + j_{A,2}^- \frac{\rho_{A0}^2}{Q_1} - j^+ \frac{\rho_A^2}{4Q_2} - j_{A,0}^- \frac{\rho_A^2}{4Q_1} \\
& + [(j^+ + j_{A,1}^-) \frac{\rho_{AB}\rho_{A0}}{Q_1} - (j^+ + j_{B,1}^-) \frac{\rho_A\rho_B}{2Q_2} \\
& + (j^+ + j_{B,1}^-) \frac{\rho_{BA}\rho_{B0}}{Q_2} - (j^+ + j_{A,1}^-) \frac{\rho_A\rho_B}{2Q_1}] = 0
\end{aligned} \tag{5.9}$$

where  $j^+$ : attachment rate,  $j_{A,i}^-$ : detachment rate of A from a site with  $i$  neighbors along kink direction,  $j_{B,i}^-$ : detachment rate of B from a site with  $i$  kink neighbors. Master equations are constructed for B kinks,

$$\begin{aligned}
& j^+ \frac{\rho_{A0}^2}{Q_1} + j_{B,2}^- \frac{\rho_{B0}^2}{Q_2} - j^+ \frac{\rho_B^2}{4Q_1} - j_{B,0}^- \frac{\rho_B^2}{4Q_2} \\
& + [(j^+ + j_{A,1}^-) \frac{\rho_{AB}\rho_{A0}}{Q_1} - (j^+ + j_{B,1}^-) \frac{\rho_A\rho_B}{2Q_2} \\
& + (j^+ + j_{B,1}^-) \frac{\rho_{BA}\rho_{B0}}{Q_2} - (j^+ + j_{A,1}^-) \frac{\rho_A\rho_B}{2Q_1}] = 0
\end{aligned} \tag{5.10}$$

Similarly, the symbolic engine correctly generates master equations for other types of kinks and the complete set is provided in Chapter 3. It can be shown that the terms in square brackets cancel out.

The master equations are then supplied to the Numerical engine for solution. The step velocity model is the aggregate of the net attachment rates of each of the growth units.

$$v = \overline{a_P}(J_A + J_B) \tag{5.11}$$

where  $\overline{a_P}$  is the average step propagation length.  $J_A$ , the net attachment rate of A is the

sum of all the attachment event rates (first bracket) and deducting all the detachment event rates (second bracket) which displace A growth units.

$$\begin{aligned}
 J_A = & j^+ \left( \frac{\rho_{B0}}{Q_2} + \frac{\rho_{A\rho_{B0}}}{Q_2} + \frac{\rho_A^2}{4Q_2} + \frac{\rho_{A\rho_B}}{2Q_2} + \frac{\rho_{BA\rho_{B0}}}{Q_2} \right) \\
 & - \left( j_{A,2}^- \frac{\rho_{A0}^2}{Q_1} + j_{A,1}^- \frac{\rho_{A\rho_{A0}}}{Q_2} + j_{A,0}^- \frac{\rho_A^2}{4Q_1} + j_{A,1}^- \frac{\rho_B\rho_A}{2Q_1} + j_{A,1}^- \frac{\rho_{A0}\rho_{AB}}{Q_1} \right)
 \end{aligned} \tag{5.12}$$

Similarly, the net attachment rate of B is the sum of all the attachment event rates (first bracket) and deducting all the detachment event rates (second bracket) which displace B growth units.

$$\begin{aligned}
 J_B = & j^+ \left( \frac{\rho_{A0}^2}{Q_1} + \frac{\rho_B\rho_{A0}}{Q_1} + \frac{\rho_B^2}{4Q_1} + \frac{\rho_{AB}\rho_{A0}}{Q_1} + \frac{\rho_B\rho_A}{2Q_1} \right) \\
 & - \left( j_{B,2}^- \frac{\rho_{B0}}{Q_2} + j_{B,1}^- \frac{\rho_B\rho_{B0}}{Q_1} + j_{B,0}^- \frac{\rho_B^2}{4Q_2} + j_{B,1}^- \frac{\rho_{A\rho_B}}{2Q_2} + j_{B,1}^- \frac{\rho_{BA\rho_{B0}}}{Q_2} \right)
 \end{aligned} \tag{5.13}$$

Since the net attachment rates are equal, to maintain the stoichiometry of the unit cell,  $J_A = J_B = J$ . The step velocity becomes  $v = 2\bar{a}_P J$ . The step velocity models in Eq. 5.12-5.13 and the master equations are effectively generated by the symbolic engine and supplied to the numerical engine for estimating NEQ kink densities and subsequently the step velocity.

### Application to Surface Kinetics: ABCD Crystal

Crystals with four molecules in the unit cell grow via lateral growth of various types of steps. Depending on the crystal topology, steps present themselves as belonging to one of the several plausible configurations, some of which are depicted in Fig. 5.7. Appendix D elaborates on assignment of configuration to steps based on the underlying PBC networks. Each of the step configurations has a unique set of *major sites* and surface events. Each of the step configurations can be depicted by distinct graph networks. Fig.

5.8 depicts the graph network for step configuration 1 with serial rows of growth units. In this section, we briefly discuss and illustrate the graph network for configuration 1. Similar to the previous steps, we start from identification of the predominant kinks and

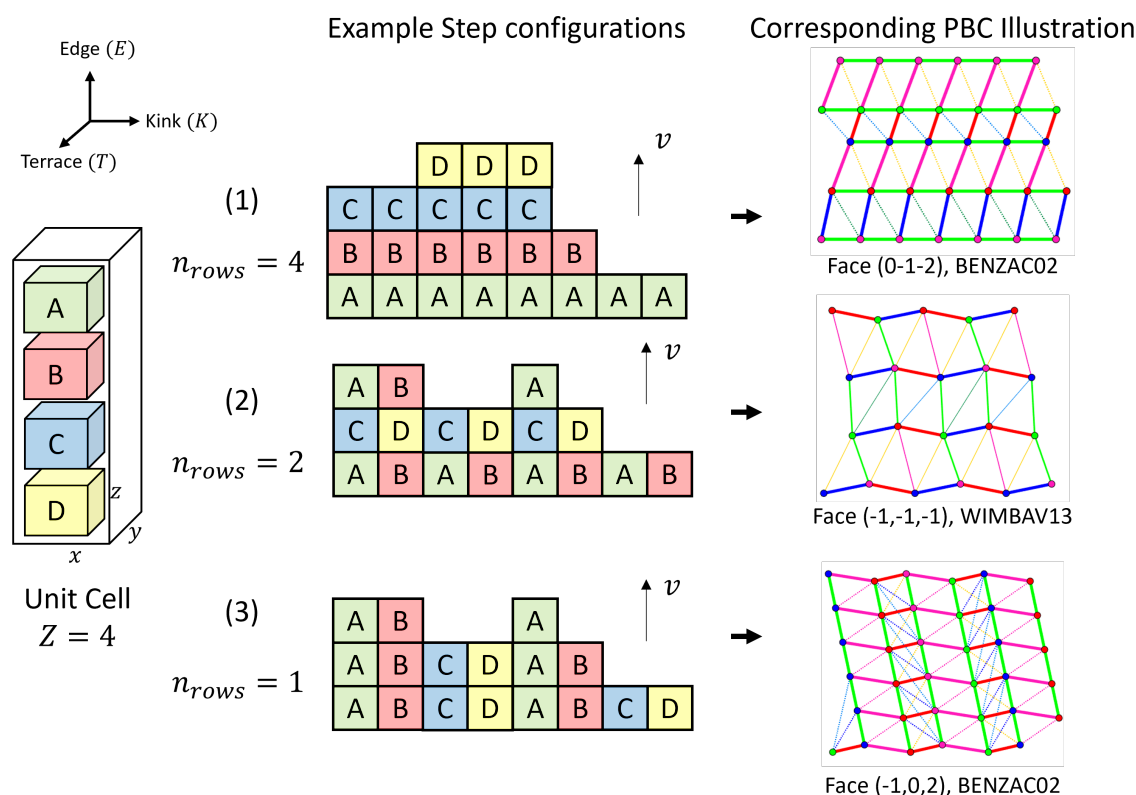


Figure 5.7: Example step configurations for crystals with 4 molecules in the unit cell: 1) rows of single growth units, 2) rows comprising of a subset of all growth units, 3) a single row-type consisting of all growth units. Illustrations of periodic bond chains for corresponding step configurations in crystal networks. PBC networks are generated using the software ADDICT.[32]

subsequently the major sites, which form the nodes within the graph network of Fig. 5.8. The most-likely events are then identified based on the interactions of major sites. The graph network representation of the surface kinetics facilitates development of steady-state equations of the predominant kinks. For instance, consider the nucleation event of A molecule atop a B edge, such an event forms A kinks and hence the rate of the event will contribute to the A kink steady-state equation. Similarly, the contributions of all

the events to the various types of kinks are collated in the form of a master equation set. For a step with four growth units and configuration type 1 with cyclic rows of A, B, C and D, the partition functions are given by,

$$Q_1 = \rho_{A0} + \rho_A/2 + \rho_B/2 + \rho_{AD}/2 + \rho_{CB}/2$$

$$Q_2 = \rho_{B0} + \rho_B/2 + \rho_C/2 + \rho_{BA}/2 + \rho_{DC}/2$$

$$Q_3 = \rho_{C0} + \rho_C/2 + \rho_D/2 + \rho_{CB}/2 + \rho_{AD}/2$$

$$Q_4 = \rho_{D0} + \rho_D/2 + \rho_A/2 + \rho_{DC}/2 + \rho_{BA}/2$$

where  $\rho_A, \rho_B, \rho_C, \rho_D$ , are the A, B, C and D single-height kinks, respectively.  $\rho_{AD}, \rho_{DC}, \rho_{CB}, \rho_{BA}$  are the double-height kinks and  $\rho_{A0}, \rho_{B0}, \rho_{C0}, \rho_{D0}$  are the respective flat edge A, B, C and D edge junctions, respectively. Parsing through the most-likely events for the ones forming or destroying specific kink types generates the master equations. The A kink master equation becomes,

$$\begin{aligned} & j^+ \frac{\rho_{D0}^2}{Q_4} + j_{A,2}^- \frac{\rho_{A0}^2}{Q_1} - j^+ \frac{\rho_A^2}{4Q_4} - j_{A,0}^- \frac{\rho_A^2}{4Q_1} \\ & + [j^+ \frac{\rho_{AD}\rho_{C0}}{Q_3} + j_{A,1}^- \frac{\rho_{AD}\rho_{A0}}{Q_1} - j^+ \frac{\rho_{APD}}{2Q_4} - j_{D,1}^- \frac{\rho_{APD}}{2Q_4}] \\ & + [j^+ \frac{\rho_{BA}\rho_{D0}}{Q_4} + j_{B,1}^- \frac{\rho_{BA}\rho_{B0}}{Q_4} - j^+ \frac{\rho_B\rho_A}{2Q_1} - j_{A,1}^- \frac{\rho_B\rho_A}{2Q_1}] = 0 \end{aligned} \quad (5.14)$$

where  $j^+$  is the attachment rate and the detachment rate  $j_{\{A,B,C,D\},i}^-$  is characterized by the growth unit detached and  $i$  neighbors along the kink axis ( $i$  broken interactions). It can be shown that the terms in square brackets cancel out. The B kink master equation

is,

$$\begin{aligned}
& j^+ \frac{\rho_{A0}^2}{Q_1} + j_{B,2}^- \frac{\rho_{B0}^2}{Q_2} - j^+ \frac{\rho_B^2}{4Q_1} - j_{B,0}^- \frac{\rho_B^2}{4Q_2} \\
& + [j^+ \frac{\rho_{BA}\rho_{D0}}{Q_4} + j_{B,1}^- \frac{\rho_{BA}\rho_{B0}}{Q_4} - j^+ \frac{\rho_B\rho_A}{2Q_1} - j_{A,1}^- \frac{\rho_B\rho_A}{2Q_1}] \\
& + [j^+ \frac{\rho_{CB}\rho_{A0}}{Q_1} + j_{C,1}^- \frac{\rho_{CB}\rho_{C0}}{Q_1} - j^+ \frac{\rho_C\rho_B}{2Q_2} - j_{B,1}^- \frac{\rho_C\rho_B}{2Q_2}] = 0
\end{aligned} \tag{5.15}$$

It can be shown that the terms in square brackets cancel out. Similarly, the rest of the master equations are effectively generated by the tool within the symbolic engine, which are then sent to the numerical engine for their solution.

## 5.5 Numeric Engine

The model equations generated by the symbolic engine are interpreted and solved within the numeric engine. The symbolic engine utilizes the SymPy library within python. The numerical engine utilizes the SciPy and NumPy libraries within python. The symbolic engine provides a nonsquare overdetermined system of equations. This is because for  $m$  predominant kink types, we have  $m$  master equations, which forms a linearly-dependent set of equations. The set is then combined with a normalization condition, east-west equivalence condition, and  $n$  configurational constraints for  $n$  growth units in the unit cell. Hence we have a total of  $n + m + 2$  algebraic equations for  $m$  kink densities to solve for. The nonlinear system solvers require a well-defined square set of equations.

Within the Numeric engine, the algebraic system of equations (in variable  $\underline{x}$ ) are cast in a matrix form  $M$  of coefficients, wherein number of rows is equal to the number of equations and number of columns is equal to the number of terms within the equation set. An additional column matrix  $\underline{y}$  consisting of the terms within the equation set is also generated, such that matrix multiplication will give the original set of algebraic equations



$\underline{x} = M\underline{y}$ . The function `rref` within SymPy library performs matrix operations on the rectangular coefficient matrix to convert it to a reduced row-echelon form  $M'$ . This allows weeding out linearly-dependent equations and transform the system of equations into a well-defined square system  $\underline{x}' = M'\underline{y}$ . The square system  $\underline{x}'$  is then fed as input to a nonlinear system solver `fsolve` in python, which uses a modified Powell method based on trust region.[34, 35]

Owing to the elementary rates  $j^+$  and  $j^-$  in Eq. 5.1, the equations have several exponential terms built into them, with widely varying exponent values depending on the magnitude of interactions along all directions which are the kink, edge and terrace axes as depicted in Fig. 5.1. With divergent parameter values, the kink densities to be solved for, are also orders of magnitude apart from each other. This results in a hyper-sensitivity to initial guess caused by the *curse of the exponential* for crystals with pronounced interaction asymmetry. The higher the interaction anisotropy, the greater is the order of magnitude difference of kink densities. Pronounced numerical instabilities are observed as follows:

1. Multiple solutions: The nonlinear set of equations may have multiple feasible solutions. Hence, proper selection of initial guess is vital.
2. Poor Convergence: For certain extreme anisotropies, the solver may fail to converge or converge slowly owing to the requirement of fine discretization and increase the computational expense.

To tackle the above challenges, we perform parametric continuation. This is where the parameters are varied incrementally and systematically from a known fixed point to the parametric values of the crystal system of interest. This is possible because we know the solution at the Kossel point. Since the kink densities for Kossel crystals (crystals with centrosymmetric molecules) can be analytically estimated.[14] We simplify

the interactions along the crystal step of interest into a reduced Kossel form such that the growth units within the steps have identical energetic environments. This can be done via averaging the interaction networks of the multiple growth units along the step. The interaction spheres can then be incrementally varied by introducing anisotropy and methodically approaching the desired fully asymmetric values from the known solution at the Kossel point. In Fig. 5.9, the final crystal step interactions are reduced to a corresponding Kossel step by dissolving asymmetries such that the growth units become identical. Anisotropy is then gradually and systematically introduced along various axes by navigating through several intermediate crystal steps. In each stage, the equation set with parameters from the intermediate crystal step are solved for kink densities which are supplied as guess values for the next stage. The process continues in an incremental manner until full anisotropy is accounted for and the parameters of the final crystal are reached.

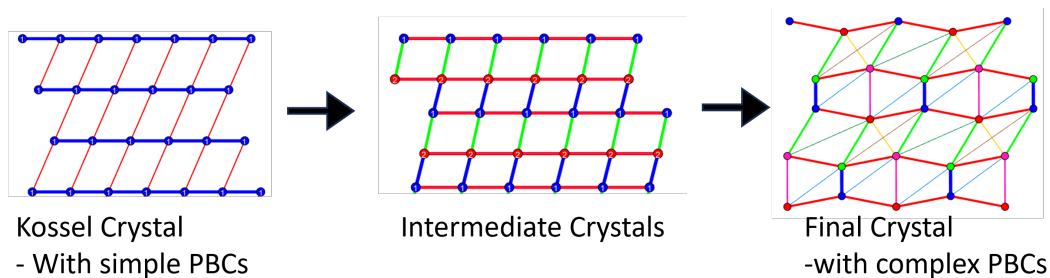


Figure 5.9: Illustration of parametric continuation performed to arrive at the solution to the final crystal step with anisotropic bonds. The solid dots are the growth units and solid lines are the interactions. Different colored lines and dots, depict distinct interactions and growth units, respectively. The interaction networks are generated using ADDICT.[32]

Subsequent calculation is the estimation of step velocity based on the model received from the symbolic engine. The estimated kink densities from the numerical system solvers are then utilized for step velocity predictions.

## 5.6 Morphology Predictions and ADDICT

The software ADDICT[32, 36, 37] is a crystal morphology prediction tool which allows calculation, visualization, and analysis of the crystal habit formed as a function of the growth environment such as temperature, supersaturation and solvent. ADDICT is a culmination of distinct calculations which constitute the multi-scale mechanistic modeling framework, solid-state periodic bond chains algorithm, solvent effects and crystallographic faces type calculations. Section 1.5 provides a comprehensive stage-wise discussion of ADDICT’s methodology to calculate morphology predictions through inputs of crystallographic cif file, Gaussian electron density calculations (partial charges on atoms), growth environment (design variables).

Such a methodology allows fast mechanistic model-based calculations for crystal morphology predictions, since it does not require some of the expensive simulation techniques. The enumerated calculations are performed in silos, which allows us to integrate the graph theoretic tool at stage 3) to provide the NEQ kink densities and step velocities, retaining the rest of ADDICT’s framework to predict morphology based on SSSF. This serves as a validation for growth models by comparing how the crystal habit fares against experimental observations for the given conditions of growth. We followed this methodology and applied it to morphology prediction of real drug molecules using CLP forcefield and vOCG solvent model.

### 5.6.1 Tazofelone

Tazofelone form III is a 5-lipoxygenase inhibitor and a potent antioxidant.[38] The crystal structure of Tazofelone with CSD ref code WIMBAV13 is used for the calculations. Tazofelone form III crystallizes in the space group  $P\bar{1}$ . The unit cell has 4 molecules in the unit cell and two asymmetric units, hence  $Z = 4$  and  $Z' = 2$ . The unit cell

parameters are  $a = 11.2917 \text{ \AA}$ ,  $b = 11.9167 \text{ \AA}$ ,  $c = 14.9597 \text{ \AA}$ ,  $\alpha = 77.827^\circ$ ,  $\beta = 75.208^\circ$ ,  $\gamma = 71.585^\circ$ . The experimental observation is taken from the literature[38], shown in Fig. 5.10a. Tazofelone crystals are grown from water under slow evaporation at room temperature. Fig. 5.10b depicts the SSSF-based morphology prediction of Tazofelone grown from water at  $T = 298K$  and  $S = 1.04$ . The Tazofelone morphology predicted by the tool is characterized by a rhomboidal plate-like shape, demonstrating good agreement with the experimental observations.

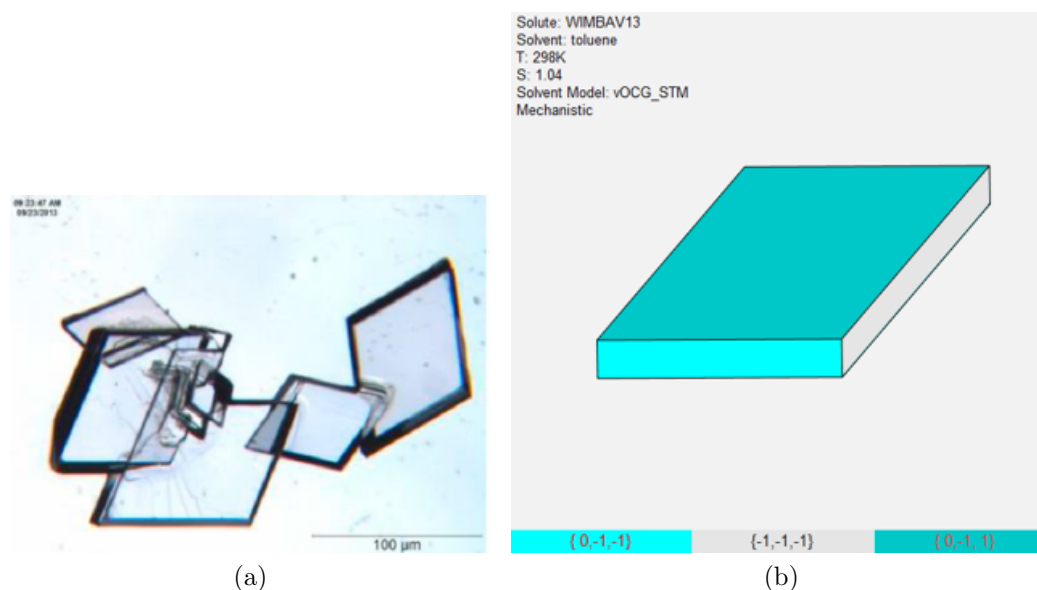


Figure 5.10: (a) Experimental shape observations of Tazofelone (CSD ref code:WIMBAV13) in toluene. Figure reproduced with permission from Price et al.[38]. Copyright 2014 Elsevier B.V. (b) Model-based in-silico morphology prediction of Tazofelone in toluene.

## 5.6.2 Benzoic Acid

Benzoic acid is a carboxylic acid, commonly used as a drug or preservative. The crystal structure of benzoic acid with CSD ref code BENZAC02 is used for the calculations. Benzoic acid molecules crystallize in the space group  $P2_1/c$ . The unit cell has 4 molecules in the unit cell and one asymmetric unit, hence  $Z = 4$  and  $Z' = 1$ . The unit cell

parameters are  $a = 5.4996\text{\AA}$ ,  $b = 5.1283\text{\AA}$ ,  $c = 21.950\text{\AA}$ ,  $\alpha = 90^\circ$ ,  $\beta = 97.37^\circ$ ,  $\gamma = 90^\circ$ . The experimental observation is taken from the literature and shown in Fig. 5.11a. Benzoic acid crystals were grown in water from cooling crystallization and allowed to cool naturally.[39] Fig. 5.11b depicts the SSSF-based morphology prediction of benzoic acid monomer grown from water at  $T = 298K$  and  $S = 1.1$ . Benzoic acid molecules often form dimers in various solvents.[40] Hence, calculations are also performed using the benzoic acid dimer as the choice of growth unit. Fig. 5.11c depicts the SSSF-based morphology prediction of benzoic acid dimer grown from water at  $T = 298K$  and  $S = 1.1$ . The in-silico prediction for the dimer is more rod-like, while the morphology predicted for the monomer is more needle-like. Both predictions demonstrate good qualitative agreement with the experimental observations.

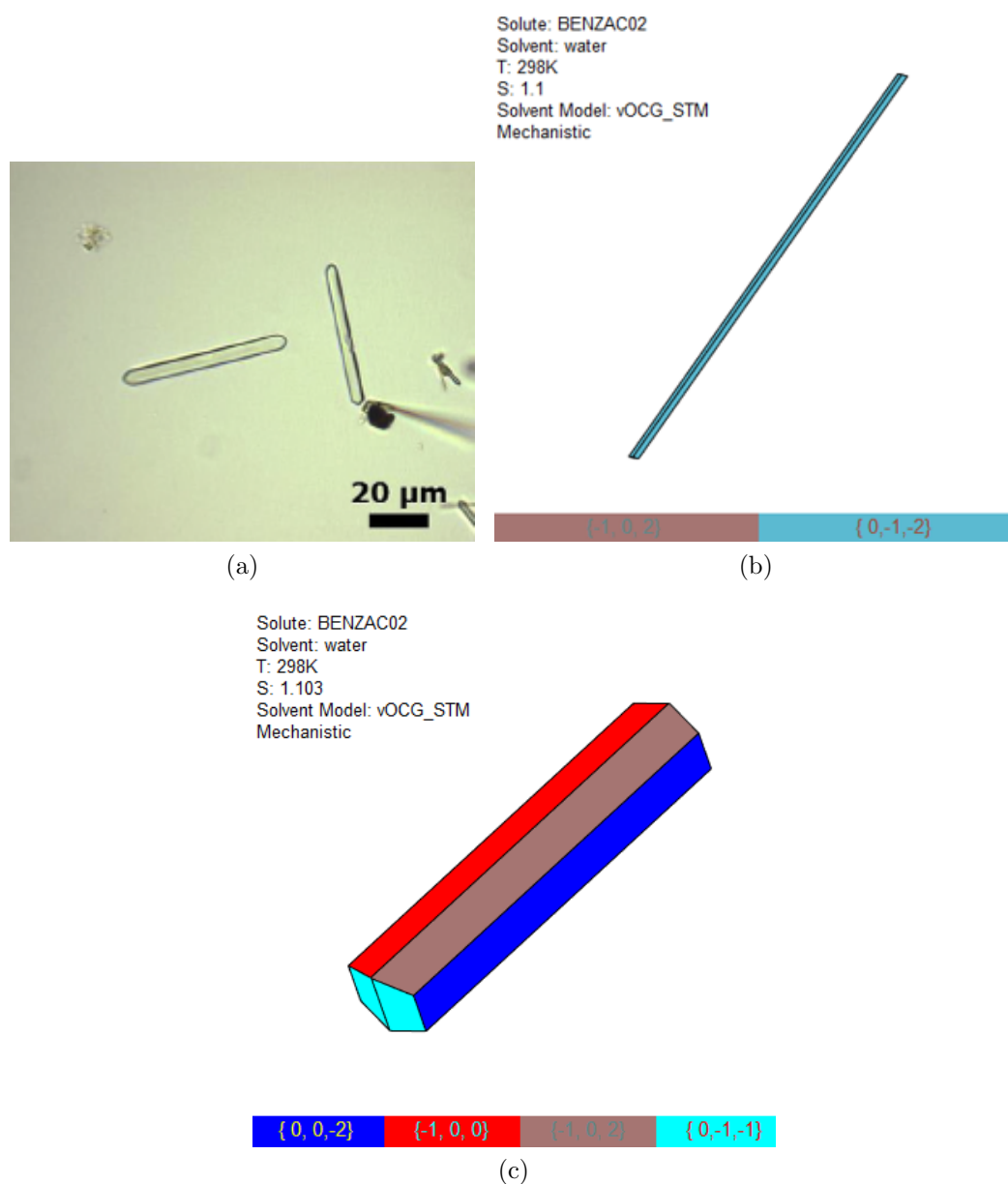


Figure 5.11: (a) Experimental shape observations of benzoic acid (CSD ref code: BENZAC02) in water. Figure reproduced with permission from Liang et al.[39]. Copyright 2017 Elsevier Ltd. (b) Model-based in-silico morphology prediction of benzoic acid monomer in water, (c) Model-based in-silico morphology prediction of benzoic acid dimer in water.

### 5.6.3 Lovastatin

Lovastatin is an API used for reducing the risks associated with cardiovascular diseases and cholesterol.[41] The crystal structure of lovastatin with CSD ref code CEKBEZ is used for the calculations. Lovastatin molecules crystallize in the space group  $P2_12_12_1$ . The unit cell has 4 molecules in the unit cell and one asymmetric unit, hence  $Z = 4$  and  $Z' = 1$ . The unit cell parameters are  $a = 22.154\text{\AA}$ ,  $b = 17.321\text{\AA}$ ,  $c = 5.968\text{\AA}$ ,  $\alpha = 90^\circ$ ,  $\beta = 90^\circ$ ,  $\gamma = 90^\circ$ . The experimental observation is taken from the literature and shown in Fig. 5.12a. Lovastatin crystals are grown in isopropanol at low supersaturation (5-10%) and at  $16^\circ\text{C}$  in a quiescent crystallizer.[4] Fig. 5.12b depicts the SSSF-based morphology prediction of lovastatin grown from isopropanol at  $T = 289\text{K}$  and  $S = 1.1$ . The in-silico lovastatin morphology predicted by the tool has a needle-like shape, demonstrating good agreement with the experimental observations.

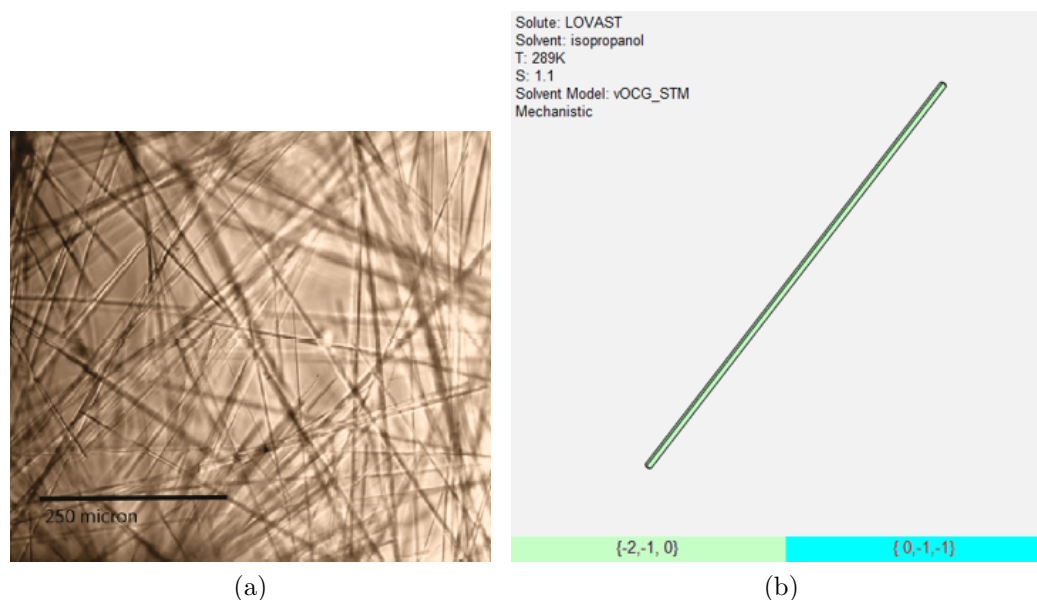


Figure 5.12: (a) Experimental shape observations of lovastatin (CSD ref code: CEKBEZ) in isopropanol. Reproduced with permission from Kuvadia and Doherty[4]. Copyright 2011 American Chemical Society. (b) Model-based in-silico morphology prediction of lovastatin in isopropanol.

## 5.7 Discussion

In previous sections, we studied the operational framework of the new symbolic-numeric tool, and its ability to generate and solve model equations based on SSSF to provide NEQ kink densities and step velocity for a given step configuration. The tool can be integrated into ADDICT to allow its application to real molecular crystals for rapid morphology predictions. The tool has been successfully tested on crystals with one, two and four noncentrosymmetric molecules in the unit cell. This leads to the question of its application to a general crystal with six, eight or more molecules in the unit cell.

A crystal type with  $n$  molecules in the unit cell comprises of different types of step configurations. The initial objective is identification of all the permissible configurations possible for steps within the crystal type. A step configuration is defined by the structural environment of growth units within the step. Identification of all configurations boils down to recognizing distinguishing environments of growth units. The configurations can be broadly categorized based on the number of growth units within a single row such as: 1) rows of a single growth unit (step 1 of Fig. 5.7), 2) rows of two growth units (step 3 of Fig. 5.7), and so on. Once the configurations are identified, the appropriate configuration must be assigned from PBC networks. Refer to Appendix D for elaborate discussions on both permissible and impermissible configurations and their assignment.

The next objective is the generation of master equations. Given the step configuration, the symbolic-numeric tool employs its graph theoretic approach to develop steady-state equations. The size and number of equations will depend on the number of growth units. Greater the number of growth units, the more will be the number of major sites, most-likely events and subsequently the number of equations. The increased complexity may have a compounded effect on numerical idiosyncrasies discussed in Section 5.5, necessitating need for advanced solvers, effective continuation techniques and scaling



methods.

## 5.8 Conclusion

We have developed a generalized nonequilibrium crystal growth model based on a steady-state framework. We programmed a symbolic-numeric tool which allows automation and computational implementation of the framework, SSSF, for variable number of noncentrosymmetric growth units in the unit cell,  $Z = 1, 2, 4$ . The tool consists of two engines: symbolic and numeric. The symbolic engine utilizes graph theory to generate the model equations of the step surface. Graph theory provides an organized framework to represent the step surface elements such as surface sites and their interactions through surface events. Such a representation allows effective transfer of information for model building in the symbolic space.

The model-equations developed in the symbolic engine are then sent to the numerical engine for their solution. The model equations are an overdefined set of algebraic equations: for  $n$  kink densities,  $n + m + 2$  equations. ( $m$  is the number of growth units along the step) The numerical engine performs matrix operations to reduce the superfluous set of equations and derive a final set of well-defined equations. A numerical system solver is then employed to arrive at the NEQ kink densities which satisfy the equations. A parametric continuation is performed, wherein the anisotropy within step interactions is dissolved to obtain reduced Kossel-equivalent interaction parameters. The solution is known for a Kossel step, and it acts as a known fixed point.[14] The interactions are then incremented systematically, by gradually introducing anisotropy to eventually reach the final step interaction parameters.

The inputs to the tool are the crystal type (e.g. Kossel, AB, ABCD, etc), the step configuration type (e.g. Kossel step, alternate A and B rows, etc.), the growth conditions

(e.g., supersaturation and temperature), and the network of interactions around all the growth units along the step. The tool allows estimation of important growth parameters in mechanistic crystal growth models, i.e., kink densities and step velocity. The integration of the tool within ADDICT allows its application to complex organic molecules for prediction of morphology from the relative growth rates of crystal facets. The graph theoretic tool-based morphology predictions are compared with experimental shapes of several drug molecules and demonstrates advantages of the tool to allow rapid crystal property predictions for real API asymmetric compounds.

The tool allows the versatility to generate model equations and solve them for a given step configuration of crystals with various growth units. The tool has been tested for crystals with  $Z = 1, 2, 4$ . For crystals with  $Z > 4$ , the tool can still be applied once the various step configurations are identified, although it has not been tested for  $Z > 4$  crystal types.

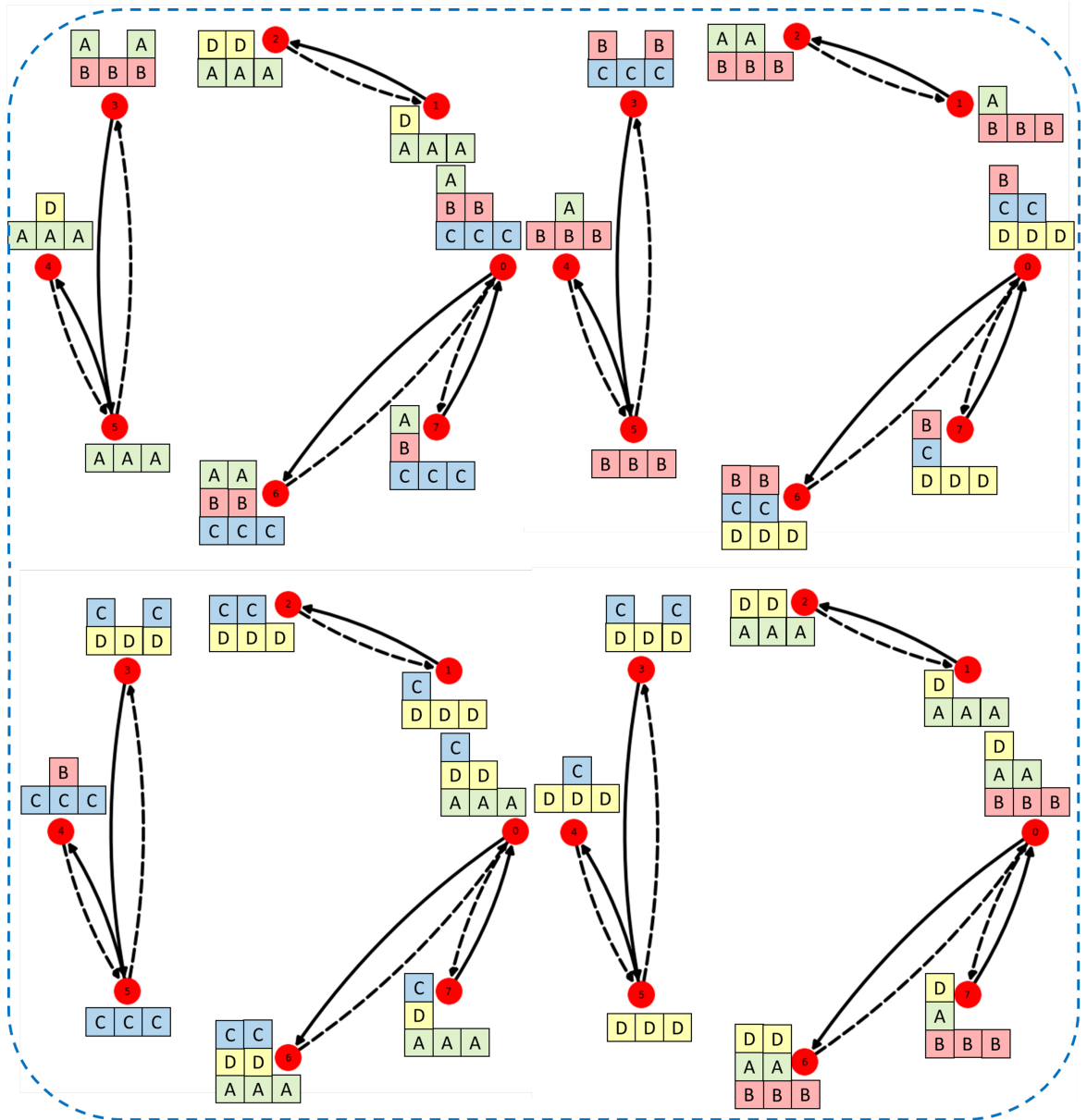


Figure 5.8: Graph network diagram for the step configuration with alternate rows of four growth units A, B, C and D. The nodes denote the *major sites* and the arcs denote the most-probable events capturing the interactions between the nodes. The attachment and detachment events are denoted by the solid and dashed lines, respectively.

# Bibliography

- (1) Snyder, R. C.; Doherty, M. F. Predicting crystal growth by spiral motion. *Proceedings of the Royal Society A: Mathematical, Physical and Engineering Sciences* **2009**, *465*, 1145–1171.
- (2) Lovette, M. A.; Doherty, M. F. Predictive modeling of supersaturation-dependent crystal shapes. *Crystal Growth & Design* **2012**, *12*, 656–669.
- (3) Tilbury, C. J.; Green, D. A.; Marshall, W. J.; Doherty, M. F. Predicting the Effect of Solvent on the Crystal Habit of Small Organic Molecules. *Crystal Growth & Design* **2016**, *16*, 2590–2604.
- (4) Kuvadia, Z. B.; Doherty, M. F. Spiral Growth Model for Faceted Crystals of Non-Centrosymmetric Organic Molecules Grown from Solution. *Crystal Growth & Design* **2011**, *11*, 2780–2802.
- (5) Cuppen, H. M.; Meekes, H.; van Veenendaal, E.; van Enkevort, W. J. P.; Bennema, P.; Reedijk, M. F.; Arsic, J.; Vlieg, E. Kink density and propagation velocity of the [010] step on the Kossel (100) surface. *Surface Science* **2002**, *506*, 183–195.
- (6) Cuppen, H. M.; Meekes, H.; van Enkevort, W. J. P.; Vlieg, E. Kink incorporation and step propagation in a non-Kossel model. *Surface Science* **2004**, *571*, 41–62.

## BIBLIOGRAPHY

---

- (7) Burton, W. K.; Cabrera, N.; Frank, F. C. The growth of crystals and the equilibrium structure of their surfaces. *Philosophical Transactions of the Royal Society of London. Series A, Mathematical and Physical Sciences* **1951**, *243*, 299–358.
- (8) Voronkov, V. V. Dislocation mechanism of growth with a low kink density. *Soviet Physics Crystallography* **1973**, *18*, 19–223.
- (9) Chernov, A. A.; Rashkovich, L. N.; Vekilov, P. G. Steps in solution growth: dynamics of kinks, bunching and turbulence. *Journal of Crystal Growth* **2005**, *275*, 1–18.
- (10) Vekilov, P. G. What determines the rate of growth of crystals from solution? *Crystal Growth and Design* **2007**, *7*, 2796–2810.
- (11) Tilbury, C. J.; Joswiak, M. N.; Peters, B.; Doherty, M. F. Modeling Step Velocities and Edge Surface Structures during Growth of Non-Centrosymmetric Crystals. *Crystal Growth & Design* **2017**, *17*, 2066–2080.
- (12) Joswiak, M. N.; Peters, B.; Doherty, M. F. Nonequilibrium Kink Density from One-Dimensional Nucleation for Step Velocity Predictions. *Crystal Growth & Design* **2018**, *18*, 723–727.
- (13) Padwal, N. A.; Doherty, M. F. Step Velocity Growth Models for Molecular Crystals: Two Molecules in the Unit Cell. *Crystal Growth & Design* **2024**, *24*, 4368–4379.
- (14) Padwal, N. A.; Doherty, M. F. Simple Accurate Nonequilibrium Step Velocity Model for Crystal Growth of Symmetric Organic Molecules. *Crystal Growth & Design* **2022**, *22*, 3656–3661.
- (15) Fan, W.; Ma, Y.; Li, Q.; He, Y.; Zhao, E.; Tang, J.; Yin, D. In *The world wide web conference*, 2019, pp 417–426.

## BIBLIOGRAPHY

---

- (16) Francesconi, E.; Frascioni, P.; Gori, M.; Marinai, S.; Sheng, J.; Soda, G.; Sperduti, A. In *International Workshop on Graphics Recognition*, 1997, pp 104–117.
- (17) Wu, Y.; Lian, D.; Xu, Y.; Wu, L.; Chen, E. In *Proceedings of the AAAI conference on artificial intelligence*, 2020; Vol. 34, pp 1054–1061.
- (18) Giuliani, A.; Krishnan, A.; Zbilut, J. P.; Tomita, M. Proteins as networks: usefulness of graph theory in protein science. *Current Protein and Peptide Science* **2008**, *9*, 28–38.
- (19) Fout, A.; Byrd, J.; Shariat, B.; Ben-Hur, A. Protein interface prediction using graph convolutional networks. *Advances in neural information processing systems* **2017**, *30*.
- (20) Danon, L.; Ford, A. P.; House, T.; Jewell, C. P.; Keeling, M. J.; Roberts, G. O.; Ross, J. V.; Vernon, M. C. Networks and the epidemiology of infectious disease. *Interdisciplinary perspectives on infectious diseases* **2011**, *2011*, 284909.
- (21) Bua, A.; Gori, M.; Santini, F. In *Artificial Neural Networks—ICANN 2002: International Conference Madrid, Spain, August 28–30, 2002 Proceedings 12*, 2002, pp 290–295.
- (22) Hartman, P.; Perdok, W. G. On the relations between structure and morphology of crystals. I. *Acta Crystallographica* **1955**, *8*, Publisher: International Union of Crystallography, 49–52.
- (23) Hartman, P.; Perdok, W. G. On the relations between structure and morphology of crystals. II. *Acta Crystallographica* **1955**, *8*, Publisher: International Union of Crystallography, 521–524.

- (24) Hartman, P.; Perdok, W. G. On the relations between structure and morphology of crystals. III. *Acta Crystallographica* **1955**, *8*, Publisher: International Union of Crystallography, 525–529.
- (25) Harary, F. Graph theory, chs. 2, 13. *Reading: Addison Wesley* **1969**.
- (26) Strom, C. Graph-theoretic construction of periodic bond chains: I. General case. *Zeitschrift für Kristallographie-Crystalline Materials* **1980**, *153*, 99–114.
- (27) Strom, C. Graph-theoretic construction of periodic bond chains: II. Ionic case. *Zeitschrift für Kristallographie-Crystalline Materials* **1981**, *154*, 31–44.
- (28) Grimbergen, R.; Meekes, H.; Bennema, P.; Strom, C.; Vogels, L. On the prediction of crystal morphology. I. The Hartman–Perdok theory revisited. *Acta Crystallographica Section A: Foundations of Crystallography* **1998**, *54*, 491–500.
- (29) Grimbergen, R. F. P.; Reedijk, M. F.; Meekes, H.; Bennema, P. Growth behavior of crystal faces containing symmetry-related connected nets: a case study of naphthalene and anthracene. *The Journal of Physical Chemistry B* **1998**, *102*, 2646–2653.
- (30) Bennema, P.; Meekes, H.; Boerrigter, S.; Cuppen, H.; Deij, M.; Van Eupen, J.; Verwer, P.; Vlieg, E. Crystal growth and morphology: New developments in an integrated Hartman-Perdok connected net roughening transition theory, supported by computer simulations. *Crystal Growth & Design* **2004**, *4*, 905–913.
- (31) Bennema, P.; Liu, X. Y.; Lewtas, K.; Tack, R.; Rijpkema, J.; Roberts, K. Morphology of orthorhombic long chain normal alkanes: theory and observations. *Journal of Crystal Growth* **1992**, *121*, 679–696.
- (32) Li, J.; Tilbury, C. J.; Kim, S. H.; Doherty, M. F. A design aid for crystal growth engineering. *Progress in Materials Science* **2016**, *82*, 1–38.

- (33) Li, J.; Tilbury, C. J.; Joswiak, M. N.; Peters, B.; Doherty, M. F. Rate Expressions for Kink Attachment and Detachment During Crystal Growth. *Crystal Growth & Design* **2016**, *16*, 3313–3322.
- (34) Powell, M. J. In *Nonlinear programming*; Elsevier: 1970, pp 31–65.
- (35) Powell, M. J. A hybrid method for nonlinear equations. *Numerical methods for nonlinear algebraic equations* **1970**, 87–161.
- (36) Landis, S.; Zhao, Y.; Doherty, M. F. Digital design of crystalline solids. *Computers & Chemical Engineering* **2020**, *133*, 106637.
- (37) Zhao, Y.; Tilbury, C. J.; Landis, S.; Sun, Y.; Li, J.; Zhu, P.; Doherty, M. F. A New Software Framework for Implementing Crystal Growth Models to Materials of Any Crystallographic Complexity. *Crystal Growth & Design* **2020**, *20*, 2885–2892.
- (38) Price, L. S.; McMahon, J. A.; Lingireddy, S. R.; Lau, S.-F.; Diserod, B. A.; Price, S. L.; Reutzel-Edens, S. M. A molecular picture of the problems in ensuring structural purity of tazofelone. *Journal of Molecular Structure* **2014**, *1078*, 26–42.
- (39) Liang, Z.; Zhang, M.; Wu, F.; Chen, J.-F.; Xue, C.; Zhao, H. Supersaturation controlled morphology and aspect ratio changes of benzoic acid crystals. *Computers & Chemical Engineering* **2017**, *99*, 296–303.
- (40) Tang, W.; Zhang, M.; Mo, H.; Gong, J.; Wang, J.; Li, T. Higher-order self-assembly of benzoic acid in solution. *Crystal Growth & Design* **2017**, *17*, 5049–5053.
- (41) Chuong, M. C.; Choy, E.; Douk, K.; Duong, L. H.; Hoang, S. K.; Le, N.; Lim, M.; Poirier, B.; Prasad, D.; Radke, M. The development of delayed-then-extended-release lovastatin tablet. *Int. J. Appl. Pharm* **2013**, *5*, 11–18.



# Chapter 6

## Summary, Conclusion and Future Directions

### 6.1 Summary

Crystal growth is a multi-scale phenomenon spanning various time and length scales, from the molecular level incorporation of growth units along surface sites to the layered growth of 2D nuclei. In contrast to the nonmechanistic models, the multi-scale mechanistic growth models best capture the physics and chemistry of crystal growth and enable environment and system-specific prediction of crystal properties. The mechanistic models offer the flexibility to capture variations in growth environments and be coupled with mass and heat transfer equations to provide a dynamic evolution of properties. However, mechanistic models hinge on fundamental understanding of the process to mathematically encapsulate the mechanisms of crystal growth.

Steps along crystals play a critical role in building faces in a layered manner. The fundamental parameters which stand out within the mechanistic growth models are the step attributes of step velocity and kink densities. The kink densities are frequently ap-

proximated to their equilibrium value and Boltzmann distribution is utilized for modeling the equilibrium kink densities. We demonstrated that kink densities are indeed strong functions of the supersaturation and hence vary with supersaturation and considerably influence the step velocity predictions. Consequently, capturing the nonequilibrium nature of kink densities by accounting for the effect of supersaturation is paramount to accurate predictions of growth rates and subsequently the crystal properties.

To that effect, we proposed the novel theory of Simplified Steady-State Framework to estimate NEQ kink densities and step velocity. SSSF is based on identification of the most concentrated surface sites and studying their interactions to identify the highest probability surface events. The rates of such events are then modeled to construct a steady-state balance on the concentration of kinks and generate the so-called *master equations*. The master equations are nonlinear in kink densities and the parameters are supersaturation, temperature and the growth unit interactions along kink, edge and terrace axes. The equations are then solved simultaneously in a nonlinear system solver to provide the NEQ kink densities in a numerical calculation. The step velocities are then estimated as a function of the calculated NEQ kink densities.

We start with application of SSSF to the simplest crystal - a Kossel Crystal (simple cubic model crystals with isotropic interactions). Centrosymmetric molecules have identical interaction spheres and behave in a *Kossel-like* manner.[1] The NEQ kink densities as well as step velocity are validated by kMC simulation data from literature. [2] The software ADDICT was deployed to enable the application of SSSF to real crystals, by integrating SSSF in place of the in-built step velocity models into ADDICT.

ADDICT[3-5] is a mechanistic crystal growth model-based morphology prediction software. The software performs solid-state crystal energetic calculations to identify the important crystal *flat F* faces and the strong chains of interaction (PBCs) which form the backbone of steps along these faces. The energetic calculations along with

in-built multi-scale growth models allow estimation of step velocities for each of the steps on each of the crystal facet. The step velocities are then used for continuum-scale models within ADDICT to estimate relative crystal growth rates of the faces. The relative growth rates allow construction of convex hull, i.e., the crystal morphology to provide rapid (order of seconds to minutes) crystal habit predictions and analysis of morphology. Such an architecture combines solid-state, surface chemistry calculations, atomistic and continuum crystal growth models, geometric construction algorithms in silos. The compartmentalization affords us the flexibility to integrate SSSF model in place of the in-built step velocity models within ADDICT's infrastructure. Thereby allowing us to test our new approach to real molecular crystals of varying levels of complexity for a wide range of growth solvents and supersaturation and temperatures, as well as polymorphs.

We then applied the SSSF model utilizing ADDICT to shape predictions for real molecular crystal of naphthalene (CSD ref code: NAPHTHA10), and orthorhombic rubrene (CSD ref code:QQQCIG08). The model-based morphology predictions demonstrate excellent agreement with experimental shape observations for a range of crystal systems.

Having successfully applied the framework to Kossel and centrosymmetric molecules, we move to crystals with the next immediate level of complexity - AB crystals (molecular crystals with two growth units in the unit cell). It should be noted that the molecules  $A$  and  $B$  are the same component and are identical in the solution phase, but incorporate into the crystal at different orientations and hence characterized as different growth units. The growth units are allowed to be symmetrically nonequivalent i.e.  $Z = 2$  and  $Z' = 1, 2$ , where  $Z$  is the number of species in the unit cell and  $Z'$  is the number of asymmetric units in the unit cell. The multiplicity of molecules within the unit cell results in different step configurations in AB crystals, such that each configuration comprises of different types

of kink sites and surface events and need to be analysed individually. In AB crystals, a total of three configurations are identified: alternate rows of A and B, alternate columns of A and B, checkered A-B pattern. The SSSF-based steady-state equations are then derived for each of the three configurations.

Unlike the Kossel crystals, for crystals with multiple growth units, the surface sites are no longer independent of each other. The sites along step surfaces are spatially correlated to maintain the step topology. This renders the Boltzmann distribution-based equilibrium models for AB crystals and beyond, inaccurate even at equilibrium let alone under the nonequilibrium conditions of growth that crystals are subjected to. This is because statistical independence of configurations is a key assumption of the Boltzmann distribution. This further reinforces the need for NEQ models for the vast majority of crystals of asymmetric molecules. SSSF offers the flexibility to account for the spatial correlations between kink sites, in the form of conditional probabilities. This allowed for effectively capturing the kink densities not only at equilibrium as depicted in Fig. 4.2, but also the NEQ nature of kink density as depicted in Fig 4.3. The step velocities, henceforth estimated from the NEQ kink densities, are compared with kMC simulations and exhibit excellent agreement for all the three step configuration types. (refer Figs. 3.9a and 4.4b) Having validated the model through simulation data, we then applied SSSF to several active pharmaceutical ingredients such as doravirine precursor (OWIVEY), celecoxib (DIBBUL),  $\beta$ -glycine (GLYCIN), trimethoprim (AMXBPM10), among others. The application to real crystals requires us to assign appropriate configurations to the PBCs identified for each of the crystal facets within ADDICT. SSSF can then be implemented for each of the steps to obtain their step velocities and subsequently the face growth rates. The model-based morphology predictions ranged a wide array of geometric shapes including needle, plate and rhomboidal shapes and display good agreement with the corresponding experimental observations.

Crystals of the immediate next complexity are the crystals with four or more molecules in the unit cell. Such crystals will naturally have multiple step configurations. In order to apply the theory to a real crystal, we must first identify all the potential configurations of steps arising for such a crystal with the specific  $Z$  value. The model equations must then be derived and solved for each of the configurations identified. Although SSSF lays out the recipe for recognizing the major sites, surface events and subsequent creation of steady-state equations, we can imagine the increase in the number of sites to account for with increase in the number of molecules in the crystal repeating unit. This prescribes the need for a practical tool with the ability to handle various crystal types with variable number of molecules in the repeating unit and the various step configurations for such crystals.

To that effect, we developed a symbolic-numerical computer program in python which effectively automates implementation of SSSF and expands the applicability to crystals with variable number of molecules in the repeating units. The computational tool comprises of two separate engines which work in conjunction to derive master equations and their solution to provide NEQ kink densities and step velocity for the step of interest. The symbolic engine performs the function of identification of the concentrated *major sites* and explores their interactions to arrive at the *most-probable surface events*. Graph network theory is utilized to represent the network of surface sites and their interactions. Such a network representation allows systematic embedding of respective node, arc and graph properties and hence derivation of steady-state equations given the step configuration of a specific crystal type. The model equations generated by the symbolic engine are then supplied as inputs to the numerical engine. The numerical engine also accepts specific crystal and growth environment parametric inputs, such as the crystal surface interactions, supersaturation and temperature. With the given conditions and model equations, the numerical engine then employs nonlinear system solvers to solve the

equations for NEQ kink densities and then uses the step velocity model (also supplied by the symbolic engine), to calculate the step velocity.

We considered the ABCD crystals (with four molecules in the repeating unit) as a proof-of-concept for our computational tool. A total of seven configurations are identified for such a crystal. The symbolic engine performs equation derivation; the numerical engine performs equation solution for all the step configurations. Similar to the AB crystals, the application of the model to real crystals requires identification of PBCs which form the basis of steps and their assignment of appropriate configuration type so the appropriate equations can be used for its step velocity calculations. The tool has been tested for several APIs such as Lovastatin (LOVAST), benzoic acid (BENZAC02), Aspirin (AC-SALA01), Tazofelone (WIMBAV13), among others. The model-based shape predictions aligned with experimental observations for the APIs and other organic molecular crystals, thereby exhibiting the potential of the framework in providing rapid in-silico morphology predictions of complex organic molecules.

To summarize, we have developed a novel theory that allows predictions of fundamental crystal growth properties such as NEQ kink densities and step velocities. This is in contrast to the previous equilibrium-based kink density models which are deficient due to their lack of accountancy of spatial correlations. The model has been validated for several complex molecular crystals with 1, 2 and 4 molecules in the unit cell. Based on the CCDC database, this constitutes to about 34000, 90000 and 200000 crystals, respectively, thereby expanding the applicability of current growth models to realistic crystals. The model has been independently tested with kMC from the literature as well as experimental data from literature. Further, we devised a computational tool for deployment of the theory to construct and solve equations for a wide range of molecular crystals with variable number of molecules in the unit cell (e.g. 1,2,4). This modeling approach will play a crucial role in guiding the design, control, and optimization of crys-

tallization processes and promote the development of complex molecular crystals with precisely tailored properties.

## 6.2 Future Directions

Reliable models are essential in all emerging areas of research. The widespread usage of crystals in industries necessitates fundamental research in mechanism of crystal growth at all length scales, from atomic to continuum, through a combination of theoretical, experimental and simulation approaches. Mechanistic crystal growth modeling continues to be a predominant avenue of research. We address scope of improvement and further areas of research in the following points:

1. Numerical Engine: For crystals with high anisotropy in interactions, the kink densities are usually several orders of magnitude apart from each other, at times as high as  $10^{20}$ . This results in numerical idiosyncrasies and a hypersensitivity to initial guess and the solver encounters difficulty resolving the solution. Parametric continuation allowed proper tracing the solution curves for different degrees of anisotropy along different crystallographic axes. However, the method falls short for some extreme crystals such as bulkier molecules with high molecular weights or extreme anisotropy crystals (difference of  $> 15k_B T$  between solid-state interactions). Examples are ritonavir and paracetamol. This necessitates alternate advanced numerical solvers with high accuracy, scaling techniques, and novel strategies to handle the wide distribution of kink densities. A potential strategy would be treating the steady-state equations like differential equations and then solving the system of steady-state and configurational constraint equations dynamically as a differential-algebraic equation initial value problem to arrive at the steady-state.

2. Periodic bond chain algorithm: ADDICT is employed in this work for application

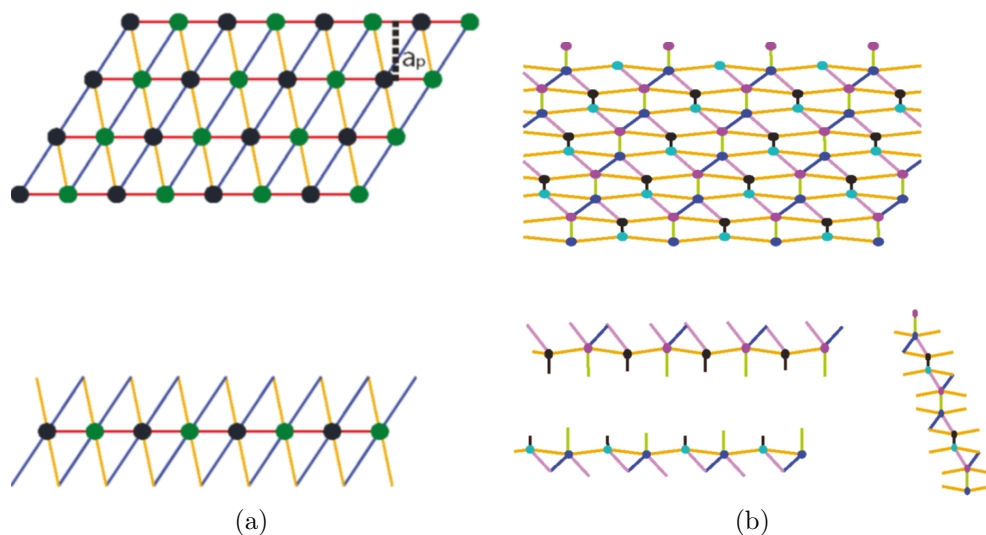


Figure 6.1: Periodic bond chain network for faces of centrosymmetric and non-centrosymmetric growth units: a)Face (110) of naphthalene (centrosymmetric growth unit) (b) Face (011) of paracetamol (non-centrosymmetric growth unit). Different line colors denote different bond energies, and the bond strength is proportional to the line thickness.[1] The PBCs are generated using the software ADDICT.[3]

of SSSF to real molecules. The PBC algorithm forms the heart of solid-state calculations within ADDICT. The algorithm is in charge of resolving the network of interactions along crystal face slices into two or more chains/vectors which encapsulate the majority of interactions within the slice. The PBCs depict most-stable steps on these faces and form the basis of interactions fed into step velocity calculations. As illustrated in Fig. 6.1, the PBC networks of centrosymmetric molecules such as naphthalene are much simpler with chains (e.g. the horizontal red-colored PBC) comprising of a single type of bond and growth units having identical interaction spheres. On the contrary for noncentrosymmetric molecules such as Paracetamol, the chains comprise of multiple types of bonds, the growth units along a chain are no longer collinear, their interaction spheres asymmetric and distinct. In such networks, account for the competing effects of chain strength and chain 'straightness'



becomes crucial. The current algorithm in ADDICT calculates a meta-parameter termed as the *attractiveness ratio* as a function of average chain strengths, angle of interactions within a chain and step propagation length, to rank the chains in the decreasing order of their *attractiveness ratios* to arrive at the best two or three PBCs. The algorithm necessitates an upgrade to state-of-the-art PBC algorithm[6, 7], which are better equipped at handling the complexity of asymmetric interaction networks.

3. Equilibrium kink density modeling of crystals with asymmetric molecules: In this work, we have proposed a framework for evaluating the NEQ kink density, which can effectively provide the equilibrium kink densities. However, the current equilibrium-based models in the literature do not account for the surface correlations between kinks. Potential research studies can explore the incorporation of surface correlations in equilibrium kink density formulations.
4. Absolute growth rate predictions: Absolute growth rate predictions hinge on estimation of elementary rate constants  $k^+$  to the *physical reaction*[8] of incorporation of molecules within the crystal surface. Merely the relative growth rates are required to predict the shape of a crystal, and hence  $k^+$  need not be estimated. This is because rate constants are all multiplicative constants in growth models and cancel out for relative growth rates in case of pure component crystals. In principle, the free energy landscape of the substrate desolvation and subsequent crystal attachment forms the basis of determination of the rate constant. Crystal growth and dissolution are complex processes with several local free energy minima separated by barriers, resulting in nucleation and crystal growth to be *rare events*. Rare event simulation sampling techniques such as Umbrella sampling[9], Metadynamics[10], Replica Exchange[11, 12] are key to understanding the chemistry and

thermodynamics at play at the most fundamental scale of crystal growth. The free energy landscape obtained from the simulations can then be used to estimate kinetic and thermodynamic parameters involved in the model: rate constants of kink attachment and detachment, detachment-to-solution work, and others. Incorporation of the values obtained from simulation would provide *in silico* absolute growth rate predictions. The simulations can also provide insights about the chemistry at play such as the effect of solvent molecules on surface events. This will be instrumental in identifying which assumptions need reassessment and enable further improvement in growth models.

5. Cocrystals and Hydrates: Pure component organic molecular crystals are the key subject of this work. For pure component crystals, the rate constants can be assumed to be uniform across all facets and hence cancel out in relative growth rate calculations. However, when the crystal comprises of multiple components such as in cocrystals and hydrates, the rate constants of elementary surface events will naturally be different for each of the distinct components. As a result, the rate constant will no longer cancel out in relative growth rate estimates. Hence rapid morphology predictions for multi-component crystals is impeded by time-intensive rate constant analysis, requiring inputs from rare event sampling techniques.
6. Rough growth regime: The stepped and kinked faces are the ones with minimal in-plane interactions, which results in low barriers to kink formation. This results in high density of kinks and growth is uniformly favorable across the face. This is in contrast to layered growth with favorable attachment propelling steps and consequently normal growth of the face. Mechanistic models cater to the layered growth regimes where the rate-determining step is the surface integration of growth units. In the rough growth regime, diffusion effects dominate and mass transfer

coefficient will determine the face growth rate. In this work, the  $S$  and  $K$  faces are arbitrarily assigned a high enough relative growth rate compared to the  $F$  face relative growth rate estimates. In order to effectively capture the growth rates of  $S$  and  $K$  faces, rough growth models are crucial which in turn call for knowledge about the mass and heat transfer conditions in the growth environment.

# Bibliography

- (1) Kuvadia, Z. B.; Doherty, M. F. Spiral Growth Model for Faceted Crystals of Non-Centrosymmetric Organic Molecules Grown from Solution. *Crystal Growth & Design* **2011**, *11*, 2780–2802.
- (2) Joswiak, M. N.; Peters, B.; Doherty, M. F. Nonequilibrium Kink Density from One-Dimensional Nucleation for Step Velocity Predictions. *Crystal Growth & Design* **2018**, *18*, 723–727.
- (3) Li, J.; Tilbury, C. J.; Kim, S. H.; Doherty, M. F. A design aid for crystal growth engineering. *Progress in Materials Science* **2016**, *82*, 1–38.
- (4) Zhao, Y.; Tilbury, C. J.; Landis, S.; Sun, Y.; Li, J.; Zhu, P.; Doherty, M. F. A New Software Framework for Implementing Crystal Growth Models to Materials of Any Crystallographic Complexity. *Crystal Growth & Design* **2020**, *20*, 2885–2892.
- (5) Landis, S.; Zhao, Y.; Doherty, M. F. Digital design of crystalline solids. *Computers & Chemical Engineering* **2020**, *133*, 106637.
- (6) Spackman, P. R.; Turner, M. J.; McKinnon, J. J.; Wolff, S. K.; Grimwood, D. J.; Jayatilaka, D.; Spackman, M. A. *CrystalExplorer*: a program for Hirshfeld surface analysis, visualization and quantitative analysis of molecular crystals. *Journal of Applied Crystallography* **2021**, *54*, DOI: 10.1107/S1600576721002910.

## BIBLIOGRAPHY

---

- (7) Bond, A. D. processPIXEL: a program to generate energy-vector models from Gavezzotti's PIXEL calculations. *Journal of Applied Crystallography* **2014**, *47*, 1777–1780.
- (8) Shell, M. S., *Thermodynamics and statistical mechanics: an integrated approach*; Cambridge University Press: 2015.
- (9) Torrie, G. M.; Valleau, J. P. Nonphysical sampling distributions in Monte Carlo free-energy estimation: Umbrella sampling. *Journal of Computational Physics* **1977**, *23*, 187–199.
- (10) Barducci, A.; Bonomi, M.; Parrinello, M. Metadynamics. *Wiley Interdisciplinary Reviews: Computational Molecular Science* **2011**, *1*, 826–843.
- (11) Hukushima, K.; Nemoto, K. Exchange Monte Carlo method and application to spin glass simulations. *Journal of the Physical Society of Japan* **1996**, *65*, 1604–1608.
- (12) Sugita, Y.; Okamoto, Y. Replica-exchange molecular dynamics method for protein folding. *Chemical physics letters* **1999**, *314*, 141–151.

# Appendix A

## Junctions, Sites and Identification of Major sites

Reproduced in part from the supplementary information with permission from:

Padwal, N.A.; Doherty, M.F., Simple Accurate Nonequilibrium Step Velocity Model for Crystal Growth of Symmetric Organic Molecules. *Crystal Growth & Design* **2022**, 22(6), 3656-3661.

DOI:10.1021/acs.cgd.1c01366. Copyright 2022 American Chemical Society.

### Introduction

The rate of step flow across crystal surfaces is crucial for mechanistic crystal growth models. The step velocity critically depends on kink density. Chapter 2 introduces Simplified Steady-State Framework for estimation of NEQ kink densities. The framework implementation initiates with determination of predominant *junctions*, which in turn enable identification of most-concentrated *major sites*. In this Appendix, we discuss the definitions of *junctions* and *major sites*, the most-likely events and derivation of master

equations.

## Junctions and Sites

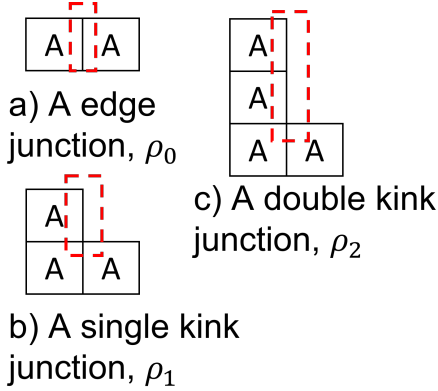


Figure A.1: Edge, kink and double-kink junctions and corresponding densities.

As depicted in Fig. A.1, *junctions* constitute the area of linkages between adjacent growth units along the step direction. The various types of kinks represent types of junction. As the kink height increases, more broken-bond interactions are exposed and the kink density reduces drastically. As a result, the single and double kinks are considered as predominant junctions within SSSF and multi-height kinks are ignored. Apart from the various types of kink junctions, an additional junction type is the edge which characterizes the flat portions of a step. An edge junction exposes the least number of broken-bond interactions and usually are more concentrated along steps. The edge and kink densities ( $\rho_0$ ,  $\rho_1$ ,  $\rho_2$ ) refer to the density of junctions. The sum of densities of all junctions must sum to 1,  $\rho_0 + \rho_1 + \rho_2 = 1$ , which gives rise to the normalization condition utilized in modeling equations. Henceforth, kink *junctions* will be referred to as simply kinks.

*Sites* are positions occupied by a growth unit along a step. *Sites* are characterised by adjoining junctions. For a Kossel crystal (orthogonal lattice with perpendicular alignment

of growth units), the various types of sites are depicted in Figs. A.4a-A.4b. A site may be subjected to 1) an attachment event such that the edge site undergoing nucleation event in configuration (1) in Fig. A.4a or 2) a detachment of growth unit from the site resulting in a new site in its place, for example, the pit-formation event at the same site in configuration (2).

## Major Sites

The predominant junctions are the single, double kinks and the edge. Since sites are made of adjoining junctions, potential sites are identified by shortlisting all possible sites that can form from the predominant junction. Major sites are the most-concentrated sites composed of the predominant junctions which are at least as dense as the least concentrated junction. In order to obtain major sites, we assume edge and kink densities to be an order of magnitude apart from each other such that  $\rho_0 \sim 0.9$ ,  $\rho_1 \sim 0.09$ ,  $\rho_2 \sim 0.009$ , as evidenced from the equilibrium models (Eqs. 1.9,2.2). This allows us to arrive at the set of major sites as depicted in the most-likely space  $M$  in Fig. A.2. The major sites are also tabulated within the *Site* column of Table A.1.

## Most-likely Events

The major sites are then subjected to attachment and detachment events to identify the most-likely events which transform sites within the space  $M$  and are responsible for transformation of major sites into other major sites. The most-likely events are depicted by solid arrows in Fig. A.2. Studying the influence of such events on formation and destruction of single and double kinks allows construction of master equations.



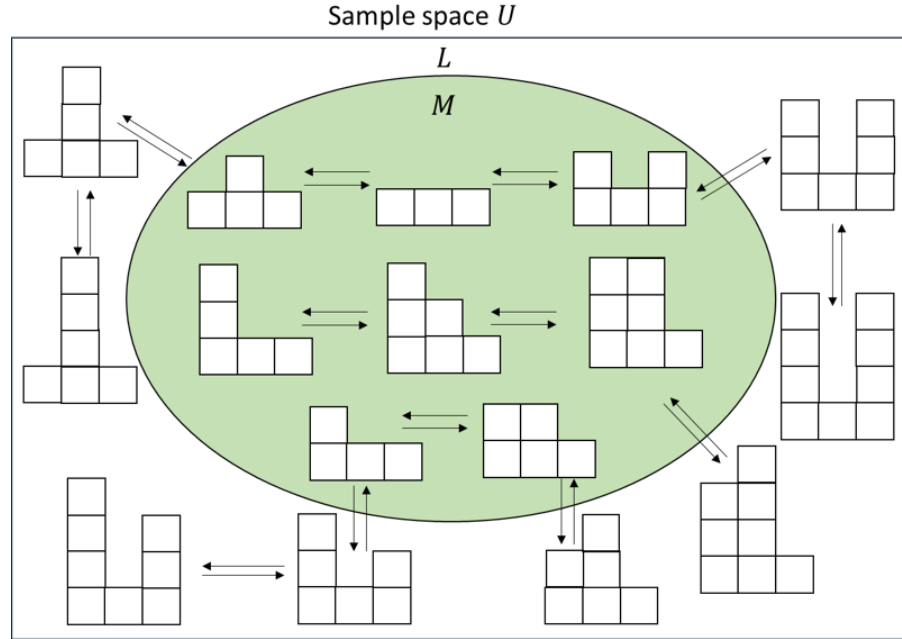


Figure A.2: Surface kinetics diagram of a step along a Kossel crystal, depicting the most-probable event space  $M$  within the sample space of all events  $U$ .

## Site density

The definition of sites as combination of junctions allows us to model densities of site configurations as the product of densities of independent junctions that form the site. This is based on the underlying assumption of negligible spatial or statistical correlation between adjacent junctions which has been found to be acceptable for Kossel crystal.[1] Hence, site densities are product of constituent junction densities. Density of an edge *site* formed by adjacent edge *junctions*, is  $\rho_0^2$ . Similarly, a kink *site* formed by adjoining kink and edge *junctions*, will have a density of  $\rho_0\rho_1$ . The positive (west-facing) and negative (east-facing) kinks contribute equally to single and double-height kink densities, respectively, since they have identical environments. Hence, positive and negative single-height kink density is  $\frac{\rho_1}{2}$  each. Positive and negative double-height kink density is  $\frac{\rho_2}{2}$  each. Consider site configuration 1 in Fig. A.4b, the site of detachment is formed by adjacent positive kinks( $\frac{\rho_1^2}{4}$ ) or negative kinks( $\frac{\rho_1^2}{4}$ ). This results in the density of such a

site to be  $\frac{\rho_1^2}{4} + \frac{\rho_1^2}{4} = \frac{\rho_1^2}{2}$ .

## Rate Model

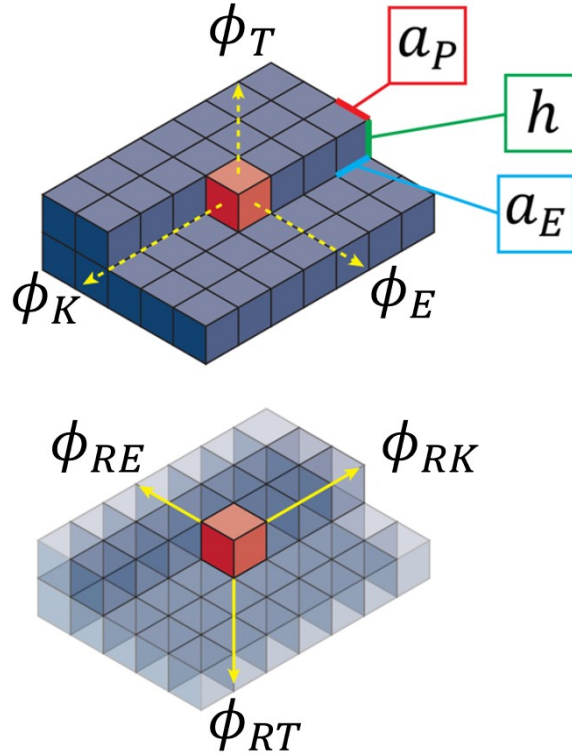


Figure A.3: Energy of interactions of a crystal growth unit in different directions. The interactions are categorised in intraedge (kink), interedge (edge), interslice (terrace) axes. The kink ( $\phi_K$ ), edge ( $\phi_E$ ) and terrace ( $\phi_T$ ) energies correspond to broken interactions along respective axes facing the solution. The reverse kink ( $\phi_{RK}$ ), reverse edge ( $\phi_{RE}$ ) and reverse terrace ( $\phi_{RT}$ ) energies correspond to satisfied interactions along respective axes that hold the growth unit to the crystal. Figure adapted from Tilbury et al.[2]

The rate model described in Section 2.3 is used for modeling rate equations and briefly described below. Treating the surface integration process like a reaction allows for modeling the rates.[3–6] Attachment rate is assumed to be independent of site, while detachment rate depends on the work of detachment [5]. The rate model used for at-

tachment and detachment rates is

$$j^+ = k^+ x_{sat} S \quad (\text{A.1})$$

$$j_i^- = k_i^- = k^+ e^{-\beta \Delta W_i} \quad (\text{A.2})$$

where  $j^+$  is the attachment rate,  $k^+$  is the attachment rate constant,  $k_i^-$  is the detachment rate constant,  $x_{sat}$  is the saturation mole fraction,  $S = \frac{x}{x_{sat}}$  is the supersaturation,  $j_i^-$  is the detachment rate from a site with  $i$  nearest-neighbors in the step direction (kink axis), and  $\Delta W_i$  is the work of detachment from site  $i$ .  $\Delta W_i$  is the summation of broken bond energy during detachment along the edge, kink or terrace axes and is given by

$$\Delta W_i = 2 (i \phi^{RK} + \phi^{RE} + \phi^{RT}) \quad (\text{A.3})$$

where,  $\phi^{RK}$ ,  $\phi^{RE}$ ,  $\phi^{RT}$  denote broken bond energies in reverse kink, reverse edge and reverse terrace directions, respectively as depicted in Fig. A.3. The prefactor of 2 accounts for the convention that  $\phi$  represents half the bond energy between growth units. The number of bonds broken depends on the type of site formed upon detachment. For example, detachment work of kink sites ( $\Delta W_1$ ) is a summation of reverse kink, edge and terrace energy. When a pit site ( $\Delta W_2$ ) is formed, reverse edge, terrace and two reverse kink bonds are broken.

$$\Delta W_2 = 2 (2 \phi^{RK} + \phi^{RE} + \phi^{RT})$$

For a Kossel crystal, which has equal bond strength in all directions ( $\phi$ ), the work of detachment for a kink and pit site is  $6\phi$  and  $8\phi$ , respectively.

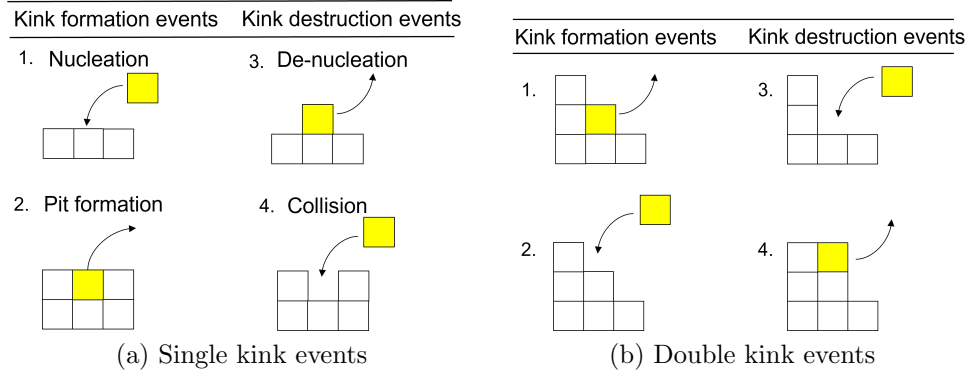


Figure A.4: Most-likely surface processes affecting single and double-kink density through creation and annihilation events.

## Simplified Steady-State Framework

The SSSF states that the concentrated major sites and most-likely events occurring along step surfaces at higher rates, will determine the major supersaturation effects. Within SSSF, master equations are constructed by balancing the rates of formation with the rates of destruction of kinks. The most-likely events allow determination of rates associated with respective kinks. The master equations are then solved simultaneously to obtain non-equilibrium kink density expressions. We will only be accounting for single-height and double-height kink junctions to maintain simplicity of the model.

For single height kinks, Fig. A.4a depicts the different events within the most-likely events, which form or destroy single-height kinks. Nucleation and pit-formation events produce kinks, while kink collision and de-nucleation events destroy kinks. A stochastic approach is used to model these processes by accounting for the attachment/detachment rate and the probability of sites (where attachment/detach occurs). For instance, process (4) in Fig. A.4a, is an attachment ( $j^+$ ) event at pit sites. Pit sites are formed by adjacent positive ( $\frac{\rho_1}{2}$ ) and negative kink ( $\frac{\rho_1}{2}$ ) junctions. Hence, the rate of the process is modeled as  $j^+ \frac{\rho_1^2}{4}$ . Note that events in Fig. A.4b also affect single-kink density, however these terms cancel out owing to the double-kink master Eq. (2.8). A factor of 2 preceding all

terms in Eq. (2.7) accounts for the creation and destruction of two single-kinks in these events.

Refer to Table A.1 for the major sites and most-likely events their influence on density of single-height kinks. The configurations in *Site* column are the major sites. These sites configurations are subjected to attachment and detachment events. The change in the number of single-height kinks upon the events is documented in respective columns. Eight major sites are obtained, out of which only six affect kink creation and annihilation. Note that that most-likely events inter-convert major sites into each other. Hence sites marked “–” in columns two and three do not qualify as major sites and are not considered for devising master equations. Balancing these rates yields a steady-state master equation for single kinks.

$$2\rho_2 \rho_0(j^+ + j_1^-) + 2\rho_0^2(j^+ + j_2^-) = 2\frac{\rho_1^2}{4}(j^+ + j_0^-) + 2\frac{\rho_1^2}{2}(j^+ + j_1^-) \quad (\text{A.4})$$

Similarly, the most-likely events that affect the density of double-height kinks are depicted in Fig. A.4b. Detachment and attachment at sites in configurations 1 and 2, respectively, forms double-height kinks. Attachment and detachment at sites in configurations 3 and 4, respectively, destroys double-height kinks. Refer to Table A.2 for list of major site configurations that affect double-height kink density. Balancing the rates yields a steady-state master equation for double-height kinks.

$$\rho_2 \rho_0(j^+ + j_1^-) = \frac{\rho_1^2}{2}(j^+ + j_1^-) \quad (\text{A.5})$$

The steady-state master equations for both the kink types, combined with the normalization condition in Eq. (A.6)

$$\rho_0 + \rho_1 + \rho_2 = 1 \quad (\text{A.6})$$

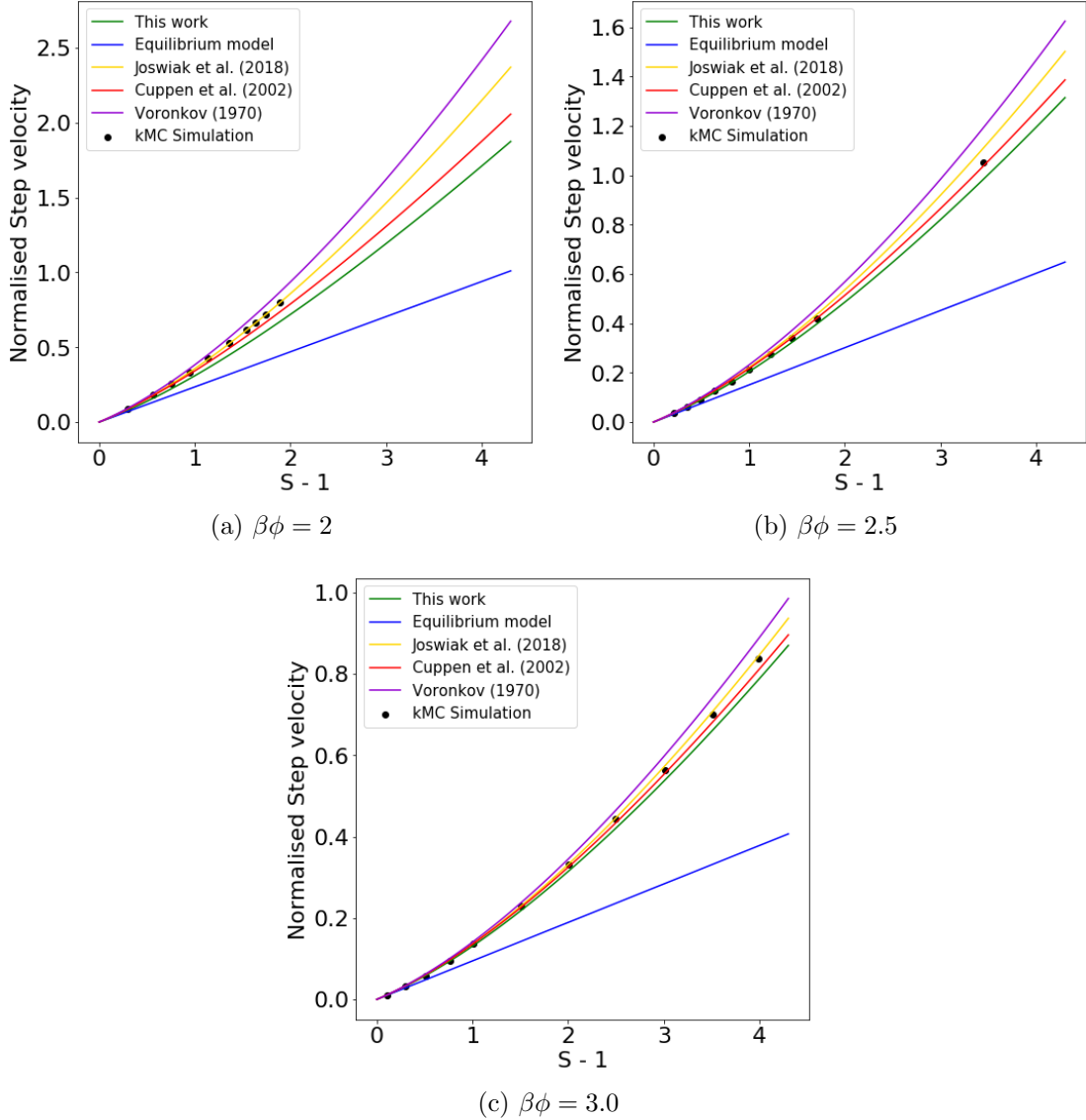


Figure A.5: Plot of normalised step velocity  $v/(a_P k^+ x_{sat})$  vs  $S - 1$  for Kossel crystals at bond energies: (a)  $\beta\phi = 2$ , (b)  $\beta\phi = 2.5$  and (c)  $\beta\phi = 3$ . kMC simulation data points at  $\beta\phi = 2, 3$  are obtained from Joswiak et al.[7] and at  $\beta\phi = 2.5$  are obtained from Cuppen et al.[8]

can be solved simultaneously to obtain the following non-equilibrium kink density expressions:

$$\rho_1 = 2 \left( \frac{-2\tilde{e}\tilde{p} + (\tilde{e} + 2\tilde{p})\sqrt{\tilde{e}\tilde{p}}}{\tilde{e}^2 + 4\tilde{p}^2} \right) \quad (\text{A.7})$$

$$\rho_2 = 2\tilde{p} \left( \frac{\tilde{e} + 2\tilde{p} - 2\sqrt{\tilde{e}\tilde{p}}}{\tilde{e}^2 + 4\tilde{p}^2} \right) \quad (\text{A.8})$$

where

$$\tilde{e} = j^+ + j_0^- = k^+ x_{sat} S + k_0^- = k^+ (x_{sat} S + e^{-\beta\Delta W_0}) \quad (\text{A.9})$$

and

$$\tilde{p} = j^+ + j_2^- = k^+ x_{sat} S + k_2^- = k^+ (x_{sat} S + e^{-\beta\Delta W_2}) \quad (\text{A.10})$$

Eqs. (A.7) and (A.8) provide non-equilibrium kink density expressions for single and double-height kinks, respectively. As evident from the rate model, supersaturation dependence derives from  $j^+$ .

Figs. A.5a, A.5b and A.5c plot normalized step velocity predicted using the non-equilibrium kink density model (Eqs. (A.7) and (A.8)), multi-height equilibrium kink density model (Eq. 2.2), and the models by Joswiak et al.[7], Cuppen et al.[8], Voronkov[9] along with kMC simulations from the literature[7, 8]. Zhang and Nancollas's[10] model aligns exactly with Voronkov's model predictions and hence not shown in Fig. A.5. Step velocity increases with supersaturation due to increase in attachment rates and kink density. Step velocity decreases with increase in  $\beta\phi$  at constant S. This is because increase in inter-molecular bond strength reduces rates of all surface processes. The model demonstrates excellent agreement with kMC simulations despite accounting for only single and double height kinks. This is in contrast to the other models, that account for kinks of all heights to infinity. As  $\phi$  increases, the contribution of multi-height kinks reduces and all the models collapse closer to the simulation points. Unlike the other models, such a simplified approach to kink density estimation allows extension to non-centrosymmetric crystals with multiple growth units.

The non-equilibrium equations, Eqs. (A.7) and (A.8) indicate non-linear dependence of kink density on supersaturation. In order to get qualitative insights on the nature of this dependence, polynomial approximations to the non-equilibrium total kink density  $\rho_T$  are obtained utilising Eq. (A.11),

$$\rho_T = \rho_{eq} + a\sigma + b\sigma^2 + c\sigma^3 + \dots \quad (\text{A.11})$$

where  $\sigma$  is the driving force  $S - 1$  and  $\rho_{eq}$  is the NEQ kink density at  $\sigma = 0$ . This value of  $\rho_{eq}$  is the SSSF-based estimate of kink density at equilibrium. Non-linear least square fitting is conducted in Python 3.7 to obtain the model coefficients using the `scipy.optimize` package. As seen in Fig. A.6, a quadratic polynomial is the lowest order fit of the non-linear function for  $\rho_T$ . This results in step velocity being third order in  $\sigma$ . The  $\sigma$  dependence of growth rate  $G$  depends on the specific growth regime. In case of the spiral growth regime, a factor of  $\ln(\sigma + 1)$  is introduced owing to critical length calculations (Section 1.2.2).

$$\rho \sim \rho_{eq} + a\sigma + b\sigma^2 \quad (\text{A.12})$$

$$v \sim (\rho_{eq} + a\sigma + b\sigma^2) \sigma \quad (\text{A.13})$$

$$G \sim (\rho_{eq} + a\sigma + b\sigma^2) \sigma \ln(\sigma + 1) \quad (\text{A.14})$$



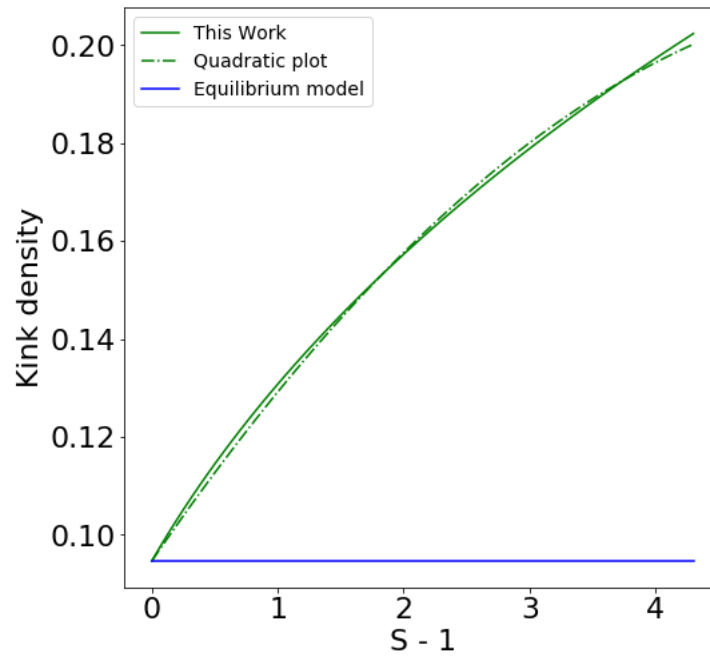


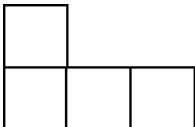
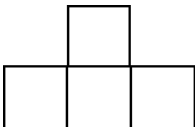
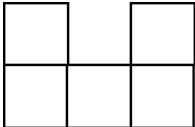


Figure A.6: Plot of total kink density,  $\rho_T$  vs driving force  $\sigma = S - 1$  at  $\beta\phi = 3$  calculated using the non-equilibrium model in Eqs. (9), (10) and (15) in the paper and its quadratic approximation.

## Configuration Tables: Kossel Step

Table A.1: Configuration table of major sites for a Kossel step and their influence on single-height kinks. The *Attachment* column denotes the change in the number of single-height kinks upon incorporation of relevant growth unit at the site of interest. The *Detachment* column denotes the change in the number of single-height kinks upon detachment of growth unit from the site of interest. Events marked ‘-’ convert the site into another out of the most-likely space and hence are not considered. The *attachment* and *detachment rate* columns provide the rate of respective elementary reactions along the step surface. The attachment rate is isotropic for all sites while detachment rate depends upon the growth unit detached and the number of neighboring kink bonds broken. The *site density* depends on the density of adjoining junctions and the appropriate partition function to account for the surface correlations. The sites are representative of their corresponding mirror images, since the east and west facing kinks have equivalent interaction networks. Similar tables can be constructed for all the predominant edge and kink types.

|   | Site  | Attachment | Detachment | Attachment rate | Detachment rate | Density of site      |
|---|---|------------|------------|-----------------|-----------------|----------------------|
| 1 |  | +2         | +2         | $j^+$           | $j_2^-$         | $\rho_0^2$           |
| 2 |  | -          | -          | $j^+$           | $j_1^-$         | $\rho_1\rho_0$       |
| 3 |  | -          | -          | $j^+$           | $j_1^-$         | $\rho_1\rho_0$       |
| 4 |  | -          | -2         | $j^+$           | $j_0^-$         | $\frac{\rho_1^2}{4}$ |
| 5 |  | -2         | -          | $j^+$           | $j_2^-$         | $\frac{\rho_1^2}{4}$ |

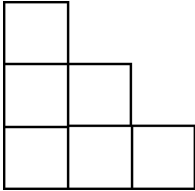
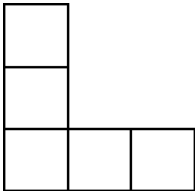
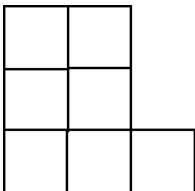


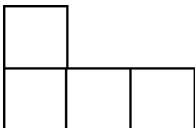
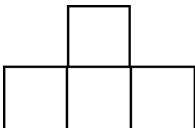
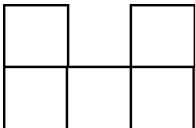
|   |  |    |    |       |         |                      |
|---|--|----|----|-------|---------|----------------------|
| 6 |   | -2 | -2 | $j^+$ | $j_1^-$ | $\frac{\rho_1^2}{2}$ |
| 7 |   | +2 | -  | $j^+$ | $j_2^-$ | $\rho_2 \rho_0$      |
| 8 |  | -  | +2 | $j^+$ | $j_1^-$ | $\rho_2 \rho_0$      |

Table A.2: Configuration table of major sites for a Kossel step and their influence on double-height kinks. The *Attachment* column denotes the change in the number of double-height kinks upon incorporation of relevant growth unit at the site of interest. The *Detachment* column denotes the change in the number of single-height kinks upon detachment of growth unit from the site of interest. Events marked '-' convert the site into another out of the most-likely space and hence are not considered. The *attachment* and *detachment rate* columns provide the rate of respective elementary reactions along the step surface. The attachment rate is isotropic for all sites while detachment rate depends upon the growth unit detached and the number of neighboring kink bonds broken. The *site density* depends on the density of adjoining junctions and the appropriate partition function to account for the surface correlations. The sites are representative of their corresponding mirror images, since the east and west facing kinks have equivalent interaction networks. Similar tables can be constructed for all the predominant edge and kink types.

|   | Site  | Attachment | Detachment | Detachment rate | Attachment rate | Density of site      |
|---|---|------------|------------|-----------------|-----------------|----------------------|
| 1 |   | -          | -          | $j^+$           | $j_2^-$         | $\rho_0^2$           |
| 2 |  | -          | -          | $j^+$           | $j_1^-$         | $\rho_1\rho_0$       |
| 3 |  | -          | -          | $j^+$           | $j_1^-$         | $\rho_1\rho_0$       |
| 4 |  | -          | -          | $j^+$           | $j_0^-$         | $\frac{\rho_1^2}{4}$ |
| 5 |  | -          | -          | $j^+$           | $j_2^-$         | $\frac{\rho_1^2}{4}$ |

|   |  |    |    |       |         |                      |
|---|--|----|----|-------|---------|----------------------|
| 6 |  | +1 | +1 | $j^+$ | $j_1^-$ | $\frac{\rho_1^2}{2}$ |
| 7 |  | -1 | -  | $j^+$ | $j_2^-$ | $\rho_2\rho_0$       |
| 8 |  | -  | -1 | $j^+$ | $j_1^-$ | $\rho_2\rho_0$       |

# Bibliography

- (1) Cuppen, H. M.; Meekes, H.; van Enckevort, W. J. P.; Bennema, P.; Vlieg, E. The effects of kink correlation and the Monte Carlo probability scheme on the step structure and velocity. *Surface science* **2003**, *525*, 1–12.
- (2) Tilbury, C. J.; Joswiak, M. N.; Peters, B.; Doherty, M. F. Modeling Step Velocities and Edge Surface Structures during Growth of Non-Centrosymmetric Crystals. *Crystal Growth & Design* **2017**, *17*, 2066–2080.
- (3) Chernov, A. A.; Rashkovich, L. N.; DeYoreo, J. J. In *AIP Conference Proceedings*, 2007; Vol. 916, pp 34–47.
- (4) Vekilov, P. G. What determines the rate of growth of crystals from solution? *Crystal Growth and Design* **2007**, *7*, 2796–2810.
- (5) Li, J.; Tilbury, C. J.; Joswiak, M. N.; Peters, B.; Doherty, M. F. Rate Expressions for Kink Attachment and Detachment During Crystal Growth. *Crystal Growth & Design* **2016**, *16*, 3313–3322.
- (6) Petsev, D. N.; Chen, K.; Gliko, O.; Vekilov, P. G. Diffusion-limited kinetics of the solution–solid phase transition of molecular substances. *Proceedings of the National Academy of Sciences* **2003**, *100*, 792–796.

## BIBLIOGRAPHY

---

- (7) Joswiak, M. N.; Peters, B.; Doherty, M. F. Nonequilibrium Kink Density from One-Dimensional Nucleation for Step Velocity Predictions. *Crystal Growth & Design* **2018**, *18*, 723–727.
- (8) Cuppen, H. M.; Meekes, H.; van Veenendaal, E.; van Enkevort, W. J. P.; Bennema, P.; Reedijk, M. F.; Arsic, J.; Vlieg, E. Kink density and propagation velocity of the [010] step on the Kossel (100) surface. *Surface Science* **2002**, *506*, 183–195.
- (9) Voronkov, V. V. Movement of an elementary step by means of formation of one-dimensional nuclei. *Soviet Physics Crystallography* **1970**, *15*, 8.
- (10) Zhang, J.; Nancollas, G. H. Kink densities along a crystal surface step at low temperatures and under nonequilibrium conditions. *Journal of Crystal Growth* **1990**, *106*, 181–190.

# Appendix B

## Analysis of AB Crystal - Configurations 2 and 3

Reproduced in part from the supplementary information with permission from:  
Padwal, N.A.; Doherty, M.F. Step Velocity Growth Models for Molecular Crystals: Two  
Molecules in the Unit Cell. *Crystal Growth & Design* **2024**, 24(11), 4368-4379.  
DOI:10.1021/acs.cgd.3c01508. Copyright 2024 American Chemical Society.

### Introduction

An organic crystal with two growth units A and B constitutes of various configurations of steps flowing across crystal surfaces as illustrated in Fig. B.1. Examples are alternating rows or columns of A and B. Each of the steps have different interaction networks, and types of kinks which interplay with other kinks in distinct ways resulting in distinct surface kinetics. Hence, the steady-state analysis for each of the configurations results in distinct master equations. Chapter 3 analyses step configuration 1 in Fig. 3.1 in detail. In this Appendix, we demonstrate application of SSSF to step configurations 2 and 3 to



derive the master equations, configurational constraints, step velocity expressions; the resultant predictions of step velocities are compared with kMC. The SSSF-based model equations are then applied for real molecular crystals of Celecoxib, beta-glycine and Piracetam, based on the workflow discussed in Section 1.5. The major site configurations are tabulated at the end of the Appendix for each of the three AB step configurations.

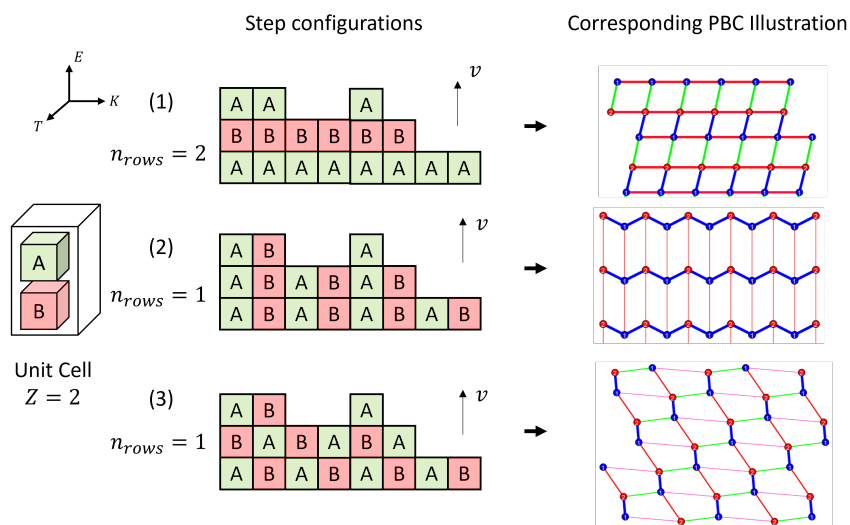


Figure B.1: Step configurations encountered on an organic crystal with two growth units A and B. PBCs are generated using the software ADDICT.[1]

## Step Configuration 2

Step configuration 2 defines a row with alternating columns of A and B. The hierarchical approach similar to the one utilized for step configuration 1 in chapter 3 is outlined below:

1. Identification of predominant junctions: Owing to thermal fluctuations, steps have a considerable concentration of kinks. The rate of step growth depends on the concentration of kink junctions along the step. Generally, the density of kinks reduces exponentially with kink height. For instance, single-height kinks are the

most densely populated kinks along the step, followed by double-height kinks and so on. We truncate the junction space at double-kinks to maintain simplicity of the framework. Step configuration 2 requires individual treatment of east and west-facing kinks since they have different interaction environments which will result in them having unequal kink densities. This is distinct from step configuration 1 in which east and west kinks have identical energetic environments and hence equal kink densities.

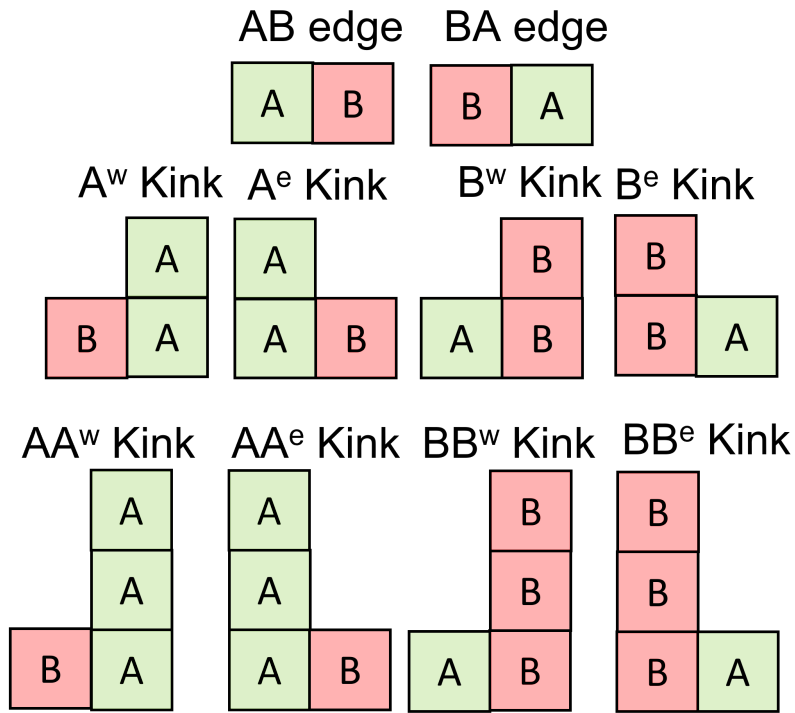


Figure B.2: Predominant junctions along step configuration 2: edge, single and double kinks. The superscripts  $e$  and  $w$  denote east and west facing kinks, respectively.

2. Identification of the major sites and most-likely surface events: Similar to the previous step configuration 1, an order-of-magnitude analysis is conducted to determine the major sites that will be encountered on the step. The sites are then subjected to attachment and detachment events to determine the most-likely events. These are the events which transform major sites into each other. Table B.3 depicts the

16 high probability sites that densely occupy configuration space along the step and their influence on the east-facing A kinks. Similar tables can be constructed for the other kink types.

3. Rate Modeling and Event Rate Modeling: The modified random rain model[2] as described in Eq. 3.1 in Chapter 3 is utilized for modeling elementary attachment and detachment rates. The attachment rate  $j^+$  is isotropic and the detachment rate  $j^-$  depends on the energy of bonds broken. The detachment rates are characterized by growth unit and number of kink neighbors. For step configurations 2 and 3, east and west facing kinks have different energetic environments and are identified as distinct junctions. As a result, the detachment rates from east and west facing kinks are distinct and subscripts  $e$  and  $w$  are added, respectively. The elementary rates of detachment of A growth unit from east and west facing kinks are  $j_{A,1,e}^-$  and  $j_{A,1,w}^-$ , respectively. Similarly, detachment rates for B growth unit from east and west facing kinks are  $j_{B,1,e}^-$  and  $j_{B,1,w}^-$ , respectively.

Event rates are then constructed accounting for elementary attachment/detachment rates and site densities. Partition functions ( $Q_1$  and  $Q_2$ ) which are collections of kink densities, arise out of conditional probabilities to account for the kink correlations. Different partition functions emerge depending on the step configuration and nature of surface correlations. For step configuration 2, analysis of all structurally permissible sets of junctions, for each of the growth units, yield two equivalent partition functions as given in Eq. B.1 and defined by a single notation  $Q$ . Appendix C provides a simpler, generalized approach for obtaining partition functions for a given step configuration.

$$Q = \rho_{BA} + \rho_A^w + \rho_B^e + \rho_{AA}^w + \rho_{BB}^e = \rho_{AB} + \rho_A^e + \rho_B^w + \rho_{AA}^e + \rho_{BB}^w \quad (\text{B.1})$$

where  $\rho_A^e$ ,  $\rho_A^w$ ,  $\rho_B^e$ ,  $\rho_B^w$ ,  $\rho_{AA}^e$ ,  $\rho_{AA}^w$ ,  $\rho_{BB}^e$ ,  $\rho_{BB}^w$ ,  $\rho_{AB}$ ,  $\rho_{BA}$  are the densities of  $A^e$  kink,  $A^w$  kink,  $B^e$  kink,  $B^w$  kink,  $AA^e$  kink,  $AA^w$  kink,  $BB^e$  kink,  $BB^w$  kink,  $AB$  edge and  $BA$  edge, respectively.

The configurational constraint, Eq. B.1, is a result of the spatial characteristics that junctions on LHS of Eq. B.1 are structurally permissible to only adjoin junctions on the RHS of Eq. B.1. Since we have a single partition function, it cancels out in the master equations (see last column in Table B.3). Hence, site densities are modeled as simply the product of kink densities without the factor of  $Q$  in master equations. However  $Q$  must be accounted for in step velocity modeling to account for the site densities. Another equation is the east and west-facing kink equivalence,

$$\rho_A^e + \rho_B^e + \rho_{AA}^e + \rho_{BB}^e - (\rho_A^w + \rho_B^w + \rho_{AA}^w + \rho_{BB}^w) = 0 \quad (\text{B.2})$$

4. Construction of Master Equations: Steady-state master equations are then constructed through accounting the effect of most-likely events on predominant junctions. The master equation for  $A^e$  kink is,

$$\begin{aligned} & (j^+ + j_{B,2}^-) \rho_{BA} \rho_{AB} + (j^+ + j_{B,1,e}^-) \rho_{AB} \rho_B^e - (j^+ + j_{A,0}^-) \rho_A^e \rho_A^w - (j^+ + j_{A,1,e}^-) \rho_{BA} \rho_A^e \\ & + [(j^+ + j_{B,1,e}^-) \rho_{BB}^e \rho_{AB} - (j^+ + j_{A,1,e}^-) \rho_A^e \rho_B^e \\ & + (j^+ + j_{A,1,e}^-) \rho_{AA}^e \rho_{BA} - (j^+ + j_{B,1,e}^-) \rho_A^e \rho_B^e] = 0 \end{aligned} \quad (\text{B.3})$$

where  $j^+$ : attachment rate,  $j_{A,i}^-$ : detachment rate of A from a site with  $i$  lateral neighbors along the kink axis,  $j_{B,i}^-$ : detachment rate of B from a site with  $i$  lateral neighbors. The additional subscript  $e$  and  $w$  is added to distinguish between detachment from east and west facing kinks, respectively. It can be shown that the terms in square brackets get cancelled through the method of substitution.

Similarly, master equations are constructed for  $A^w$  kink,

$$\begin{aligned}
& (j^+ + j_{B,2}^-) \rho_{BA} \rho_{AB} + (j^+ + j_{B,1,w}^-) \rho_{BA} \rho_B^w - (j^+ + j_{A,0}^-) \rho_A^e \rho_A^w - (j^+ + j_{A,1,w}^-) \rho_{AB} \rho_A^w \\
& \quad + [(j^+ + j_{B,1,w}^-) \rho_{BB}^w \rho_{BA} - (j^+ + j_{A,1,w}^-) \rho_A^w \rho_B^w] \\
& \quad + (j^+ + j_{A,1,w}^-) \rho_{AA}^w \rho_{AB} - (j^+ + j_{B,1,w}^-) \rho_A^w \rho_B^w = 0
\end{aligned} \tag{B.4}$$

$B^e$  kink,

$$\begin{aligned}
& (j^+ + j_{A,2}^-) \rho_{BA} \rho_{AB} + (j^+ + j_{A,1,e}^-) \rho_{BA} \rho_A^e - (j^+ + j_{B,0}^-) \rho_B^e \rho_B^w - (j^+ + j_{B,1,e}^-) \rho_{AB} \rho_B^e \\
& \quad + [(j^+ + j_{B,1,e}^-) \rho_{BB}^e \rho_{AB} - (j^+ + j_{A,1,e}^-) \rho_A^e \rho_B^e] \\
& \quad + (j^+ + j_{A,1,e}^-) \rho_{AA}^e \rho_{BA} - (j^+ + j_{B,1,e}^-) \rho_A^e \rho_B^e = 0
\end{aligned} \tag{B.5}$$

$B^w$  kink,

$$\begin{aligned}
& (j^+ + j_{A,2}^-) \rho_{BA} \rho_{AB} + (j^+ + j_{A,1,w}^-) \rho_{AB} \rho_A^w - (j^+ + j_{B,0}^-) \rho_B^e \rho_B^w - (j^+ + j_{B,1,w}^-) \rho_{BA} \rho_B^w \\
& \quad + [(j^+ + j_{B,1,w}^-) \rho_{BB}^w \rho_{BA} - (j^+ + j_{A,1,w}^-) \rho_A^w \rho_B^w] \\
& \quad + (j^+ + j_{A,1,w}^-) \rho_{AA}^w \rho_{AB} - (j^+ + j_{B,1,w}^-) \rho_A^w \rho_B^w = 0
\end{aligned} \tag{B.6}$$

$AA^e$  kink,

$$(j^+ + j_{B,1,e}^-) \rho_A^e \rho_B^e - (j^+ + j_{A,1,e}^-) \rho_{AA}^e \rho_{BA} = 0 \tag{B.7}$$

$AA^w$  kink,

$$(j^+ + j_{B,1,w}^-) \rho_A^w \rho_B^w - (j^+ + j_{A,1,w}^-) \rho_{AA}^w \rho_{AB} = 0 \tag{B.8}$$

$BB^e$  kink,

$$(j^+ + j_{A,1,e}^-) \rho_A^e \rho_B^e - (j^+ + j_{B,1,e}^-) \rho_{BB}^e \rho_{AB} = 0 \tag{B.9}$$

$BB^w$  kink,

$$(j^+ + j_{A,1,w}^-)\rho_A^w\rho_B^w - (j^+ + j_{B,1,w}^-)\rho_{BB}^w\rho_{BA} = 0 \quad (\text{B.10})$$

$AB$  edge,

$$\begin{aligned} & -(j^+ + j_{B,2}^-)\rho_{BA}\rho_{AB} - (j^+ + j_{A,2}^-)\rho_{BA}\rho_{AB} - (j^+ + j_{B,1,e}^-)\rho_{AB}\rho_B^e \\ & -(j^+ + j_{A,1,w}^-)\rho_{AB}\rho_A^w + (j^+ + j_{A,0}^-)\rho_A^e\rho_A^w + (j^+ + j_{B,0}^-)\rho_B^e\rho_B^w \\ & + (j^+ + j_{A,1,e}^-)\rho_{BA}\rho_A^e + (j^+ + j_{B,1,w}^-)\rho_{BA}\rho_B^w + [(j^+ + j_{B,1,w}^-)\rho_A^w\rho_B^w \\ & - (j^+ + j_{A,1,w}^-)\rho_{AA}^w\rho_{AB} + (j^+ + j_{A,1,e}^-)\rho_A^e\rho_B^e - (j^+ + j_{B,1,e}^-)\rho_{BB}^e\rho_{AB}] = 0 \end{aligned} \quad (\text{B.11})$$

$BA$  edge,

$$\begin{aligned} & -(j^+ + j_{B,2}^-)\rho_{BA}\rho_{AB} - (j^+ + j_{A,2}^-)\rho_{BA}\rho_{AB} - (j^+ + j_{A,1,e}^-)\rho_{BA}\rho_A^e \\ & -(j^+ + j_{B,1,w}^-)\rho_{BA}\rho_B^w + (j^+ + j_{A,0}^-)\rho_A^e\rho_A^w + (j^+ + j_{B,0}^-)\rho_B^e\rho_B^w \\ & + (j^+ + j_{B,1,e}^-)\rho_{AB}\rho_B^e + (j^+ + j_{A,1,w}^-)\rho_{AB}\rho_A^w + [(j^+ + j_{B,1,e}^-)\rho_A^e\rho_B^e \\ & - (j^+ + j_{A,1,e}^-)\rho_{AA}^e\rho_{BA} + (j^+ + j_{A,1,w}^-)\rho_A^w\rho_B^w - (j^+ + j_{B,1,w}^-)\rho_{BB}^w\rho_{BA}] = 0 \end{aligned} \quad (\text{B.12})$$

respectively.

5. Solving Master Equations: The above system of master equations are linearly dependent and must be augmented with the configurational constraints. The configurational constraints devised in Eqs. B.1 and B.2 are appended to the system of master equations to be solved simultaneously. The master equations satisfy the stoichiometric condition that the net attachment rates of each of the growth units in the unit cell must be equal to maintain the overall stoichiometry of the unit cell (i.e.,  $J_A = J_B$  is linearly dependent on the master equations). The equations are also appended with the normalization condition, which ensures the summation of kink densities is unity. The corresponding set of 10 equations in 10 unknowns

in Eq. B.13 is linearly independent and is solved simultaneously to obtain NEQ kink densities. The NEQ kink densities subsequently determine the step velocities through the net attachment rates in Eqs. B.14, B.15.

$$\begin{aligned}
& (j^+ + j_{B,2}^-) \rho_{BA} \rho_{AB} + (j^+ + j_{B,1,e}^-) \rho_{AB} \rho_B^e - (j^+ + j_{A,0}^-) \rho_A^e \rho_A^w \\
& \quad - (j^+ + j_{A,1,e}^-) \rho_{BA} \rho_A^e = 0 \\
& (j^+ + j_{B,2}^-) \rho_{BA} \rho_{AB} + (j^+ + j_{B,1,w}^-) \rho_{BA} \rho_B^w - (j^+ + j_{A,0}^-) \rho_A^e \rho_A^w \\
& \quad - (j^+ + j_{A,1,w}^-) \rho_{AB} \rho_A^w = 0 \\
& (j^+ + j_{A,2}^-) \rho_{BA} \rho_{AB} + (j^+ + j_{A,1,e}^-) \rho_{BA} \rho_A^e - (j^+ + j_{B,0}^-) \rho_B^e \rho_B^w \\
& \quad - (j^+ + j_{B,1,e}^-) \rho_{AB} \rho_B^e = 0 \\
& (j^+ + j_{B,1,e}^-) \rho_A^e \rho_B^e - (j^+ + j_{A,1,e}^-) \rho_{AA}^e \rho_{BA} = 0 \\
& (j^+ + j_{B,1,w}^-) \rho_A^w \rho_B^w - (j^+ + j_{A,1,w}^-) \rho_{AA}^w \rho_{AB} = 0 \\
& (j^+ + j_{A,1,e}^-) \rho_A^e \rho_B^e - (j^+ + j_{B,1,e}^-) \rho_{BB}^e \rho_{AB} = 0 \\
& (j^+ + j_{A,1,w}^-) \rho_A^w \rho_B^w - (j^+ + j_{B,1,w}^-) \rho_{BB}^w \rho_{BA} = 0 \\
& \rho_A^e + \rho_B^e + \rho_{AB}^e + \rho_{BA}^e - (\rho_A^w + \rho_B^w + \rho_{AB}^w + \rho_{BA}^w) = 0 \\
& \rho_{BA} + \rho_A^w + \rho_B^e + \rho_{AA}^w + \rho_{BB}^e - (\rho_{AB} + \rho_A^e + \rho_B^w + \rho_{AA}^e + \rho_{BB}^w) = 0 \\
& \rho_{BA} + \rho_{AB} + \rho_A^e + \rho_A^w + \rho_B^e + \rho_B^w + \rho_{AA}^e + \rho_{AA}^w + \rho_{BB}^e + \rho_{BB}^w - 1 = 0
\end{aligned} \tag{B.13}$$

6. Step velocity modeling: The net attachment rates of A and B growth units are

$$\begin{aligned}
J_A = & j^+ \left( \frac{\rho_{BA} \rho_{AB}}{Q} + \frac{\rho_B^e \rho_{AB}}{Q} + \frac{\rho_B^e \rho_B^w}{Q} + \frac{\rho_{BB}^e \rho_{AB}}{Q} + \frac{\rho_A^e \rho_B^e}{Q} \right) \\
& + j^+ \left( \frac{\rho_B^w \rho_{BA}}{Q} + \frac{\rho_{BB}^w \rho_{BA}}{Q} + \frac{\rho_A^w \rho_B^w}{Q} \right) \\
& - (j_{A,2}^- \frac{\rho_{BA} \rho_{AB}}{Q} + j_{A,1,e}^- \frac{\rho_A^e \rho_{BA}}{Q} + j_{A,0}^- \frac{\rho_A^e \rho_A^w}{Q} + j_{A,1,e}^- \frac{\rho_{AA}^e \rho_{BA}}{Q} + j_{A,1,e}^- \frac{\rho_A^e \rho_B^e}{Q}) \\
& - (j_{A,1,w}^- \frac{\rho_A^w \rho_{AB}}{Q} + j_{A,1,w}^- \frac{\rho_{AA}^w \rho_{AB}}{Q} + j_{A,1,w}^- \frac{\rho_A^w \rho_B^w}{Q})
\end{aligned} \tag{B.14}$$

$$\begin{aligned}
J_B = & j^+ \left( \frac{\rho_{AB}\rho_{BA}}{Q} + \frac{\rho_A^e \rho_{BA}}{Q} + \frac{\rho_A^e \rho_A^w}{Q} + \frac{\rho_{AA}^e \rho_{BA}}{Q} + \frac{\rho_A^e \rho_B^e}{Q} \right) \\
& + j^+ \left( \frac{\rho_A^w \rho_{AB}}{Q} + \frac{\rho_{AA}^w \rho_{AB}}{Q} + \frac{\rho_A^w \rho_B^w}{Q} \right) \\
- & (j_{B,2}^- \frac{\rho_{AB}\rho_{BA}}{Q} + j_{B,1,e}^- \frac{\rho_B^e \rho_{AB}}{Q} + j_{B,0}^- \frac{\rho_B^e \rho_B^w}{Q} + j_{B,1,e}^- \frac{\rho_{BB}^e \rho_{AB}}{Q} + j_{B,1,e}^- \frac{\rho_A^e \rho_B^e}{Q}) \\
& - (j_{B,1,w}^- \frac{\rho_B^w \rho_{BA}}{Q} + j_{B,1,w}^- \frac{\rho_{BB}^w \rho_{BA}}{Q} + j_{B,1,w}^- \frac{\rho_A^w \rho_B^w}{Q})
\end{aligned} \tag{B.15}$$

The step velocity is then given by,

$$v = a_P (J_A + J_B) \tag{B.16}$$

where  $a_P$  is the average propagation length.

## Step Configuration 3

Step configuration 3 defines a face pattern with checkered A and B growth units. Within the context of the hieredgehical approach undertaken previously, we analyze configuration 3 in a similar manner as follows,

1. Identification of predominant junctions: The predominant junctions are the ones expected to occur most frequently on the surface configuration landscape. Such junctions exposing minimal broken-energy interactions at the surface are identified as the different types of edge, single kink and double kink. Increasing kink height increases the interactions and reduces their density along the edge drastically. Predominant junctions for step configuration 3 are: AB edge, BA edge, east and west facing A kink, B kink, AB kink and BA kink. Similar to step configuration 2, east and west facing kinks warrant individual treatments since they are characterized by different broken interactions at the junction.



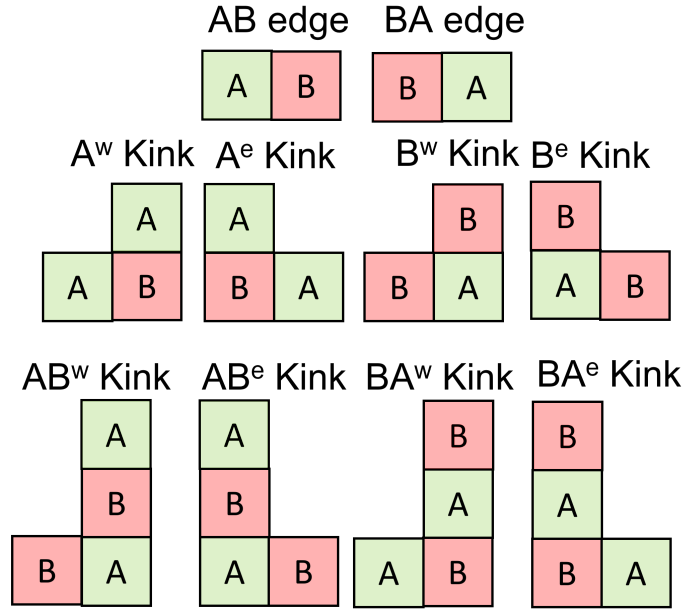


Figure B.3: Predominant junctions along step configuration 3: edge, single and double kinks. The superscript *e* and *w* denote east and west facing kinks, respectively.

2. Identification of most-likely events: Table B.4 lists all the major sites observed along the step, most-likely events, corresponding rates, densities and influence on east-facing A kinks. Each of the sites are subjected to attachment and detachment events to determine the most-likely events that influence the density of east-facing A kinks. Similar tables can be constructed for other kink types.
  
3. Rate Modeling and event rate modeling: Similar to previous configurations, the the rate model in Eq. 3.1 is utilized for attachment and detachment rates. Event rates are then obtained by accounting for the density of major sites observed along the step and the elementary attachment and detachment rates. Owing to the commutative nature of intersection probabilities[3], the following partition functions

are obtained.

$$Q_1 = (\rho_{AB} + \rho_{AB}^e + \rho_{BA}^w) + \rho_A^e + \rho_A^w \quad (\text{B.17})$$

$$= (\rho_{BA} + \rho_{BA}^e + \rho_{AB}^w) + \rho_A^e + \rho_A^w \quad (\text{B.18})$$

$$Q_2 = (\rho_{AB} + \rho_{AB}^e + \rho_{BA}^w) + \rho_B^e + \rho_B^w \quad (\text{B.19})$$

$$= (\rho_{BA} + \rho_{BA}^e + \rho_{AB}^w) + \rho_B^e + \rho_B^w \quad (\text{B.20})$$

This provides us with the configurational constraint,

$$\hat{\rho} = \rho_{AB} + \rho_{AB}^e + \rho_{BA}^w = \rho_{BA} + \rho_{BA}^e + \rho_{AB}^w \quad (\text{B.21})$$

The partition functions for this step configuration become,

$$Q_1 = \hat{\rho} + \rho_A^e + \rho_A^w \quad (\text{B.22})$$

$$Q_2 = \hat{\rho} + \rho_B^e + \rho_B^w \quad (\text{B.23})$$

#### 4. Construction of Master Equations:

The master equation for  $A^e$  kink is,

$$\begin{aligned} (j^+ + j_{B,2}^-) \frac{\rho_{BA}\rho_{AB}}{Q_2} + (j^+ \rho_{BA} + j_{B,1,e}^- \rho_{AB}) \frac{\rho_B^e}{Q_2} - (j^+ + j_{A,0}^-) \frac{\rho_A^e \rho_A^w}{Q_1} - (j^+ \rho_{AB} \\ + j_{A,1,e}^- \rho_{BA}) \frac{\rho_A^e}{Q_1} 2j^+ \frac{\rho_{AB}\rho_{BA}}{Q_2} + 2j_{B,1,e}^- \frac{\rho_{BA}\rho_{AB}}{Q_2} \\ - 2(j^+ + j_{A,1,e}^-) \frac{\rho_A^e \rho_A^e}{Q_1} = 0 \end{aligned} \quad (\text{B.24})$$

where  $j^+$ : attachment rate,  $j_{A,i}^-$ : detachment rate of A from a site with  $i$  lateral

neighbors,  $j_{B,i}^-$ : detachment rate of B from a site with  $i$  lateral neighbors. The additional subscript  $e$  and  $w$  is added to distinguish between detachment from east and west facing kinks, respectively. It can be shown that the terms in square brackets get cancelled through the method of substitution. Similarly, master equations are constructed for  $A^w$  kink,

$$\begin{aligned}
& (j^+ + j_{B,2}^-) \frac{\rho_{BA}\rho_{AB}}{Q_2} + (j^+ \rho_{AB} + j_{B,1,w}^- \rho_{BA}) \frac{\rho_B^w}{Q_2} - (j^+ + j_{A,0}^-) \frac{\rho_A^e \rho_A^w}{Q_1} \\
& - (j^+ \rho_{BA} + j_{A,1,w}^- \rho_{AB}) \frac{\rho_A^w}{Q_1} 2j^+ \frac{\rho_{AB}^w \rho_{AB}}{Q_2} + 2j_{B,1,w}^- \frac{\rho_{BA}^w \rho_{BA}}{Q_2} \\
& - 2(j^+ + j_{A,1,w}^-) \frac{\rho_A^w \rho_A^w}{Q_1} = 0
\end{aligned} \tag{B.25}$$

$B^e$  kink,

$$\begin{aligned}
& (j^+ + j_{A,2}^-) \frac{\rho_{BA}\rho_{AB}}{Q_1} + (j^+ \rho_{AB} + j_{A,1,e}^- \rho_{BA}) \frac{\rho_A^e}{Q_1} - (j^+ + j_{B,0}^-) \frac{\rho_B^e \rho_B^w}{Q_2} \\
& - (j^+ \rho_{BA} + j_{B,1,e}^- \rho_{AB}) \frac{\rho_B^e}{Q_2} 2j^+ \frac{\rho_{BA}^e \rho_{AB}}{Q_1} + 2j_{A,1,e}^- \frac{\rho_{AB}^e \rho_{BA}}{Q_1} \\
& - 2(j^+ + j_{B,1,e}^-) \frac{\rho_B^e \rho_B^e}{Q_2} = 0
\end{aligned} \tag{B.26}$$

$B^w$  kink

$$\begin{aligned}
& (j^+ + j_{A,2}^-) \frac{\rho_{BA}\rho_{AB}}{Q_1} + (j^+ \rho_{BA} + j_{A,1,w}^- \rho_{AB}) \frac{\rho_A^w}{Q_1} - (j^+ + j_{B,0}^-) \frac{\rho_B^e \rho_B^w}{Q_2} \\
& - (j^+ \rho_{AB} + j_{B,1,w}^- \rho_{BA}) \frac{\rho_B^w}{Q_2} 2j^+ \frac{\rho_{BA}^w \rho_{BA}}{Q_1} + 2j_{A,1,w}^- \frac{\rho_{AB}^w \rho_{AB}}{Q_1} \\
& - 2(j^+ + j_{B,1,w}^-) \frac{\rho_B^w \rho_B^w}{Q_2} = 0
\end{aligned} \tag{B.27}$$

$AB^e$  kink,

$$j_{A,1,e}^- \frac{\rho_A^e \rho_A^e}{Q_1} + j^+ \frac{\rho_B^e \rho_B^e}{Q_2} - j^+ \frac{\rho_{AB}^e \rho_{BA}}{Q_2} - j_{A,1,e}^- \frac{\rho_{AB}^e \rho_{BA}}{Q_1} = 0 \tag{B.28}$$

$AB^w$  kink,

$$j_{A,1,w}^- \frac{\rho_A^w \rho_A^w}{Q_1} + j^+ \frac{\rho_B^w \rho_B^w}{Q_2} - j^+ \frac{\rho_{AB}^w \rho_{AB}}{Q_2} - j_{A,1,w}^- \frac{\rho_{AB}^w \rho_{AB}}{Q_1} = 0 \quad (\text{B.29})$$

$BA^e$  kink,

$$j_{B,1,e}^- \frac{\rho_B^e \rho_B^e}{Q_2} + j^+ \frac{\rho_A^e \rho_A^e}{Q_1} - j^+ \frac{\rho_{BA}^e \rho_{AB}}{Q_1} - j_{B,1,e}^- \frac{\rho_{BA}^e \rho_{AB}}{Q_2} = 0 \quad (\text{B.30})$$

$BA^w$  kink,

$$j_{B,1,w}^- \frac{\rho_B^w \rho_B^w}{Q_2} + j^+ \frac{\rho_A^w \rho_A^w}{Q_1} - j^+ \frac{\rho_{BA}^w \rho_{BA}}{Q_1} - j_{B,1,w}^- \frac{\rho_{BA}^w \rho_{BA}}{Q_2} = 0 \quad (\text{B.31})$$

$BA$  edge,

$$\begin{aligned} & -(j^+ + j_{B,2}^-) \frac{\rho_{BA} \rho_{AB}}{Q_2} - (j^+ + j_{A,2}^-) \frac{\rho_{BA} \rho_{AB}}{Q_1} + (j^+ + j_{A,0}^-) \frac{\rho_A^e \rho_A^w}{Q_1} \\ & \quad + (j^+ + j_{B,0}^-) \frac{\rho_B^e \rho_B^w}{Q_2} \\ & + [j_{A,1,e}^- \frac{\rho_A^e \rho_A^e}{Q_1} + j^+ \frac{\rho_B^e \rho_B^e}{Q_2} - j^+ \frac{\rho_{AB}^e \rho_{BA}}{Q_2} - j_{A,1,e}^- \frac{\rho_{AB}^e \rho_{BA}}{Q_1} \\ & + j_{B,1,w}^- \frac{\rho_B^w \rho_B^w}{Q_2} + j^+ \frac{\rho_A^w \rho_A^w}{Q_1} - j^+ \frac{\rho_{BA}^w \rho_{BA}}{Q_1} - j_{B,1,w}^- \frac{\rho_{BA}^w \rho_{BA}}{Q_2}] = 0 \end{aligned} \quad (\text{B.32})$$

$AB$  edge,

$$\begin{aligned} & -(j^+ + j_{A,2}^-) \frac{\rho_{BA} \rho_{AB}}{Q_1} - (j^+ + j_{B,2}^-) \frac{\rho_{BA} \rho_{AB}}{Q_2} + (j^+ + j_{B,0}^-) \frac{\rho_B^e \rho_B^w}{Q_2} \\ & \quad + (j^+ + j_{A,0}^-) \frac{\rho_A^e \rho_A^w}{Q_1} \\ & + [j_{A,1,w}^- \frac{\rho_A^w \rho_A^w}{Q_1} + j^+ \frac{\rho_B^w \rho_B^w}{Q_2} - j^+ \frac{\rho_{AB}^w \rho_{AB}}{Q_2} - j_{A,1,w}^- \frac{\rho_{AB}^w \rho_{AB}}{Q_1} \\ & + j_{B,1,e}^- \frac{\rho_B^e \rho_B^e}{Q_2} + j^+ \frac{\rho_A^e \rho_A^e}{Q_1} - j^+ \frac{\rho_{BA}^e \rho_{AB}}{Q_1} - j_{B,1,e}^- \frac{\rho_{BA}^e \rho_{AB}}{Q_2}] = 0 \end{aligned} \quad (\text{B.33})$$

respectively. Notice that  $Q_1$  and  $Q_2$  are distinct and do not cancel out in these equations.

5. Solving Master Equations: Similar to the previous configurations, the above set of master equations are linearly dependent and need to be supplemented with additional equations for a unique solution. The configurational and normalization conditions provide the necessary number of equations for a linearly independent set of equations. Similar to previous configurations, the master equations are consistent with the stoichiometric constraint and  $J_A = J_B$  is linearly dependent on the

master equations. The resulting 10 equations in 10 unknowns is given below.

$$\begin{aligned}
& (j^+ + j_{B,2}^-) \frac{\rho_{BA}\rho_{AB}}{Q_2} + (j^+ \rho_{BA} + j_{B,1,e}^- \rho_{AB}) \frac{\rho_B^e}{Q_2} - (j^+ + j_{A,0}^-) \frac{\rho_A^e \rho_A^w}{Q_1} \\
& \quad - (j^+ \rho_{AB} + j_{A,1,e}^- \rho_{BA}) \frac{\rho_A^e}{Q_1} \\
& \quad + 2j^+ \frac{\rho_{AB}^e \rho_{BA}}{Q_2} + 2j_{B,1,e}^- \frac{\rho_{BA}^e \rho_{AB}}{Q_2} - 2(j^+ + j_{A,1,e}^-) \frac{\rho_A^e \rho_A^e}{Q_1} = 0 \\
& (j^+ + j_{A,2}^-) \frac{\rho_{BA}\rho_{AB}}{Q_1} + (j^+ \rho_{BA} + j_{A,1,w}^- \rho_{AB}) \frac{\rho_A^w}{Q_1} - (j^+ + j_{B,0}^-) \frac{\rho_B^e \rho_B^w}{Q_2} \\
& \quad - (j^+ \rho_{AB} + j_{B,1,w}^- \rho_{BA}) \frac{\rho_B^w}{Q_2} \\
& \quad + 2j^+ \frac{\rho_{BA}^w \rho_{BA}}{Q_1} + 2j_{A,1,w}^- \frac{\rho_{AB}^w \rho_{AB}}{Q_1} - 2(j^+ + j_{B,1,w}^-) \frac{\rho_B^w \rho_B^w}{Q_2} = 0 \\
& \quad j_{A,1,e}^- \frac{\rho_A^e \rho_A^e}{Q_1} + j^+ \frac{\rho_B^e \rho_B^e}{Q_2} - j^+ \frac{\rho_{AB}^e \rho_{BA}}{Q_2} - j_{A,1,e}^- \frac{\rho_{AB}^e \rho_{BA}}{Q_1} = 0 \\
& \quad j_{A,1,w}^- \frac{\rho_A^w \rho_A^w}{Q_1} + j^+ \frac{\rho_B^w \rho_B^w}{Q_2} - j^+ \frac{\rho_{AB}^w \rho_{AB}}{Q_2} - j_{A,1,w}^- \frac{\rho_{AB}^w \rho_{AB}}{Q_1} = 0 \\
& \quad j_{B,1,e}^- \frac{\rho_B^e \rho_B^e}{Q_2} + j^+ \frac{\rho_A^e \rho_A^e}{Q_1} - j^+ \frac{\rho_{BA}^e \rho_{AB}}{Q_1} - j_{B,1,e}^- \frac{\rho_{BA}^e \rho_{AB}}{Q_2} = 0 \\
& \quad j_{B,1,w}^- \frac{\rho_B^w \rho_B^w}{Q_2} + j^+ \frac{\rho_A^w \rho_A^w}{Q_1} - j^+ \frac{\rho_{BA}^w \rho_{BA}}{Q_1} \\
& \quad \quad - j_{B,1,w}^- \frac{\rho_{BA}^w \rho_{BA}}{Q_2} = 0 \\
& (j^+ + j_{B,2}^-) \frac{\rho_{BA}\rho_{AB}}{Q_2} + (j^+ + j_{A,2}^-) \frac{\rho_{BA}\rho_{AB}}{Q_1} - (j^+ + j_{A,0}^-) \frac{\rho_A^e \rho_A^w}{Q_1} \\
& \quad - (j^+ + j_{B,0}^-) \frac{\rho_B^e \rho_B^w}{Q_2} = 0 \\
& \quad \rho_A^e + \rho_B^e + \rho_{AB}^e + \rho_{BA}^e - (\rho_A^w + \rho_B^w + \rho_{AB}^w + \rho_{BA}^w) = 0 \\
& \quad \rho_{AB} + \rho_{AB}^e + \rho_{BA}^w - (\rho_{BA} + \rho_{BA}^e + \rho_{AB}^w) = 0 \\
& \rho_{BA} + \rho_{AB} + \rho_A^e + \rho_A^w + \rho_B^e + \rho_B^w + \rho_{AB}^e + \rho_{AB}^w + \rho_{BA}^e + \rho_{BA}^w - 1 = 0
\end{aligned} \tag{B.34}$$

6. Step velocity modeling: The net attachment rates of A and B growth units are,

$$\begin{aligned}
J_A = & j^+ \left( \frac{\rho_{AB}\rho_{BA}}{Q_2} + \frac{\rho_B^e\rho_{BA}}{Q_2} + \frac{\rho_B^e\rho_B^w}{Q_2} + \frac{\rho_{AB}^e\rho_{BA}}{Q_2} + \frac{\rho_B^e\rho_B^e}{Q_2} \right) \\
& + j^+ \left( \frac{\rho_B^w\rho_{AB}}{Q_2} + \frac{\rho_{AB}^w\rho_{AB}}{Q_2} + \frac{\rho_B^w\rho_B^w}{Q_2} \right) \\
- & \left( j_{A,2}^- \frac{\rho_{BA}\rho_{AB}}{Q_1} + j_{A,1,e}^- \frac{\rho_A^e\rho_{BA}}{Q_1} + j_{A,0}^- \frac{\rho_A^e\rho_A^w}{Q_1} + j_{A,1,e}^- \frac{\rho_{BA}\rho_{AB}^e}{Q_1} + j_{A,1,e}^- \frac{\rho_A^e\rho_A^e}{Q_1} \right) \\
& - \left( j_{A,1,w}^- \frac{\rho_A^w\rho_{AB}}{Q_1} + j_{A,1,w}^- \frac{\rho_{AB}\rho_{AB}^w}{Q_1} + j_{A,1,w}^- \frac{\rho_A^w\rho_A^w}{Q_1} \right)
\end{aligned} \tag{B.35}$$

$$\begin{aligned}
J_B = & j^+ \left( \frac{\rho_{BA}\rho_{AB}}{Q_1} + \frac{\rho_A^e\rho_{AB}}{Q_1} + \frac{\rho_A^e\rho_A^w}{Q_1} + \frac{\rho_{BA}^e\rho_{AB}}{Q_1} + \frac{\rho_A^e\rho_A^e}{Q_1} \right) \\
& + j^+ \left( \frac{\rho_A^w\rho_{BA}}{Q_1} + \frac{\rho_{BA}^w\rho_{BA}}{Q_1} + \frac{\rho_A^w\rho_A^w}{Q_1} \right) \\
- & \left( j_{B,2}^- \frac{\rho_{AB}\rho_{BA}}{Q_2} + j_{B,1,e}^- \frac{\rho_B^e\rho_{AB}}{Q_2} + j_{B,0}^- \frac{\rho_B^e\rho_B^w}{Q_2} + j_{B,1,e}^- \frac{\rho_{AB}\rho_{BA}^e}{Q_2} + j_{B,1,e}^- \frac{\rho_B^e\rho_B^e}{Q_2} \right) \\
& - \left( j_{B,1,w}^- \frac{\rho_B^w\rho_{BA}}{Q_2} + j_{B,1,w}^- \frac{\rho_{BA}\rho_{BA}^w}{Q_2} + j_{B,1,w}^- \frac{\rho_B^w\rho_B^w}{Q_2} \right)
\end{aligned} \tag{B.36}$$

The set of master equations automatically satisfy the stoichiometric constraint  $J_A = J_B$ . This can be shown by simple rearrangement of Eqns. B.34. The step velocity is then given by,

$$v = a_P(J_A + J_B) \tag{B.37}$$

where  $a_P$  is the average propagation length.

## Results

In Fig. B.4, we apply our SSSF model to a non-Kossel crystal graph[5, 6] based on naphthalene crystal structure[7]. The step configurations in Fig. B.1 correspond to specific steps on facets of the crystal graph such that step configuration 1 corresponds to step  $[01\bar{1}]$  on face (011), step configuration 2 corresponds to step  $[100]$  on face (001) of the crystal graph and step configuration 3 corresponds to step  $[011]$  on face (100) of

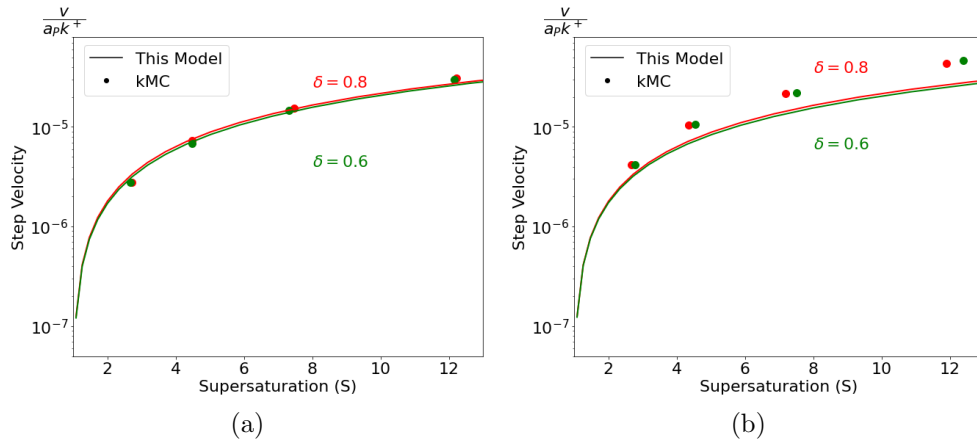


Figure B.4: Normalized step velocity vs supersaturation  $S$  for (a)  $[100]$  step on non-Kossel (001) face (step configuration 2), (b)  $[011]$  step on non-Kossel (100) face (step configuration 3) of a naphthalene crystal graph. The step velocity is normalized by  $a \frac{k_B T}{h} \equiv a \rho k^+$ , where  $a$  is the step propagation length and  $h$  is the Planck's constant. The solid lines are generated by our model, dots depict kMC data taken from literature[4]. The two colors correspond to the two different values of  $\delta$ . (Refer Cuppen et al.[4])

the crystal graph. For both step configurations shown in Fig. B.4, step velocity displays nonlinear increase with supersaturation owing to increase in the number of kink sites for attachment as well as increase in the frequency of attachment. Similar to step velocity behavior observed previously in Fig. 3.9, step velocity reduces with increase in interaction anisotropy due to kink cycle formation resulting in association of kinks. However, the dependence of step velocity on  $\delta$  is much less pronounced for step configurations 2 and 3. The deviation of model predictions from kMC for step configuration 3 may be due to increase in the contributions of events out of the most-likely space at higher supersaturations.

## OWIVEY Case study: Intermediate calculations

Table B.1 reports values of intermediate variables for morphology predictions reported in Chapter 3 of OWIVEY-ethanol system at  $S = 1.5$  and temperature of 273 K. CLP



forcefield[8] was employed for solid-state calculations to obtain PBC directions and their bond strengths. The model-based morphology prediction for OWIVEY constitutes the *flat F* faces (0 $\bar{1}$ 1), (0 $\bar{1}$ 0) and ( $\bar{1}$  $\bar{1}$ 1). Fig. B.5 provides network of interactions across the crystal *F* faces of OWIVEY. Fig. B.6 provides shape of the spirals for the crystal *F* faces of OWIVEY. The van-Oss-Chaudhary-Good solvent model[9, 10] was employed to obtain solvent-modified bond energies. A rate constant of  $k^+ = 10^5/s$  was used for step velocity calculations. The rate constant cancels out during estimation of relative growth rates and hence does not affect the morphology predictions.

Table B.1: OWIVEY - ethanol system calculation results for intermediate variables including:  $\phi_{PBC}$  - average strength of periodic bond chain in kcal/mol,  $a_P$  - average propagation length in  $\text{\AA}$ ,  $a_E$  - average growth unit width along the step in  $\text{\AA}$ ,  $l_c$  - critical length of the step in  $\text{\AA}$ ,  $v$  - step velocity in  $\text{\AA}/s$ , conf - step configuration type from Fig. 3.1,  $d_{hkl}$  - interplanar spacing of the face in  $\text{\AA}$ ,  $G$  - growth rate of the face and  $R$  - relative growth rate of the face.

| Face                     | Step                        | kcal/mol<br>$\phi_{PBC}$ | $\text{\AA}$<br>$a_P$ | $\text{\AA}$<br>$a_E$ | $\text{\AA}$<br>$l_c$ | $\text{\AA}/s$<br>$v$ | conf | $\text{\AA}$<br>$d_{hkl}$ | $G$                   | $R$  |
|--------------------------|-----------------------------|--------------------------|-----------------------|-----------------------|-----------------------|-----------------------|------|---------------------------|-----------------------|------|
| (0 $\bar{1}$ 1)          | [100]                       | 3.68                     | 5.407                 | 6.604                 | 5.958                 | $3.50 \times 10^{-3}$ | 1    | 8.173                     | $3.62 \times 10^{-6}$ | 1    |
|                          | [ $\bar{1}\bar{1}\bar{1}$ ] | 5.805                    | 5.097                 | 7.006                 | 72.074                | $2.97 \times 10^{-3}$ | 3    |                           |                       |      |
|                          | [0 $\bar{1}\bar{1}$ ]       | 1.79                     | 3.229                 | 11.057                | 40.315                | $1.85 \times 10^{-3}$ | 1    |                           |                       |      |
|                          | [ $\bar{1}\bar{1}1$ ]       | 5.805                    | 5.097                 | 7.006                 | 72.074                | $4.19 \times 10^{-4}$ | 3    |                           |                       |      |
|                          | [011]                       | 1.79                     | 3.229                 | 11.057                | 40.315                | $8.76 \times 10^{-6}$ | 1    |                           |                       |      |
|                          | [111]                       | 5.84                     | 6.137                 | 5.818                 | 29.827                | $2.10 \times 10^{-4}$ | 2    |                           |                       |      |
| (0 $\bar{1}$ 0)          | [ $\bar{1}$ 00]             | 3.68                     | 5.039                 | 6.604                 | 5.965                 | $5.40 \times 10^{-5}$ | 1    | 8.769                     | $1.26 \times 10^{-5}$ | 3.49 |
|                          | [ $\bar{1}$ 01]             | 6.41                     | 5.415                 | 6.146                 | 34.81                 | $3.37 \times 10^{-3}$ | 3    |                           |                       |      |
|                          | [001]                       | 1.63                     | 3.299                 | 10.089                | 21.263                | $2.39 \times 10^{-3}$ | 1    |                           |                       |      |
|                          | [101]                       | 8.535                    | 5.632                 | 5.909                 | 45.643                | $3.39 \times 10^{-3}$ | 3    |                           |                       |      |
|                          | [100]                       | 3.68                     | 5.039                 | 6.604                 | 5.958                 | $1.56 \times 10^{-3}$ | 1    |                           |                       |      |
|                          | [10 $\bar{1}$ ]             | 6.41                     | 5.415                 | 6.146                 | 34.81                 | $3.04 \times 10^{-3}$ | 3    |                           |                       |      |
|                          | [00 $\bar{1}$ ]             | 1.63                     | 3.299                 | 10.089                | 21.266                | $2.02 \times 10^{-4}$ | 1    |                           |                       |      |
|                          | [ $\bar{1}$ 0 $\bar{1}$ ]   | 8.535                    | 5.632                 | 5.909                 | 45.643                | $2.14 \times 10^{-3}$ | 3    |                           |                       |      |
| ( $\bar{1}$ $\bar{1}$ 1) | [011]                       | 1.79                     | 5.467                 | 11.057                | 40.315                | $2.49 \times 10^{-3}$ | 1    | 4.827                     | $2.44 \times 10^{-5}$ | 6.74 |
|                          | [101]                       | 8.535                    | 10.231                | 5.909                 | 45.643                | $6.24 \times 10^{-3}$ | 3    |                           |                       |      |
|                          | [ $\bar{1}\bar{2}\bar{1}$ ] | 2.375                    | 5.828                 | 10.374                | 30.535                | $1.28 \times 10^{-3}$ | 3    |                           |                       |      |
|                          | [0 $\bar{1}\bar{1}$ ]       | 1.79                     | 5.467                 | 11.057                | 40.315                | $2.58 \times 10^{-4}$ | 1    |                           |                       |      |
|                          | [ $\bar{1}$ 0 $\bar{1}$ ]   | 8.535                    | 10.231                | 5.909                 | 45.643                | $5.94 \times 10^{-3}$ | 3    |                           |                       |      |
|                          | [ $\bar{1}$ 21]             | 2.375                    | 5.828                 | 10.374                | 30.535                | $2.91 \times 10^{-3}$ | 3    |                           |                       |      |

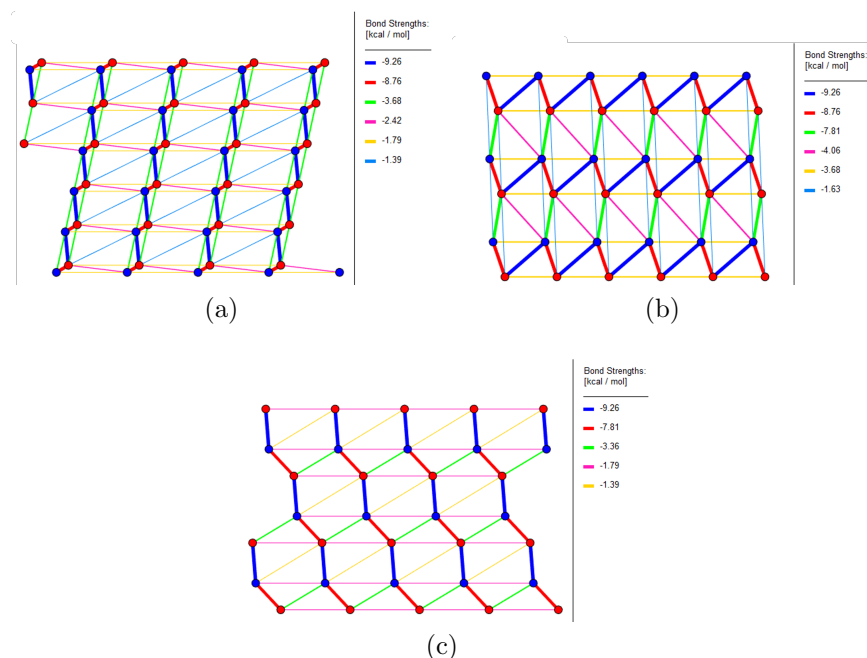


Figure B.5: Periodic bond chain networks across the following *flat F* faces of OWIVEY (A)  $(0\bar{1}1)$ , (B)  $(0\bar{1}0)$ , and (C)  $(\bar{1}\bar{1}1)$ . PBCs are generated using the software ADDICT.[1]

## Morphology Predictions

### B.0.1 Celecoxib in Toluene

Celecoxib is an API molecule which grows in the P-1 space group and has the CSD ref code DIBBUL. The unit cell parameters are  $a = 10.136$ ,  $b = 16.778$ ,  $c = 5.066$ ,  $\alpha = 97.62^\circ$ ,  $\beta = 100.65^\circ$ ,  $\gamma = 95.95^\circ$ . We utilized the CLP forcefield[8] to model the solid-state interactions between the growth units and the vOCG[9, 10] solvent model to calculate the solvent-modified bond energies. We then applied the SSSF model as discussed in Section 1.5 to estimate kink densities and step velocities of the steps of crystal facets, to obtain the morphology prediction depicted in Fig. B.7a. The predicted morphology demonstrates a rectangular plate-like behaviour and is in good agreement with the experimentally observed crystal shape of Celecoxib depicted in Fig. B.7b.[11]

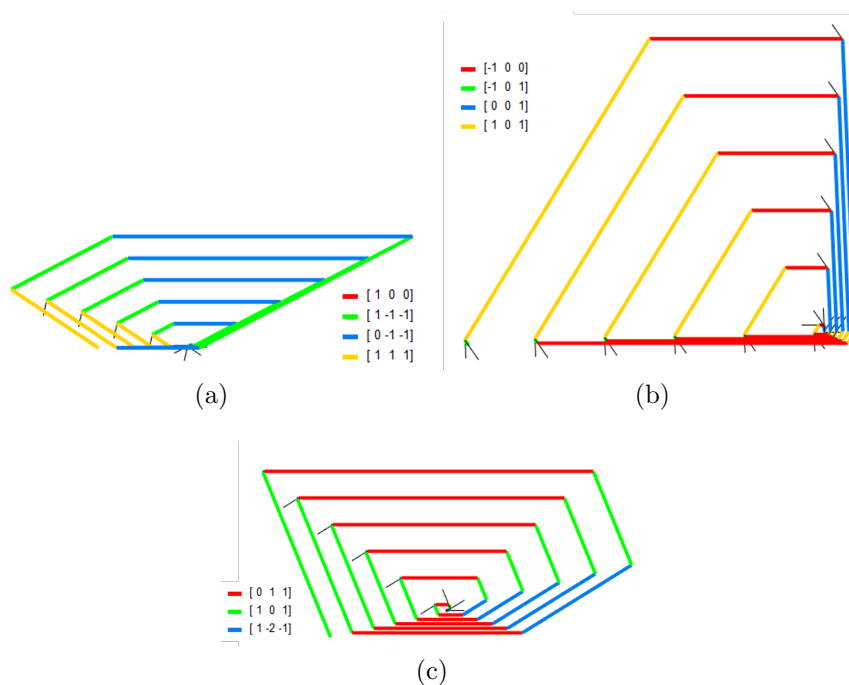


Figure B.6: Spiral shapes for the following  $F$  faces of OWIVEY (A)  $(0\bar{1}1)$ , (B)  $(0\bar{1}0)$ , and (C)  $(\bar{1}\bar{1}1)$ . Spiral shapes are generated using the software ADDICT.[1]

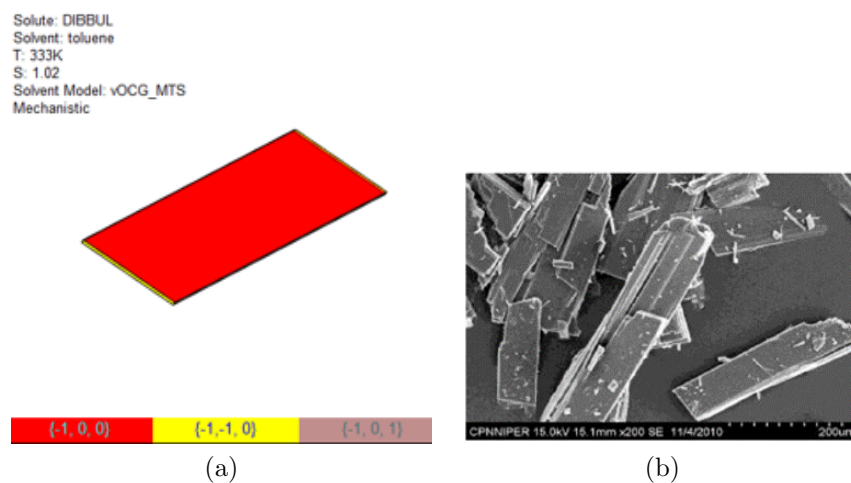


Figure B.7: a) SSSF model-based morphology prediction of Celecoxib grown in toluene at 333 K and  $S = 1.02$  b) SEM photographs of celecoxib recrystallized from toluene at 60°C. Figure reproduced with permission from Modi et al.[11]. Copyright 2013 American Chemical Society.

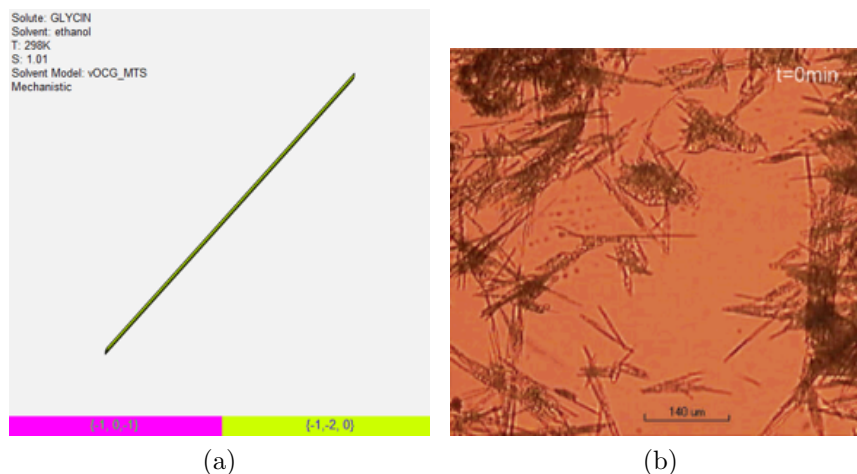


Figure B.8: a) SSSF model-based morphology prediction of  $\beta$ -glycine grown in ethanol at 298K and  $S = 1.01$ , b) Snapshot of  $\beta$ -glycine grown in (v/v) water-ethanol solvent mixture. Figure reproduced with permission from Ferrari et al.[12]. Copyright 2003 American Chemical Society.

### B.0.2 $\beta$ -glycine in Ethanol

The  $\beta$  polymorph of glycine grows in the P21 space group and has the CSD ref code GLYCIN. The unit cell parameters are  $a = 5.077$ ,  $b = 6.268$ ,  $c = 5.380$ ,  $\alpha = 90^\circ$ ,  $\beta = 113.20^\circ$ ,  $\gamma = 90^\circ$ . Similar to previous examples, we used the CLP forcefield[8] and vOCG[9, 10] solvent model to calculate solid-state interactions and subsequently the solvent-modified bond energies, respectively. We then applied the SSSF model as discussed in Section 1.5 to estimate kink densities and step velocities for each of the steps of crystal facets, to obtain the in-silico morphology prediction depicted in Fig. B.8a. The SSSF-model predicts needle-like behaviour and is in excellent agreement with the experimentally observed crystal shape of  $\beta$ -glycine as depicted in Fig. B.8b.[12]

### B.0.3 Piracetam in Isopropanol

Piracetam is an API molecule which grows in the P-1 space group and has the CSD ref code BISMEV. The unit cell parameters are  $a = 6.403$ ,  $b = 6.618$ ,  $c = 8.556$ ,  $\alpha = 79.85^\circ$ ,

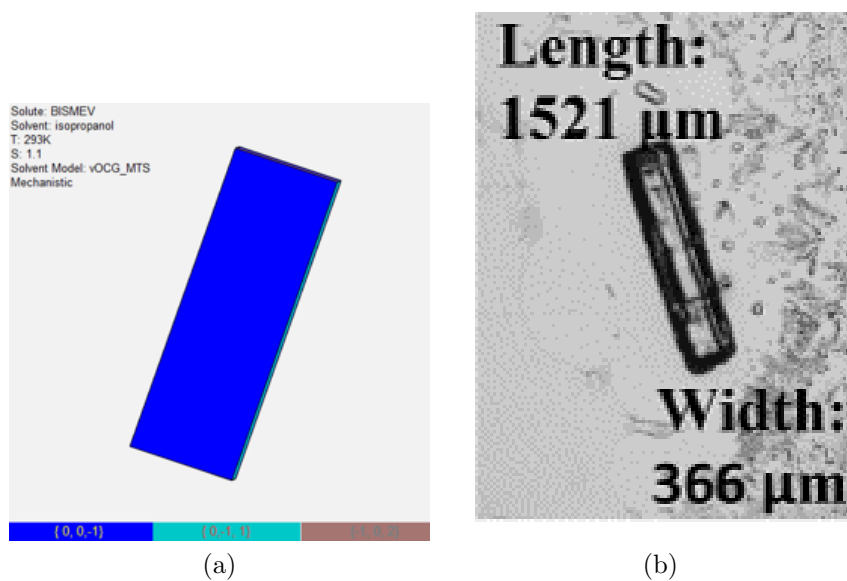
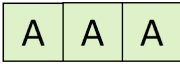
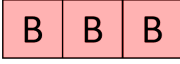
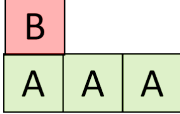
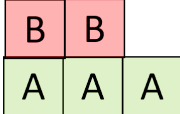
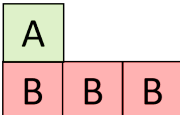


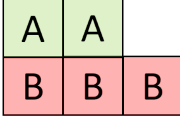
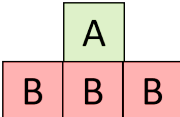
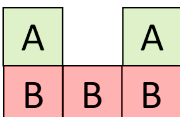
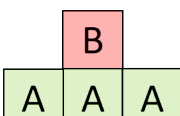
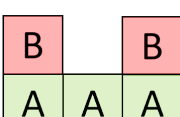
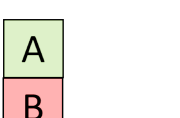

Figure B.9: a)SSSF model-based morphology prediction of Piracetam grown in isopropanol at 293 K and  $S = 1.1$ , b) Micrograph of Piracetam polymorph II crystals grown in isopropanol. Figure reproduced with permission from Lynch et al.[13]. Copyright 2021 American Chemical Society.

$\beta = 102.39^\circ$ ,  $\gamma = 91.09^\circ$ . We then applied the SSSF model as discussed in Section 1.5, employing the CLP forcefield[8] and the vOCG[9, 10] solvent model to calculate the nonequilibrium kink densities and step velocities of all the steps of crystal facets. The predicted morphology as depicted in Fig. B.9a demonstrates a rectangular plate-like behaviour and is in good agreement with the experimentally observed crystal shape of Piracetam as depicted in Fig. B.9b.[13]

## Configuration Tables: Major Sites for the three step configurations

Table B.2: Configuration table of major sites for step configuration 1 and their influence on A kinks. The *Attachment* column denotes the change in the number of A kinks upon incorporation of relevant growth unit at the site of interest. The *Detachment* column denotes the change in the number of A kinks upon detachment of growth unit from the site of interest. Events marked ‘-’ convert the site into another out of the most-likely space and hence are not considered. The *attachment* and *detachment rate* columns provide the rate of respective elementary reactions along the step surface. The attachment rate is isotropic for all sites while detachment rate depends upon the growth unit detached and the number of neighboring kink bonds broken. The *site density* depends on the density of adjoining junctions and the appropriate partition function to account for the surface correlations. The sites are representative of their corresponding mirror images, since the east and west facing kinks have equivalent interaction networks. Similar tables can be constructed for all the predominant edge and kink types.

|   | Site  | Attachment | Detachment | Attachment rate | Detachment rate | Density of site                |
|---|---|------------|------------|-----------------|-----------------|--------------------------------|
| 1 |  | 0          | +2         | $j^+$           | $j_{A,2}^-$     | $\frac{\rho_{A0}^2}{Q_1}$      |
| 2 |  | +2         | 0          | $j^+$           | $j_{B,2}^-$     | $\frac{\rho_{B0}}{Q_2}$        |
| 3 |  | 0          | -          | $j^+$           | $j_{A,2}^-$     | $\frac{\rho_B \rho_{A0}}{Q_1}$ |
| 4 |  | -          | 0          | $j^+$           | $j_{B,1}^-$     | $\frac{\rho_B \rho_{B0}}{Q_2}$ |
| 5 |  | 0          | -          | $j^+$           | $j_{B,2}^-$     | $\frac{\rho_A \rho_{B0}}{Q_2}$ |

|    |   |    |    |       |             |                                   |
|----|---|----|----|-------|-------------|-----------------------------------|
| 6  |    | -  | 0  | $j^+$ | $j_{A,1}^-$ | $\frac{\rho_A \rho_{A0}}{Q_1}$    |
| 7  |    | -  | -2 | $j^+$ | $j_{A,0}^-$ | $\frac{\rho_A^2}{4Q_1}$           |
| 8  |    | -2 | -  | $j^+$ | $j_{B,2}^-$ | $\frac{\rho_A^2}{4Q_2}$           |
| 9  |   | -  | 0  | $j^+$ | $j_{B,0}^-$ | $\frac{\rho_B^2}{4Q_2}$           |
| 10 |  | 0  | -  | $j^+$ | $j_{A,2}^-$ | $\frac{\rho_B^2}{4Q_1}$           |
| 11 |  | +1 | -  | $j^+$ | $j_{A,2}^-$ | $\frac{\rho_{AB} \rho_{A0}}{Q_1}$ |
| 12 |  | -1 | -1 | $j^+$ | $j_{B,1}^-$ | $\frac{\rho_A \rho_B}{2Q_2}$      |

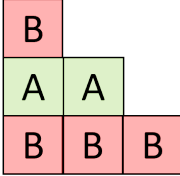
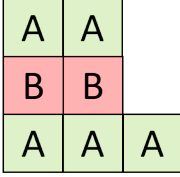
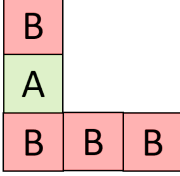
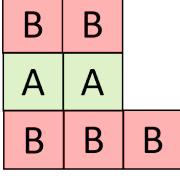
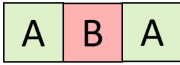
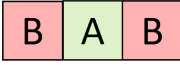
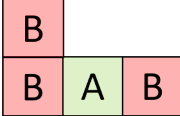
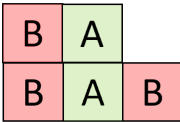
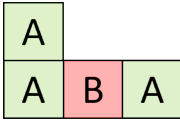
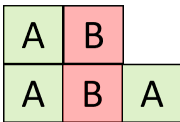
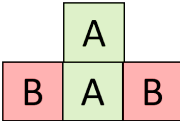
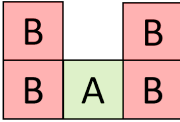
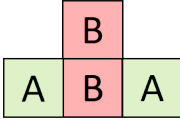
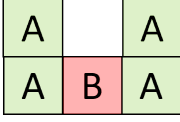
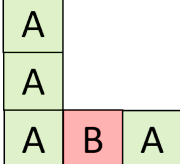
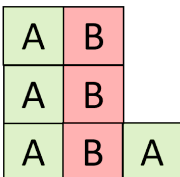
|    |   |    |    |       |             |                                   |
|----|---|----|----|-------|-------------|-----------------------------------|
| 13 |    | -1 | -1 | $j^+$ | $j_{A,1}^-$ | $\frac{\rho_B \rho_A}{2Q_1}$      |
| 14 |    | -  | +1 | $j^+$ | $j_{A,1}^-$ | $\frac{\rho_{A0} \rho_{AB}}{Q_1}$ |
| 15 |   | +1 | -  | $j^+$ | $j_{B,2}^-$ | $\frac{\rho_{BA} \rho_{B0}}{Q_2}$ |
| 16 |  | -  | +1 | $j^+$ | $j_{B,1}^-$ | $\frac{\rho_{BA} \rho_{B0}}{Q_2}$ |



Table B.3: Configuration table of major sites for step configuration 2 and their influence on east-facing A kinks. The *Attachment* column denotes the change in the number of east A kinks upon incorporation of relevant growth unit at the site of interest. The *Detachment* column denotes the change in the number of east A kinks upon detachment of growth unit from the site of interest. Events marked ‘-’ convert the site into another out of the most-likely space and hence are not considered. The *attachment* and *detachment rate* columns provide the rate of respective elementary reactions along the step surface. The attachment rate is isotropic for all sites while detachment rate depends upon the growth unit detached and the number of neighboring bonds broken. The *site density* depends on the density of adjoining junctions and the partition function to account for the surface correlations. Sites 3-6 and 11-16 will have corresponding west-facing counterparts, which are left out of the table because of their lack of impact on east-facing A kinks. Construction of master equations for west-facing kinks will require the consideration of corresponding west-facing sites. Similar tables can be constructed for all the predominant edge and kink types.

|   | Site  | Attachment | Detachment | Attachment rate | Detachment rate | Density of site                |
|---|---|------------|------------|-----------------|-----------------|--------------------------------|
| 1 |    | 0          | +1         | $j^+$           | $j_{B,2}^-$     | $\frac{\rho_{AB}\rho_{BA}}{Q}$ |
| 2 |  | +1         | 0          | $j^+$           | $j_{A,2}^-$     | $\frac{\rho_{BA}\rho_{AB}}{Q}$ |
| 3 |  | +1         | -          | $j^+$           | $j_{A,2}^-$     | $\frac{\rho_B^e \rho_{AB}}{Q}$ |
| 4 |  | -          | -1         | $j^+$           | $j_{A,1,e}^-$   | $\frac{\rho_A^e \rho_{BA}}{Q}$ |
| 5 |  | -1         | -          | $j^+$           | $j_{B,2}^-$     | $\frac{\rho_A^e \rho_{BA}}{Q}$ |

|    |   |    |    |       |               |                                   |
|----|---|----|----|-------|---------------|-----------------------------------|
| 6  |    | -  | +1 | $j^+$ | $j_{B,1,e}^-$ | $\frac{\rho_B^e \rho_{AB}}{Q}$    |
| 7  |    | -  | -1 | $j^+$ | $j_{A,0}^-$   | $\frac{\rho_A^e \rho_A^w}{Q}$     |
| 8  |    | 0  | -  | $j^+$ | $j_{A,2}^-$   | $\frac{\rho_B^e \rho_B^w}{Q}$     |
| 9  |   | -  | 0  | $j^+$ | $j_{B,0}^-$   | $\frac{\rho_B^e \rho_B^w}{Q}$     |
| 10 |  | -1 | -  | $j^+$ | $j_{B,2}^-$   | $\frac{\rho_A^e \rho_A^w}{Q}$     |
| 11 |  | +1 | -  | $j^+$ | $j_{B,2}^-$   | $\frac{\rho_{AA}^e \rho_{BA}}{Q}$ |
| 12 |  | -  | +1 | $j^+$ | $j_{B,1,e}^-$ | $\frac{\rho_{BB}^e \rho_{AB}}{Q}$ |

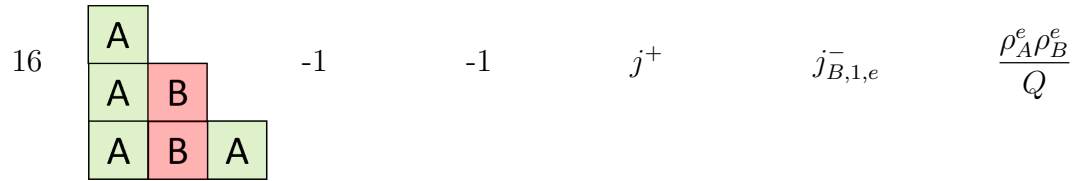
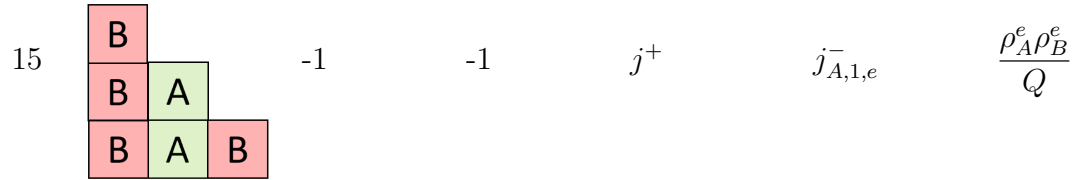
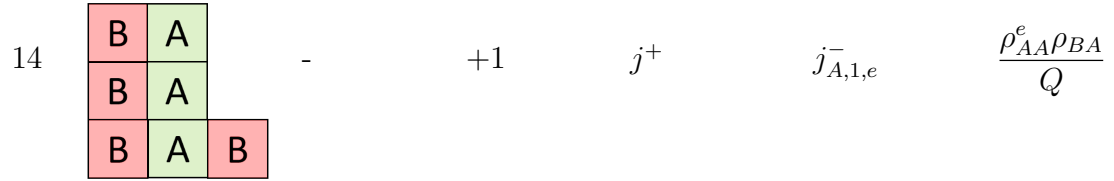
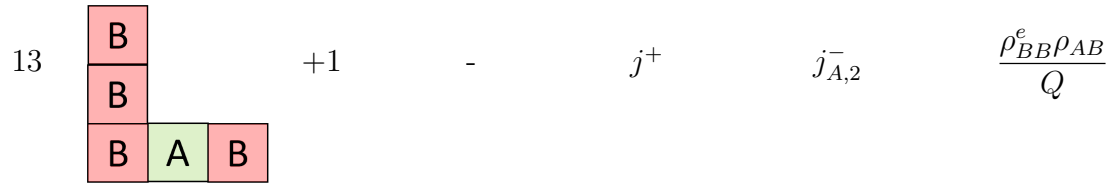
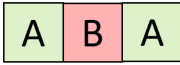
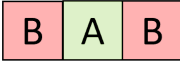
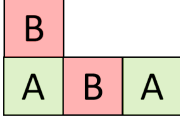
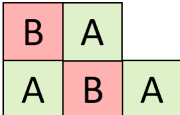
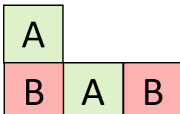
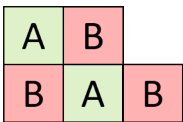
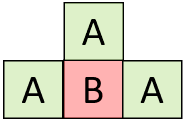
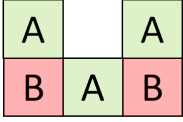
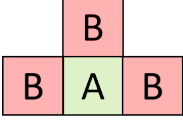
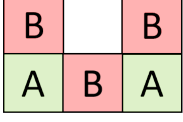
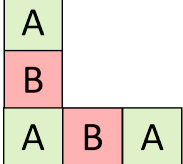
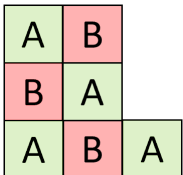
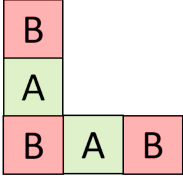
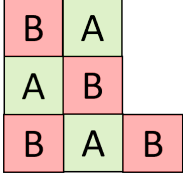
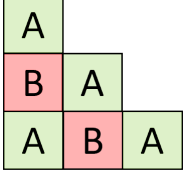
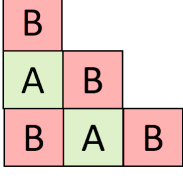


Table B.4: Configuration table of major sites for step configuration 3 and their influence on east-facing A kinks. The *Attachment* column denotes the change in the number of A kinks upon incorporation of relevant growth unit at the site of interest. The *Detachment* column denotes the change in the number of A kinks upon detachment of growth unit from the site of interest. Events marked ‘-’ convert the site into another out of the most-likely space and hence are not considered. The *attachment* and *detachment rate* columns provide the rate of respective elementary reactions along the step surface. The attachment rate is isotropic for all sites while detachment rate depends upon the growth unit detached and the number of neighboring bonds broken. The *site density* depends on the density of adjoining junctions and the appropriate partition function to account for the surface correlations. Sites 3-6 and 11-16 will have corresponding west-facing counterparts, which are left out of the table because of their lack of impact on east-facing A kinks. Construction of master equations for west-facing kinks will require the consideration of corresponding west-facing sites. Similar tables can be constructed for all the predominant edge and kink types.

|   | Site  | Attachment | Detachment | Attachment rate | Detachment rate | Density of site                  |
|---|---|------------|------------|-----------------|-----------------|----------------------------------|
| 1 |    | +1         | +1         | $j^+$           | $j_{B,2}^-$     | $\frac{\rho_{AB}\rho_{BA}}{Q_2}$ |
| 2 |  | 0          | 0          | $j^+$           | $j_{A,2}^-$     | $\frac{\rho_{BA}\rho_{AB}}{Q_1}$ |
| 3 |  | +1         | -          | $j^+$           | $j_{B,2}^-$     | $\frac{\rho_B^e \rho_{BA}}{Q_2}$ |
| 4 |  | -          | -1         | $j^+$           | $j_{A,1,e}^-$   | $\frac{\rho_A^e \rho_{BA}}{Q_1}$ |
| 5 |  | -1         | -          | $j^+$           | $j_{A,2}^-$     | $\frac{\rho_A^e \rho_{AB}}{Q_1}$ |

|    |   |    |    |       |               |                                     |
|----|---|----|----|-------|---------------|-------------------------------------|
| 6  |    | -  | +1 | $j^+$ | $j_{B,1,e}^-$ | $\frac{\rho_B^e \rho_{AB}}{Q_2}$    |
| 7  |    | -  | -1 | $j^+$ | $j_{A,0}^-$   | $\frac{\rho_A^e \rho_A^w}{Q_1}$     |
| 8  |    | -1 | -  | $j^+$ | $j_{A,2}^-$   | $\frac{\rho_A^e \rho_A^w}{Q_1}$     |
| 9  |   | -  | 0  | $j^+$ | $j_{B,0}^-$   | $\frac{\rho_B^e \rho_B^w}{Q_2}$     |
| 10 |  | 0  | -  | $j^+$ | $j_{B,2}^-$   | $\frac{\rho_B^e \rho_B^w}{Q_2}$     |
| 11 |  | +2 | -  | $j^+$ | $j_{B,2}^-$   | $\frac{\rho_{AB}^e \rho_{BA}}{Q_2}$ |
| 12 |  | -  | +2 | $j^+$ | $j_{B,1}^-$   | $\frac{\rho_{AB} \rho_{BA}^e}{Q_2}$ |

|    |   |    |    |       |               |                                       |
|----|---|----|----|-------|---------------|---------------------------------------|
| 13 |    | 0  | -  | $j^+$ | $j_{A,2}^-$   | $\frac{\rho_{BA}^e \rho_{AB}^e}{Q_1}$ |
| 14 |    | -  | 0  | $j^+$ | $j_{A,1,e}^-$ | $\frac{\rho_{BA}^e \rho_{AB}^e}{Q_1}$ |
| 15 |   | -2 | -2 | $j^+$ | $j_{A,1,e}^-$ | $\frac{\rho_A^e \rho_A^e}{Q_1}$       |
| 16 |  | 0  | 0  | $j^+$ | $j_{B,1,e}^-$ | $\frac{\rho_B^e \rho_B^e}{Q_2}$       |

# Bibliography

- (1) Li, J.; Tilbury, C. J.; Kim, S. H.; Doherty, M. F. A design aid for crystal growth engineering. *Progress in Materials Science* **2016**, *82*, 1–38.
- (2) Li, J.; Tilbury, C. J.; Joswiak, M. N.; Peters, B.; Doherty, M. F. Rate Expressions for Kink Attachment and Detachment During Crystal Growth. *Crystal Growth & Design* **2016**, *16*, 3313–3322.
- (3) Dekking, F. M.; Kraaikamp, C.; Lopuhaä, H. P.; Meester, L. E., *A Modern Introduction to Probability and Statistics: Understanding why and how*; Springer: 2005; Vol. 488.
- (4) Cuppen, H. M.; Meekes, H.; van Enkevort, W. J. P.; Vlieg, E. Kink incorporation and step propagation in a non-Kossel model. *Surface Science* **2004**, *571*, 41–62.
- (5) Grimbergen, R.; Meekes, H.; Bennema, P.; Strom, C.; Vogels, L. On the prediction of crystal morphology. I. The Hartman–Perdok theory revisited. *Acta Crystallographica Section A: Foundations of Crystallography* **1998**, *54*, 491–500.
- (6) Bennema, P. In *Handbook of Crystal Growth, Vol. 1A*, Hurle, D. T. J., Ed.; Elsevier: Amsterdam, 1993; Chapter 7, p 477.
- (7) Grimbergen, R. F. P.; Reedijk, M. F.; Meekes, H.; Bennema, P. Growth behavior of crystal faces containing symmetry-related connected nets: a case study of naph-

- thalene and anthracene. *The Journal of Physical Chemistry B* **1998**, *102*, 2646–2653.
- (8) Gavezzotti, A. Efficient computer modeling of organic materials. The atom–atom, Coulomb–London–Pauli (AA-CLP) model for intermolecular electrostatic-polarization, dispersion and repulsion energies. *New Journal of Chemistry* **2011**, *35*, 1360–1368.
- (9) Van Oss, C. J.; Chaudhury, M.; Good, R. J. Monopolar surfaces. *Advances in Colloid and Interface Science* **1987**, *28*, 35–64.
- (10) Van Oss, C.; Good, R.; Chaudhury, M. Additive and nonadditive surface tension components and the interpretation of contact angles. *Langmuir* **1988**, *4*, 884–891.
- (11) Modi, S. R.; Dantuluri, A. K.; Puri, V.; Pawar, Y. B.; Nandekar, P.; Sangamwar, A. T.; Perumalla, S. R.; Sun, C. C.; Bansal, A. K. Impact of crystal habit on biopharmaceutical performance of celecoxib. *Crystal Growth & Design* **2013**, *13*, 2824–2832.
- (12) Ferrari, E. S.; Davey, R. J.; Cross, W. I.; Gillon, A. L.; Towler, C. S. Crystallization in polymorphic systems: the solution-mediated transformation of  $\beta$  to  $\alpha$  glycine. *Crystal Growth & Design* **2003**, *3*, 53–60.
- (13) Lynch, A.; Soto, R.; Rasmuson, Å. Single Crystal Growth Kinetics of Two Polymorphs of Piracetam. *Crystal Growth & Design* **2021**, *21*, 5631–5640.



# Appendix C

## Surface Partition Functions and Configuration Constraints

Reproduced in part with permission from:

Padwal, N. A.; Doherty, M. F. Nonequilibrium Crystal Growth Model for Organic Molecules of Real API Complexity. *Crystal Growth & Design*. (Manuscript under review)

In order to maintain the local step structure, the distribution of kinks along the step is spatially correlated. The correlated nature of surface kinks in case of step configurations with multiple growth units is discussed in Chapter 3. The inability of equilibrium kink density models in accounting for these correlations, yields them deficient. Being a kinetics-based modeling approach, SSSF provides the organisation to appropriately account for the probability of surface sites and the rate of elementary events along steps. Within the steady-state approach of SSSF, surface correlations are captured through conditional probabilities and arise in the form of surface partition functions and the configurational constraints.

For a given step configuration, partition functions are collections of kink densities

arising out of constraints to maintain surface topology. For a given step configuration, the neighboring environment of growth units is fixed by crystallography of the unit cell. In order to maintain the step configuration, incoming molecules from the solution can only be docked in specific orientations depending on the spatial location. This restricts permissible neighboring kinks. For instance, consider configuration 3 of an AB crystal in Fig. B.1. Given the presence of A growth unit at a step location, the structurally permissible kinks around the growth unit are constrained to be only a subset of the predominant junctions, which are on either sides of the growth unit as depicted in Fig. C.1.

$$Q_1 = (\rho_{AB} + \rho_{AB}^e + \rho_{BA}^w) + \rho_A^e + \rho_A^w \quad (\text{C.1})$$

$$= (\rho_{BA} + \rho_{BA}^e + \rho_{AB}^w) + \rho_A^e + \rho_A^w \quad (\text{C.2})$$

where  $\rho_A^e$ ,  $\rho_A^w$ ,  $\rho_B^e$ ,  $\rho_B^w$ ,  $\rho_{AA}^e$ ,  $\rho_{AA}^w$ ,  $\rho_{BB}^e$ ,  $\rho_{BB}^w$ ,  $\rho_{AB}$ ,  $\rho_{BA}$  are the densities of  $A^e$  kink,  $A^w$  kink,  $B^e$  kink,  $B^w$  kink,  $AA^e$  kink,  $AA^w$  kink,  $BB^e$  kink,  $BB^w$  kink,  $AB$  edge and  $BA$  edge, respectively.

When the same procedure is repeated for growth unit B, we get the following equation,

$$Q_2 = (\rho_{AB} + \rho_{AB}^e + \rho_{BA}^w) + \rho_B^e + \rho_B^w \quad (\text{C.3})$$

$$= (\rho_{BA} + \rho_{BA}^e + \rho_{AB}^w) + \rho_B^e + \rho_B^w \quad (\text{C.4})$$

In this case, since the sets of kink types on either side of the growth units are different, we get the following constraint,

$$\hat{\rho} = \rho_{AB} + \rho_{AB}^e + \rho_{BA}^w = \rho_{BA} + \rho_{BA}^e + \rho_{AB}^w \quad (\text{C.5})$$

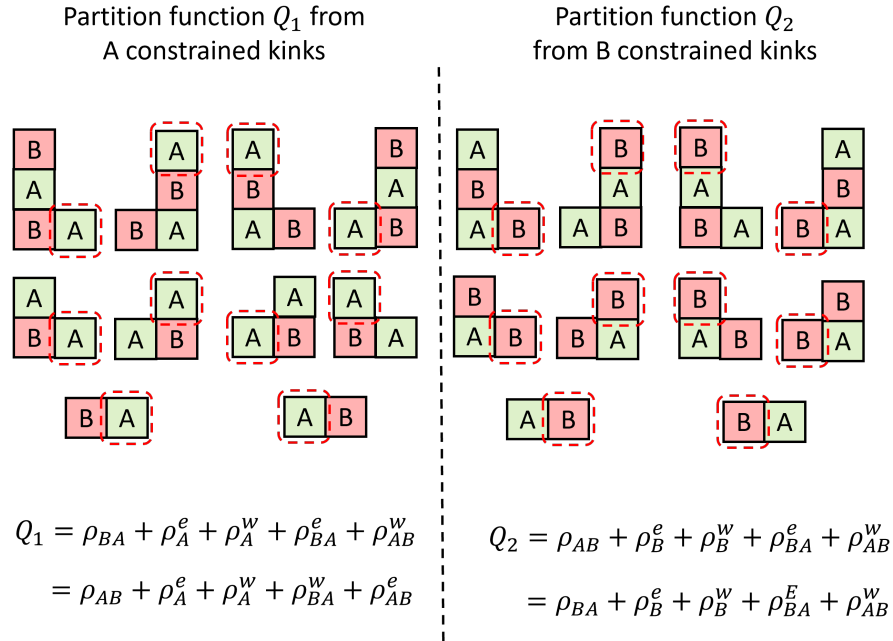


Figure C.1: Collections of kink types constrained by growth units along step configuration with checkered pattern of A and B growth units, resulting in partition functions  $Q_1$  and  $Q_2$ , respectively.

This is the configurational constraint arising out of the restriction placed on possible kink structures by growth units, The partition functions for this step configuration can be simplified as follows,

$$Q_1 = \hat{\rho} + \rho_A^e + \rho_A^w \tag{C.6}$$

$$Q_2 = \hat{\rho} + \rho_B^e + \rho_B^w \tag{C.7}$$

For certain configurations such as the one with alternate rows of A and B, in case of identical sets on either sides of A and B, there will be no configurational constraint as discussed in Chapter 3. Nonetheless, we obtain two partition functions for each of the growth units.

For crystals with four growth units in the unit cell, consider the step configuration 1 with rows of a single growth unit in Fig. C.2. The partition functions are determined

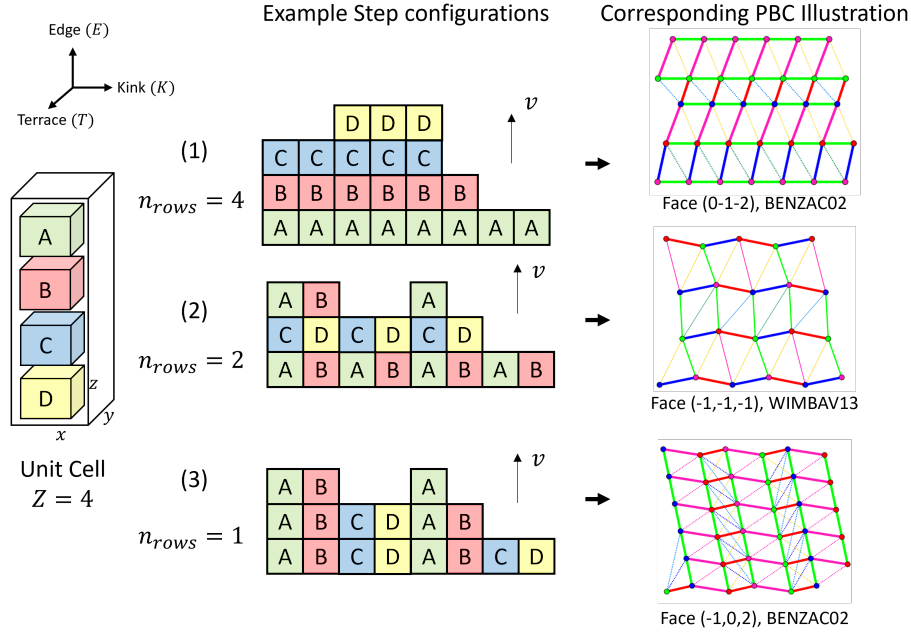


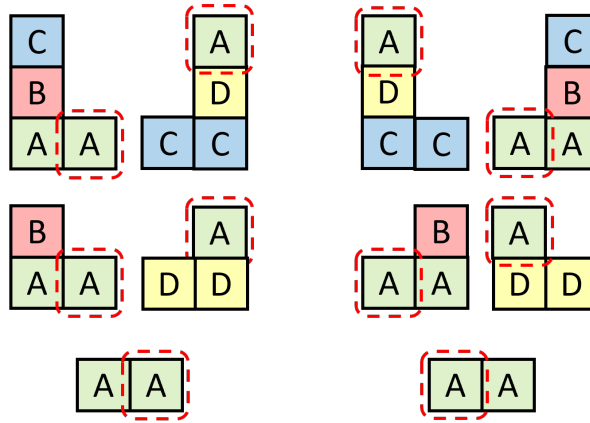
Figure C.2: Some configuration types of steps on crystals with four growth units in the unit cell namely A, B, C and D.

by studying the groups of kink densities permissible on both ends of the growth units as depicted in Fig. C.3 for an A growth unit. Similar partition functions are constructed for the rest of the growth units and are given below.

$$\begin{aligned}
 Q_1 &= \rho_{A0} + \rho_A/2 + \rho_B/2 + \rho_{AD}/2 + \rho_{CB}/2 \\
 Q_2 &= \rho_{B0} + \rho_B/2 + \rho_C/2 + \rho_{BA}/2 + \rho_{DC}/2 \\
 Q_3 &= \rho_{C0} + \rho_C/2 + \rho_D/2 + \rho_{CB}/2 + \rho_{AD}/2 \\
 Q_4 &= \rho_{D0} + \rho_D/2 + \rho_A/2 + \rho_{DC}/2 + \rho_{BA}/2
 \end{aligned} \tag{C.8}$$

where  $\rho_A, \rho_B, \rho_C, \rho_D$ , are the A, B, C and D single-height kinks, respectively.  $\rho_{AD}, \rho_{DC}, \rho_{CB}, \rho_{BA}$  are the double-height kinks and  $\rho_{A0}, \rho_{B0}, \rho_{C0}, \rho_{D0}$  are the respective flat edge A, B, C and D edge junctions, respectively. Step configurations with single growth unit rows results in east and west kink types to be identical and hence considered in combination, give rise to the factors of one half in Eq. C.8. In a similar fashion, partition functions

Partition function  $Q_1$  from  
A constrained kinks



$$Q_1 = \rho_{A0} + \frac{\rho_B}{2} + \frac{\rho_A}{2} + \frac{\rho_{CB}}{2} + \frac{\rho_{AD}}{2}$$

Figure C.3: Collections of kink types constrained by A growth unit along step configuration 1 with rows of growth units, resulting in the partition function  $Q_1$ . PBCs are generated using the software ADDICT.[1]

and configuration constraints are derived for each of the other step configurations. This allows effective capture of spatial correlations between kink types owing to step topology.

# Bibliography

- (1) Li, J.; Tilbury, C. J.; Kim, S. H.; Doherty, M. F. A design aid for crystal growth engineering. *Progress in Materials Science* **2016**, *82*, 1–38.

## Appendix D

# Identification & Assignment of Step Configuration for $Z = 4$ Crystal

Reproduced in part with permission from:

Padwal, N. A.; Doherty, M. F. Nonequilibrium Crystal Growth Model for Organic Molecules of Real API Complexity. *Crystal Growth & Design*. (Manuscript under review)

The identification of permissible configurations can be simplified through a categorization of configuration types with 1, 2 or more growth units per row. A permissible configuration is one where a particular growth unit has identical interaction environment irrespective of its position along the step. This is because crystals are characterized by long range order, where the unit cell is the minimum repeating unit. Translation of the unit cell along the three axes yields the crystal structure of the compound. The unit cell may consist of multiple growth units. Each growth unit within the unit cell is characterized by unique interaction networks. Nonetheless, the translational symmetry of crystals ensures that a particular growth unit will have identical interaction network irrespective of its position in the crystal lattice. By extension, a particular growth unit must also

have identical environments at all positions in a step configuration. All the permissible step configurations for a  $Z = 4$  crystal are given in Fig. D.1.



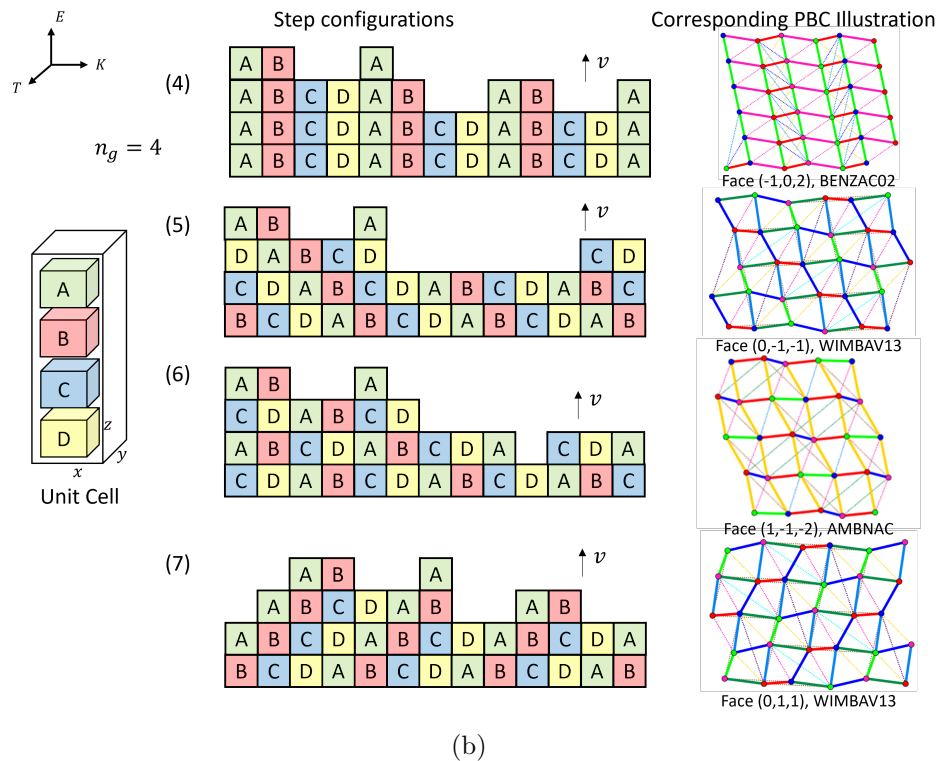
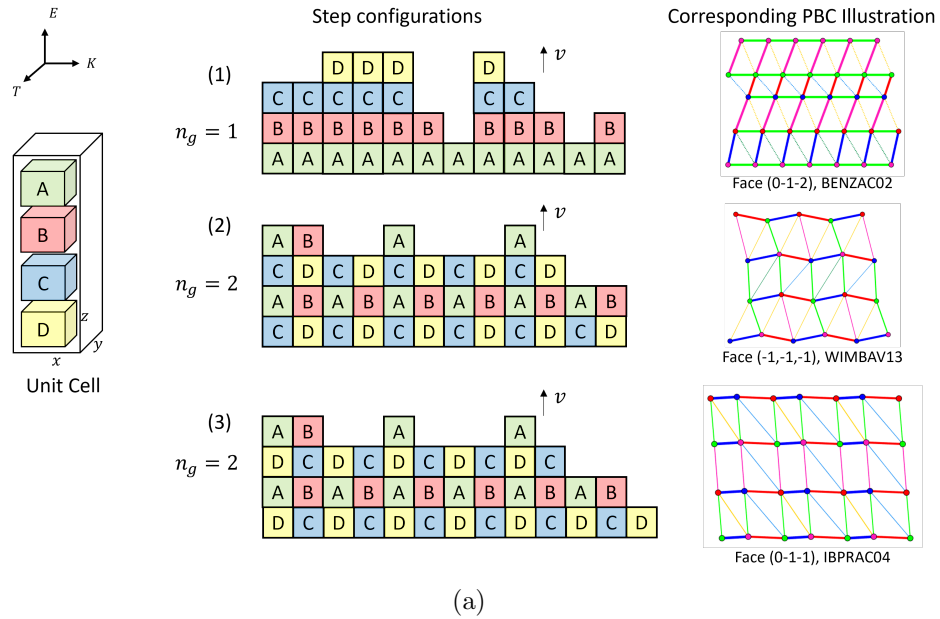


Figure D.1: All permissible step configuration types for a crystal with four growth units A, B, C, D in the unit cell. PBC networks are generated using the software ADDICT.[1]

Based on the number of growth units per row  $n_g$ , the  $Z = 4$  crystal has the following

types of configurations: 1) configuration 1 with  $n_g = 1$ ; 2) configurations 2 and 3 with  $n_g = 2$ ; 3) configurations 4, 5, 6 and 7 with  $n_g = 4$ . However, configurations 2 and 3 are equivalent because they have identical topology with C and D growth units swapped. The equation sets can be reproduced from each other by simply exchanging the definitions of growth units C and D. Hence, effectively  $Z = 4$  crystals have steps belonging in a total of six permissible configurations.

The crystallographically impermissible configurations are disqualified because they have identical growth units in more than one kind of interaction environment. Examples of such configurations are given in Fig. D.2 for an ABCD and AB crystal types. It is important to identify all possible step configurations growing along crystal facets of multi-growth unit crystals. Study of PBC networks of actual compounds can help assess and validate configuration types as provided by the PBC illustrations in Fig. D.1.

Application of SSSF to real molecules requires assignment of appropriate configuration to PBC networks of various step structures. In case of nonorthogonal lattices much like the PBC illustrations of model step configurations in Fig. D.1, the configuration assignment is based on the directions of strongest PBCs along the face slice.[1]

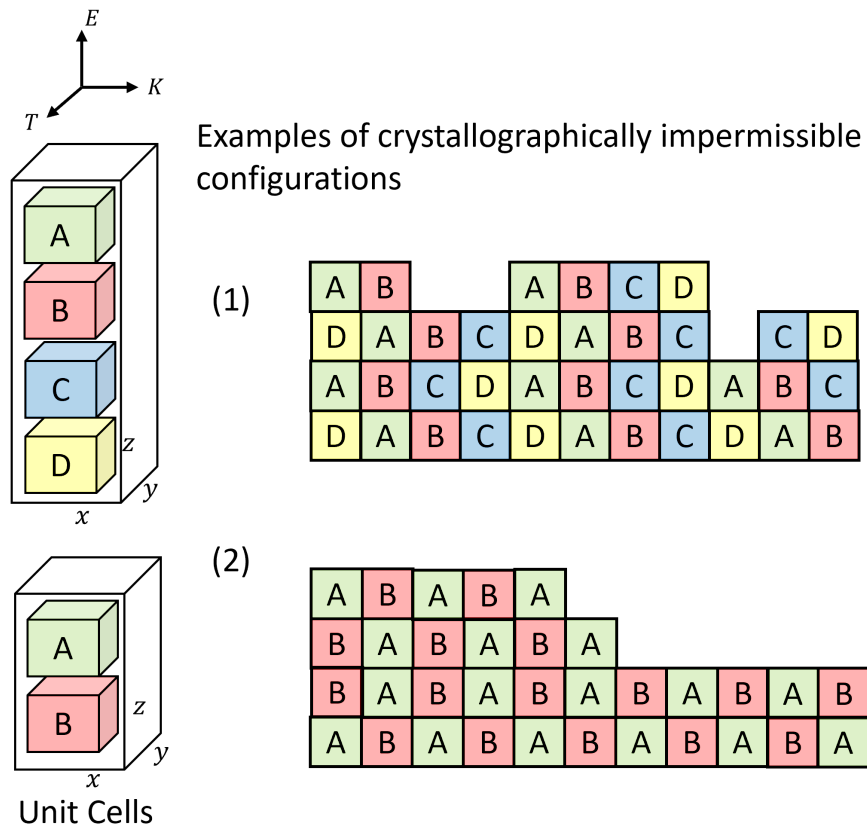


Figure D.2: Examples of crystallographically impermissible configurations in a crystal with 4 and 2 growth units in the unit cell, respectively.

# Bibliography

- (1) Li, J.; Tilbury, C. J.; Kim, S. H.; Doherty, M. F. A design aid for crystal growth engineering. *Progress in Materials Science* **2016**, *82*, 1–38.

# Appendix E

## SSSF & Kink Cycle Frameworks: Similarities and Differences

Reproduced in part from the supplementary information with permission from:  
Padwal, N.A.; Doherty, M.F., Simple Accurate Nonequilibrium Step Velocity Model for  
Crystal Growth of Symmetric Organic Molecules. *Crystal Growth & Design* **2022**, 22(6),  
3656-3661.

DOI:10.1021/acs.cgd.1c01366. Copyright 2022 American Chemical Society.

Kuvadia and Doherty[1] formulate steady-state equations in terms of probabilities of kink state  $k$  by balancing flux into and out of state  $k$  via attachment and detachment of growth units. In such a framework, a cyclic progression of kink types is assumed, referred to in the paper as the kink cycle approach. The probabilities can be interpreted as relative kink densities such that  $P_k = \frac{\rho_k}{\sum \rho}$  where  $\rho_k$  is the kink density of kink type  $k$ .

$$P_{k-1}\alpha + P_{k+1}\nu_{k+1} = P_k(\alpha + \nu_k) \quad (\text{E.1})$$

where state  $k = 1, 2, 3, \dots, n$ ,  $n$  is the number of different kink types in a single orientation,  $\alpha$  is the isotropic attachment rate,  $\nu_k$  is the detachment rate at state  $k$  ( $\alpha \equiv j^+$ ,  $\nu_k \equiv j_k^-$ ). The states repeat periodically: for  $n = 4$ ,  $k = 1$  to 4 such that when  $k = 1$ , in Eq. E.1,  $k - 1$  is 4. Similarly for  $k = 4$ ,  $k + 1$  is 1. For  $n = 4$ , we get the following set of steady-state equations,

$$\begin{aligned}
 P_4\alpha + P_2\nu_2 &= P_1(\alpha + \nu_1) \\
 P_1\alpha + P_3\nu_3 &= P_2(\alpha + \nu_2) \\
 P_2\alpha + P_4\nu_4 &= P_3(\alpha + \nu_3) \\
 P_3\alpha + P_1\nu_1 &= P_4(\alpha + \nu_4)
 \end{aligned}
 \tag{E.2}$$

Note that the above set of equations generated from the kink cycle framework do not account for 1D nucleation and assumes step progression is a culmination of attachment at various kink states and not limited by 1D nucleation. Hence the equations do not include edge densities and are expressed entirely in terms of kink state probabilities. At steady-state, the kink rate is defined as the net rate of incorporation of growth units at kinks.

$$u = n(\alpha P_k - \nu_{k+1} P_{k+1}) \tag{E.3}$$

The kink rate  $u$  is constant across all kink types as evidenced via rearrangement of Eq. E.1. The set of equations in Eqs. E.2 is linearly dependent and hence combined with the normalization condition to be solvable.

$$\sum_k^n P_k = P_1 + P_2 + P_3 + P_4 = 1 \tag{E.4}$$

Solving Eqs. E.2-E.4 gives the following expression for kink rate  $u$ ,

$$u = n[P_k\alpha - P_{k+1}\nu_{k+1}] \quad (\text{E.5})$$

$$= n \frac{(\alpha^n - \nu^{(n)})}{\sum_{r=1}^n \alpha^{n-r} \nu^{(r-1)}} \quad (\text{E.6})$$

The kink rate is then used for modeling step velocity as,

$$v = a_P \rho_T u \quad (\text{E.7})$$

where  $a_P$  is the propagation length, and the total kink density  $\rho_T = \sum \rho$  is obtained by equilibrium kink density models defined by Kuvadia and Doherty[1].

The SSSF models step velocity as the summation of net attachment rates  $J_k$  at all kink types. Eqns. 3.25-3.26, B.14-B.15, B.35-B.36 provide net attachment rate expressions for step configurations 1, 2 and 3, respectively. The net attachment rates are summations of individual event rates, which are expressed as products of specific site density (product of kink densities) and elementary rate within SSSF. Alternatively, the kink cycle approach also expresses  $J_k$  in terms of individual event rates, which in turn are expressed as product of the specific kink density and elementary rate. This is because SSSF treats an event as occurring at sites, while the kink cycle approach treats an event as occurring at kinks. Such a distinction allows the SSSF to account for the nucleation rates as well and obtain steady-state equations directly in terms of the kink densities ( $\rho_k$ ) instead of the state probabilities ( $P_k$ ). In order to interpret the kink cycle approach through the SSSF

lens, we expand the step velocity as follows,

$$v = a_P \sum_{k=1}^n J_k \quad (\text{E.8})$$

$$= a_P \sum_{k=1}^n \rho_k (\alpha - \nu_k) \quad (\text{E.9})$$

For  $n = 4$  and  $k = 1$  to 4 we get,

$$v = a_P(\rho_1(\alpha - \nu_1) + \rho_2(\alpha - \nu_2) + \rho_3(\alpha - \nu_3) + \rho_4(\alpha - \nu_4)) \quad (\text{E.10})$$

Multiplying and dividing by the total kink density  $\rho_T$ , followed by reorganization of terms gives,

$$v = a_P(\rho_1 + \rho_2 + \rho_3 + \rho_4)(P_1(\alpha - \nu_1) + P_2(\alpha - \nu_2) + P_3(\alpha - \nu_3) + P_4(\alpha - \nu_4)) \quad (\text{E.11})$$

$$= a_P \rho_T ((P_1\alpha - P_2\nu_2) + (P_2\alpha - P_3\nu_3) + (P_3\alpha - P_4\nu_4) + (P_4\alpha - P_1\nu_1)) \quad (\text{E.12})$$

$$= a_P \rho_T \times 4(P_1\alpha - P_2\nu_2) \quad (\text{E.13})$$

$$= a_P \rho_T u \quad (\text{E.14})$$

Therefore, the SSSF accounts for attachment and detachment events at kink types along with several other events such as formation of adatoms, denucleation and formation of pits. Hence SSSF encompasses all events accounted for by the kink cycle approach and some more. Moreover, the SSSF equations are written in terms of edge and kink densities and hence the solution provides true steady-state kink densities as opposed to the probabilities  $P_k$  in the kink cycle approach.



# Bibliography

- (1) Kuvadia, Z. B.; Doherty, M. F. Spiral Growth Model for Faceted Crystals of Non-Centrosymmetric Organic Molecules Grown from Solution. *Crystal Growth & Design* **2011**, *11*, 2780–2802.